Novel Magnetic Materials Based on Macrocyclic Ligands:

Towards High Relaxivity Contrast Agents and Mononuclear Single-Molecule Magnets

Emma Stares

A thesis submitted to the Department of Chemistry

in partial fulfillment of the requirements for the Degree of Doctor of Philosophy

Supervised by

Professor Melanie Pilkington

Brock University

St. Catharines Ontario, Canada

August 2015

Abstract

The preparation and characterization of coordination complexes of Schiff-base and crown ether macrocycles is presented, for application as contrast agents for magnetic resonance imaging, **Project 1**; and single-molecule magnets (SMMs), **Projects 2** and **3**.

In **Project 1**, a family of eight Mn^{II} and Gd^{III} complexes of N_3X_2 (X = NH, O) and N_3O_3 Schiff-base macrocycles were synthesized, characterized, and evaluated as potential contrast agents for MRI. *In vitro* and *in vivo* (rodent) studies indicate that the studied complexes display efficient contrast behaviour, negligible toxicity, and rapid excretion.

In **Project 2**, Dy^{III} complexes of Schiff-base macrocycles were prepared with a view to developing a new family of mononuclear Ln-SMMs with pseudo-D_{5h} geometries. Each complex displayed slow relaxation of magnetization, with magnetically-derived energy barriers in the range $U_{eff} = 4 – 24$ K.

In **Project 3**, coordination complexes of selected later lanthanides with various crown ether ligands were synthesized. Two families of complexes were structurally and magnetically analyzed: ‘axial’ or sandwich-type complexes based on 12-crown-4 and 15-crown-5; and ‘equatorial’ complexes based on 18-crown-6. Magnetic data are supported by *ab initio* calculations and luminescence measurements. Significantly, the first mononuclear Ln-SMM prepared from a crown ether ligand is described.

Acknowledgments

First and foremost, thank you to Dr. Melanie Pilkington for her patient guidance over the past four-and-a-half years. Thank you for having great ideas, for turning us all into independent researchers (whether we like it or not!), and for being a kind, funny and supportive boss.

A huge thank you to all the members the Pilkington Group, past and present, for the fun, friendship and support; with a special shout-out to the 'originals:' Shari, Roger, Roland, Peter, and Nick H who showed me all their wise lab ways; to Majeda, Marnie, Jeff, Kevan and John for all the great chats; and to our Cairns neighbours Terry, Nick M, and Kseniya for the coffee runs, Lester Ds and movie nights, and general good times.

Thank you to my committee members, Dr. Travis Dudding and Dr. Theocharis Stamatatos, for their ongoing help and advice.

A special thank you to Dr. Stamatatos and Dr. Jeremy Rawson (University of Windsor) for teaching me to interpret magnetic data and answering a lot of questions along the way; also to Dr. Fereidoon Razavi for allowing us so much time on the MPMS and PPMS, and to Jory Korobanik, for showing me how to use them.

A great big hug goes to Majeda Al Hareri for her summer of dedicated synthetic work on the crown project; and an 'air high five' to Jeffery Regier, for figuring out the mystery that is MOLCAS and performing calculations on the crown complexes.

Thanks to the wonderful Tim Jones for his mass spectrometry measurements, especially on our finicky Schiff-base macrocyclic complexes; and to Razvan Simonescu, for his help gathering high-field relaxivity measurements on the NMR machines.

Thank you to Dr. Warren Foltz and Dr. Deborah Scollard (STTARR), and the staff at the Animal Resource Center, for their guidance and help with designing and performing the animal studies; and to Dr. Meegan Larsen (Mbed Pathology) for her work performing necropsies and histopathology.

Special thanks also to our collaborators for their important contributions to this thesis: Yassine Beldjoudi (University of Windsor) and Dr. John Wallis (Nottingham Trent University) for performing TGA and powder diffraction measurements; Dr. Fereidoon Razavi (Brock University) for the heat capacity measurements; Dr. Ian Brindle and Yong Wang (Brock University) for ICP-MS measurements; Dr. Steve Kornic (McMaster University) for far-IR and Raman measurements; and Dr. Rute Ferreira (University of Aveiro) for gathering and modelling the luminescence data.

Finally, thank you to my family and friends; and especially my amazing husband Dave, for his unfailing encouragement and support.

Table of Contents

List of Tables

List of Figures

List of Schemes

List of Abbreviations

0-D	zero-dimension
1-D	one-dimension
2-D	two-dimension
3-D	three-dimension
Å	angstrom
B.M.	Bohr magneton
br	broad (NMR and IR peak descriptor)
calcd.	calculated
C	Curie constant
°C	degrees celsius
$CDCl_3$	deuterated chloroform
CH_3	methyl
CH_2Cl_2	dichloromethane
CH_3CN	acetonitrile
CN	cyanide
CSM	continuous shape measure
d	doublet
D	zero-field splitting parameter
dd	doublet of doublets
DCM	dichloromethane
DMF	dimethyl formamide
DMSO	dimethyl sulfoxide
EI	electron impact ionization
Et	ethyl
Et_3N	triethyl amine
Et_2O	diethyl ether
EtOAc	ethyl acetate

EtOH	ethanol
FAB	fast-atom bombardment
g	grams
g	g-factor, proportionality constant
h	hour(s)
H	applied magnetic field
H_c	coercive magnetic field
HOMO	highest occupied molecular orbital
HS	high spin
Hz	hertz
i-Pr	isopropyl
IR	infrared
J	coupling constant (NMR); total angular momentum quantum number
K	Kelvin
KBr	potassium bromide
L	total orbital angular momentum quantum number
LIESST	light-induced excited state spin trapping
LS	low spin
LUMO	lowest unoccupied molecular orbital
m	multiplet
mol	moles
M	magnetization
min	minutes
M_J	secondary total angular momentum quantum number
MeOH	methanol
mL	milliliters
mmol	millimole
M.p	melting point
M_r	remnant magnetization
ms	millisecond

M_S	spin quantum number
MS	mass spectrometry
m/z	mass/charge ratio
NaCl	sodium chloride
NaOH	sodium hydroxide
NMR	nuclear magnetic resonance
nm	nanometer
Ph	phenyl
ppm	parts per million
py	pyridine
R	agreement factor
r.t.	room temperature
s	singlet
S	total spin angular momentum quantum number
SCO	spin crossover
SCM	single chain magnets
SMM	single molecule magnets
SOC	spin-orbit coupling
SQUID	superconducting quantum interference device
str	stretch
t	triplet
T	temperature
T_c	critical temperature
T_N	Neel temperature
THF	tetrahydrofuran
tlc	thin layer chromatography
U_{eff}	effective anisotropy barrier
UV-visible	ultra violet-visible
μ_B	Bohr magneton
μ_{eff}	magnetic moment
ZFS	zero-field splitting

λ	wavelength
χ	magnetic susceptibility
χ_M	molar magnetic susceptibility

List of Publications

Chapter 1:

Coordination complexes of 15-membered pentadentate aza, oxoaza and thiaaza Schiff-base macrocycles: old complexes offer new attractions.

E. L. Gavey and M.Pilkington, Coord. Chem. Rev. **2015**, *296*, 125

Chapter 2:

Methods and compounds for enhancing contrast in magnetic resonance imaging (MRI).

E. L. Gavey and M. Pilkington, U.S. Provisional Patent Application No. 62/174,752, filed June 12, 2015.

Chapter 3:

Slow relaxation in the first pentaaza Dy^{III} macrocyclic complex.

E.L. Gavey, Y. Beldjoudi, J.M. Rawson, T. Stamatatos and M. Pilkington, Chem. Commun. **2014**, *50*, 3741.

Chapter 4:

Placing a crown on Dy^{III} - a dual property Ln^{III} complex displaying optical properties and SMM behaviour.

E. L. Gavey, M. Al Hareri, J. Regier, L. D. Carlos, R. A.S. Ferreira, F. S. Razavi, J. M. Rawson and M. Pilkington, J. Mat. Chem. C **2015,** *3*, 7738.

1 INTRODUCTION

Over the last two decades, the field of molecular magnetism has enjoyed a surge of popularity. My research focusses on the development of new magnetic materials from macrocyclic ligands for application in two areas: the development of novel contrast agents for magnetic resonance imaging (MRI), and the study of lanthanide single-molecule magnets (Ln-SMMs). The two classes of ligand utilized are Schiff-base macrocycles, and crown ethers. The division of my work into three projects based on ligand class and application is shown below.

Project	Class of cyclic ligand	Metal ion(s) coordinated	Magnetic behaviour studied	Application
1 (Ch. 2)	Schiff-base macrocycles	Mn^{II} and Gd^{III}	Relaxivity	MRI contrast agents
2 (Ch. 3)	Schiff-base macrocycles	Dy^{III}	Dc and ac susceptibility	Mononuclear SMMs
3 (Ch. 4)	Crown ethers	Tb^{III}, Dy^{III}, Ho^{III}, Er^{III}	Dc and ac susceptibility	Mononuclear SMMs

This introductory section is divided into two parts. Firstly, the principles behind the two *applications* of my work are given: the theory of magnetic resonance imaging and recent advances in small-molecule contrast agents are discussed (Section 1.1), and an overview of the origins of magnetic behaviour, with a focus on mononuclear single-molecule magnets, is presented (Section 1.2). Secondly, an introduction to the *ligand classes* is given: magnetic materials based on Schiff-base macrocycles are reviewed (Section 1.3), and a brief background to crown ethers is presented (Section 1.4).

1.1 MRI contrast agents

1.1.1 MRI theory

Magnetic resonance imaging (MRI) is a medical technique used to provide 2- and 3D images of tissues and organs in the body. This powerful tool is used to detect, diagnose and monitor diseases including cancer,[1] Alzheimer's[2] and Parkinson's.[3] MRI offers several advantages over other imaging modalities such as X-ray, PET and CT scans in that it is a non-invasive technique, does not require high-energy radiation, and has excellent spatial resolution in the sub-millimeter range.[4]

An MRI image is generated from the nuclei of the hydrogen atoms of water molecules. Since the protons are spinning charged particles, each proton generates a small magnetic moment. In the absence of an applied magnetic field, the spins of these protons are randomly oriented. When a field is applied along, say, the *z*-axis, the individual moments align parallel or antiparallel to the *z* direction. Slightly more spins align parallel than antiparallel, resulting in an overall magnetic moment in the *z* direction (Figure 1).[5] This is known as longitudinal magnetization, M_z. The presence of the field also causes the nuclei to 'wobble' on their axes. This 'wobbling' or precession, occurs at a characteristic frequency directly proportional to the strength of the magnetic field, B_0 (T). The characteristic frequency is called the Larmor frequency, ω_0 (MHz).[5] The ratio of ω_0/B_0 is given by the gyromagnetic ratio, γ_0, which is specific to a given nucleus. The gyromagnetic ratio of ^{1}H is 42.58 MHz/T.[5]

Following alignment, an electromagnetic pulse is applied to the system with precisely enough energy to rotate the longitudinal magnetization vector by exactly 90°, so

that it lies in the transverse plane (Figure 1.1, right). This transverse magnetization, M_{xy}, precesses around the *z* axis, and this rotation gives rise to an alternating current which is the signal recorded as an MRI image.[5]

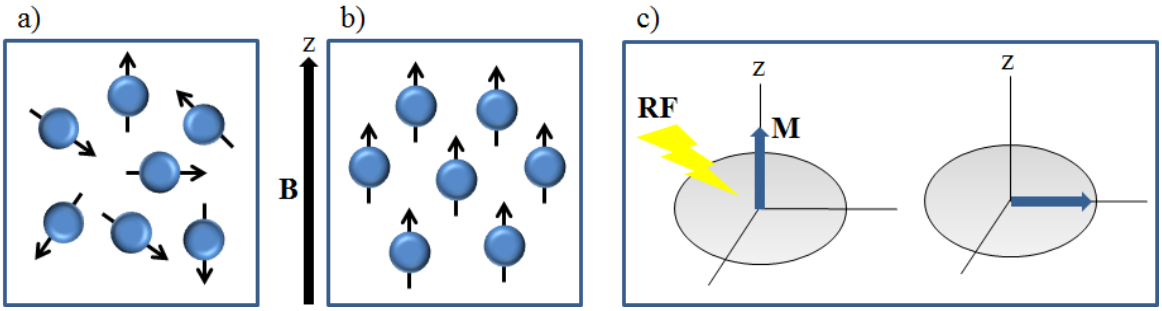

Figure 1.1 a) In the absence of an applied field, the spins of the water protons are randomly oriented; b) when a field **B** is applied, the spins align in the z direction, resulting in longitudinal magnetization **M**; c) when a specific radiofrequency (RF) pulse is applied, the magnetization rotates 90° into the transverse plane. Adapted from Reference 5.

The transverse magnetization M_{xy} decays by two relaxation processes: longitudinal and transverse relaxation. *Longitudinal relaxation*, or spin-lattice relaxation, involves a loss of energy from the precessing magnetic vector to the surrounding environment, causing the signal to decay slowly from the *xy* plane back to the *z* direction. *Transverse relaxation*, or spin-spin relaxation, does not involve a loss of energy; rather, the precessing transverse moments lose their phase coherence, so the individual vectors in the transverse plane begin to cancel each other out, leading to a loss of the MRI signal. Longitudinal and transverse relaxation are described by the relaxation time parameters T_1 and T_2 respectively (s), and are depicted in Figure 1.2.[5]

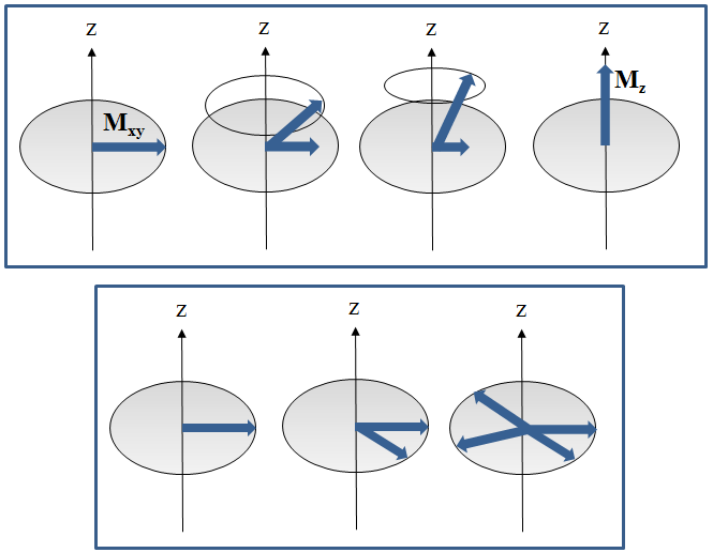

Figure 1.2 The two processes by which transverse magnetization relaxes: top, longitudinal relaxation; bottom, transverse relaxation. Adapted from Reference 5.

Water protons in different tissues and organs of the body have different intrinsic T_1 and T_2 relaxation times, as do healthy versus diseased portions of the same tissue. This results in the natural contrast on an MRI scan. An MRI scan can be 'weighted' to T_1 or T_2, depending on which parameter would allow best visualization of the desired tissue.

Sometimes the natural contrast due to the differences in the biological environments of water protons does not provide enough intensity difference on an MRI image for sufficient detail to be seen. *Contrast agents* are compounds administered to enhance an MRI image, by increasing the signal intensity. Of the 1.5 million MRI scans performed in Canada each year, about a third use contrast agents. Contrast agents contain a paramagnetic ion or ions, which change the local magnetic field strength of a tissue, and interact with the surrounding protons of water molecules, shortening the T_1 and T_2 relaxation times.[5]

Contrast agents can be divided into small-molecule agents, and nanosized agents. 'Small-molecule' agents are complexes smaller than 10 nm in diameter, usually comprising one metal center bound to an organic chelating ligand. In contrast, 'nanosized' agents are the broad class of slightly larger compounds, including both macromolecular agents (liposomal systems, polymers and dendrimers), and inorganic bulk particles. Small-molecule agents are the first and largest class of compounds studied as potential imaging agents; they account for 90% of contrast agent use today; and are the focus of the work presented in **Chapter 2** of this thesis. Therefore these agents will be the most thoroughly reviewed in this introductory section.

1.1.2 Development of contrast agent theory:

Dominated by Gd^{III}(1980-2005)

From 1988, when the first contrast agent was approved for use in humans, until 2006, research into small-molecule agents was focused primarily on complexes of Gd^{III}. This ion has two important properties: seven unpaired electrons, the most of any metal ion; and a slow electronic relaxation time.[4] This latter point sets Gd^{III} apart from other lanthanides which also have large numbers of unpaired electrons since its electronic spin states are much more long-lived, in the range 10^{-8}-10^{-9} s, allowing sufficient interaction between the paramagnetic metal in a given electronic state, and the surrounding water molecules.[4]

The effectiveness of a contrast agent is described by its relaxivity, r_1 or r_2 ($s^{-1}\cdot mM^{-1}$), where:

$$r_1 = \frac{1/T_1}{c} \qquad \text{and} \qquad r_2 = \frac{1/T_2}{c}$$

High values of r_1 and r_2 are desirable. The vast majority of small-molecule agents are utilized as T_1 agents, in T_1-weighted scans. Thus r_1 is the relaxivity parameter usually reported in the literature, and unless otherwise stated, 'relaxivity' will refer to r_1 in the following discussion. Relaxivity is dependent on both the magnetic field applied, and the temperature of the measurement, and so values for these parameters should accompany r_1 values. Most clinical MRI scans are performed in a field of 1.5 T (corresponding to a frequency of 64 MHz based on the ^1H Larmor frequency), however 'low-field scans' as low as 0.3 T (13 MHz) and 'high-field scans' up to 3 T (125 MHz) are also carried out.[4]

The relaxivity effect of a contrast agent is due to dipole-dipole interactions between the nuclei (protons) of water molecules, and the unpaired electrons of the metal center. Relaxation occurs via both an *inner-sphere* mechanism, through the direct interaction of coordinated water molecules with the metal center; and via an *outer-sphere* mechanism, through the indirect effect of the metal center on bulk, non-coordinated water. Based on the 'Solomon-Bloembergen-Morgan Theory' of relaxation, a thorough mathematical model for dipolar interactions developed between 1948 and 1961, the relaxivity of a contrast agent may be maximized by optimizing several key parameters: i) the number of inner-sphere water molecules, described by the hydration number **q**; ii) the length of time inner-sphere water molecules remain coordinated, given by the residence time $\boldsymbol{\tau_M}$, and reflected in the water exchange rate $\boldsymbol{k_{ex}}$; and iii) the rate at which the molecule 'tumbles,' described by the rotational correlation time (time taken for a rotation

of 1 radian), $\boldsymbol{\tau_R}$.[4,5] These parameters are summarized in Figure 1.3. Additional parameters include the interaction of the metal center with outer-sphere water molecules; and the electronic relaxation behaviour of the metal center.[4]

Relaxivity increases as q, τ_R, and k_{ex} increase: in other words, a good contrast agent will bind at least one water molecule, effectively cause it to relax, and then efficiently exchange that water molecule for another to repeat the process in a catalytic fashion.[6]

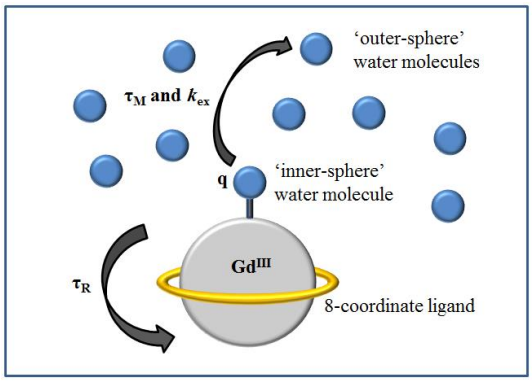

Figure 1.3 Factors affecting relaxivity, where q is the hydration number, τ_M is the water residence time, k_{ex} is the water exchange rate, and τ_M is the rotational correlation time.[4,5]

The design of ligands for small-molecule contrast agents (specifically, Gd^{III} agents during the development of the field from 1980-2005) has centered on two factors: optimizing the parameters described above, for high relaxivity/efficacy; and creating agents which will be stable *in vivo*. Free Gd^{III} has long been recognized as biologically toxic: studies in the 1990s in rats and mice showed significant dose-related toxic effects upon intravenous administration of $GdCl_3$, particularly in the lungs, kidneys and spleen.[7,8] Thus the synthesis of complexes which are both thermodynamically stable and kinetically inert is very important.

1.1.2.1 DTPA and DOTA ligand systems

Two key ligand families have been thoroughly investigated with regards to Gd^{III} contrast agents: the linear chelating ligand DTPA (diethylenetriaminepentaacetic acid) and its derivatives, and the macrocyclic ligand DOTA (tetraazacyclodecanetetraacetic acid) and its derivatives.

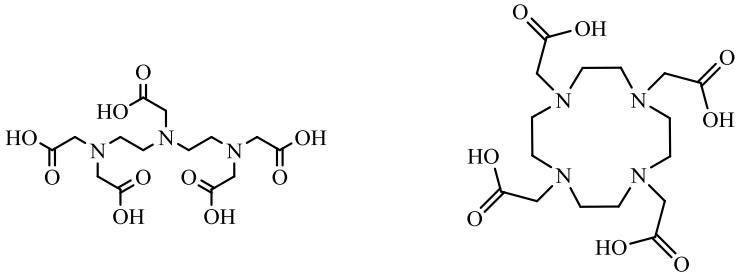

The chelating ligand DTPA binds in an octadentate fashion to Gd^{III} via the three backbone nitrogen atoms and five (deprotonated) oxygen atoms. One inner-sphere water molecule is also bound, resulting in a complex with distorted tricapped trigonal prismatic geometry (Figure 1.4, left).

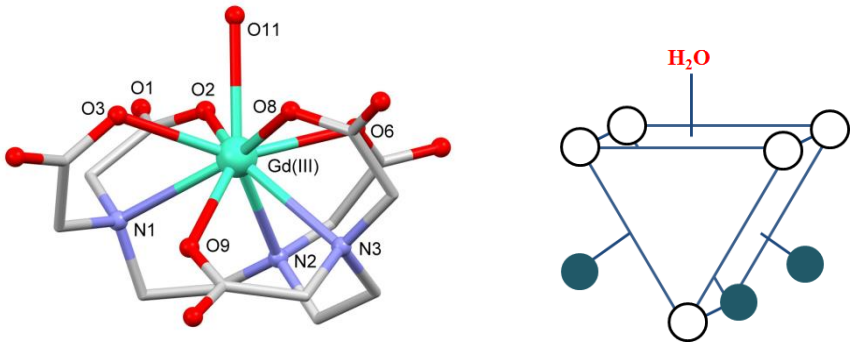

Figure 1.4 Left, crystal structure of $[Gd(DTPA)]^{2-}$. Hydrogen atoms and silver counter ions are omitted for clarity.[9] Right, Schematic showing the tricapped trigonal prismatic geometry of Gd^{III}-DTPA type complexes. blue circles = backbone nitrogen atoms; open circles = donor atoms of pendant arms.[10]

The Gd^{III}-DTPA complex has a relaxivity of 3.4 $mM^{-1}\cdot sec^{-1}$ (20 MHz, 37°C, in water).[4] Along with DTPA itself, Gd^{III} complexes of five derivatives of this macrocycle are approved for clinical use, including ligands with pendant ether, phosphate, and amide groups (Figure 1.5). These derivatives exhibit similar distorted TTP geometries, with the single bound water molecule occupying a 'capped' position opposite the backbone nitrogen atoms (Figure 1.4, right).[4]

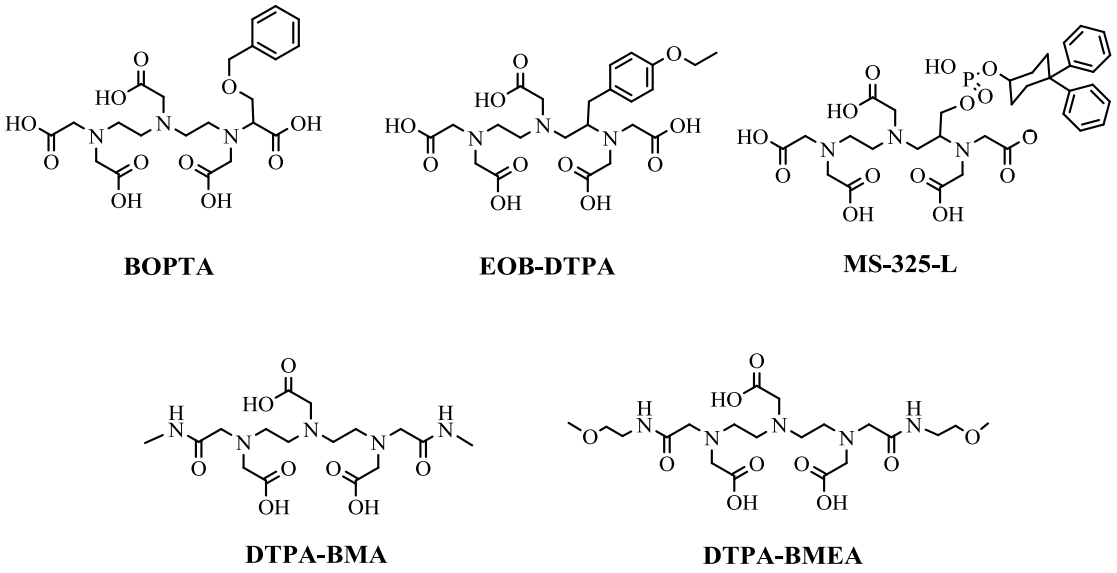

Figure 1.5 Derivatives of DTPA approved for clinical use.[10]

The macrocyclic ligand DOTA also binds in an octadentate fashion, with the four nitrogen atoms forming a plane parallel to, but offset from, the four oxygen atoms of the pendant carboxylic arms. A coordinating water molecule binds above the O_4 plane to give a capped square antiprismatic geometry (Figure 1.6). Complexes of DOTA and its derivatives may be described using three parameters: d, the distance between the N_4 and O_4 planes; ψ, the angle at which the O_4 plane is rotated from the N_4 plane; and ω, the

minimum O-Gd-O angle, also called the 'opening angle.'[4] The key parameter which determines whether a water molecule binds to the Gd^{III} in a DOTA-type complex is the opening angle: ω must be >135° in order for a water molecule to coordinate.[4]

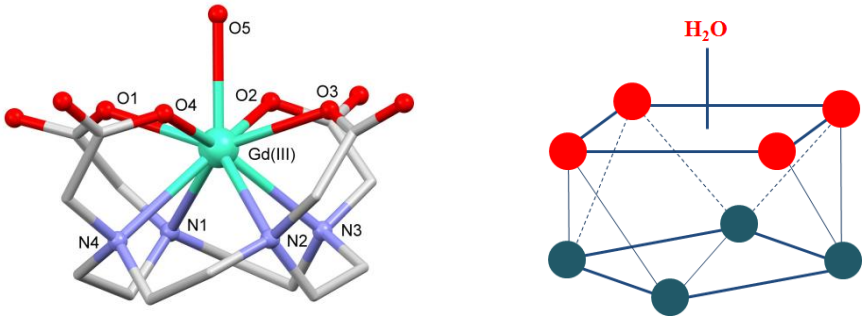

Figure 1.6 Left, crystal structure of $[Gd(DOTA)]^{2-}$. Hygrogen atoms and sodium counter ions are omitted for clarity.[11] Right, schematic showing the capped square antiprismatic geometry of Gd^{III}-DOTA type complexes. Red circles = backbone oxygen atoms; blue circles = pendant nitrogen atoms.[10]

Gd^{III} complexes of two derivatives of DOTA have been approved for clinical use in Canada, both of which have a carboxylic arm substituted by a pendant alcohol (HP-DO3A and DO3A-butrol, Figure 1.7).

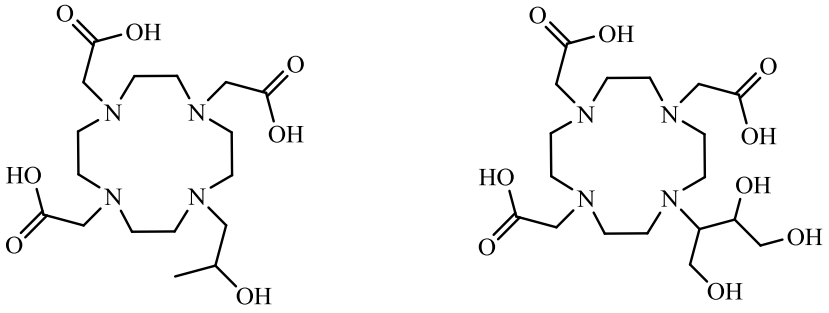

Figure 1.7 Derivatives of DOTA approved for clinical use in Canada. [10]

The formula, drug name, active component and key MRI properties of each of the nine contrast agents approved for use in North America based on DTPA and DOTA are summarized in Table 1.1.

		r_1, r_2 ($s^{-1} \cdot mM^{-1}$)[12]				
Drug Name	**Formula Active Component**	***H_2O 0.47T 37°***	***Plasma 1.5 T 37°***	***Plasma 3 T 37°***	**Clearance**	**Use**
Magnevist	$(MEG)_2[Gd(DTPA)H_2O]$ gadopentetate	**3.4**, 4.0	**4.1**, 4.6	**3.7**, 5.2	renal 1.60 h	CNS, whole body
Eovist or Primovist	$Na_2[Gd(EOB\text{-}DTPA)H_2O]$ gadoxetate	**5.3**, 6.2	**6.9**, 8.7	**6.2**, 11	renal/hepatic 50:50**	liver
Ablavar or Vasovist	$Na_3[Gd(MS\text{-}325\text{-}L)H_2O]$ gadofosveset	**5.8**, 6.7	**19**, 34	**9.9**, 60	renal/hepatic 91:9 18.5 h	blood pool
Multihance	$(MEG)_2[Gd(BOPTA)H_2O]$ gadobenate	**4.2**, 4.8	**6.3**, 8.7	**5.5**, 11	renal/hepatic 96:4 1.2-2 h	CNS, liver
Omniscan	$[Gd(DTPA\text{-}BMA)H_2O]$ gadodiamide	**3.5**, 3.8	**4.3**, 5.2	**4.0**, 5.6	renal 1.30 h	CNS, whole body
OptiMARK	$[Gd(DTPA\text{-}BMEA)H_2O]$ gadoversetamide	**4.2**, 5.2	**4.7**, 5.2	**4.5**, 5.9	renal 1.73 h	CNS, whole body
Dotarem*	$(MEG)[Gd(DOTA)H_2O]$ gadoterate	**3.4**, 4.1	**3.6**, 4.3	**3.5**, 4.9	renal**	CNS, whole body
Prohance	$[Gd(HP\text{-}DO3A)H_2O]$ gadoteridol	**3.1**, 3.7	**4.1**, 5.0	**3.7**, 5.7	renal 1.57 h	CNS, whole body
Gadavist	$[Gd(DO3A\text{-}butrol)H_2O]$ gadobutrol	**3.7**, 5.1	**5.2**, 6.1	**5.0**, 7.1	renal**	CNS, whole body

Table 1.1 Summary of the Gd^{III}-based contrast agents (MEG = meglumine cation, $C_7H_{18}NO_5^+$).[4,10] *Dotarem is not approved for use in Canada, but is approved for use in the USA. **Clearance time data unavailable.

The agents listed in Table 1.1 can be classified in several ways: linear *vs.* macrocyclic, ionic *vs.* neutral, and by site of action. All act as T_1 contrast agents, but they can be divided into whole-body, vascular, and organ-specific agents. *Whole-body* agents such as Gd^{III}-DOTA and Gd^{III}-DTPA distribute into the intravascular and extracellular fluid space of the body post-injection, in contrast to *vascular* agents (Gd^{III}-MS-325-L), which remain in the blood pool; and *organ-specific* agents, such as Gd^{III}-EOB-DTPA,

which is selectively taken up by the liver.[4] The most common dosage is 0.01 $mmol \cdot kg^{-1}$ at a concentration of 0.5 $mol \cdot L^{-1}$, administered intravenously.[4]

For decades, aqueous relaxivities measured in a field of 0.47 T (20 MHz) were the primary reported values with regards to a Gd^{III}-based contrast agents.[10] It is only in recent years that the relaxivities of the approved agents in human plasma at much more clinically relevant fields of 1.5 and 3 T have been reported.[12-14] For this reason, unless otherwise stated, quoted relaxivities of any agent refer to aqueous solutions. From the table above, it is clear that in spite of an increasing understanding of the factors affecting relaxivity, ligand design for the tuning of these parameters is non-trivial. Relaxivity values of small-molecule Gd^{III} agents have not been significantly improved since Gd^{III}-DTPA was first approved 25 years ago: 4.2 $mM^{-1} \cdot sec^{-1}$ for the most powerful whole-body agent Gd^{III}-BOPTA, versus 3.4 $mM^{-1} \cdot sec^{-1}$ for Gd^{III}-DTPA (aq., 20 MHz). The similarity in values is due to the single bound water present in each complex. When relaxivity is measured in plasma at stronger magnetic fields, slightly higher values are observed, with the exception of the vascular agent Gd^{III}-MS-325-L (Ablavar), for which the r_1 value increases from 5.8 to 19 $mM^{-1} \cdot sec^{-1}$ (aq., 20 MHz → plasma, 64 MHz). The reason for this significant increase is that Gd^{III}-MS-325-L binds with human serum albumin (HSA) *in vivo*, resulting in a macromolecular structure with very slow tumbling and thus drastically increased relaxivities.[15]

As mentioned earlier, along with exhibiting effective relaxivity behaviour, Gd^{III}-based complexes must be stable *in vivo*. Both the thermodynamic and kinetic stability of Gd^{III} complexes of DOTA and DTPA derivatives have been well-studied. Due to the chelate and macrocyclic effects, all nine complexes listed in Table 1.1 are very

thermodynamically stable, with stability constants $\log K_{GdL}$ ranging from 16 – 24 (measured in solutions of 0.1 $mol \cdot L^{-1}$ KCl of NMe_4Cl).[4] Gd^{III}-DOTA is more stable than Gd^{III}-DTPA: $\log K_{GdL}$ = 25.3 *vs.* 22.2.[16] The replacement of a carboxylic group with a pendant alcohol to give Gd^{III}-HP-DO3A and Gd^{III}-DO3A-butrol leads to a small decrease in stability: $\log K_{GdL}$ = 23.8 and 20.8 respectively.[16,17] With regards to derivatives of DTPA, the incorporation of pendant amide functionalities causes a more significant decrease in $\log K_{GdL}$ (to 16.8 for both Gd^{III}-DTPA-BMA and –BMEA),[18] while the substitution of an organophosphate arm to give Gd^{III}-MS-325-L resulted in a slight increase in stability (23.2).[19] Most of these stability changes can be attributed to the effect of different substituents on the basicity of the backbone nitrogen atoms: more basic nitrogen atoms = a more thermodynamically stable complex.[4]

Although the small-molecule Gd^{III}-based agents exhibit high thermodynamic stability, *kinetic* stability presents more of an issue. Two undesirable kinetic processes which lead to free Gd^{III} *in vivo* are transmetallation, and dissociation.[4] With regards to transmetallation, the two ions most likely to compete with Gd^{III} in the body are Zn^{II} and Ca^{II}. To this end, the stability of Gd^{III}-DOTA and –DTPA type complexes have been investigated in aqueous solutions of neutral pH, in the presence of Zn^{II} ions.[20] The most kinetically inert complexes with respect to transmetallation were Gd^{III} complexes of macrocyclic DOTA and its derivatives: less than 10% of Gd^{III} centers were displaced after 72 hours. Gd^{III}-DTPA exhibited significantly more transmetallation, with 20% displacement in less than 5 hours. Systems with pendant amide arms resulted in even faster transmetallation, while functionalization on the ethylene linkers resulted in more stable complexes.[4,20] The kinetics of the second process, acid-assisted dissociation, were

examined using solutions of the complexes in 0.1 $mol \cdot L^{-1}$ [H+]. Gd^{III}-DTPA proved to have a dissociation rate constant *k* of 1.2 x 10^3 s^{-1}, two orders of magnitude higher than that of Gd^{III}-DOTA: 0.021 x 10^3 s^{-1}.[4,10] However, pre-clinical *in vivo* studies indicated that the rapid excretion of both families of small-molecule Gd^{III} agents would allow the vast majority of Gd^{III} ions to leave the body in chelated form. [4]

1.1.2.2 Non-DOTA/DTPA systems

Aside from derivatives of these two ligand families, few altogether new ligand systems have been investigated with a view to Gd^{III} agents. One new class of Gd^{III} agent was developed by Raymond and co-workers, based on hydroxopyridinone (HOPO) ligands. These systems comprise three bidentate HOPO moieties linked via a non-coordinating amine backbone. The resulting hexadentate ligands have only oxygen donors, ideal for binding to the oxophilic Gd^{III} ion. The authors note that the mixed N/O donor set of the approved agents is due more to synthetic accessibility than design.[21] The first HOPO system reported was Gd^{III}-TREN-1-Me-3,2-HOPO (Figure 1.8), in which two water molecules are directly bound to the Gd^{III}, resulting in a large increase in relaxivity compared to the DOTA and DTPA systems: r_1 = 10.5 $mM^{-1} \cdot sec^{-1}$ (20 MHz, 37°C).[22] A further promising feature of this system was that the NMRD profile showed a maximum relaxivity at high, clinically relevant fields, in contrast to the approved systems which display their highest relaxivities below 10 MHz.[22] This feature is due to the fact that the water exchange rate for the HOPO-based complexes is close to the optimal value associated with a water residence time of τ_R = 10 ns.[4] In addition, the HOPO-based ligands exhibit good selectivity for Gd^{III} over competing ions such as Zn^{II} and Ca^{II}.[22,23]

In spite of its clear potential, the Gd^{III}-TREN-1-Me-3,2-HOPO complex was not particularly water soluble. Thus Raymond and co-workers have developed an extended family of HOPO-based systems[23] incorporating solubilizing functionalities, such as pendant hydroxyl groups, or mixed 'heteropodal' HOPO ligands, with a second binding modality such as salicylamide.[24] Although no pre-clinal studies have yet been performed, research into this promising family of systems is ongoing.[22]

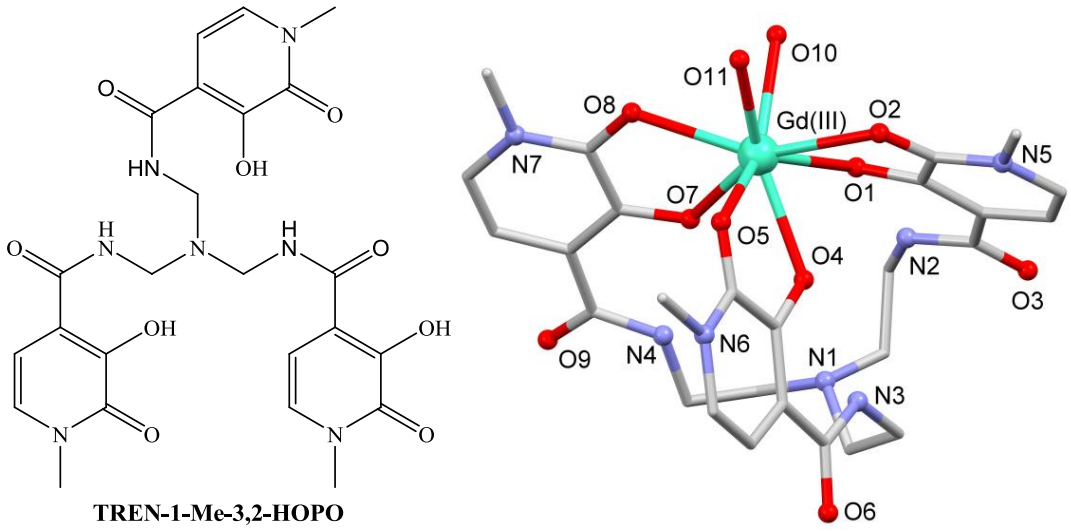

Figure 1.8 Left, the hexadentate TREN-1-Me-3,2-HOPO ligand; right, structure of Gd^{III}-TREN-1-Me-3,2-HOPO.[22]

1.1.2.3 Gd^{III}-based agents and NSF

As described above, the physical factors governing relaxivity were investigated primarily via the study of small-molecule Gd^{III} agents. As noted earlier, a key additional feature of any compound intended for use in humans is that it be non-toxic. Although it was reported early on in contrast agent development that the free Gd^{III} ion had toxic effects in rats and mice,[7,8,25] the chelating and macrocyclic ligands utilized in the

approved Gd^{III} ions were considered to confer sufficient stability on the resulting complexes for safe *in vivo* use.

However, in 2006, a link was found between Gd^{III}-based agents and the acquired disorder nephrogenic systemic fibrosis, or NSF,[26] a debilitating and sometimes fatal disorder in patients with suppressed renal function involving a hardening of the skin, joints, muscles of the heart, and the walls of organs such as the liver.[27] A strong causative link was quickly established between this disease and Gd^{III}-based agents, in particular Omniscan and Magnevist, with the absence of any other common factor between the hundreds of patients afflicted.[26] A possible reason for the previous oversight of the link, in spite of the decades-long history of Gd^{III}-based agent use, is the lag time of at least 25 days before the onset of symptoms.

Following this discovery, there was an immediate surge in publications discussing the safety of Gd^{III}-based agents, both with regards to NSF,[28-30] and a more general investigation into the effects of these agents on heart and kidney health.[31,32] In parallel, the discovery spurred a renewed interest in small molecule agents based on alternate paramagnetic ions: in particular, Mn^{II}.

1.1.3 Advances in small molecule agents:

The rise of Mn^{II}

Although Gd^{III}-based small molecule agents were the focus of attention from 1980-2005, Mn^{II} was actually the very first paramagnetic ion to be considered for enhancing MRI contrast, by the 'Father of MRI' himself, Lauterbur, in 1978.[33] Lauterbur used $MnCl_2$ to visualize diseased versus healthy heart tissue in dogs. Like Gd^{III}, Mn^{II} has several attractive features: a large number of unpaired electrons (S = 5/2), and a long

electronic relaxation time. The key difference between the two ions is that unlike Gd^{III}, Mn^{II} is a biologically essential element, acting as a cofactor for several important enzymes including arginase, the final enzyme in the urea cycle;[34] and glutamine synthetase, which metabolizes nitrogen.[35] The human body requires the maintenance of a serum concentration of at least 0.5 μg/L of Mn^{II} for optimal health.[36] However, in excess, free Mn^{II} can cause toxic effects. Due to its size similarity to Ca^{II}, Mn^{II} binds with ease to Ca^{II} binding sites and can be readily transported across the blood-brain barrier,[37] where it accumulates and causes Parkinson's-like symptoms, including tremors and muscle stiffness: a condition known as 'Manganism.'[38]

The oral contrast agent Lumenhance® was briefly approved by the FDA in 1997 for use in gastrointestinal imaging, but was quickly removed from the market due to toxicity concerns: the active compound was the salt $MnCl_2$, which becomes free Mn^{II} of the form $[Mn(H_2O)_6]^{2+}$ *in vivo*.[39] $MnCl_2$ is now prohibited for use in clinical settings: although Mn^{II} is less toxic than Gd^{III}, and as a free ion exhibits a high r_1 relaxivity of 6.76 $mM^{-1}\cdot sec^{-1}$, it still requires chelation for biocompatibility.[40,41] Currently, there is one Mn^{II}-based MRI contrast agent which is not approved for use in Canada, but is approved for use elsewhere in North America. Teslascan®, or Mangafodipir, consists of a Mn^{II} ion bound to the linear chelating ligand $DPDP^{2-}$ (dipyridoxyl diphosphate). Teslascan is administered intravenously, and acts as a positive-enhancement liver-specific agent.[42] The ligand $DPDP^{2-}$ is a vitamin B12 analogue, which is retained by hepatocytes.[43] At a frequency of 20 MHz in aqueous solution, Teslascan has relaxivity values of $r_1 = 2.8$ and $r_2 = 3.7$ $mM^{-1}\cdot sec^{-1}$.[44]

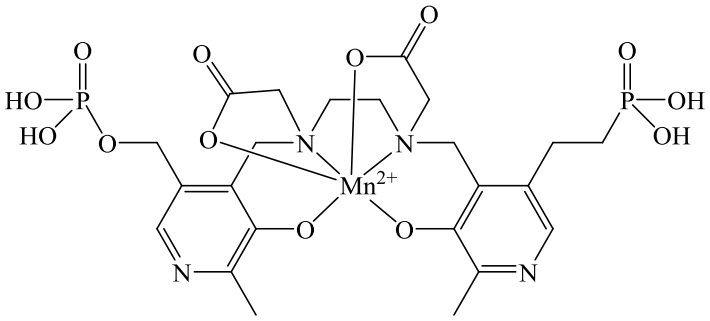

Figure 1.9 Structure of the Mn^{II}-based contrast agent Teslascan.[43]

Over the last decade, publications involving Mn^{II} MRI agents have soared, in parallel with publications discussing the safety concerns surrounding the use of Gd^{III}-based agents. As was the case with Gd^{III}, the search for appropriate low molecular weight ligands centers on a balance between two factors: in order to prevent the release of free Mn^{II}, a ligand system should confer both thermodynamic stability and kinetic inertness on the resulting complex, while still allowing at least one water molecule to directly coordinate to the metal center for high relaxivity.

1.1.3.1 Classes of ligand

Like Gd^{III}, Mn^{II} is a hard acid, and so both linear and macrocyclic ligands with N and O donor atoms have been investigated for Mn^{II}, including the DOTA and DTPA systems exploited for Gd^{III} agents. However, the two ions have several differences: Mn^{II} has a lower charge, a smaller ionic radius, and a preference for coordination numbers of 6 or 7. These differences mean that Mn^{II} and Gd^{III} complexes of the same or similar ligands may have very different properties.

Linear ligands investigated for use in Mn^{II}-based agents are predominantly polyaminocarboxylates, with two or three amine groups: EDTA and DTPA derivatives

respectively (Figure 1.10). The monoamine derivative NTA (Figure 1.10) was determined to be too unstable for *in vivo* use, due to the rapidity of dissociation.[45]

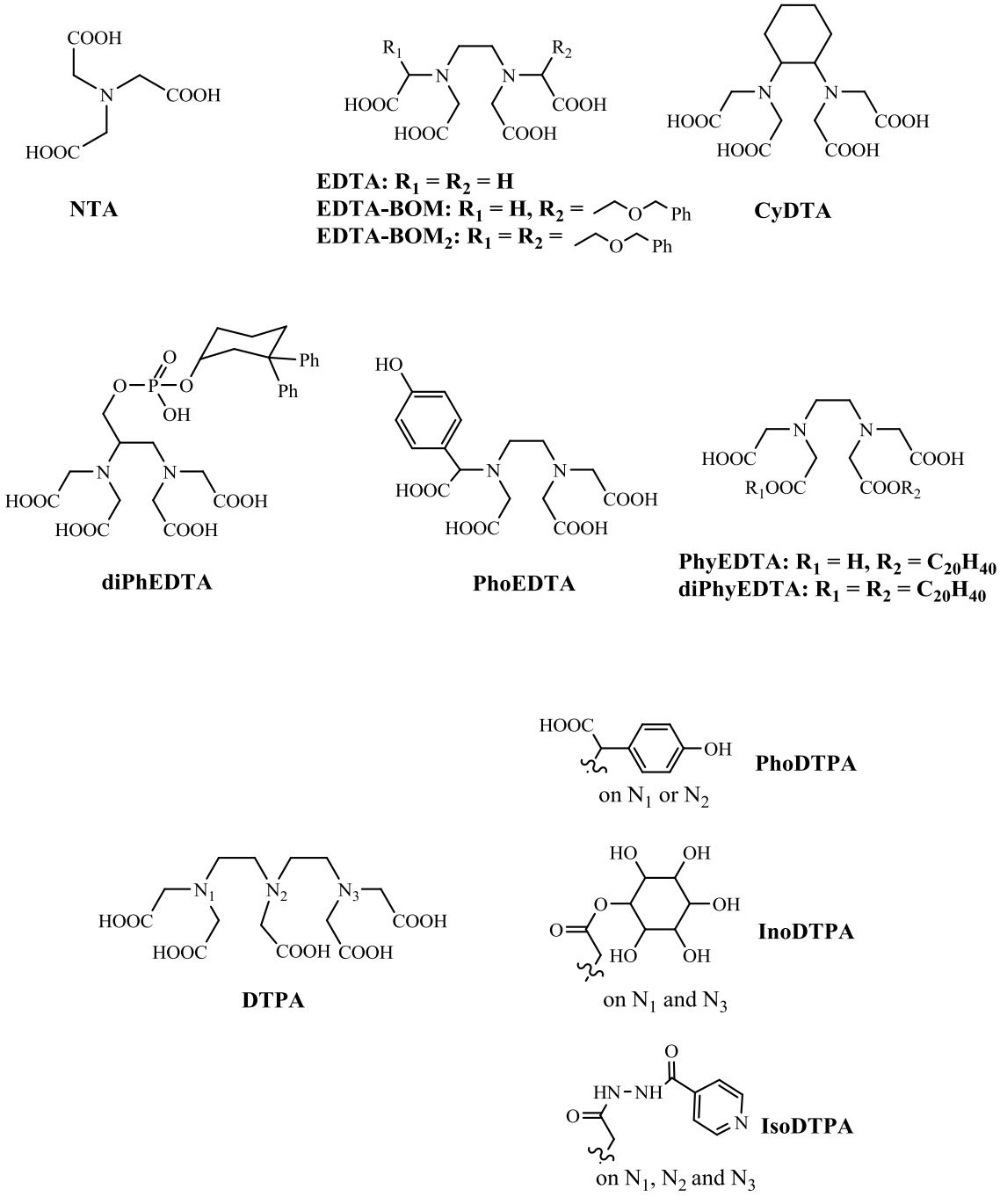

Figure 1.10 Linear chelating ligands studied for use in Mn^{II}-based contrast agents.[40,41]

The first of the polyaminocarboxylate family to be studied for its contrast potential was the EDTA complex of Mn^{II}, $Na_2[Mn(EDTA)]$.[46] The ligand binds in a hexadentate fashion, with the remaining coordination position filled by a bound water molecule. The high denticity of EDTA confers thermodynamic stability on the complex, and indeed an early toxicity study in rats showed that the LD_{50} for this compound was over 30x higher than that of $MnCl_2$.[46] Surprisingly, given the bound water, its r_1 relaxivity was low: 1.7 $mM^{-1}\cdot sec^{-1}$ (130 MHz, 22°C).[47] An array of EDTA derivatives have been investigated, all resulting in similar 7-coordinate Mn^{II} complexes with a single inner-sphere water molecule. The cyclohexyl derivative CyDTA yielded a comparable aqueous r_1 value of 1.5 $mM^{-1}\cdot sec^{-1}$, under a stronger magnetic field (500 MHz, 25°C).[48] The similar relaxivities are somewhat surprising, given that the water-exchange rate k_{ex} of the EDTA complex is 3x faster than that of the CyDTA complex.[48] The benzyloxymethyl derivatives EDTA-BOM and EDTA-BOM_2 resulted in Mn^{II} complexes with higher aqueous r_1 relaxivities of 3.6 and 4.3 $mM^{-1}\cdot sec^{-1}$ respectively (20 MHz, 37°C);[49] however, the most important observation concerning these complexes was their tendency to bind to HSA *in vivo*, in an analogous fashion to the approved Gd^{III}-agent Ablavar, resulting in massively increased relaxivities: 55.3 and 48.0 $mM^{-1}\cdot sec^{-1}$ respectively (20 MHz, 37°C, HSA).[49] A similar binding phenomenon was observed for the phosphate and phenoxy derivatives diPhEDTA[50] and PhoEDTA[51] (Figure 1.10), which have aqueous r_1 relaxivities of 5.8 and 3.7 $mM^{-1}\cdot sec^{-1}$ respectively (20 MHz, 25 and 37°C). The latter species is based on the amino acid tyrosine, and was designed to target melanoma.[51] The highest aqueous relaxivity of a Mn^{II} complex of an EDTA derivative was reported for the phytanyl ester of EDTA (PhyEDTA), where phytanyl is a diterpenoid alkane with the

formula $C_{20}H_{42}$. PhyEDTA is an amphiphilic ligand, and the resulting Mn^{II}-PhyEDTA self-assembled into a liquid crystalline phase with high r_1 and r_2 relaxivities of 8.9 and 11.6 $mM^{-1}\cdot sec^{-1}$ (20 MHz, 25°C).[52] Interestingly, the diester derivative Mn^{II}- diPhyEDTA exhibited drastically lower relaxivity values, due to the lack of crystalline order.[52]

Like EDTA, the octadentate ligand DTPA forms a very thermodynamically stable complex with Mn^{II}; however, this ligand coordinatively saturates the metal ion, preventing inner-sphere water binding. As in the case of Teslascan, the relaxivity effect of DTPA-Mn^{II} type complexes results from the slow release of free Mn^{II} ions *in vivo*. Various analogues of DTPA have been synthesized with a view to increased solubility, bulk, and targeting potential. Phenolic groups have been appended (PhoDTPA, Figure 1.10), modelled after the functional group of the amino acid tyrosine, resulting in low r_1 values of 1.6 – 1.7 $mM^{-1}\cdot sec^{-1}$ (20 MHz, 25°C).[51] Inositol, which has 6 hydroxyl groups for added hydrophilicity (inoDTPA),[53] and isoniazid, an antituberculosis drug for organ-specific imaging (isoDTPA) have also been appended.[54] These modifications resulted in high relaxivity values of 5.6 (200 MHz) and 6.9 $mM^{-1}\cdot sec^{-1}$(80 MHz) respectively. [41,53,54]

There are three main classes of *macrocyclic* ligand which have been studied for use in Mn^{II}-based agents: flexible cyclic polyamines (predominantly aza- and azaoxa-crowns); rigid cyclic polyamines; and porphyrins. Macrocyclic ligands confer additional stability on their complexes due to the macrocyclic effect.

The class of flexible cyclic polyamine ligands predominantly comprises aza- and azaoxa-crown ethers (Figure 1.11).

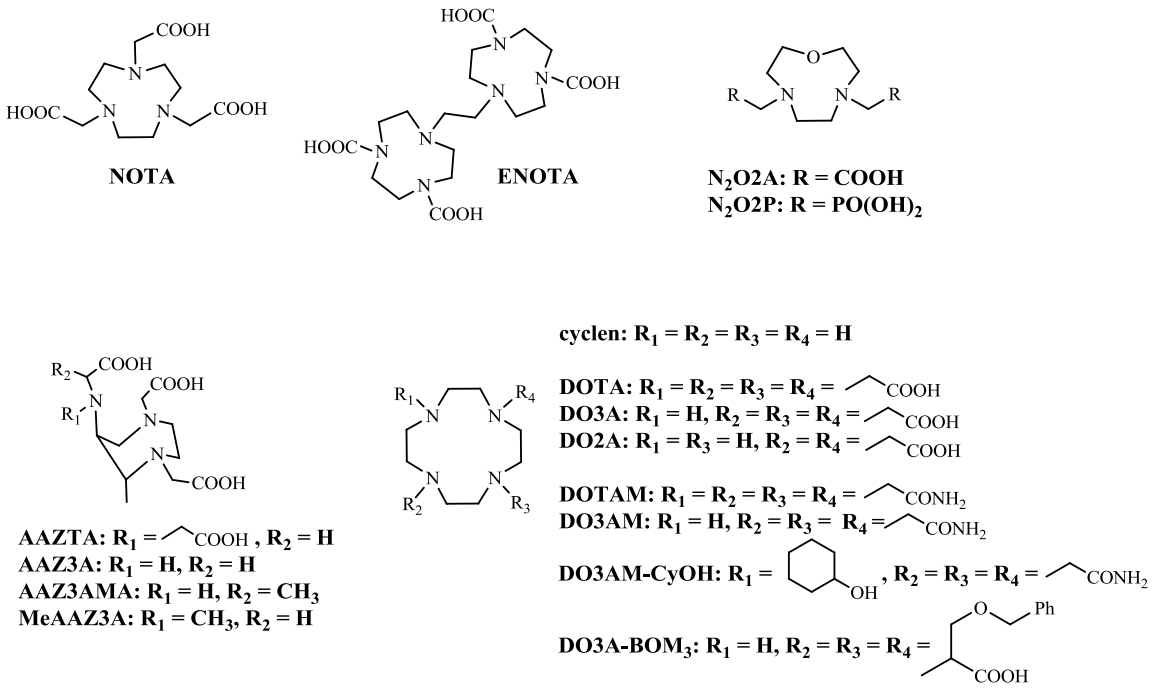

Figure 1.11 Flexible cyclic polyamine ligands studied for use in Mn^{II}-based contrast agents.[40,41]

NOTA and its derivatives have three donor nitrogen atoms in a nine-membered ring. NOTA forms a 6-coordinate complex with Mn^{II}, coordinatively saturating the metal and leading to a very low relaxivity due to only outer-sphere contributions.[55] However, when two NOTA units are covalently tethered via tertiary amine linkages, the resulting bicyclic ligand ENOTA has two pentadentate binding pockets, each of which may contain a single 6-coordinate Mn^{II} ion additionally bound to one water molecule.[56] Mn^{II}_2-ENOTA has an r_1 value of 2.7 $mM^{-1}\cdot sec^{-1}$ (20 MHz, 37°C), fairly low considering the total of two bound water molecules per dinuclear complex.[56] The issue of coordination sphere saturation has also been addressed by the substitution of an oxygen for one of the backbone nitrogen atoms, forming N_2O2A and its phosphonic derivative N_2O2P.[57] ^{17}O NMR measurements indicated that while Mn^{II}-N_2O2P is 6-coordinate, Mn^{II}-N_2O2A in

solution exists in equilibrium between the 6-coordinate monohydrated and 7-coordinate bishydrated species.[57] In spite of the lower hydration number, Mn^{II}-N_2O2P has a significantly higher r_1 relaxivity (4.29 *vs.* 3.20 $mM^{-1}\cdot sec^{-1}$, 20 MHz, 37°C), due to its rate of water exchange being 100x faster than that of the carboxylate species Mn^{II}-N_2O2A.[40,41]

Another family of macrocyclic N_3 ligands include derivatives of the seven-membered ring AAZTA (Figure 1.11), containing two in-ring nitrogen donors, with a third nitrogen present as a pendant amine. While the Mn^{II} complex of AAZTA is very stable, this 6-coordinate species has no inner sphere water molecules.[58] The removal of a carboxylate group to give the three substituted amine derivatives shown in Figure 1.11 allows for the potential binding of a water molecule; in fact, the Mn^{II} complexes of AAZ3A, MeAAZ3A and AAZ3AMA exist in equilibrium between the non-hydrated and monohydrated species.[59] The relaxivities of the three derivatives depicted decrease in the order AAZ3A > MeAAZ3A > AAZ3AMA, in keeping with the extent of the hydration equilibrium observed via ^{17}O NMR measurements: the Mn^{II} complexes of the three ligands have hydration numbers of 0.63, 0.32 and 0.24 respectively, yielding r_1 relaxivities in the range 1.6 – 2.5 $mM^{-1}\cdot sec^{-1}$ (20 MHz, 37°C).[40,41,59]

Several derivatives of the aza-crown cyclen have been studied. The tetracarboxylate ligand DOTA forms a stable 6-coordinate complex with Mn^{II}, but like its N_3 analogue NOTA, has no inner-sphere water molecules in solution and displays purely outer-sphere relaxation.[55] A systematic study of several derivatives of DOTA was performed by Wang and Westmoreland in 2009, including the tricarboxylate and dicarboxylate ligands DO3A and DO2A, and the tetraamide and triamide derivatives

DOTAM, DO3AM and DO3AM-CyOH (Figure 1.11).[60] The authors found that the 6-coordinate complex Mn^{II}-DO2A exhibited the highest relaxivity of 6.2 $mM^{-1}\cdot sec^{-1}$ (20 MHz, 37°C), while the 8-coordinate complex Mn^{II}-DOTAM had the lowest relaxivity of 0.9 $mM^{-1}\cdot sec^{-1}$ (20 MHz, 37°C).[60] The 7-coordinate complexes of DO3A, DO3AM, DO3AM-CyOH and DOTA-BOM_3 exhibited intermediate values. The authors suggested that 6- and 7-coordinate complexes were able to temporarily widen their coordination spheres to accept an additional ligand (H_2O) in solution, accounting for the higher relaxivities observed for these systems, while 8-coordinate complexes were unable to do so, as evidenced by the low relaxivity of Mn^{II}-DOTAM.[60] In addition, the authors suggested that increased steric bulk on the pendant arms of the macrocyclic ligand would hinder the expansion of the coordination sphere, a possible reason why the observed relaxivity of 7-coordinate Mn^{II}-DOTA-BOM_3 was 1.6 $mM^{-1}\cdot sec^{-1}$ (20 MHz, 25°C),[49] lower than the less hindered 7-coordinate complexes DO3AM and DO3AM-CyOH (3.3 and 4.7 $mM^{-1}\cdot sec^{-1}$ at 20 MHz and 37°C respectively). This study was significant because it related the coordination number of a Mn^{II} complex to its relaxivity; and because it showed that complexes with no inner-sphere water molecules in the solid state were still worth investigating for relaxivity behaviour in solution.[40,41]

Closely related to this family of flexible cyclic polyamines are the rigid analogues shown in Figure 1.12, functionalized by the incorporation of a pyridine unit into the macrocyclic backbone. This class of macrocycle is most relevant to the systems described in **Chapter 2**.

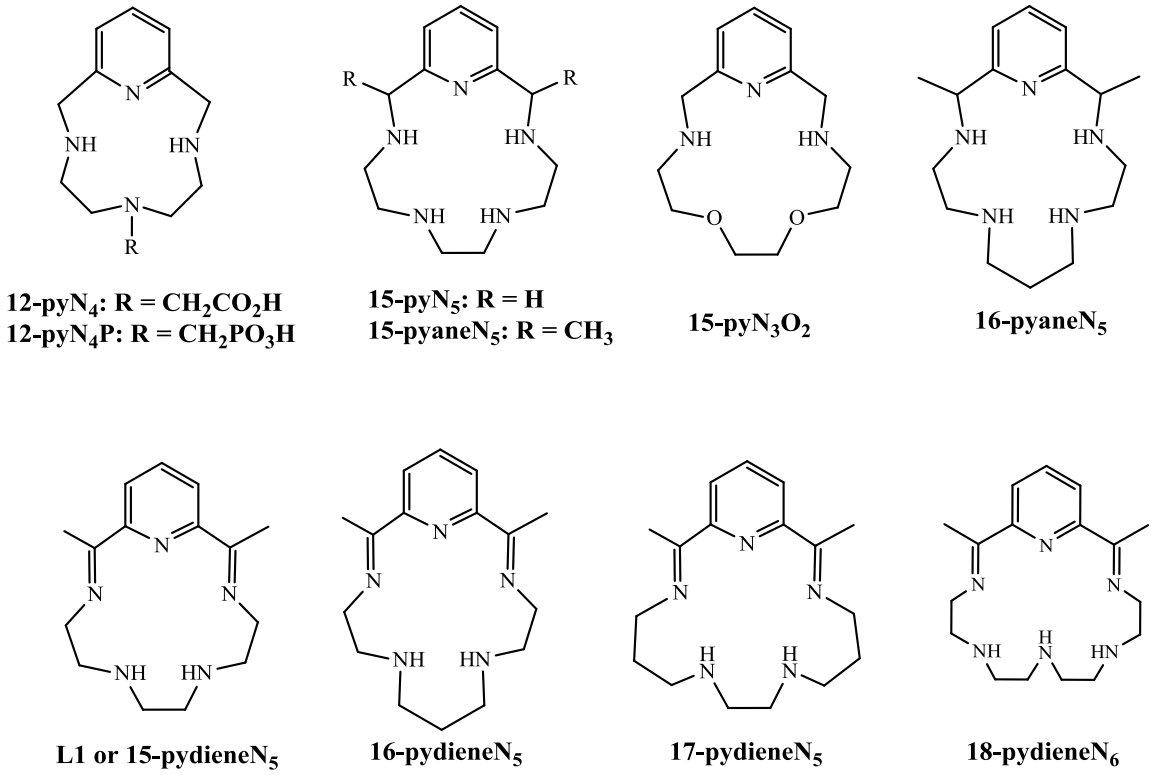

Figure 1.12 Pyridine-functionalized macrocyclic ligands.[40,41]

In an early report by Jackels and co-workers in 1992, the NMRD profiles of several pyridine-functionalized N_5 and N_6 macrocycles were studied. NMRD, or nuclear magnetic resonance dispersion, relates the strength of an applied magnetic field to the observed r_1 relaxivity of a system. Jackels performed NMRD experiments on the saturated systems 15-pyaneN_5 and 16-pyaneN_5, as well as the *bis*(imine) unsaturated systems 15-pydieneN_5, 16-pydieneN_5, 17-pydieneN_5, and 18-pydieneN_6 (Figure 1.12).[61] He noted several structure-activity relationships: higher relaxivity values were observed for the unsaturated systems over the saturated systems, and for the smaller macrocyclic cavity sizes over the larger cavity sizes (15 >16 >17 >18). Jackels also used EPR in conjunction with the relaxivity data to draw conclusions about the symmetry and

coordination environments of the Mn^{II} complexes. The smaller macrocyclic systems 15-pyaneN_5, 16-pyaneN_6, 15-pydieneN_5, and 16-pydieneN_5 bound in a pentadentate fashion, equatorial to the Mn^{II} ion, with two axially-bound water molecules in solution; while the larger macrocycles were slightly puckered, and formed 6-coordinate complexes with a single water additionally bound.[61] Two related saturated systems were studied in detail recently by Drahos and co-workers: 15-pyN_5 and 15-pyN_3O_2.[62] As previously observed by Jackels, these systems formed 7-coordinate complexes with Mn^{II} in solution, with r_1 relaxivities of 3.13 and 3.61 $mM^{-1}\cdot sec^{-1}$ respectively (20 MHz, 37°C).[62] Drahos also examined the pyridine-functionalized DOTA derivatives 12-pyN_4 and 12-pyN_4P.[63] While the resulting Mn^{II} complexes exhibit high thermodynamic stability, the relaxivity values of 1.94 and 2.32 $mM^{-1}\cdot sec^{-1}$ (20 MHz, 37°C) are not a marked improvement on previously published values, likely due to the very slow water exchange; and the two complexes are very kinetically labile, with instantaneous and rapid dissociation at pH = 6 observed respectively.[63]

Although the Mn^{II} complexes of 15-pyN_5 and 15-pyN_3O_2 were recently investigated with a view to understanding structure-relaxivity correlation, these systems act as very aggressive mimics of the important enzyme superoxide dismutase (SOD).[64] For this reason, they and related systems are not candidates for *in vivo* imaging.[40] In contrast to the saturated macrocycles 15-pyN_5 and 15-pyN_3O_2, the unsaturated *bis*(imine) derivative **L1** does not act as a SOD mimic. However, somewhat surprisingly, after the initial NMRD study in 1992, this system has not been revisited as a potential contrast agent by Drahos and co-workers, or any other researchers to date, nor have any of its N_3X_2 or N_3X_3 analogues (X = NH, O).

A third class of macrocyclic ligand which has been increasingly exploited for small molecule agents are the porphyrins. These conjugated, N-heterocyclic macrocycles were known to form complexes with high stability constants, and had been reported to selectively accumulate in tumours:[65] two desirable traits. After the Mn^{II} complex of the tetraphenylsulfonated porphyrin $TPPS_4$ (Figure 1.13) was observed to have a relaxivity of 10.4 $mM^{-1}\cdot sec^{-1}$ (20 MHz, 37°C), higher than $MnCl_2$, a flurry of research activity into this family was sparked.[66] The tri- and bi-sulfonated derivatives $TPPS_3$[67] and $TPPS_2$[68] were examined, with Mn^{II}-$TTPS_3$ yielding the most promising *in vivo* relaxivity results when tested with human breast carcinoma cells. In a similar study, the phthalocyanine derivative of $TPPS_4$, PcS_4, was reported to have a similarly high relaxivity of 10.4 $mM^{-1}\cdot sec^{-1}$ (10.7 MHz), and was selectively retained by tumor tissue over muscle or kidney tissue for 24 hours.[69] An even higher aqueous relaxivity of 13.0 $mM^{-1}\cdot sec^{-1}$ (20 MHz) was reported for the Mn^{II} complex tetraphenylporpyrin TPP, but surprisingly a study involving hepatocellular carcinomas did not show selective tumor enhancement until after 3 hours.[70] The fully carboxylate-substituted derivative uroporphyrin (UROP-1) selectively accumulates in rat brain tumors, providing persistant image enhancement with an aqueous relaxivity of 4.75 $mM^{-1}\cdot sec^{-1}$ (10 MHz).[71] The related ligands mesoporphyrin[72] and hematoporphyrin[73] have also been studied, and although both allow for excellent tumour visualization, the toxicity of these compounds has remained an issue: a third of the rats injected with hematoporphoryn at a dosage of 38 $\mu mol\cdot kg^{-1}$ did not survive.[73] A more recent porphyrin derivative is the amphiphilic ligand HOP-8P, which was studied in mice models and found to accumulate in cancerous cells in mice, while being thoroughly cleared from circulation after 24 hours.[74] Mn^{II} metalloporphyrins

clearly have application for tumor-specific imaging, especially in brain, breast and liver tissue. Toxicity remains a noted concern, and significant *in vivo* work in this regard is required before these compounds are suitable for clinical trials.[40]

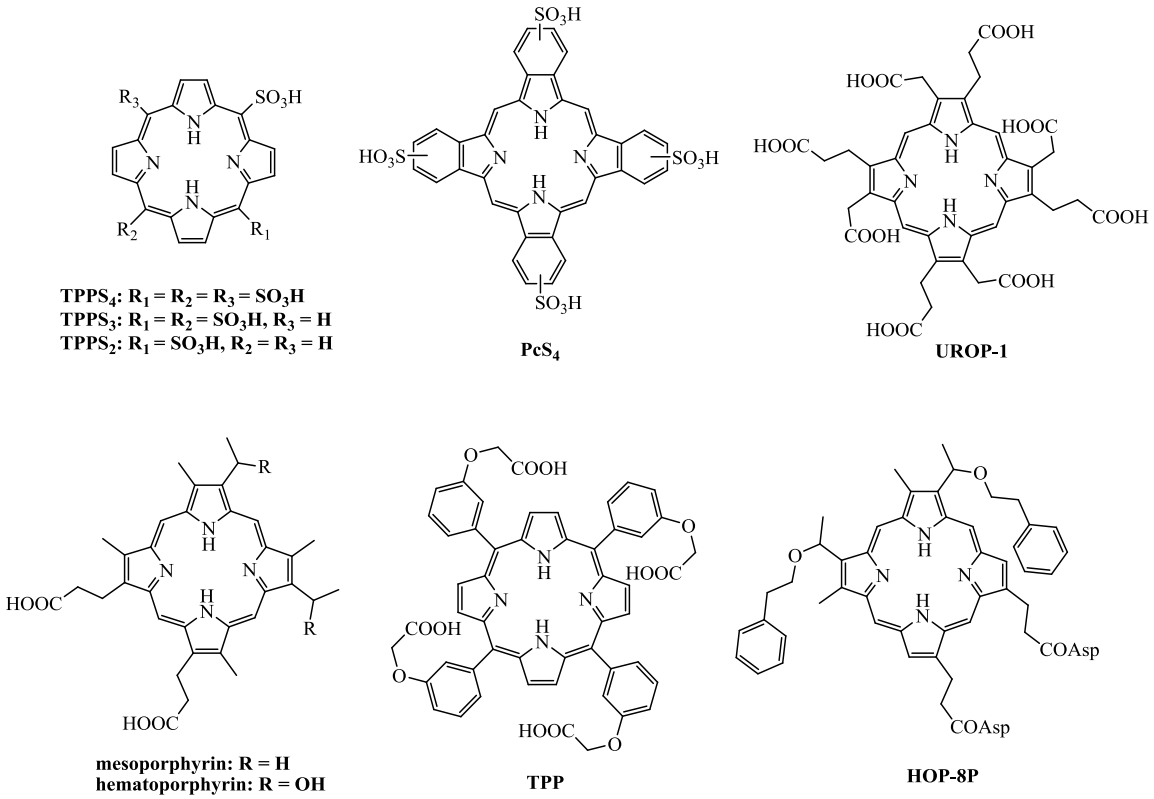

Figure 1.13 Selected porphyrin-based macrocyclic ligands studied for use in Mn^{II}-based contrast agents.[40]

1.1.3.2 Nanosized agents and small molecule agents

As well as the development of new small-molecule contrast agents, a variety of nanosized agents have also been investigated. These can be divided into macromolecular agents, and inorganic bulk particles. *Macromolecular agents* include liposomal systems, polymers and dendrimers. Liposomal systems involve the encapsulation of an MRI agent into a liposome. A major advantage of liposomal delivery is that liposomes can be temperature-sensitive, allowing for a thermal report via MRI; and a drug may be co-

encapsulated, for dual-action imaging and therapy: theranostics.[75,76] Dendrimeric and polymeric systems have the advantage of incorporating multiple paramagnetic centers, and having tunable substituents/peripheries, for desirable physical or functional properties such as solubility or selectivity.[40] For instance, Mn^{II}-DTPA units have been linked via water-soluble polysaccharides to give a multi-center MRI contrast agent;[77] and a recent dendrimeric system incorporated the Mn^{II}-DOTA moiety into a lysine-based nanoglobule, for targeted tumor imaging.[78] From these examples, it can be seen that advances in small-molecule agents (higher relaxivity, lower toxicity) may be harnessed for use in many nanosized systems also: a new higher relaxivity small molecule agent may be encapsulated into a liposome, linked to a polymer chain, or appended to a dendritic branch.

As can be seen from the reports above, there is an ongoing search for effective paramagnetic contrast agents with high biostability. While there has been a dramatic shift in research interest towards Mn^{II}-based agents in the face of increasing concerns about the toxicity of Gd^{III}, the focus of ligand design for small molecule contrast agents has not changed: chelates which allow for high relaxivity via inner-sphere water molecules, fast water exchange, and slow tumbling; and which result in kinetically and thermodynamically stable systems. **Chapter 2** focusses on the synthesis of a promising family of small molecule Mn^{II} and Gd^{III} agents formed from Schiff-base macrocycles using the technique of metal templation.

1.2 Molecule-based magnetism

Lanthanide single molecule magnets (Ln-SMMs) are the second class of magnetic material involved in my research. An introduction to the origins of magnetic behaviour will be presented, and an overview of molecule-based magnets will be given, before the field of mononuclear Ln-SMMs is discussed.

1.2.1 Origins of magnetic behaviour

As early as 600 BC, the attraction of iron to lodestone was described by the ancient Greek philosopher Thales. Centuries later, around 1100 AD, the Chinese used this property to develop the first navigational compasses. Today, the applications of magnetism are astounding in number. From health care to entertainment, from a tiny USB key to a giant generator, magnetic devices are interwoven into our modern existence.

1.2.1.1 Fundamental magnetic behavior: diamagnetism and paramagnetism

The phenomenon of magnetism arises from the movement of electrons, which gives rise to spin angular momentum, S and orbital angular momentum L. The motion of each electron induces a small magnetic moment. The vector sum of these individual magnetic moments of electrons within an atom combine to give the overall magnetic moment of the atom.

There are two kinds of magnetic phenomenon which may be exhibited by an individual atom or molecule: diamagnetism and paramagnetism. *Diamagnetism* is due to the presence of paired electrons in atomic or molecular orbitals. The magnetic moments of paired electrons within an orbital cancel each other out, giving a net magnetic moment

of 0 for paired electrons. Diamagnetism results in the slight repulsion of a substance from an applied magnetic field. It is a temperature independent behavior, exhibited by all atoms and molecules containing at least one pair of electrons.

Paramagnetism results from the presence of one or more unpaired electrons in an atomic or molecular orbital, which gives rise to a net magnetic moment, or spin. Paramagnetism results in the attraction of a substance to an applied field, and is typically temperature dependent.[79]

1.2.1.2 Bulk magnetic behavior: para-, ferro-, antiferro- and ferrimagnetism

A bulk sample comprising multiple paramagnetic atoms or molecules with interacting spins will exhibit bulk magnetic behaviour. The magnetic behavior of a species can be determined by studying its magnetic susceptibility. Susceptibility, χ (dimensionless), describes the magnetization of a species in the presence of an external magnetic field (Eqn. 1.1):

$$\boldsymbol{\chi = \frac{M}{H}} \qquad \textbf{Eqn. 1.1}$$

where M is magnetization, and H is the applied magnetic field.[80] This equation is valid for weak magnetic fields.

Susceptibility can be converted to mass susceptibility, χ_g ($cm^{3}\cdot g^{-1}$), or molar susceptibility, χ_M ($cm^{3}\cdot mol^{-1}$). Molar susceptibility is the measure of susceptibility most commonly used.

There are four main classes of bulk magnetic behavior: paramagnetism, ferromagnetism, antiferromagnetism and ferrimagnetism (Figure 1.14).

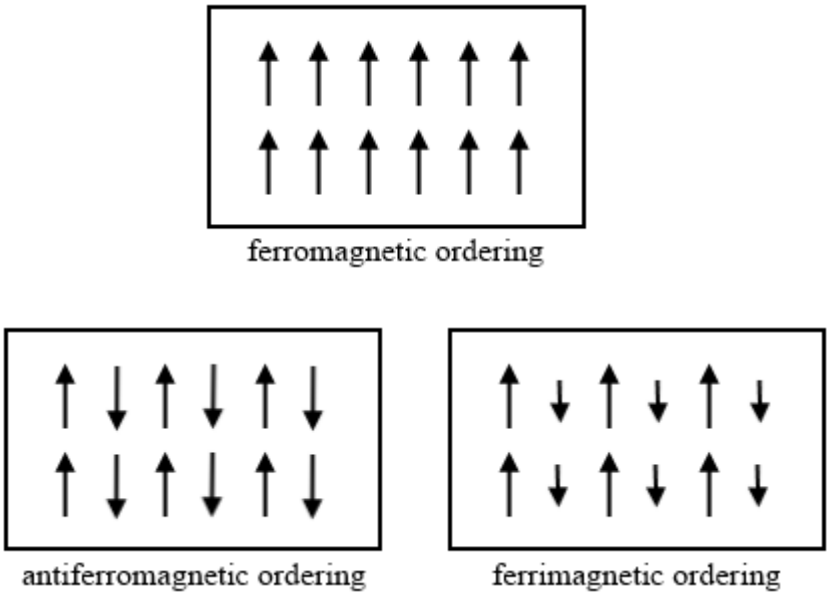

Figure 1.14 The common types of bulk magnetic spin ordering, at absolute zero and in the absence of an external magnetic field.[81]

Paramagnetic behavior in a bulk solid occurs when the spins of the paramagnetic atoms or molecules do not interact, but are randomly oriented. In the absence of an external magnetic field, a paramagnetic species will have no net magnetic moment. When an external field is applied, the spins of the atoms or molecules will align with the applied field, resulting in a weak attraction. The molar susceptibility of a paramagnetic material is both temperature dependent and field dependent.

The temperature dependence of χ_M is described by the Curie law:

$$\boldsymbol{\chi_M = \frac{N_A g^2 \mu_\beta{}^2}{3k_B T} S(S+1)} \qquad \textbf{Eqn. 1.2}$$

where N_A is Avogadro's number, g is the Landé g-factor, μ_β is the Bohr magneton, k_B is the Boltzmann constant, T is the temperature, and *S* is the spin quantum

number, equal to half the number of unpaired electrons.[80] This expression is often simplified to:

$$\chi_M = \frac{C}{T} \qquad \textbf{Eqn. 1.3}$$

where C is the Curie constant (emu K mol^{-1}). This version of the equation clearly shows the inverse relationship between χ_M and T for a paramagnetic material..[79]

The magnetization of a paramagnet is also field dependent. At low fields (keeping temperature constant), there is a linear relationship between magnetization and magnetic field. This is given by M = χH (Eqn. 1, rearranged; Figure 1.15). At higher magnetic field strengths, this relationship ceases to exist. Rather, as the field strength increases (keeping T constant), M approaches the saturation magnetization M_s (emu·G·mol^{-1}) (Eqn. 1.4; Figure 1.15):

$$M_S = \mu_\beta N_A S g \qquad \textbf{Eqn. 1.4}$$

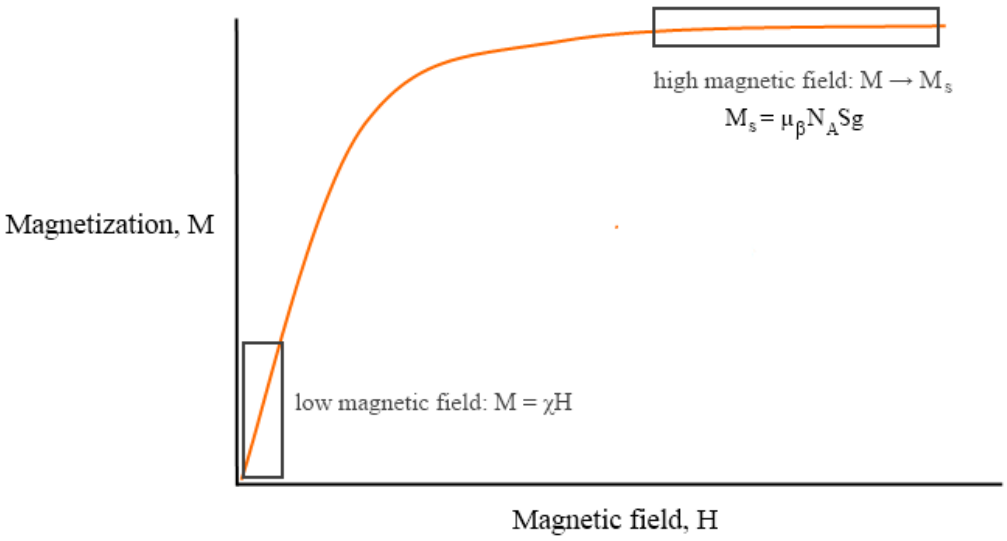

Figure 1.15 Plot of M *vs.* H for a paramagnetic material.[79]

A rearrangement of Eqn. 1.4 gives:

$$\frac{M_S}{\mu_\beta N_A} = Sg = n \qquad \textbf{Eqn. 1.4b}$$

where $\frac{M_S}{\mu_\beta N_A}$ is the 'reduced magnetization,' and n is the number of unpaired electrons in the atom or molecule. Thus the saturation magnetization can be used to find the spin of a paramagnetic species.[80]

The remaining three key types of bulk magnetic behavior (ferromagnetism, antiferromagnetism and ferrimagnetism), involve long-range ordering of magnetic spins.

Ferromagnetic behavior occurs in a bulk solid when adjacent magnetic spins are aligned parallel to each other. In the absence of an external magnetic field, a ferromagnetic species will have a large net magnetic moment. However, ferromagnets usually exist as a group of domains. Each domain consists of a number of aligned spins. In the absence of a magnetic field, the domains are randomly oriented; so although each domain has a net magnetic moment, the bulk ferromagnet will appear to have a net magnetic moment of 0. In the presence of an external field, the domains align and the ferromagnet experiences a strong attraction to the field.[79]

Antiferromagnetic behavior is observed when adjacent magnetic spins of the same magnitude are aligned antiparallel to each other. The magnetic moments of the adjacent spins cancel out, leading to a net magnetic moment of 0 in the absence of an applied field. In the presence of a magnetic field, 3D-ordered antiferromagnetic materials are weakly repelled, in a similar manner to diamagnetic materials.[79]

Ferrimagnetic materials also have an antiparallel arrangement of spins; however the spins differ in magnitude, leading to an overall net magnetic moment in the absence of a magnetic field. Like ferromagnets, ferrimagnets exist in domains, so a bulk ferromagnet may also appear to have no magnetic moment in the absence of an external field. In the presence of a field, the domains align, and the ferrimagnet is attracted to the magnetic field.[79]

Ferromagnets, antiferromagnets and ferrimagnets only exhibit long-range ordering below specific temperatures. Above the Curie temperature T_c (for ferromagnets and ferrimagnets) and the Néel temperature T_N (for antiferromagnets), the thermal energy is large enough to overcome the magnetic order present in the solids. Above T_c or T_N, these classes of material lose their long-range ordering and act as paramagnets.

Bulk magnetic behavior can be described in terms of the relationship between magnetic susceptibility and temperature. As mentioned earlier, paramagnetic materials exhibit an inverse relationship between χ_M and T, given by the Curie law $\chi_M = \frac{C}{T}$. Thus the plot of the susceptibility-temperature product $\chi_M T$ *vs.* T is a straight line for paramagnetic materials. Due to their long-range magnetic ordering, ferromagnets, antiferromagnets and ferrimagnets deviate from this line (Figure 1.16).[79]

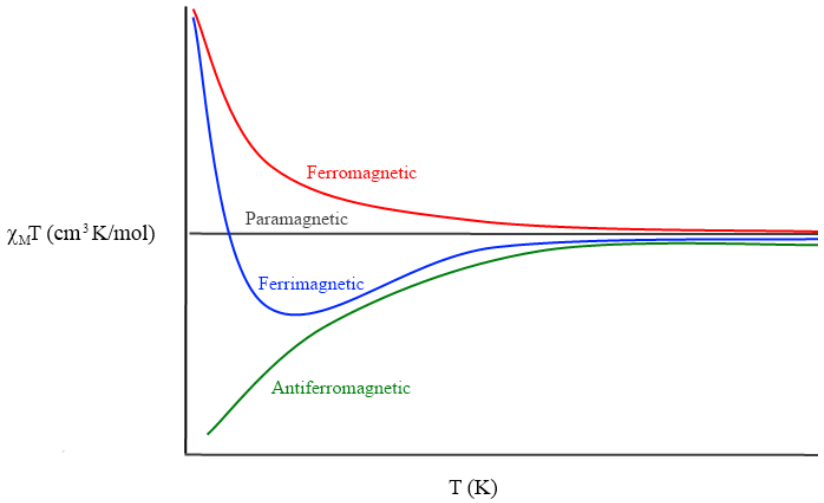

Figure 1.16 Plot of susceptibility-temperature product $\chi_M T$ *vs.* T for the four main classes of bulk magnetic behavior. Redrawn from Reference 79.

A plot of inverse susceptibility $\frac{1}{\chi_M}$ *vs.* T is also informative. A pure paramagnet exhibits a linear relationship between $\frac{1}{\chi_M}$ and T, with a slope equal to the Curie constant C. Ferromagnets and antiferromagnets deviate from such linear behavior due to their spin-spin interactions (Figure 1.17).

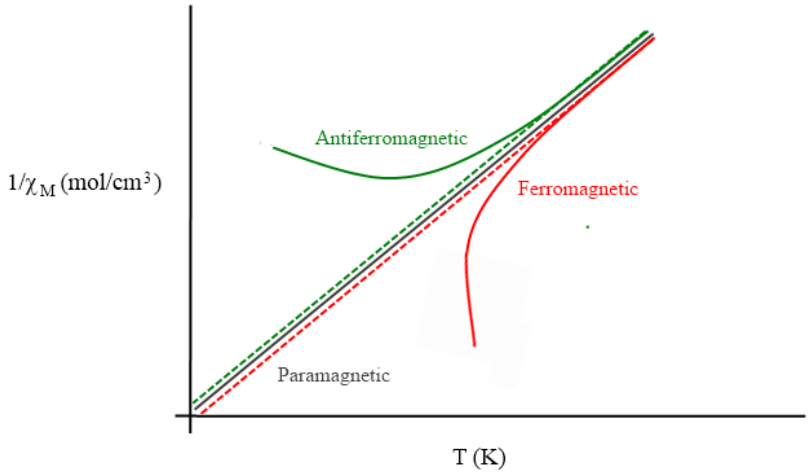

Figure 1.17 Plot of inverse susceptibility $\frac{1}{\chi_M}$ *vs.* T for paramagnetic, ferromagnetic and antiferromagnetic materials. Redrawn from Reference 79.

This deviation can be quantified using the Curie-Weiss law (Eqn. 1.5):

$$\chi_M = \frac{C}{(T-\theta)} \qquad \textbf{Eqn. 1.5}$$

where θ is the Weiss constant. The sign of the Weiss constant indicates whether the spin-spin interactions are ferromagnetic (positive θ) or antiferromagnetic (negative θ). The magnitude of the Weiss constant is proportional to the strength of the interaction. Susceptibility data may be usefully fit to the Curie-Weiss equation in the temperature range $T > 5\ \theta$.[79,81]

1.2.1.3 Hysteresis

Ferromagnetic and ferrimagnetic substances exhibit a property called hysteresis: a history-dependence to the magnetic behaviour. In the presence of an external magnetic field, as discussed above, the domains of these species align parallel to the field, and the ferromagnetic or ferrimagnetic material becomes magnetized, reaching a saturation of its magnetization. When the magnetic field is reduced to 0, the magnetization does not return to 0; instead, a 'remnant magnetization' M_r remains. This is due to some of the magnetic domains remaining in alignment. The magnetic field which must be applied in order to return the magnetization to 0 is the 'coercive field,' $^{+}$/- H_c. This spontaneous magnetization after a magnetic field is applied and removed is known as hysteresis, and presents as a characteristic hysteresis loop on a plot of M *vs.* H (Figure 1.18). A broad hysteresis loop (large H_c) indicates a 'hard' magnet, or a permanent magnet: a substance which is magnetized in the presence of a magnetic field, and retains that magnetization long after the field is removed. A narrow loop (small H_c) suggests a 'soft' magnet.[79]

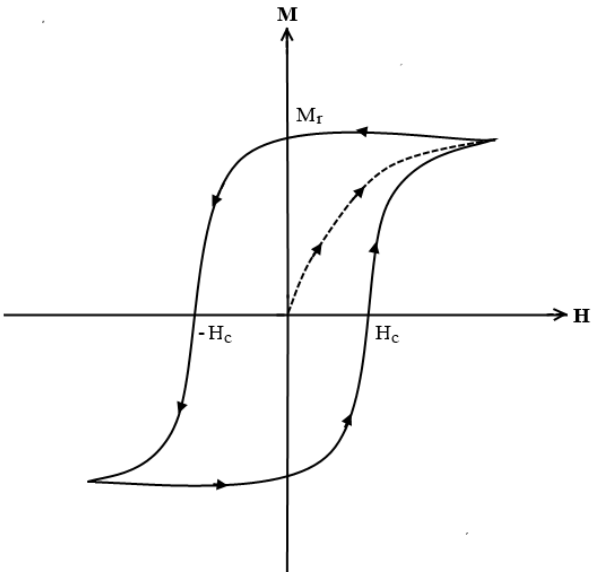

Figure 1.18 Representation of a hysteresis loop, showing the remnant magnetization M_r and the coercive fields +/- H_c.

Hysteresis is a desirable quality of a magnetic material for device applications because it confers a bistability or magnetic memory on the compound. That is, at the same field, a species with hysteresis can exist in one of two magnetic states, depending on its immediate magnetic history.

1.2.2 Classical magnets *vs.* molecule-based magnets

Having discussed the origins of magnetic behaviour, it is worth clarifying the distinction between the terms classical magnets and molecule-based magnets.

The magnets discovered by the ancient Greeks and Chinese were *classical magnets*. Classical magnets are inorganic network solids. They display bulk magnetic behaviour which is 'atom-based,' arising from the presence of unpaired electrons in the *d*-orbitals of transition metals, or the *f*-orbitals of lanthanides. The spins of these electrons

interact in 3-dimensions, often through direct bonds between spin centers. These materials are usually produced by high-temperature metallurgical methods. Examples include metals (Fe, Co, Ni), heterometallics ($SmCo_5$, $Nd_2Fe_{14}B$), and metal oxides (Fe_2O_3, Cr_2O_3).[82] Until recently, classical magnets were the only type employed in technological applications.

In the 1980s, the first *molecule-based ferromagnet* was reported: an organic-based, zero-dimensional ferromagnet, $[Fe(C_5Me_5)_2]^{\cdot+}[TCNE]^{\cdot-}$ (TCNE= tetracyanoethylene).[83] In contrast to the 'atom-based' magnetism of classical magnets, molecule-based magnets such as this species display 'molecule-based' magnetism, with isolated spin centers not directly linked via covalent bonds. Molecular magnets may be organic radicals, coordination complexes, or hybrid organic/inorganic species; and may have unpaired electrons not only in *d*- or *f*-orbitals, but also in σ- and π-molecular orbitals formed from *s*- and *p*-atomic orbitals.[82]

Molecule-based magnets have several advantages over classical magnets. Molecular magnets may be formed using the synthetic techniques of organic and coordination chemistry, an alternative to the harsh conditions required for the synthesis of classical magnets. These techniques also offer an increased ability to control and alter the magnetic properties of a species, because the magnetic properties of the bulk solid depend on the spatial relationship and co-operative interactions of the spin sites on a molecular level.[82] Furthermore, it is proposed that these synthetic methods should allow for the facile combination of magnetic character with other useful or interesting features, such as electrical, optical and mechanical properties.[80] Molecular magnets tend to be easier to process than classical magnets, as they are less dense and more soluble.[82] As

well as these synthetic advantages, many molecule-based magnets also exhibit mechanical flexibility, high strength, and biocompatibility.[84] Finally, molecule-based magnetism offers unique opportunities for the miniaturization of switching, sensing and data storage devices.

Both classical and molecule-based magnets exhibit the major types of magnetic ordering: antiferromagnetism, ferromagnetism, and ferrimagnetism, as well as other cooperative behaviours (Table 1.2).

Magnetic behaviour	Classical magnet	Molecule-based magnet
Antiferromagnetic	MnO[85]	$Mn[N(CN)_2]$[86]
Ferromagnetic	CrO_2[87]	$[Fe(C_5Me_5)_2]^{\cdot+}[TCNE]^{\cdot-}$ [83]
Ferrimagnetic	Fe_3O_4[88]	Mn^{II} nitronyl nitroxide chains[89]

Table 1.2 Examples of magnetic behaviour in classical *vs.* molecule-based magnets. Adapted from Reference 84.

Molecule-based magnets can be classified in several ways, including: by the magnetic behaviour exhibited (some classes shown above in Table 1.2); by the nature of the molecules (organic radicals, coordination complexes, or hybrid organic/inorganic species); or by the dimensionality of the molecules (0-D, 1-D, 2-D or 3-D).[84,92,93]

Two classes of molecule-based magnets which do not have a classical analogue are single-molecule magnets (SMMs) and single-chain magnets (SCMs). **Chapters 3** and **4** of my thesis focus on SMMs, so an introduction to this class of compound will now be presented.

1.2.3 Single-molecule magnets

Single-molecule magents (SMMs) are individual coordination complexes, which can be magnetized in the presence of an applied magnetic field, and exhibit slow relaxation of that magnetization below a certain temperature (the blocking temperature, T_B). Like ferromagnets and ferrimagnets, SMMs display magnetic hysteresis. However, unlike ferromagnets and ferrimagnets, SMMs exhibit their slow relaxation on an individual molecular level, rather than as a property of the bulk solid. In order to act as an SMM, a compound must have a bistable electronic ground state; that is, the lowest energy M_J or M_S sub-level must exists as a doublet, with the two orientations of that ground state doublet separated by a large energy, or *anisotropy barrier* (U). The large barrier traps the magnetic moment of an SMM in one orientation, preventing rapid relaxation of its magnetization. This barrier results from the presence of magnetic anisotropy: a directional dependence to the magnetization. In the absence of a magnetic field, the direction in which the spin of a magnetically anisotropic material spontaneously wants to align is known as the 'easy axis.'

Magnetic anisotropy is due to *zero-field splitting* (ZFS), described by the parameter D. ZFS refers to the loss of degeneracy of the M_S or M_J sub-levels, even in the absence of an applied magnetic field. ZFS is due to: spin-orbit coupling (rare for transition metals); the coordination geometry of the metal center(s); the overall symmetry of the molecule; and bulk crystal packing. It is easiest to talk about ZFS in terms of 3d transition metals, for which a 'spin only' approximation may often be made: the magnetism can be considered as being due solely to spin angular momentum, because of the quenching of orbital angular momentum in many cases. ZFS for a transition metal is

primarily due to the coordination environment and molecular symmetry. A transition metal ion, complex or cluster may thus be described primarily by its total spin quantum number, S, and by its spin multiplicity: $(2S+1)$. The spin multiplicity is equal to the number of M_S sub-levels the system has, ranging in value from $-S$ to S.

Let us consider a system with $S = 1$. The three M_S sub-levels are +1, 0 and -1. If there is no ZFS, the M_S sub-levels are degenerate in the absence of a magnetic field, and are split only once an external field is applied (Zeeman splitting). When ZFS is present ($D \neq 0$), the M_S sub-levels are not degenerate, even in the absence of an applied field. The energy of each sub-level is given by Eqn. 1.6:

$$E(M_S) = g \cdot \mu_\beta \cdot H \cdot M_S + D M_S^2 \qquad \textbf{Eqn. 1.6}$$

Each M_S sub-level is populated by a different number of spins at a given temperature. The difference between the populations of each sub-level is what gives rise to magnetization in the sample. Species with large values of S have greater magnetization, because the M_S levels are further apart in energy.

If there is no applied field (i.e. $H = 0$), then the $g \cdot \mu_\beta \cdot H \cdot M_S$ term = 0. In that case, if D is positive, the $M_S = 0$ is the sub-level which is lowest in energy, while if D is negative, then the $M_S = +1$ and $M_S = -1$ sub-levels are lowest (Figure 1.19).[94]

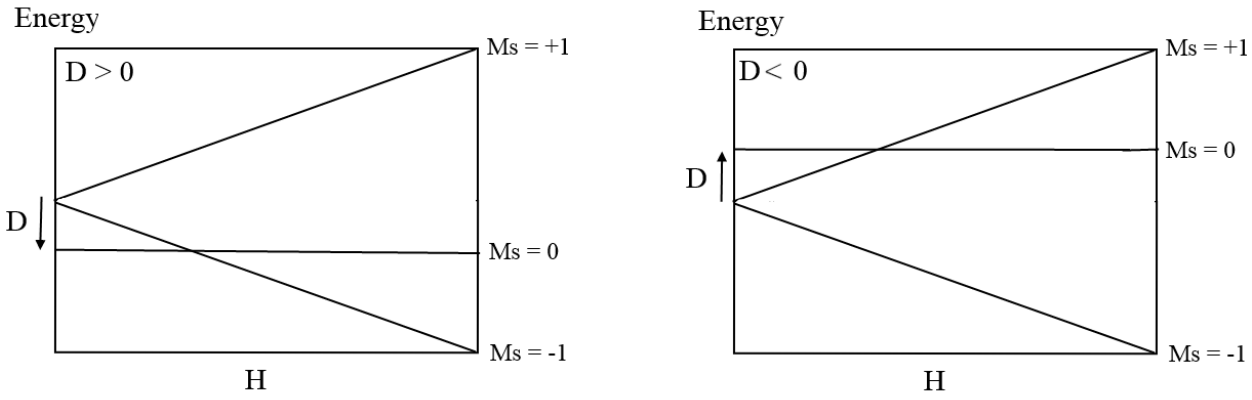

Figure 1.19 Depiction of the lowest-lying sub-levels when D is positive or negative, and how the energies of the states change when a magnetic field is applied. Adapted from Reference 94.

Considering the case when D is positive: when a field is applied, the M_S = -1 state crosses the M_S = 0 state and is populated because it is lowest in energy, resulting in sample magnetization (Figure 1.9). When the field is removed, the system readily relaxes (depopulates) from M_S = -1 to M_S = 0. From the M_S = 0 level, the M_S = +1 and M_S = -1 states can be equally thermally populated, because at 0 field they are degenerate.

Considering the case when D is negative: when a field is applied, the M_S = -1 state loses degeneracy with the M_S = +1 sub-level, and becomes populated, leading to magnetization (Figure 1.9). When the field is removed, the system must go through the higher energy M_S = 0 state before it can return to the lower energy M_S = +1 state. Thus when D is negative, there is an energy barrier between -1 and +1 magnetization states. This energy barrier (U, cm^{-1}) causes the slow relaxation of magnetization in SMMs.[94]

The accepted equation for U (for transition metal SMMs) is given by Eqn. 1.7:

$$U_{eff} = |D| S^2 \qquad \textbf{Eqn. 1.7}$$

for integer spins; $|D|(S^2-1/4)$ for non-integer.

Each M_S state corresponds to a specific orientation of the magnetization (or projection of the total spin angular momentum S) with repect to the easy axis of anisotropy, with a specific energy (Figure 1.20). Alignment of the magnetization parallel to the axis of anisotropy (0° or 180°, Figure 1.20) is energetically preferred.[95]

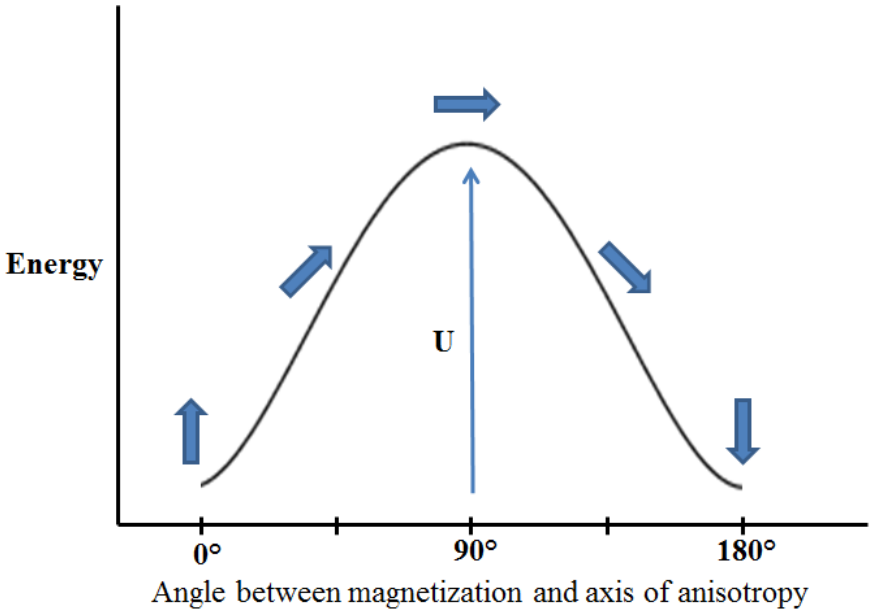

Figure 1.20 Schematic showing the preference of an SMM system for the magnetization to be aligned parallel to the easy axis of anisotropy. Adapted from Reference 95.

The $M_S = +S$ and $M_S = -S$ states can be thought of as lying on either side of a 'double well potential' (shown in Figure 1.21 for an $S = 10$ system), with the energy

barrier $|D|S^2$ between them. Overcoming U by thermal excitation to go from $M_S = -S$ to $M_S = +S$ is the 'classical' process by which magnetic relaxation occurs (purple arrows, Figure 1.21). A second mechanism of relaxation involves the phenomenon of quantum tunnelling of magnetization (QTM), which occurs when electrons 'tunnel' between degenerate m_S states without overcoming the anisotropy barrier.[94] Quantum tunnelling is present at low temperatures when there is significant mixing between energetically degenerate microstates, and results in an 'effective' anistropy barrier U_{eff} which is lower than the anisotropy barrier U. It is desirable that QTM be non-existent, or very slow, in order for the energy barrier U_{eff} to be as high as possible.[95]

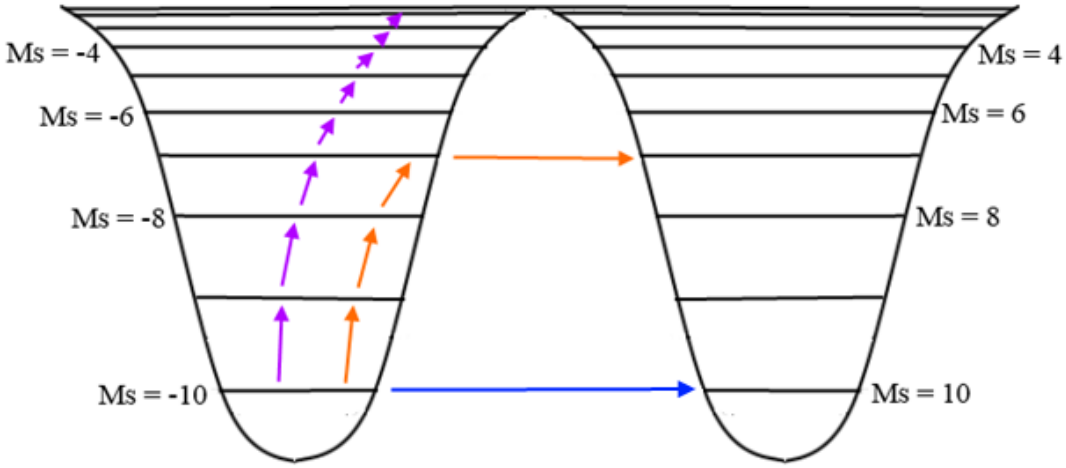

Figure 1.21 Depiction of classical relaxation (purple arrows), quantum tunneling (QT, blue arrows), and thermally-assisted QT (orange arrows) in an $S = 10$ system.

The first SMM was reported by Sessoli and Christou in 1993,[96] who described a cluster which has come to be known as Mn_{12}-acetate, comprising eight Mn^{III} ions ($S = 2$) and four Mn^{IV} ions ($S = 3/2$), giving rise to an $M_S = +/-10$ ground state. The cluster

displayed slow relaxation of magnetization below a blocking temperature of 10 K, with an energy barrier U_{eff} = 51 cm^{-1}.

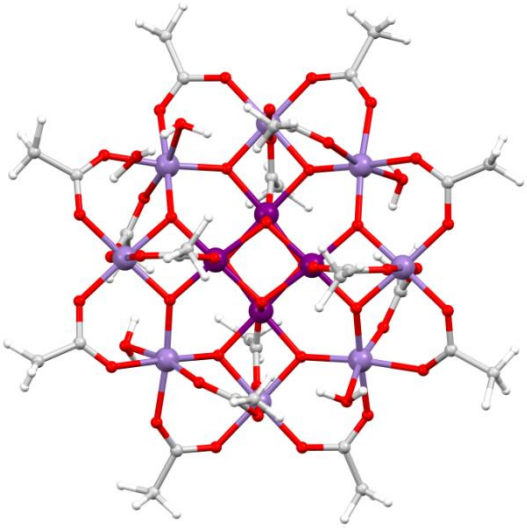

Figure 1.22 Structure of the first reported SMM, Mn_{12}-Ac.[96,97]. Dark purple = Mn^{IV}, light purple = Mn^{III}.

When this intriguing behaviour was described, the research interest of the magnetic community was thoroughly piqued and a large number of SMMs have since been reported. The majority are clusters formed from transition metals such as manganese, iron or nickel, with oxo or acetate ligands.[98,99] Although over 20 years have now passed, the record barrier for a polynuclear transition metal complex is 62 cm^{-1}, for a dinuclear Co^{II} complex[100] – similar in magnitude to that of the first Mn_{12} system investigated. However, although a major improvement in anisotropy barrier has not been realized for TM clusters, the many clusters which have been reported have been vital for the development of SMM theory, especially with regards to the relationship between the size of the energy barrier, the total molecular spin, and the easy axis anisotropy. In addition, the synthetic strategies used to make these clusters are now finding application

in fields such as magnetic refrigerants.[101] High nuclearity clusters have the major advantage of reaching nanoscale proportions via a 'bottom-up' rather than 'top-down' approach.[102]

Since the size of the energy barrier for transition metal clusters is given by $U = |D| S^2$, initial efforts in the development of TM-SMMs focussed on maximizing the total spin, *S*, by incorporating a large number of metal centers in a single complex. However, the importance of also optimizing D became increasingly clear when a complex containing 19 manganese centers was found to have a very small U_{eff} due to its high symmetry.[103] The anisotropy of a system is, however, much more difficult to design and control, especially in a polynuclear cluster. Due to their large intrinsic single-ion anisotropy, lanthanides quickly emerged as key metal centers for the development of SMMs. Lanthanides have now been employed in both mixed *d-f* and pure *4f* clusters, leading to energy barriers up to 5x higher than those observed for TM-cluster-SMMs (Table 1.3).[104,105] Research into lanthanide-containing clusters is moving increasingly towards the formation of multifunctional molecular magnetic materials, incorporating a second useful or interesting physical property such as optical activity.[106,107]

In addition, the use of lanthanide ions has driven the emergence of an entirely new class of SMM: SMMs containing a single metal center, or mononuclear SMMs. Mononuclear lanthanide SMMs (Ln-SMMs) will be discussed in the following section.

	Class	Metal ion(s)	Formula	U_{eff} (cm^{-1})	Ref.
Polynuclear	3*d*	Co_2	$[Co(hfpip)_2(L')]_2$	62	[100]
		Mn_6	$[Mn_6O_2(L'')_6(O_2CPh)_2(EtOH)_4]$	60	[108]
	mixed *d*-*f*	Fe_2Dy	$[Fe_2Dy(L''')_2(H_2O)]ClO_4{\cdot}2H_2O$	319	[104]
	4*f*	Dy_5	$[Dy_5(\mu_5\text{-}O)(\mu_3\text{-}O^iPr)_4(O^iPr)_5])$	367	[105]
Mononuclear	3*d*	Fe	$[Fe(C(SiMe_3)_3)_2]^-$	226	[109]
	4*f*	Tb	$[Tb(Pc)(^tBuPc)]$	652	[110]

Table 1.3 A comparison of the largest anisotropy barrier observed for different classes of SMM. Key: hfpip = 1,1,1,5,5,5- hexafluoro-4-(4-tert-butylphenylimino)-2-pentanonate; L′ = a didiazo-dipyridine ligand; L″H_2 = salicylaldoxime; L‴=2,2′,2″-(((nitrilotris(ethane-2,1-diyl))tris(azanediyl))tris(methylene))tris(4-chlorophenol).

1.2.4 Lanthanide single-molecule magnets (Ln-SMMs)

1.2.4.1 Electronic structure and anisotropy of Ln^{III} ions

Unlike transition metals, the orbital angular momenta of lanthanide ions often large and unquenched, and thus spin-orbit coupling must be considered. For this reason, the electronic states of the lanthanides are best described by a $^{2S+1}L_J$ 'term symbol.' The ^{2S+1}L 'term' describes inter-electronic interactions: spin-spin coupling and orbit-orbit coupling, given by the total spin and orbital angular momentum quantum number *S* and *L* respectively. *S* is given in the form of the spin multiplicity (2*S*+1), while *L* is represented by letters, where 0, 1, 2, 3, 4 = S, P, D, F, G. Each term is split into $^{2S+1}L_J$ 'levels' by spin-orbit coupling, where *J* is the Russell-Saunders coupled total angular momentum quantum number, and may take values from $J = |S+L|$ to $|S-L|$.

Table 1.4, below, gives relevant parameters for each Ln^{III} ion, including the ground state term symbol and g value of each free ion.[95]

Ln^{III}	Atomic number	Configuration	Ground state term symbol ($^{2S+1}L_J$)	Landé g-factor	Distribution of f electron density
La^{III}	57	$[Xe]4f^0$	$^1S_0$	-	n/a
Ce^{III}	58	$[Xe]4f^1$	$^2F_{5/2}$	6/7	Oblate
Pr^{III}	59	$[Xe]4f^2$	$^3H_4$	4/5	Oblate
Nd^{III}	60	$[Xe]4f^3$	$^4I_{9/2}$	8/11	Oblate
Pm^{III}	61	$[Xe]4f^4$	$^5I_4$	3/5	Prolate
Sm^{III}	62	$[Xe]4f^5$	$^6H_{5/2}$	2/7	Prolate
Eu^{III}	63	$[Xe]4f^6$	$^7F_0$	-	Isotropic
Gd^{III}	64	$[Xe]4f^7$	$^8S_{7/2}$	2	Isotropic
Tb^{III}	65	$[Xe]4f^8$	$^7F_6$	3/2	Oblate
Dy^{III}	66	$[Xe]4f^9$	$^6H_{15/2}$	4/3	Oblate
Ho^{III}	67	$[Xe]4f^{10}$	$^5H_8$	5/4	Oblate
Er^{III}	68	$[Xe]4f^{11}$	$^4I_{15/2}$	6/5	Prolate
Tm^{III}	69	$[Xe]4f^{12}$	$^3H_6$	7/6	Prolate
Yb^{III}	70	$[Xe]4f^{13}$	$^2F_{7/2}$	8/7	Prolate
Lu^{III}	71	$[Xe]4f^{14}$	$^1S_0$	-	Isotropic

Table 1.4 Parameters for the Ln^{III} ions. Adapted from Reference 95.

Each $^{2S+1}L_J$ level is composed of $(2J+1)$ M_J microstates or sub-levels. The presence of a crystal field causes a slight but non-negligible perturbation of the energy levels, resulting in 'Stark' splitting of the M_J microstates.[111] Splitting of the terms due to spin-orbit coupling is of the order ~10,000 cm^{-1} in magnitude, while splitting of the levels into M_J microstates due to crystal field splitting is of the order ~100 cm^{-1}. It is the energy barrier between the two orientations of the lowest-energy M_J microstate that causes the

slow relaxation in Ln SMMs. For Ln^{III} ions with an odd number of electrons (Kramers ions), the M_J microstates are arranged as doublets: these ions always meet the requirement of an SMM for a bistable electronic ground state. For non-Kramers Ln^{III} ions, the M_J states may be arranged as singlets or doublets, and thus these ions may not necessarily meet the bistability requirement. It should be noted that the highest value M_J state is not necessarily the lowest in energy. The splitting of the ^6H term of Dy^{III} into the ^6H_J levels by spin-orbit coupling, and the splitting of the ground state $^6H_{15/2}$ level into the $(2J+1)$ M_J microstates by the crystal field, is depicted below (Figure 1.23).

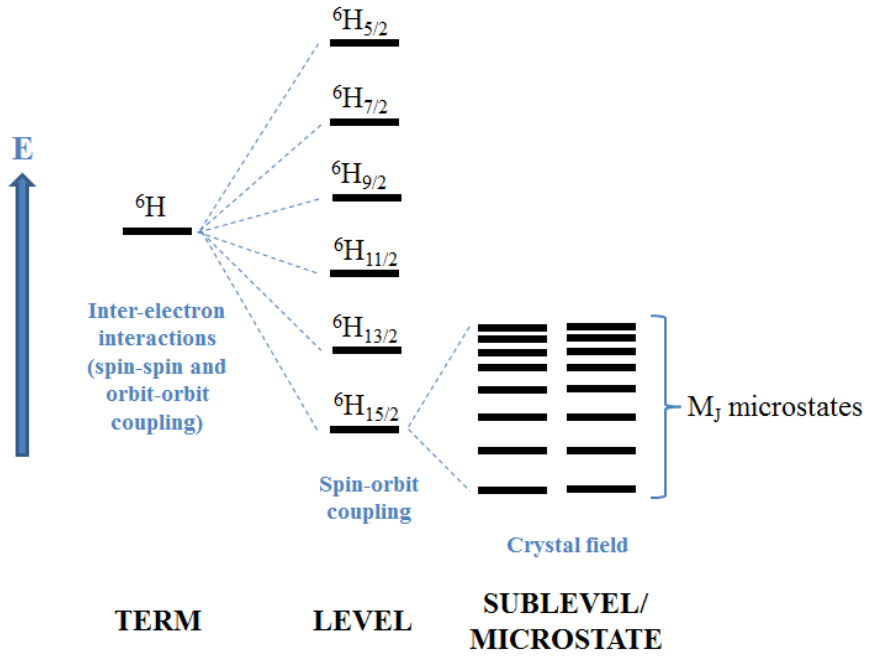

Figure 1.23 The splitting of the ^6H term of a Dy^{III} ion by spin-orbit coupling and crystal field. Only the M_J microstates of the lowest-energy $^6H_{15/2}$ level are shown. Adapted from Reference 95.

As was mentioned earlier, the magnetic anisotropy (due to ZFS) of a transition metal cluster arises primarily as a result of the structural arrangement of the metal ions and ligands: the coordination geometries, molecular symmetry, and crystal packing;

while the intrinsic anisotropy of most lanthanide ions is primarily due to the presence of spin-orbit coupling (SOC). In addition, the large ground state *S* of transition metal cluster SMMs arises from the coupled spins of multiple metal centers, whereas the large ground state *J* of the lanthanides utilized in Ln-SMMs is a feature of the individual metal ions. For these reasons, lanthanide-based SMMs allow for the presence of SMM behaviour in complexes containing just one metal ion, referred to as single ion magnets (SIMs), or mononuclear SMMs.

1.2.4.2 Observing SMM behaviour

The presence of SMM behaviour is usually determined by performing low-temperature magnetic measurements using a SQUID or PPMS magnetometer. The most common method involves measuring the susceptibility response of the sample in an oscillating magnetic field, produced by an alternating current (ac). In an SMM, the anisotropy barrier U causes the magnetization to lag behind the oscillating field, resulting in a phase shift, φ, relative to the field. Ac susceptibility can therefore be separated into two components, the in-phase, or real, component χ', and the out-of-phase, or imaginary, component χ''. These two components are given by Eqns. 1.8a and b, below.[112]

$$\chi' = \chi\cos\varphi \qquad \textbf{Eqn. 1.8a}$$

$$\chi'' = \chi\sin\varphi \qquad \textbf{Eqn. 1.8b}$$

The amount of 'lag' for a given SMM depends upon the frequency of the oscillation of the field: the faster the ac field oscillates, the less opportunity the magnetization has to overcome the anisotropy barrier and relax. For this reason the hallmark of an SMM is a frequency-dependence to the out-of-phase component of the ac

susceptibility, usually observed in a plot of χ'' *vs.* T (Figure 1.25, later) or χ'' *vs.* frequency.

A second method for determining the presence of SMM behaviour involves performing a dc field scan at one or more very low temperatures. The field is increased from 0 to +H, and then cycled back from +H to –H to +H again.[95] The presence of a hysteresis loop in the plot of M *vs.* H indicates the presence of an energy barrier to magnetic relaxation.

The key parameters used to describe SMM behaviour may be extracted from the magnetic data. The effective anisotropy barrier U_{eff}, as well as a number of other parameters, may be calculated from the ac susceptibility data. This is discussed in Chapters 3 and 4. The blocking temperature T_B can be directly seen as the temperature at which a hysteresis loop is observed in a plot of M *vs.* H. It should be noted that T_B depends on the measurement sweep rate, for which there is no standard value; so it can be difficult to compare T_B values between complexes.[111]

1.2.4.3

1.2.4.4 Mononuclear Ln-SMMs

The first Ln-SMMs, which were also the first *mononuclear* SMMs, were published by Ishikawa in 2003.[113] He described two double-decker phthalocyanine-based complexes, $[Bu_4N][Pc_2Ln]$, where Ln = Dy^{III} and Tb^{III} (Figure 1.24).

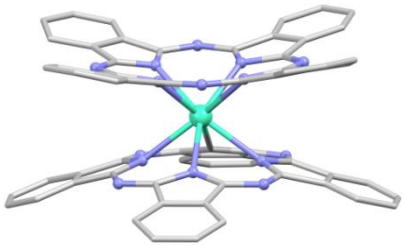

Figure 1.24 Structure of the anion portion of the first two reported SMM complexes, where lavender = N, green = Tb^{III}, Dy^{III}.[113,114]

The Ln^{III} metal centers (Ln = Tb, Dy) exhibited 8-coordinate, square antiprismatic geometries. The slow relaxation of magnetization was observed by applying an alternating current of various frequencies to a crystalline sample of each complex at low temperature. Figure 1.25 depicts the magnetic behaviour of the Dy^{III} complex. The χ'' *vs.* T plot clearly shows the frequency-dependence of the magnetization of this compound, which is the characteristic mark of an SMM.[113] The Tb^{III} complex displayed a barrier to relaxation of U_{eff} = 566 cm^{-1}, significantly higher than any barrier which had been yet observed for a transition metal cluster SMM.

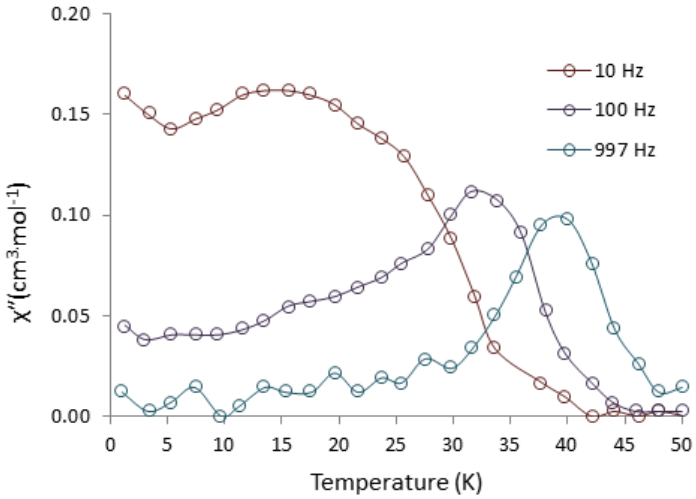

Figure 1.25 χ'' *vs.* T plot for $[Bu_4N][Pc_2Dy]$. Reproduced from Reference 113.

Since Ishikawa's initial work, now over ten years ago, interest in Ln-SMMs has grown exponentially. Well over 100 such complexes have now been reported. The class of Ln-SMMs of interest with respect to my research is that of mononuclear Ln-SMMs: those which contain a single Ln metal ion. These mononuclear Ln-SMMs are typically classified according to three criteria: (i) the type of metal ion; (ii) the geometry, and/or (iii) the class of ligand.

The five lanthanide ions which have utilized in the synthesis of mononuclear Ln-SMMs are Tb^{III}, Dy^{III}, Ho^{III}, Er^{III} and Yb^{III}.[111] Since the *f*-orbitals of these lanthanides are more than half-filled, they have large spin-orbit coupled *J* values in the ground state (ranging from 6 to 8). Of these five, Dy^{III}, Er^{III} and Yb^{III} are Kramers ions, while Tb^{III} and Ho^{III} are not. Dy^{III} and Tb^{III} are by far the most exploited, with over 30 examples of each reported; while there are fewer than 10 mononuclear SMMs based on Ho^{III}, Er^{III} and Yb^{III}.[95]

The most common class of ligand exploited in Ln-SMM synthesis comprises phthalocyanine and its derivatives. *Bis*(phthalocyanine) complexes with the same double-decker structure and square antiprismatic geometry as the complexes reported by Ishikawa have continued to lead the field. Phthalocyanine may be derivatized in numerous ways, yielding Pc ligands substituted with nitrile groups, long alkyl chains, bulky aromatic esters, and trifluoromethane moieties.[95] The resulting $[LnPc]_2$ complexes may be positive, negative, or neutral in charge; and most are redox active. Another major class of ligand is acetylacetonate (acac) and its β-diketonate derivatives. Several SMMs have been reported comprising a Ln^{III} ion surrounded in a distorted square antiprismatic geometry with three β-diketonate ligands and two mono- or one bidentate neutral

donor.[115] Other studied ligand classes include nitronyl-nitroxide ligands, carbon-donor ligands such as cyclopentadienide ($[Cp]^-$) and cyclooctatetraenide ($[COT]^{2-}$), and organometallic polyoxometallate ligands.[116] An additional array of ligands with O (hydroxy and carboxy) and N (amine, oxime, imine, pyridine) donors have been utilized also, and have been thoroughly reviewed by Layfield and co-workers.[111]

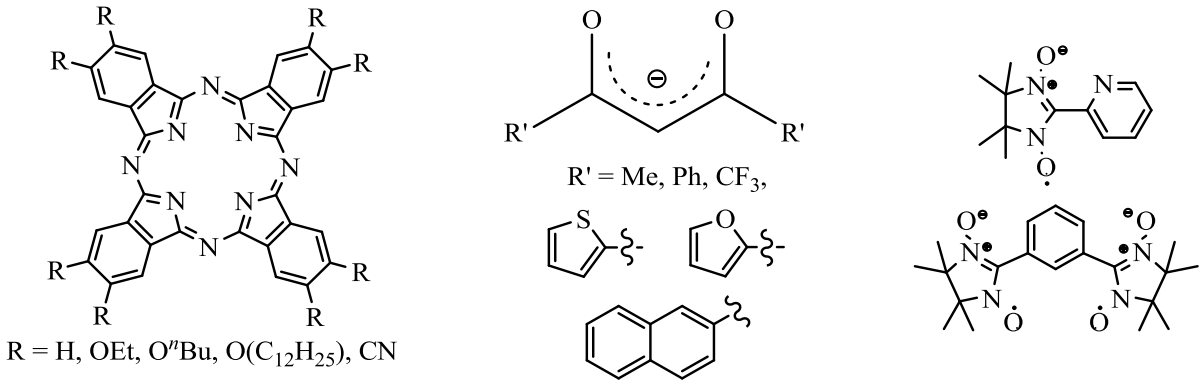

Figure 1.26 Representative ligands from (left to right) the phthalocyanine, β-diketone and nitroxyl radical families. Adapted from Reference 111.

There is a reason why *bis*(phthalocyanine) complexes dominate the Ln-SMM landscape. Recently, Rinehart and Long presented a simple model to help predict ligand geometries which would enhance the single-ion anisotropy of the lanthanides.[117] The model is based on the fact that the *f* orbitals have a strong angular dependence; that is, the charge cloud for a given *f* orbital may be described as prolate (elongated along the *z*-axis), oblate (expanded in the *xy* plane), or isotropic/spherical.[117] Since the population of the *f* orbitals for a given lanthanide is readily determined using Hund's rules, the overall shape of the 4*f* cloud of each lanthanide may in turn be described as prolate, oblate or spherical. The distribution of the electron density for each lanthanide is presented in

Table 1.4. Long postulated that the magnetic anisotropy of an oblate lanthanide ion would be enhanced by the presence of a crystal field with electron density located axially, above and below the *xy* plane; while the anisotropy of a prolate ion would be enhanced by electron density located equatorially, in the *xy* plane (Figure 1.27).[117] These arrangements would minimize the repulsive interactions between the electron clouds of the metal ion and ligand(s), giving rise to $M_J = J$ states parallel and antiparallel to the molecular axis, or *z*-axis. [117] As can be seen in Table 1.4, both Tb^{III} and Dy^{III} have oblate electron clouds, and thus their anisotropy would theoretically be enhanced by the axially located charge density of ligands bound in a sandwich-type conformation. [117]

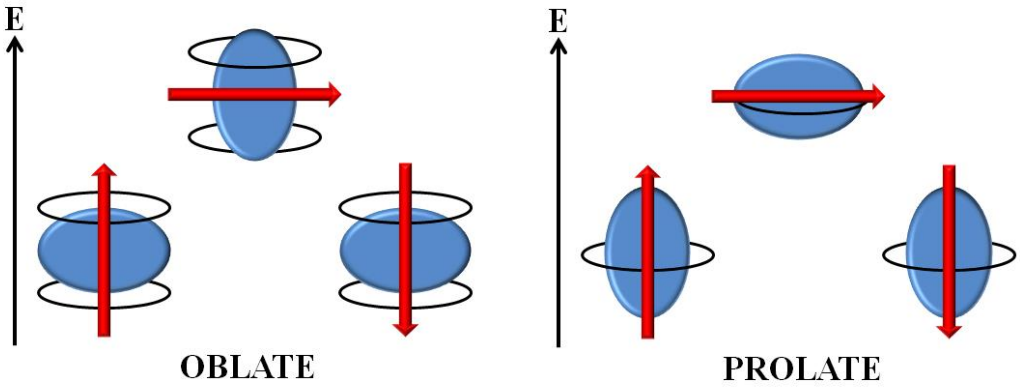

Figure 1.27 Representation of low and high energy states for (left) an oblate charge cloud in an axial crystal field, and (right) a prolate charge cloud in an equatorial crystal field. The blue ovals represent the 4*f* electron density, the black circles represent ligand electron density, and the red arrows represent the orientation of the projection of the spin-orbit coupled *J* state: large M_J values are lowest in energy for the depicted crystal fields. Adapted from Reference 117.

The enhancement of the anisotropy of Tb^{III} and Dy^{III} by the square antiprismatic environment of a *bis*(phthalocyanine) ligand field helps to explain why D_{4d} complexes of these two ions are so ubiquitous amongst Ln-SMMs. The record U_{eff} barrier of ~650 cm^{-1} is held by a substituted *bis*(phthalocyanine) complex of Tb^{III},[110] and in fact, the vast majority of the mononuclear Ln-SMMs with the top twenty highest anisotropy barriers (>390 cm^{-1}) are such complexes. Tb^{III} is responsible for the highest barriers, likely because its *f* electron cloud has more angular dependence; but Dy^{III} has been utilized in more SMMs, because it always has a doubly degenerate ground state. Although the 8-coordinate, square antiprismatic geometry associated with the *bis*(phthalocyanine) complexes is by far the most common geometry, a number of other coordination environments have been reported for the metal centers of Ln-SMMs (Table 1.5). Reported barriers for non-phthalocyanine mononuclear lanthanide complexes range in magnitude from 130 cm^{-1} to 3 cm^{-1}.[95, 111]

Coord. No.	Reported geometries
6	trigonal prism, octahedron
7	capped octahedron, capped trigonal prism
8	square antiprism, cube, biaugmented trigonal prism, triangular dodecahedron
9	capped square antiprism, muffin, hula hoop
10	sphenocorona, tetradecahedron
12	icosahedron

Table 1.5 Coordination geometries reported for Ln-SMMs.[95]

1.2.4.5 Rational design of Ln-SMMs

The exciting potential uses for SMMs as high density information storage devices, as qubits for quantum computing, and in molecular spintronics, have been well-described.[118-123] However, before these species can be practically applied, the temperatures at which SMM behaviour is observed must be significantly increased, to at least liquid nitrogen levels. Currently, the highest T_B (temperature at which hysteresis is observed) reported for a Ln-SMM, mononuclear or otherwise, is 8.3 K.[124] In order to rationally design SMM systems with predictable, applicable magnetic properties, a greater understanding of the relationship between structure and magnetism is required. In this regard, mononuclear SMMs are very desirable, because their comparable simplicity makes magneto-structural correlation more achievable.

The electrostatic theory of Long, described above, is useful in helping to explain the relaxation behaviour of many Ln-SMMs. However, as interest in ligand design for rational synthesis of SMMs increases, so does the importance of an even more detailed understanding of magneto-structural correlation. The effect of even minute changes in coordination geometry on the anisotropy of a system was shown by Sessoli and co-workers in their wonderfully detailed magnetic and electronic study on the Dy^{III} complex of the macrocyclic ligand DOTA.[125] Rare geometries, such as those discussed in **Chapter 3**, and tunable systems in which one or more structural parameters can be systematically modified, such as those discussed in **Chapter 4**, offer a unique opportunity to examine the subtleties of magneto-structural correlation.

1.3 Schiff-base macrocycles:

Applications in molecule-based magnetic materials

As mentioned earlier, my work involves two classes of macrocyclic ligand. The complexes synthesized in my first and second projects (**Chapters 2-3**) are Schiff-base macrocycles, based on a 15-membered, pentadentate macrocyclic system (Figure 1.28).

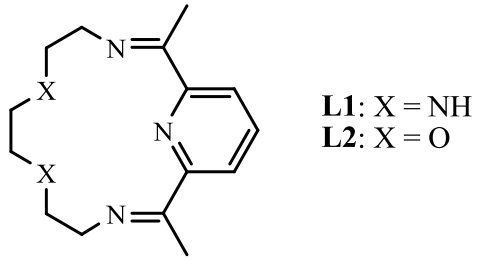

Figure 1.28 The 'parent' pentadentate macrocycles **L1** and **L2**.

A brief overview of complexes based on this macrocyclic system will now be presented. Firstly, mononuclear complexes of macrocycles **L1** and **L2** are discussed, with emphasis on the early structural elucidation and coordination geometries of the transition metal complexes; the unique SCO transition of a [Fe(**L2**)$CN)_2$] complex; and a discussion of related rare earth complexes. Secondly, selected higher-order magnetic structures based on complexes of these ligands are presented.[126]

Schiff bases containing an imine or azomethine group (-R_2C=N-R; where R = an aryl or alkyl group) formed via the condensation of a primary amine with an active carbonyl are named after the Italian chemist Hugo Schiff who first discovered them.[127] The reaction to prepare a Schiff base is reversible, occurring via a carbinolamine intermediate which typically requires the removal of water to push the equilibrium to the right in order to obtain the compounds in good yields (Scheme 1.1).

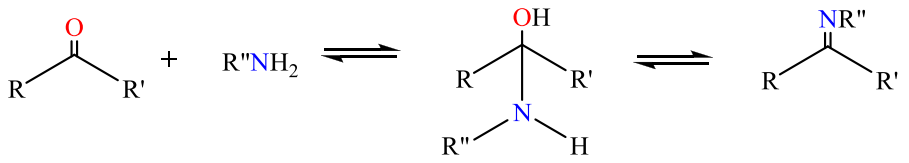

Scheme 1.1 Schiff-base formation.

The 15-membered Schiff-base macrocycles discussed in this section are formed by the [1+1] metal-templated condensation of a diamine and a diketone (Scheme 1.2). The role of the metal ion in the cyclization reaction is to pre-organize the molecular precursors via the formation of a metal complex, thus the size and charge of the metal ions employed are important considerations. The pyridyl head groups serve to increase the rigidity of the ligand which is kinetically favourable for the templation reaction.

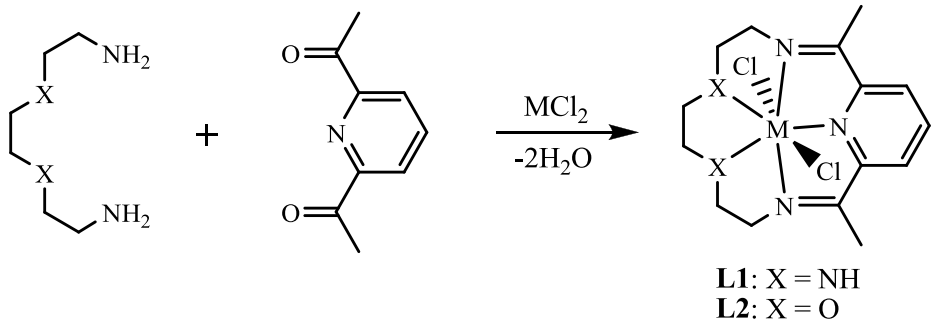

Scheme 1.2 General synthesis of a 15-membered N_3X_2 Schiff-base macrocycle via metal templation around a metal chloride salt.

1.3.1 Mononuclear complexes

Transition metal complexes: structural reports

The N_5 macrocycle **L1** was first reported in 1967, when Hawkinson described the crystal structure of an $[Fe(\mathbf{L1})(NCS)_2]ClO_4$ complex (Figure 1.29), and noted the unusual

seven coordinate pentagonal bipyramidal geometry of the central Fe^{III} ion.[128] The macrocycle was synthesized following Scheme 1.2, above, via the condensation of 2,6-diacetylpyridine and triethylenetetramine. At this time, **L1** was only the second reported example of a macrocyclic ligand prepared via a metal templation strategy.

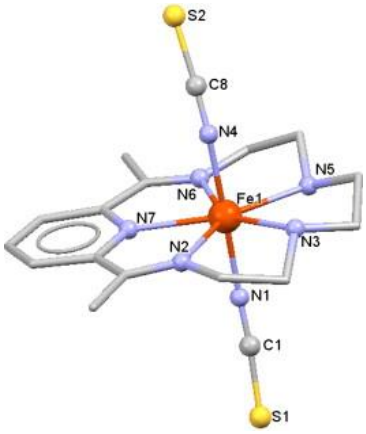

Figure 1.29 The molecular structure of the first N_5 macrocyclic complex $[Fe(\mathbf{L1})(NCS)_2]ClO_4$.[128,129] The ClO_4^- counter ion and H-atoms are omitted for clarity.

Ten years later, Nelson and co-workers described the preparation of a family of coordination complexes of **L1** via templation by a series of metal cations, where M^{II} = Mn, Fe, Co, Ni, Cu, Zn, and Mg. Interestingly, when X = O and M = Ag^I or Pb^{II}, the related 30-membered [2+2] macrocycle formed in high yield, indicating that both the size of the cation and its affinity for the X substituents on the diamine precursor direct the preferred course of the condensation reaction.

Following the synthesis of the $[Mg(\mathbf{L1})(H_2O)Cl]Cl$ complex, the Mg^{II} cation was exploited as a template for the synthesis of the chloride, perchlorate, tetraphenylborate and thiocyanate derivatives of **L1** and **L2.**[130] Although no single crystal X-ray diffraction data were collected for this series of complexes (other than the Mg^{II} complex), imine

bond formation was confirmed by IR spectroscopy, with each complex exhibiting a $\nu_{C=N}$ stretch at 1650 cm^{-1}, consistent with formation of the Schiff base bis(imine) bond. The templating role of the Mg^{II} cation was demonstrated by the failure of the macrocycle to form in the absence of a metal cation. For these reactions, in the absence of any metal ion, an oily product or a mixture of products was obtained in which the carbonyl groups of the diketone starting material were observed in the IR spectra. The IR spectra also indicated the presence of bound water molecules for each of the complexes with the exception of the thiocyanate derivative. Consistent with this, the electronic spectra indicated that the chloride, perchlorate and tetraphenylborate derivatives were salts, with non-coordinating counter ions balancing the charge of the bis(aqua) complexes; while the thiocyanate derivative was a neutral complex, with two coordinating counter ions. Mass spectra of the complexes did not show parent ion peaks, but the spectra of the chloride derivatives did contain fragment ions corresponding to the loss of a single chloride ion from complexes of **L1** and **L2** respectively. ^{1}H and ^{13}C NMR data for selected complexes were in agreement with the suggested macrocyclic structures. Given the data, a seven-coordinate pentagonal-bipyramidal geometry was assigned to all of the complexes.[130]

A second series of studies were then carried out where the counter ion and axial ligands were kept constant, while the nature of the templating metal ion was varied. Following this strategy, the thiocyanate derivatives of the Mn^{II}, Fe^{II}, Zn^{II} and Cd^{II} complexes of **L1** and **L2** were prepared.[131] This family of complexes was similarly characterized by IR and electronic spectroscopy, elemental analysis and mass spectrometry. The crystal structure of [Mn(**L2)**$(NCS)_2$] was determined and was the first reported structure of a macrocyclic complex of **L2**. This complex, like other members of

the series, has a pentagonal bipyramidal geometry with axial thiocyanate ligands, similar to the [Fe(**L1**)$(NCS)_2$]ClO_4 complex presented in Figure 1.29. Given that the IR spectra of the Fe^{II}, Zn^{II}, and Cd^{II} dithiocyanate complexes were almost identical, a pentagonal bipyramidal geometry was assigned to all four complexes.[131]

Fe^{II} complex: SCO behaviour

Of all the structurally described transition metal complexes, by far the most magnetically interesting and well-studied is the Fe^{II} *bis*(cyanide) complex of **L2**: [Fe(**L2**)$(CN)_2$]. Following the structural reports by Nelson and Drew described above, attention shifted towards the magnetic properties of the Fe^{II} complexes of **L1** and **L2.** Nelson reported that while the metal center of [Fe(**L1**)$(CN)_2$] exhibited a low spin (LS) ground state at ambient temperatures, the N_3O_2 analogue displayed a thermally-induced spin crossover (SCO) transition.[132] At low temperatures (<150 K), the system adopts a low spin (LS), S = 0 state, while at high temperatures (>230 K), the complex was present solely in the HS S = 2 state. The thermal transition was reversible, with $T_c^{\uparrow}$ = 222 K, giving a hysteresis loop with a width 15 K. The LS complex was assumed to be 6-coordinate; but the HS geometry could not be assigned due to the lack of X-ray quality crystals.[132] Powder diffraction data suggested that the transition was accompanied by a change in unit cells likely due to a change in geometry. After Nelson's initial work, investigation into the unusual SCO behaviour of [Fe(**L2**)$(CN)_2$] lay largely dormant for twenty years until it was revisited by Sato in 2001, who confirmed that the room temperature crystal structure of the HS [Fe(**L2**)$(CN)_2$]·H_2O complex was 7-coordinate, as postulated earlier by Nelson, with the macrocycle acting as an essentially planar

pentadentate ligand, and the two cyanide ligands occupying the axial positions.[133] Several years later, Letard conclusively proved the presence of a structural transformation when he reported the LS molecular structure of the complex, with the Fe^{II} ion in a 6-coordinate, distorted octahedral environment following the breaking of an Fe-O bond.[134] This conversion is particularly interesting since it is completely reversible in the solid state. Such a structurally characterized, reversible change in coordination geometry accompanying a thermal SCO transition (Figure 1.30) was unprecedented in the chemical literature.

Sato and co-workers also studied the photomagnetism of this complex, and found that the complex also exhibits a photo-induced SCO transition, displaying the LIESST effect. The observed T_c(LIESST) of 130 K is currently one of the highest relaxation temperature reported for any mononuclear Fe^{II} complex, and represents an important step towards the application of such compounds in molecular devices.

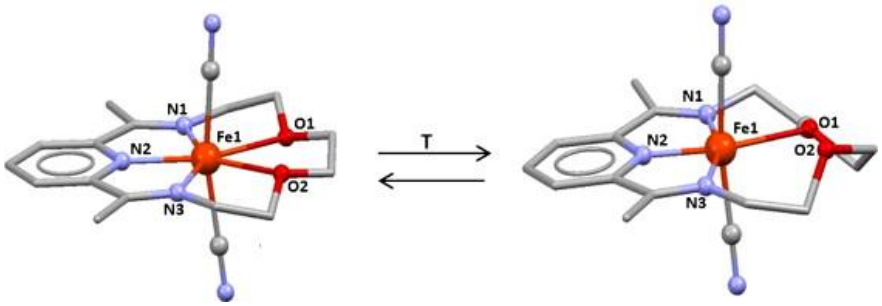

Figure 1.30 Molecular structures of [Fe(**L2**)$(CN)_2$]·H_2O, in the HS (left) and LS (right) states showing the reversible transition from 7-coordinate to 6-coordinate geometry, H-atoms are omitted for clarity.

Rare earth complexes

For more than a decade, the Radecka-Paryzeck group has been working towards incorporating rare earth elements into **L2** and other Schiff base macrocyclic systems. Initially, the Y^{III} chloride and perchlorate complexes of **L2** were formed via metal templation.[135] A 7-coordinate geometry was assigned to the complexes with two water molecules filling the axial positions and the chloride and perchlorate anions acting as counter ions. Seven coordinate complexes of Y^{III} are quite rare,[136] and this was the first reported example of a Y^{III} ion acting as the templating agent for the synthesis of a pentadentate Schiff base macrocycle. Soon after these studies, the metal-templated synthesis of several lanthanide complexes of **L2** were reported.[137] The heavier lanthanides (Dy^{III}, Tm^{III}, Lu^{III} and Er^{III}) were found to template the formation of **L2**.[137] Characterization by IR, mass spectrometry and elemental analysis suggested that the complexes have 7-coordinate pentagonal bipyramidal geometry with the five donor atoms of the macrocyclic ring bound to the lanthanide ion, along with two water molecules in the axial positions. The chloride and perchlorate anions were concluded to be present as non-coordinating counter ions, although there was no crystallographic evidence available to corroborate this. The lighter lanthanide ions (La^{III}, Sm^{III}, and Eu^{III}) proved to be less effective as templating agents, yielding acyclic products.[137] These results confirmed the dependence of metal templation on the ratio of metal ion size to potential macrocyclic cavity with the larger early lanthanides unable to template macrocycle formation. A similar study was performed by Bastida and co-workers with regards to the related hindered macrocycle **L3**, as well as its formyl derivative **L3b**.[138]

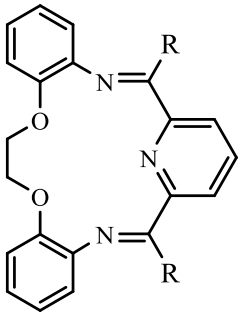

L3: R = CH_3
L3b: R = H

Attempts were made to template the formation of each macrocycle around the trivalent lanthanide series La^{III}-Er^{III} with nitrate and perchlorate counter ions. Although no X-ray quality crystals could be isolated, the resulting products were characterized by elemental analysis, conductance, infrared spectroscopy, FAB mass spectrometry, and magnetic moment. Elemental analysis gave varying degrees of fit for complexes with the formulae $[Ln(\mathbf{L})]X_3 \cdot xH_2O \cdot y$EtOH, where **L** = **L3** or **L3b**, and X = NO_3^- or ClO_4^-. FAB mass spectrometry proved uninformative, with no clear molecular ion peaks apparent. IR spectroscopy confirmed imine bond formation, and indicated that in complexes of both **L3** and **L3b**, bound perchlorate ions were present, due to the splitting of the peak around 1114 cm^{-1}. However, no firm coordination assignments could be made due to the lack of X-ray structural data.[138]

1.3.2 Polynuclear complexes

Over the last two decades, mononuclear complexes of **L1** and **L2** have been increasingly exploited as building blocks for the development of more structurally complex magnetic materials, including 1-D linear chains, as well 2-D and 3-D higher order structures. The majority of the compounds within this class are heterometallic materials assembled via the reaction of **L1** or **L2** with a secondary polycyanometalate

building block. Mn^{II} complexes of either **L1** or **L2** are by far the most commonly exploited; Fe^{II} complexes of **L1** were also utilized along with three examples of higher order structures assembled from Co^{II} macrocycles of **L2**. In each case the macrocyclic bound metal center possesses pentagonal bipyramidal geometry and the polycyanometalate building blocks include di-, tetra-, or hexacyano 3*d* ions, as well as hepta- or octacyano 4*d* and 5*d* linkers. Additionally, cyanometalate precursors with blocking ligands, as well as non-polycyanometalate linkers such as azide, dicyanamido and a TCNQ radical have also been employed.

The magnetic properties of the resulting 1-, 2- and 3-D structural topologies are summarized in Table 1.6.[126]

$[ML]^{n+}$	Linker	Dimensionality	Metal Center / Geometry	∠ M-NC (°)[††]	Exchange Interactions	$\|J\|$ (cm^{-1})	Magnetic Behaviour	Ref.
Dicyanometalates								
$[Mn(\mathbf{L1})]^{2+}$	$[Ag(CN)_2]^-$	1D – infinite	Mn^{II} PB-7 Ag^{I} L-2	166	AF Mn^{II}-Mn^{II}	0.065(2)	-	[139]
$[Mn(\mathbf{L1})]^{2+}$	$[Au(CN)_2]^-$	1D – infinite	Mn^{II} PB-7 Au^{I} L-2	166	AF Mn^{II}-Mn^{II}	0.23(3)	-	[139]
$[Mn(\mathbf{L2})]^{2+}$	$[Ag(CN)_2]^-$	1D – infinite	Mn^{II} PB-7 Ag^{I} L-2	165	AF Mn^{II}-Mn^{II}	0.15(6)	-	[139]
$[Mn(\mathbf{L2})]^{2+}$	$[Au(CN)_2]^-$	1D – infinite	Mn^{II} PB-7 Au^{I} L-2	164	AF Mn^{II}-Mn^{II}	0.13(5)	-	[139]
Tetracyanometalates								
$[Mn(\mathbf{L2})]^{2+}$	$[M(CN)_4]^{2-}$	1D – infinite	Mn^{II} PB-7 Ni/Pd/Pt^{II} SP-4	151 - 154	P	n/a	-	[140]
Hexacyanometalates								
$[Mn(\mathbf{L2})]^{2+}$	$[Fe(CN)_6]^{4-}$	1D – trinuclear	Mn^{II} PB-7. LS Fe^{II} OC-6	156	F Mn^{II}-Mn^{II}	0.045	-	[140]
$[Mn(\mathbf{L2})]^{2+}$	$[Cr(CN)_6]^{3-}$	1D – infinite and trinuclear	Mn^{II} PB-7 Cr^{III} OC-6	156 - 159	F/AF Mn^{II}-Cr^{III}	7.5(7)	-	[140]
$[Mn(\mathbf{L2})]^{2+}$	$[Fe(CN)_6]^{3-}$	1D – infinite and trinuclear	Mn^{II} PB-7 LS Fe^{III} OC-6	159 - 160	F Mn^{II}-Fe^{III}	not modelled	-	[140]
$[Mn(\mathbf{L2})]^{2+}$	$[Cr(CN)_6]^{4-}$	1D – trinuclear	Mn^{II} PB-7 Cr^{II} OC-6	145 - 157	AF Mn^{II}-Cr^{II}	9.8	-	[141]
$[Mn(\mathbf{L2})]^{2+}$	$[Cr(CN)_6]^{3-}$	1D – trinuclear	Mn^{II} PB-7 Cr^{III} OC-6	162	AF Mn^{II}-Cr^{III}	6.52	-	[141]
$[Mn(\mathbf{L2})]^{2+}$	$[Fe(CN)_6]^{3-}$	1D – trinuclear	Mn^{II} PB-7. LS Fe^{III} OC-6	165	F Mn^{II}-Fe^{III}	not given	-	[141]

$[Fe(\mathbf{L2})]^{2+}$	$[Cr(CN)_6]^{3-}$	1D – trinuclear	HS Fe^{II} PB-7 Cr^{III} OC-6	155	F Fe^{II}-Cr^{III}	3.76(6)	SMM U_{eff} = 44.3 K	[142]
$[Mn(\mathbf{L1})]^{2+}$	$[Fe(CN)_6]^{3-}$	1D – pentanuclear	Mn^{II} PB-7 LS Fe^{III} OC-6	144 - 155	3 AF, 1 F Mn^{II}-Fe^{III}	0..3, 1.5, 1.6, 2.6	-	[143]
$\{[Co(\mathbf{L2})]^{2+}\}_2$	$[Fe(CN)_6]^{4-}$	1D – infinite	Co^{II} PB-7 LS Fe^{II} OC-6	161	F Co^{II}-Co^{II}	5.4	-	[144]
$[Mn(\mathbf{L2})]^{2+}$	$[Co(CN)_6)]^{4-}$	1D – trimer	Mn^{II} PB-7 Co^{III} OC-6	166	P	n/a	-	[141]
$[Mn(\mathbf{L2})]^{+}$	$[Fe(CN)_6)]^{3-}$	2D – lattice	Mn^{II} PB-7 LS Fe^{III} OC-6	160 -161	AF Mn^{II}-$Fe1^{III}$ AF Mn^{II}-$Fe2^{III}$	J_1 = 2.1 J_2 = 1.6	FI ordering T_c = 6.4 K	[140]
$[Co(\mathbf{L1})]^{2+}$	$[Cr(CN)_6]^{3-}$	3D – nanotubular	HS Co^{II} PB-7 LS Cr^{III} OC-6	155	F Co^{II}-Cr^{III}	1.2	F ordering < 12 K	[145]
$[Fe(\mathbf{L1})]^{2+}$	$[Co(CN)_6]^{3-}$	2D – brickwall	HS Fe^{II} PB-7 LS Co^{III} OC-6	154 - 165	P	n/a	-	[146]
$[Co(\mathbf{L2})]^{2+}$	$[Fe(CN)_6]^{3-}$	2D – honeycomb	HS Co^{II} PB-7 LS Fe^{III} OC-6	150 - 159	F Co^{II}-Fe^{III}	not given	F ordering < 3K	[146]
Heptacyanometalates								
$[Mn(\mathbf{L2})]^{2+}$	$[Mo(CN)_7]^{4-}$	1D – trimer	Mn^{II} PB-7 Mo^{III} PB-7	146 - 150	AF Mn^{II}-Mo^{III}	not given	-	[147]
$[Mn(\mathbf{L2})]^{2+}$	$[Mo(CN)_7]^{4-}$	2D - network	Mn^{II} PB-7 Mn^{II} PB-7 Mo^{III} PB-7 Mo^{IV} SA-8	143 - 151	F ([148]), AF ([149]) Mn^{II}-Mo^{III}	not given ([148]) 6.9 ([149])	F ordering < 3K ([148])†	[148], [149]
$[Mn(\mathbf{L1})]^{2+}$	$[Mo(CN)_7]^{4-}$	0D – cluster	Mn^{II} BP-7 Mo^{III} PB-7	140 -160	AF overall	not given	glassy behaviour	[150]
$[Mn(\mathbf{L2})]^{2+}$	$[Mo(CN)_7]^{4-}$	2D – layers	Mn^{II} PB-7 Mo^{III} PB-7	134 - 151	AF Mn^{II}-Mo^{III}	not given	F ordering < 3 K	[149]
$[Mn(\mathbf{L2})]^{2+}$	$[Mo(CN)_7]^{4-}$	2D – ladder	Mn^{II} PB-7	143 - 156	AF Mn^{II}-Mo^{III}	not given	SMM	[149]

			Mo^{III} CTP-7. Mo^{IV} SA- 8 .				U_{eff} = 8.1 K	
$[Mn(\mathbf{L2})]^{2+}$	$[Mo(CN)_7]^{4-}$	1D - trinuclear	Mn^{II} PB-7 Mo^{IV} SQ-8	145	AF Mn^{II}-Mn^{II}	1.46×10^{-2}	-	[149]
Octacyanometalates								
$[Mn(\mathbf{L1})]^{2+}$	$[Nb(CN)_8]^{4-}$	1D – infinite	Mn^{II} PB-7 Nb^{IV} SQ-8	151- 155	AF	not given	-	[151]
$[Fe(\mathbf{L1})]^{2+}$	$[Nb(CN)_8]^{4-}$	1D – infinite	Fe^{II} PB-7 Nb^{IV} SQ-8	153 - 160	AF	20	SCM U_{eff} = 7.4 K	[152]
$[Mn(\mathbf{L1})]^{2+}$	$[Mo(CN)_8]^{4-}$	1D – infinite	Mn^{II} PB-7 $Mo^{IV} \rightarrow Mo^{V}$ SQ-8	155 151	before illumination: AF Mn^{II}-Mn^{II} after illumination: AF Mn^{II}-Mo^{V}	not given	after illumination/ photo-oxidation: ferromagnetic chain	[153]
$[Fe(\mathbf{L1})]^{3+}$	$[W(CN)_8]^{4-}$	2D – honeycomb	HS Fe^{III} PB-7 W^{IV} DD-8	161 158	AF Fe^{III}-Fe^{III}	not given	-	[154]
'Blocked' complexes								
*$[Fe(\mathbf{L2})](CN)_2$	$[Mn(hfac)_2]$	1D – infinite	LS/HS Fe^{II} PB-7 HS Mn^{II} OC-6	no single crystal data	AF HS Fe^{II}-Mn^{II} (after illumination)	0.10	LIESST effect	[155]
$[Mn(\mathbf{L1})]^{2+}$	$[Fe(bpb)(CN)_2]^{-}$	1D – infinite	Mn^{II} PB-7 LS Fe^{III} OC-6	162, 155	AF Mn^{II}-Fe^{III}	$\lvert J_1\rvert$ = 1.16(2), $\lvert J_2\rvert$ = 0.10(3)	-	[156]
$[Mn(\mathbf{L2})]^{2+}$	$[Fe(bpb)(CN)_2]^{-}$	1D – infinite	Mn^{II} PB-7 LS Fe^{III} OC-6	159, 147	AF Mn^{II}-Fe^{III}	$\lvert J_1\rvert$ = 3.10(1), $\lvert J_2\rvert$ = 0.25(1)	-	[156]
$[Mn(\mathbf{L1})]^{2+}$	$[Fe(bpClb)(CN)_2]^{-}$	1D – infinite	Mn^{II} PB-7 LS Fe^{III} OC-6	163, 155	AF Mn^{II}-Fe^{III}	$\lvert J_1\rvert$ = 1.10(1), $\lvert J_2\rvert$ = 0.139(8)	-	[156]
$[Mn(\mathbf{L2})]^{2+}$	$[Fe(bpClb)(CN)_2]^{-}$	1D – infinite	Mn^{II} PB-7 LS Fe^{III} OC-6	148, 167	AF Mn^{II}-Fe^{III}	$\lvert J_1\rvert$ = 1.99(6), $\lvert J_2\rvert$ = 0.57(1)	-	[156]
$[Mn(\mathbf{L2})]^{2+}$	$[Fe(bpBrb)(CN)_2]^{-}$	1D – infinite	Mn^{II} PB-7 LS Fe^{III} OC-6	167, 153	AF Mn^{II}-Fe^{III}	$\lvert J_1\rvert$ = 1.23(1), $\lvert J_2\rvert$ =	-	[156]

						0.13(5)		
*[Fe(**L1**)(CN_2)]	[Mn(saltmen)(H_2O)]$^+$	1D – trinuclear	HS Fe^{II} PB-7 HS Mn^{III} OC-6	174, 176	AF Fe^{II}-Mn^{III}	0.66(9)	-	157
*[Fe(**L1**)(CN_2)]	[Mn(saltmen)(H_2O)]$^+$	1D – infinite	LS Fe^{II} OC-6 → HS Fe^{II} PB-7 HS Mn^{III} OC-6	168, 175	dominant AF, very weak F Mn^{III}-Mn^{III} (when Fe^{II} is LS)	$\|J_1\|$ = 0.76(4), $\|J_2\|$ = 0.02(8)	SMM (when Fe^{II} is LS) U_{eff} = 13.9 K photoswitchable	157
[Mn(**L1**)]$^{2+}$	[Fe(salen)($CN)_2$]$^+$	1D – infinite	Mn^{II} PB-7 LS Fe^{III} OC-6	152, 149	AF Mn^{II}-Fe^{III}	$\|J_1\|$ = 3.25(1) $\|J_2\|$ = 0.78(5)	-	158
[Mn(**L2**)]$^{2+}$	[Fe(salen)($CN)_2$]$^+$	1D – infinite	Mn^{II} PB-7 LS Fe^{III} OC-6	154	AF Mn^{II}-Fe^{III}	$\|J_1\|$ = 2.67(6) $\|J_2\|$ = 0.46(5)	-	158
Other								
[Mn(**L1**)]$^{2+}$	N_3^-	1D – infinite	Mn^{II} PB-7	n/a	AF Mn^{II}-Mn^{II}	4.8	-	159
[Mn(**L1**)]$^{2+}$	$[N(CN)_2]^-$	1D – infinite	Mn^{II} PB-7	n/a	AF Mn^{II}-Mn^{II}	0.49	-	160
[Mn(**L1**)]$^{2+}$	$TCNQ^-$	1D – infinite	Mn^{II} PB-7	n/a	AF Mn^{II}-Mn^{II}	0.18 (theoretical) 0.15 (EPR)	-	161
[Fe(**L1**)]$^{2+}$	CN^-	1D- infinite	Fe^{II} PB-7	158.35	AF Fe^{II}-Fe^{II} canted ∠6.3 °	J = -4.37	AF; spin canting; metamagnet SCM	162

Table 1.6 Summary of the magnetic properties of the polynuclear structures based on **L1** and **L2**.[126]

†† This M-NC angle is that involving the macrocyclic metal center.
* = cyanide bridges initially coordinated to macrocyclic complex

PB-7 = pentagonal bipyramidal
OC-6 = octahedral
SA-8 = square antiprismatic
DD-8 = triangular dodecahedral
CTP-7 = capped trigonal prism

HS = high spin
LS = low spin
FI = ferrimagnetic
AF = antiferromagnetic
F = ferromagnetic

SMM = single-molecule magnet
SCM = single chain magnet
dist. = distorted

From Table 1.6, it can be seen that the most common metal-metal interaction displayed by the polynuclear structures is the M-NC-M′ superexchange interaction, between the M of the $[M(N_3O_2)]^{n+}$ unit and the M′ of the secondary $[M'(CN)_x]^{m-}$ building block. The strength and sign of these interactions are dictated by the nature of the orbital overlap between the bridging ligand, and both the geometry and d^n configurations of the two metal ions.[163]

As well as the more common ferromagnetic and antiferromagnetic ordering, several polynuclear species based on **L1** and **L2** have been reported which display SMM or SCM behaviour. Sato and co-workers treated an $[Fe(\mathbf{L2})]^{2+}$ building block with a $[Cr(CN)_6]^{3-}$ salt to afford the trinuclear complex $[(Fe(\mathbf{L2})(H_2O))_2Cr(CN)_6]ClO_4{\cdot}3H_2O$. The complex demonstrates slow relaxation of magnetization above 2 K, displaying frequency dependence in both the in- and out-of-phase components of the ac susceptibility (Figure 1.31). The relaxation time follows the Arrhenius law with an energy barrier of U_{eff} = 44 K and a relaxation time, $\tau_0 = 1.4 \times 10^{-9}$ s.[142] This complex was the first example of an Fe^{II}-based cyano-bridged SMM.

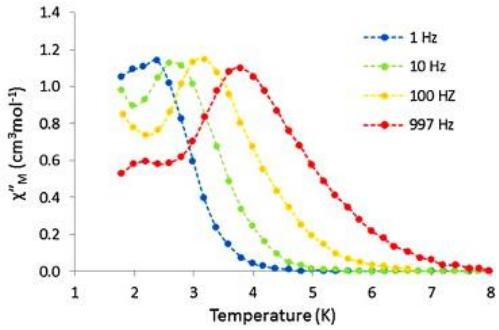

Figure 1.31 Frequency dependence of the imaginary susceptibility (χ''_M) versus temperature for Sato's trinuclear SMM in an applied field of 3 Oe. Adapted from Reference 142.

More recently, Clerac´ and co-workers formed the first photomagnetic chain comprising SMM units linked by SCO complexes.[157] The *bis*(cyanide) complex [Fe(**L1**)(CN_2)] was mixed with [Mn(saltmen)(H_2O)]$^+$ (saltmen = N,N-(1,1,2,2-tetramethylethylene)bis(salicylideneiminate) to afford the linear chain [{Mn(saltmen)}$_2$Fe(**L1**)$CN)_2$](ClO_4)2·0.5$C_4H_{10}O$·0.5H_2O, with a wave-like topology comprising trinuclear Mn^{III}-NC-Fe^{II} subunits.[157]

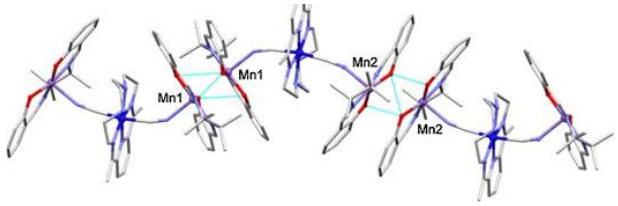

Figure 1.32 A representation of the coordination chain [Mn_2(saltmen)$_2$Fe(**L1**)$(CN)_2$]$^{2+}$ with hydrogen atoms, perchlorate anions, and interstitial solvent molecules omitted for clarity.[157]

Dc and ac magnetic measurements were performed, and the complex exhibited a χ_MT value of 5.9 cm^3·K·mol^{-1}, indicating that the Fe^{II} ion in each trinuclear subunit is LS (S = 0). The complex comprises two crystallographically distinct [Mn_2(saltmen)$_2$] units, each dominated by a different exchange interaction: one ferromagnetic, one antiferromagnetic.[157] Ac magnetic measurements reveal slow relaxation of magnetization arising from the {Mn_2(saltmen)$_2$} units, with an energy barrier of 13.9 K. Photomagnetic studies show that the LS [Fe(**L1**)$(CN)_2$] unit can be reversibly converted to the HS state, allowing for a photoswitchable magnetic interaction between the HS Fe^{II} and Mn^{III} ions.[157]

Dunbar and co-workers have utilized the low symmetry/high spin building block $[Mo^{III}(CN)_7]^{4-}$ to synthesize two species with SMM properties. The anaerobic reaction of $[Mo(CN)_7]^{4-}$ with $[Mn(\mathbf{L1})(H_2O)_2]^{2+}$ afforded a docosanuclear Mo_8Mn_{12} cluster (Figure 1.33).[150] Not only is this compound the first discrete complex based on a $[Mo(CN)_7]^{4-}$ building block, but it also has the most paramagnetic centers together with one of the largest ground-state spin values (S = 31) reported for a cyanide cluster to date, again emphasizing the enormous potential of the pentadentate macrocyclic building block as a precursor to magnetically interesting topologies.

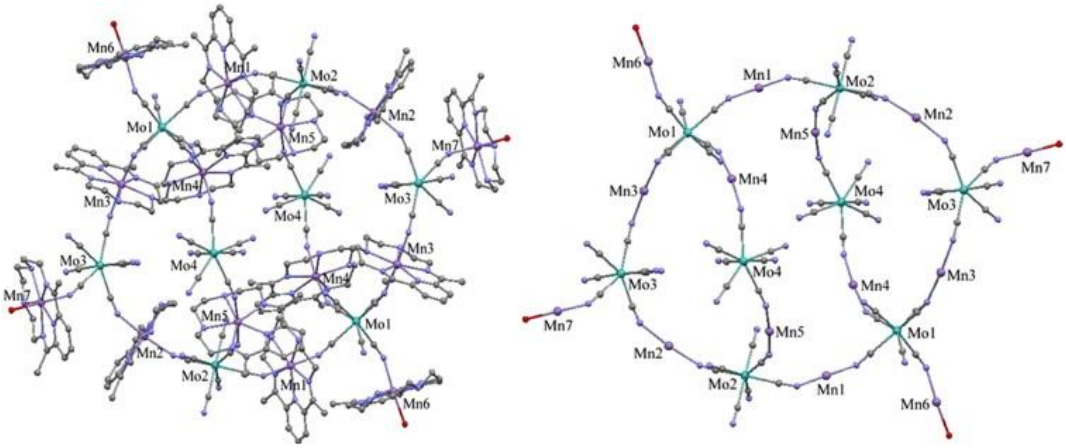

Figure 1.33 Ball and stick representation of complete (left) and skeleton (right) depiction of the backbone of the magnetic Mo_8Mn_{12} cluster.[150]

Detailed magnetic studies of the cluster between 2 and 300 K revealed antiferromagnetic interactions between spin carriers, slow relaxation of magnetization, and a hysteresis loop at 1.8 K. The broad maxima in the ac susceptibility data is consistent with glass-like behaviour.[150] The reaction of the same heptacyanometalate with $[Mn(\mathbf{L2})(H_2O)_2]^{2+}$ yielded several different condition-dependent species, including a ladder-like complex with the formula

$\{[(\mathbf{L2})Mn(H_2O)][Mo^{III}(CN)_7][Mn(\mathbf{L2})]_3[Mo^{IV}(CN)_8]\cdot 29H_2O\}_n$, with alternating Mo^{III} and Mo^{IV} units in a 1:1 ratio.[149] Ac studies (1.8-5 K, 5.0 Oe ac field, zero applied dc field) revealed a frequency dependence in the out-of-phase susceptibility, consistent with SMM behaviour. The energy barrier to relaxation was estimated to be 8.0 K.[149]

Venkatakrishnan and co-workers used an $[Nb(CN)_8]^{4-}$ building block in conjunction with the $[Fe(\mathbf{L1})]^{2+}$ macrocycle to synthesize a an infinite polymeric species with the stoichiometry $[(H_2O)Fe(\mathbf{L1})(Nb(CN)_8)Fe(\mathbf{L1})]_n$, comprising both left-handed and right-handed helical chains.[152] As intended, the complex demonstrated SCM properties with a magnetic hysteresis loop observed between 2 and 10 K. Slow relaxation of the magnetization was observed due to the high energy barrier for magnetic reversal resulting from the strong exchange interactions between the Fe^{II} and Nb^{IV} centers, and the structural anisotropy associated with the incorporation of the low-symmetry heptacoordinate $[Fe(\mathbf{L1})]^{2+}$ complex.[152] These significant and predicted SCM properties highlight the potential of the $[Fe(\mathbf{L1})]^{2+}$ building block for the self-assembly of molecule-based magnets.

It can thus be seen that the Fe^{II} complex of the macrocycle **L2** has been well-studied as a SCO system, and that Fe^{II}, Mn^{II}, Cr^{II} and Co^{II} complexes of **L1** and **L2** have been exploited for the synthesis of higher-order magnetic structures with a variety of topologies and behaviours.

Two areas of magnetic interest which have not yet been explored are: testing the relaxivities of Mn^{II} and Gd^{III} complexes of an extended family of these macrocycles as potential contrast agents; and studying high anisotropy mononuclear lanthanide

complexes of the macrocycles as possible single-molecule magnets. These topics are the focus of **Chapters 2** and **3** respectively.

1.4 Crown ethers: A brief background

1.4.1 Historical perspective

Cyclic polyethers, or crown ethers, were accidentally discovered by Pederson in the 1960s, while he was attempting to synthesize multidentate phenolic ligands.[164,165] Pederson very quickly realized the unprecedented stability with which his first crown ether ligand, dibenzo 18-crown-6, bound the alkali cations, K^+ and Na^+. Embarking on a detailed study of the hitherto unknown cyclic ethers, Pederson synthesized dozens of ligands with ring sizes up to 60 atoms, containing up to 10 oxygen atoms; as well as nitrogen and sulphur derivatives.[164] His general synthetic method, still employed today, involved Williamson ether synthesis – the reaction of a *bis*(chloro)ether with a dihydroxyether in the presence of a base.[164,165] Some of his extended family of cyclic polyethers were excellent complexing agents; many were not. Pederson identified the best candidates for complexation as the crown ethers with up to 10 oxygen atoms, separated by ethylene linkers.[164] Representative examples of this class are shown below.

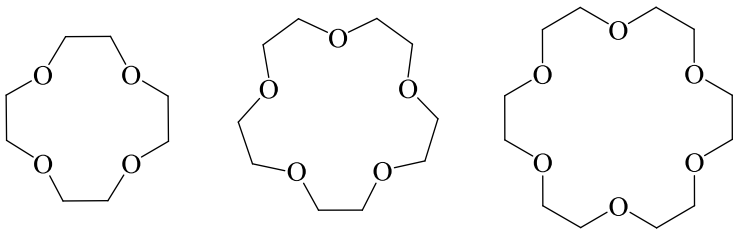

12-crown-4 15-crown-5 18-crown-8

These simple cyclic ligands demonstrate remarkable selectivity and specificity, and due to the chelate effect are able to bind with varying degrees of strength to both metal and non-metal cations, including alkali and alkaline earth metals, ammonium ions, and certain transition metal ions. Pederson found that a given cation had an optimal crown ether ring size for preferred binding within the plane of the crown ring, based on the relationship between cavity diameter and cation ionic radius. Pederson also noted that cations were able to form complexes with crown ethers smaller than this optimal size by forming 'sandwich' structures of two cyclic ethers per cation. For his seminal work in this field, Pederson was awarded the 1987 Nobel prize for Chemistry, together with Cram and Lehn.[164]

Since their discovery, crown ethers have played an important role in the advancement of supramolecular chemistry, particularly in the area of host-guest chemistry.[166] The ability of crown ethers to mimic the host-guest behaviour of biological molecules such as enzymes has made them a useful model for processes like cross-membrane cation carriage[167] for pharmaceutical development. Crown ethers have been largely employed in the areas of ion extraction and transport,[168] uses which point to their promise as ion scavengers within the body or environment. Other uses include application as phase transfer catalysts,[169,170] as well as in chiral recognition and enantiomeric resolution.[171,172] Along with the thia-crown and aza-crown species first described by Pederson himself, well-studied derivatives of the crown ethers include lariat ethers (crown ethers with a pendant side arm)[173] and cryptands (bi- and polycyclic crown derivatives).[174]

1.4.2 Lanthanide complexes of crown ethers

Chapter 4 of this thesis focusses on a thorough exploration of certain later lanthanide (Tb^{III}, Dy^{III}, Ho^{III}, and Er^{III}) complexes of 12-crown-4, 15-crown-5 and 18-crown-6. Lanthanide complexes of these crown ethers are relatively rare. The majority of the almost 400 12-crown-4 complexes reported in the literature contain alkali or alkali earth metals. Fewer than 20 publications describe Ln^{III}-12C4 complexes. Many of these lanthanide complexes were reported by Rogers and coworkers in a succession of papers in *Inorg. Chim. Acta* in the late 1980s.[175-178] Rogers' work included a series of complexes of the form $[Ln(12\text{-crown-}4)(H_2O)_5]Cl_3 \cdot nH_2O$, synthesized using hydrated $LnCl_3$ salts (Ln = every trivalent lanthanide but Pm^{III}).[178] Each complex in the series exhibited a 'half-sandwich' structure, with the lanthanide ion lying out of the plane of the crown – perhaps predictably, as the ionic radii of these ions when 9-coordinate range from 1.03-1.22 Å, unlikely to allow in-plane binding within the 12-crown-4 macrocyclic cavity, 1.2-1.5 Å in diameter.[164] Aside from this report, there are five additional 12-crown-4 structures of the four later lanthanides noted above: additional half-sandwich complexes of Dy^{III}, Ho^{III}, and Er^{III} with both chloride and water bound;[178] and two 9-coordinate full-sandwich reports of a Ho^{III} complex, with a coordinated methyl group and $Al(CH_3)_4^-$ counter ions;[179] and an Er^{III} complex, with a bound acetonitrile and three $SbCl_6^-$ counter ions.[180]

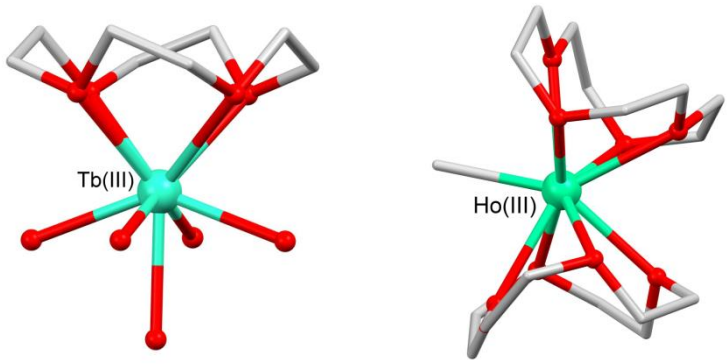

Figure 1.34 Left, representative half-sandwich complex from the [Ln(12-crown-4)$(H_2O)_5$]$Cl_3 \cdot n H_2O$ series;[178] right, full-sandwich Ho^{III} complex.[179] Hydrogen atoms, lattice water molecules, and non-coordinating counter ions are omitted for clarity.

Although slightly more lanthanide complexes of 15-crown-5 are reported, none at all contain Tb^{III}, Dy^{III}, Ho^{III}, or Er^{III}. The lanthanide complexes of 15-crown-5 which are described, however, also show out-of-plane lanthanide binding, in keeping with the ionic radius of 1.7-2.2 Å for this macrocycle.[164] Three distinct topologies have been reported for these complexes: half-, full- and pseudo-sandwich structures. Half-sandwich complexes of the Ln^{III} ions Ce-Nd, Sm-Eu, and Yb-Lu have been described, the majority of which include bidentate coordinating nitrate counter ions, giving an 11-coordinate geometry;[181,182] or coordinating chloride ions, giving an 8-coordinate geometry.[183] Three 10-coordinate full-sandwich structures have been published: complexes of Sm^{II} and Eu^{II} with perchlorate counter ions;[184,185] and a complex of Pr^{III} with $Al(CH_3)_4^-$ counter ions.[186] Pseudo-sandwich complexes of La^{III} and Sm^{III} were described,[187] in which one 15-crown-5 ligand is directly coordinated to the lanthanide ion, with the remaining four positions of the 9-coordinate binding sphere filled with water molecules, which in turn are hydrogen-

bound to a second crown ether. The hydrated perchlorate salts of the metals were used for the formation of these complexes. Figure 1.35 illustrates the three binding topologies described above.

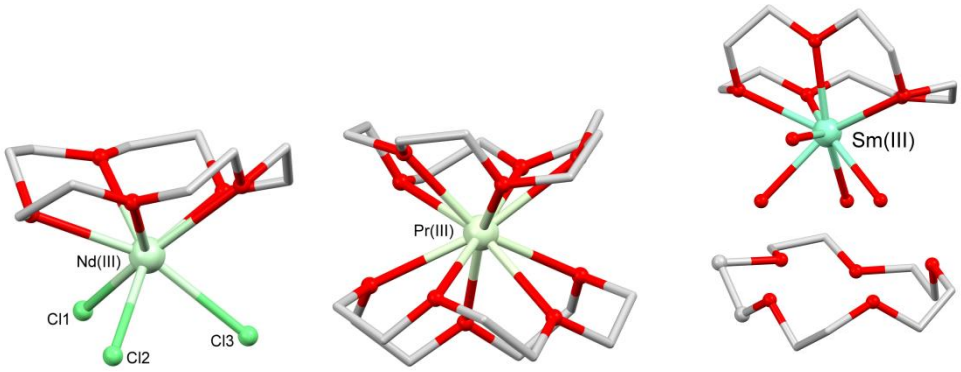

Figure 1.35 Left, a Nd^{III} half-sandwich complex;[183] center, a Pr^{III} full-sandwich complex;[186] right, a Sm^{III} pseudo-sandwich complex.[187] Hydrogen atoms, lattice water molecules and non-coordinating counter ions are omitted for clarity.

In contrast to the out-of-plane binding exhibited by the lanthanide complexes of 12-crown-4 and 15-crown-5, the lanthanide complexes of 18-crown-6 show in-plane binding of the metal ions, in keeping with the ligand's larger ionic radius of 2.6-3.2 Å. Two Tb^{III} and two Dy^{III} complexes have been reported, each showing the crown ether bound in a slightly puckered fashion, equatorial to the lanthanide ion.[175,177,188,189] Three additional monodentate ligands (water, chloride, thiocyanate) are bound in each case: one above, and two below the plane (Figure 1.36). To the best of my knowledge, there are no structural reports of Ho^{III} or Er^{III} complexes of 18-crown-6 published to date.

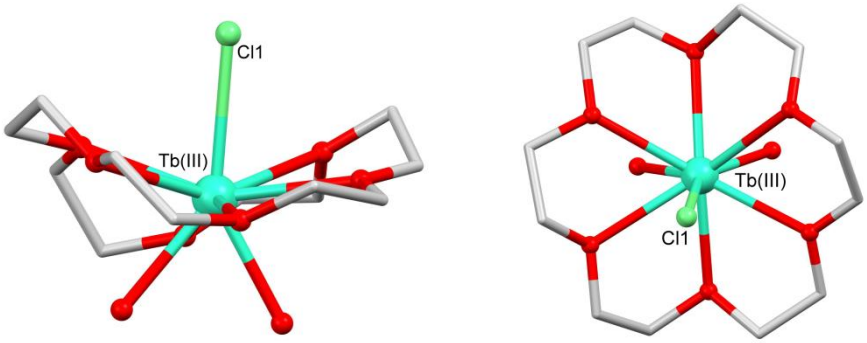

Figure 1.36 Equatorially-bound Tb^{III}-18-crown-6 complex.[175] Hydrogen atoms, lattice water molecules and non-coordinating counter ions are omitted for clarity.

1.4.3 Luminescence of lanthanide-crown ether complexes

The majority of the lanthanide-crown reports noted above detailed synthetic and crystallographic information without a detailed discussion of the physical properties.[185-187,190,191] In particular, a discussion of magnetic properties remains entirely absent to date from this class of compound. There are, however, several reports describing the emission properties of the complexes.[192,193]

1.4.3.1 Introduction to lanthanide luminescence

Luminescence refers to the emission of light as an excited molecule returns to its ground state. In photoluminescence, the excited state is generated by the absorption of light in the UV-visible region of the electromagnetic spectrum (λ = 1–700 nm, or 14.3–10,000 × 10^3 cm^{-1}). Following absorption of light of a certain energy, non-radiative vibrational relaxation to the emitting state occurs, before a lower-energy photon is emitted. The resulting difference in wavelength of the absorbed and emitted photons is called the Stokes shift.[194] Photoluminescence is *fluorescent* if it does not involve a change in spin (for instance, ligand $S_1 \rightarrow S_0$, or Yb^{III} $^2F_{5/2} \rightarrow {}^2F_{7/2}$), while *phosphorescence*

describes transitions involving a spin-flip, and intersystem crossing between states of different multiplicities (such as ligand $T_1 \rightarrow S_0$, or Dy^{III} $^4F_{9/2} \rightarrow {}^6H_{5/2)}$. The timescale of fluorescence is 10^{-9} – 10^{-7} sec, while the timescale of phosphorescence is much longer (10^{-3} – 10^{2} sec).[195]

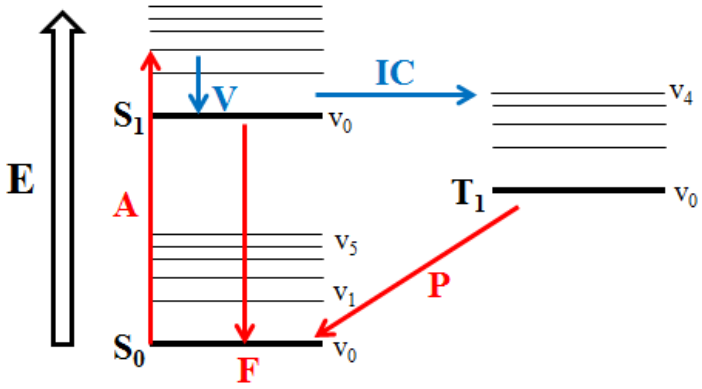

Figure 1.37 Jablonsky diagram showing absorption (**A**), vibrational relaxation (**V**), fluorescence (**F**), intersystem crossing (**IC**), and phosphorescence (**P**).

Electronic transitions within lanthanide ions may be intra-configurational 4*f*-4*f*, inter-configurational 4*f*-5*d*, or charge-transfer transitions between the metal and ligand. The transitions of particular interest in lanthanide luminescence are the 4*f*-4*f* transitions, because these transitions produce extremely sharp, narrow emission bands characteristic of a given metal. Although 4*f*-4*f* transitions are 'forbidden' (highly improbable) by the Laporte parity selection rule, they can still occur in the presence of a ligand field which disrupts the orbital symmetry in an analogous fashion to 'forbidden' *d*-*d* transitions for transition metal ions. The main luminescent transitions for each lanthanide from Pr^{III} to Yb^{III} are listed below, along with an energy diagram showing partial splitting of the Ln^{III} electronic energy levels.

Ln^{III}	Excited state	Final state	J	Type of lum.	Color of emission
Pr^{III}	$^1G_4$	^3H_J	4-6	P	NIR
	$^1D_2$	^3F_J	2-4	P	NIR
	$^3P_0$	^3H_J	2-6	F	orange
Nd^{III}	$^4F_{3/2}$	^4I_J	9/2-15/2	F	NIR
Sm^{III}	$^4G_{5/2}$	^6H_J	5/2-15/2	P	orange
Eu^{III}	$^5D_0$	^7F_J	0-6	P	red
Gd^{III}	$^6P_{7/2}$	$^8S_{7/2}$		P	UV
Tb^{III}	$^5D_4$	^7F_J	6-0	P	green
Dy^{III}	$^4F_{9/2}$	^6H_J	15/2-5/2	P	yellow/orange
Ho^{III}	$^5F_5$	^5I_J	8-4	F	NIR
	$^5S_2$	^5I_J	8-4	F	green
Er^{III}	$^4S_{3/2}$	^4I_J	15/2-9/2	F	
	$^4I_{13/2}$	$^4I_{15/2}$		F	NIR
Tm^{III}	$^1G_4$	^3H_J	6-4	P	
Yb^{III}	$^2F_{5/2}$	$^2F_{7/2}$		F	NIR

Table 1.7 Luminescent *f-f* transitions of the lanthanides, where P = phosphorence and F = fluorescence. Adapted from Reference 196.

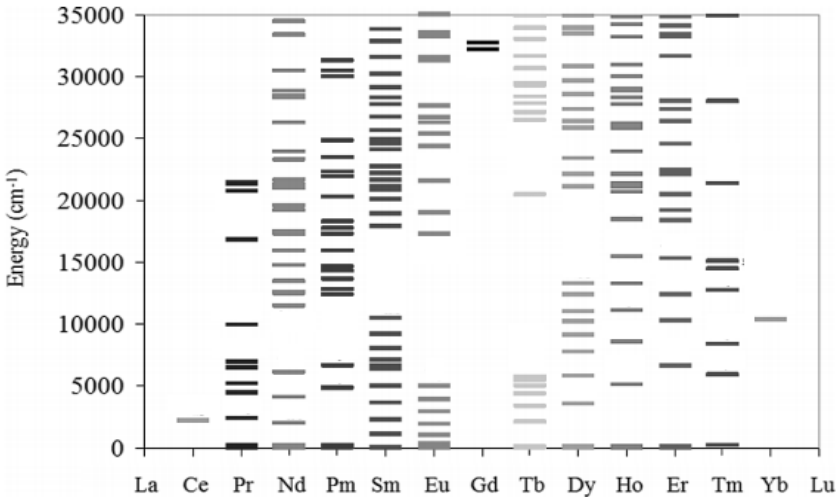

Figure 1.38 Splitting of the electronic energy levels of the lanthanides. Adapted from Reference 196.

The main issue in lanthanide luminescence is the weakness of their emission, due to the forbidden nature of the 4*f*-4*f* transitions. The emission efficiency of a given complex is described by the quantum yield, φ, where $\varphi = \frac{\text{number of photons emitted}}{\text{number of photons absorbed}}$. A large quantum yield corresponds to a high intensity band. Sensitization is the process of enhancing the quantum yield of an emission band, via 'the antenna effect'; a strongly absorbing chromophore transfers energy to the lanthanide excited states, which undergo quick internal conversion to the emitting state (Fig. 6). The emission band occurs at the characteristic wavelength for a given metal, but with much greater intensity than normal. Two common energy transfer pathways are the Dexter mechanism, involving double-electron exchange; and the through-space electrostatic multi-polar Forster mechanism.[195] An effective antenna should have a high molar absorptivity ε, and the triplet state of the ligand should be at least 1850 cm^{-1} higher in energy than the metal ion emitting state, to avoid re-population of the ligand triplet.[197]

To date, lanthanide luminescence has been predominantly exploited in medicinal biotechnology due to the pure-colour and tunable emission, and the long excited-state lifetimes. Eu^{III} and Tb^{IIII} are the most commercially exploited lanthanides, because they have both long lifetimes and quantum yields typically greater than 10%.[197] The applications of these compounds include use in bioimaging and sensing, luminescent stains, optical amplifiers, and lighting devices and displays.[198-200] These applications make use of the sharp emission bands corresponding to transitions between electronic *terms* or *levels* (a change in *L* or *J*).[201]

1.4.3.2 Emission of Ln-crown complexes

Over the past decade, Belian and co-workers have published a number of papers discussing the luminescent properties of lanthanide complexes of crown ethers, utilizing additional chromophoric ligands as antennae. In a 2011 study, Eu^{III}, Tb^{III} and Gd^{III} were complexed to 12-crown-4 and 15-crown-5, in addition to water, phenanthroline (phen), 2,2′-bipyridine (2,2′-bipy), or a combination of these ligands.[202] The solid state crystal structures of the complexes were not measured, but the compositions were determined by elemental analysis. Due to the non-chromophoric nature of the crown ether ligands, as well as the quenching effect of bound water molecules, the complexes in which the coordination sphere involved a crown and water molecules displayed quantum efficiencies as low as 15.7%.[202] The two N-heterocyclic ligands served as effective antennae. The Tb^{III} complexes displayed the most consistently intense emission, while an Eu^{III} complex had the highest quantum efficiency of 71.6%, observed for the [Eu(15-crown-5)$(phen)_2$]Cl_3 complex.[202]

In a similar study, Eu^{III}, Gd^{III} and Tb^{III} complexes of 12-crown-4 and 15-crown-5 with terpyridine (terpy) antennae ligands were studied.[203] Both solid state and aqueous emission properties were examined. Aqueous luminescence is particularly important for potential biological applications, such as in immunoassays. In a comparison of the quantum yields for aqueous solutions of [Eu(12-crown-4)(terpy)(H_2O)]Cl_3 and [Eu(15-crown-5)(terpy)]Cl_3, the respective values of φ = 7.4% and 4.3% suggest that the 12-crown-4 complex is of more biological interest.[203]

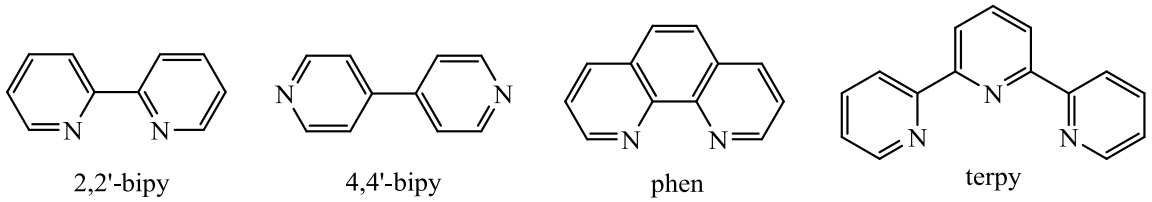

Figure 1.39 Antennae ligands utilized in lanthanide-crown ether luminescence.

Belian and co-workers also reported the luminescent properties of a novel dinuclear, mixed-crown system: a Eu^{III}-12C4 complex and a Tb^{III}-18C6 complex bridged by a 4,4′-bipyridyl (4,4′-bipy) ligand.[204] Although single crystals were not studied, the proposed structure is shown below (Figure 1.40). Interestingly, the complex emitted yellow light in the solid state, in contrast to the usual red and green emission exhibited by mononuclear Eu^{III} and Tb^{III} complexes respectively. In the same work, mononuclear 12-crown-4 and 18-crown-6 complexes of Eu^{III}, Tb^{III} and Gd^{III} were studied, with water molecules filling the remaining positions in the coordination spheres. Although quantum yields were not discussed, the expected transitions between the lanthanide energy levels were observed; in particular, the $^5D_0 \rightarrow {}^7F_{0\text{-}2}$ transitions for Eu^{III}, and the $^5D_4 \rightarrow {}^7F_{6\text{-}3}$ transitions for Tb^{III}.[204]

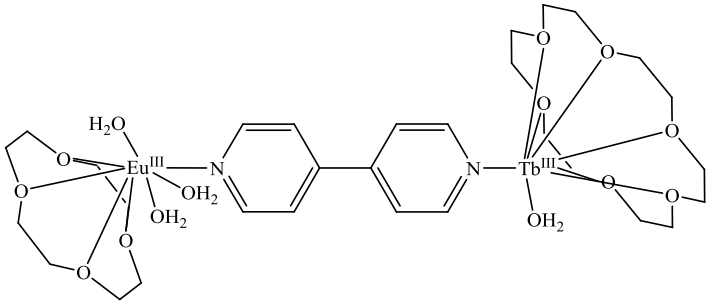

Figure 1.40 The heterodinuclear lanthanide-crown ether complex reported by Belian *et al*; chloride counter ions omitted.[204]

An additional report by Belian and co-workers involved supramolecular lanthanide-crown ether systems, in which the effect of a crown ether (18-crown-6 or dibenzo-18-crown-6) on the luminescence of a Eu^{III}(β-diketonate) complex was studied.[205] In these complexes, the crown ether was not directly coordinated, but was present as a lattice molecule. The supramolecular complexes displayed quantum yields of approximately 26% (*vs.* 29% for the complex in the absence of a crown); and were photochemically stable. Tris(β-diketonate) lanthanide complexes were mentioned in Section 1.2.4, in the context of mononuclear single-molecule magnets; however, β-diketonate complexes of Eu^{III} and Sm^{III} in particular have been studied for their luminescent properties, because conjugated β-diketonates act as strong antennae.[205]

The research impetus behind the reports discussed above was to probe the effect of ligand field on lanthanide luminescence, with a view to luminescent probe development. Crown ethers were chosen as ligands for study in spite of their non-chromophoric nature because of the stability they confer upon their complexes both in solid and solution states due to the macrocyclic effect.[202,204] However, as well as the emission bands corresponding to transitions between *terms* and *levels*, mentioned in the above reports, lanthanide emission can also provide information regarding the energy differences between electronic *microstates* or *sublevels*, which are important in single-molecule magnetism. That is, emission spectra can show the Stark splitting of the ground state $^{2S+1}L_J$ multiplet into its component M_J microstates/sublevels. This electronic structural information is gleaned from the fine structure of the highest-energy emission band in a luminescence spectrum. The relationship between magnetic behaviour and

luminescence-derived M_J energies in the context of lanthanide-crown complexes has not yet been explored, and is discussed in **Chapter 4**.

1.4.4 Crown ethers in molecular magnetism

Most of the structural reports described in Section 1.1.2 were published before 2003, when the anisotropy of lanthanide ions first began to be harnessed for the synthesis of SMMs. For this reason, the potential of crown ether-lanthanide complexes for use as molecule-based magnetic materials has not been investigated.

However, the first report of a *transition metal*-crown ether complex displaying slow magnetic relaxation was reported during the preparation of this thesis.[206] An 8-coordinate 'sandwich' complex with the formula $[Co(12\text{-crown-}4)_2](I_3)_2(12\text{-crown-}4)$ (Figure 1.41) was reported by Chen and co-workers, which exhibited SMM behaviour in an applied field of 500 Oe. The barrier to relaxation was calculated to be 17.0 cm^{-1}. Although this U_{eff} value is not an improvement on the highest barrier observed for a mononuclear transition metal complex (226 cm^{-1}, for a 2-coordinate Fe^{I} complex[109]), the report is significant as it represents the highest coordination number of any mononuclear transition metal SMM.[206] In addition, the metallocrown derivative of 12-crown-4, 12-metallocrown-4, has been increasingly exploited in single-molecule magnetism over the past five years.[207]

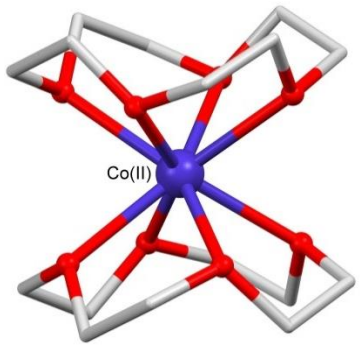

Figure 1.41 Structure of the Co^{II}-crown ether SMM reported by Chen and co-workers Hydrogen atoms, non-coordinating lattice molecules and counter ions are omitted for clarity.[206]

To date, crown ethers have remained unexplored as a class of ligand for the synthesis of *lanthanide*-based SMMs. However, the wide array of known and commercially available crown derivatives suggest that lanthanide-crown ether compounds may represent a tunable family of complexes, through which the effects of structural variation on magnetic behaviour may be investigated with unprecedented ease. This topic is the focus of **Chapter 4**.

2 RESULTS AND DISCUSSION FOR PROJECT 1:

Mn^{II} and Gd^{III} complexes of Schiff-base macrocycles as potential MRI contrast agent[*]

2.1 Introduction

Project 1 involves the synthesis of Mn^{II} and Gd^{III} complexes of Schiff-base macrocycles as potential MRI contrast agents. As discussed in Section 1.1, the majority of the contrast agents clinically approved for use in Canada are 'small-molecule' agents: mononuclear complexes of Gd^{III} with a chelating or macrocyclic ligand.

To briefly re-iterate the requirements for a contrast agent: in order to display relaxivity behaviour, a contrast agent must have at least one paramagnetic metal center, whose magnetic moment can interact with the moment of water protons; and at least one coordinated water molecule in aqueous solution. Relaxivity can be maximized by increasing the number of bound water molecules, increasing the water exchange rate, and decreasing the rate of molecular tumbling. Along with efficiently relaxing water protons, a contrast agent must also be stable *in vivo* with regards to both dissociation and transmetallation, due to the bio-toxicity of free Gd^{III} and Mn^{II}. There is an on-going search for new MRI contrast agents which are both effective and safe; in particular, in the field of small-molecule agents there is a renewed interest in complexes based on Mn^{II},

[*] Note concerning labelling: Macrocyclic ligands are labelled **L1-L6**. Organic building blocks for a given ligand **LX** are labelled **Xa, Xb** etc. Inorganic complexes based on a given ligand **LX** are labelled **X.1, X.2** etc.

due to the recent discovery of the link between the disorder nephrogenic systemic fibrosis and Gd^{III}-based agents.

Small [1+1] Schiff-base macrocycles, or *bis*(imine) macrocycles, have been heavily underutilized in this regard. These macrocycles are formed via the metal-templated condensation of a diamine and a diketone (Scheme 2.1). As mentioned earlier, a great deal of research effort has been invested worldwide on the synthesis and characterization of coordination complexes of 15- to 18-membered *bis*(imine) or Schiff-base macrocycles with N_3X_2 or N_3X_3 donor atom sets (X = O, NH).[126] These complexes have been thoroughly and cleverly exploited as building blocks for the formation of higher order magnetic structures (Section 1.4). However, very few macrocyclic complexes within this class have been explored as possible MRI contrast agents.

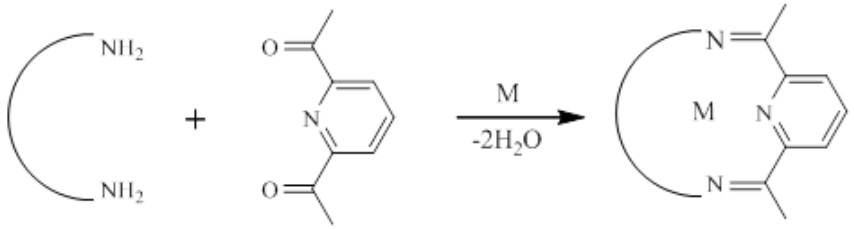

Scheme 2.1 Metal-templated synthesis of a [1+1] Schiff-base macrocycle from diacetylpyridine and a generalized diamine.

Section 1.1 detailed a 1992 study concerning the field-dependent relaxivity profiles of four Mn^{II} complexes of Schiff-base macrocycles: 15-, 16- and 17-membered N_5 systems, and an 18-membered N_6 system (Figure 1.12). Higher relaxivity values were observed for these unsaturated systems in comparison to their saturated (amine) analaogues, due to the enhanced rigidity provided by the pyridine head-unit. Furthermore,

higher relaxivities were also observed for the 15- and 16-membered rings when compared to the 17- and 18-membered rings. This second observation was attributed to the planar, equatorial binding mode of the smaller macrocycles, allowing for the coordination of two axial water molecules in solution.

In spite of the promising relaxivities observed, to-date these systems have not been investigated further. This is surprising, given that the amine analogue of **L1** was recently re-examined, in spite of the fact that this system displays lower relaxivity than **L1**, and is well-known to be a superoxide dismutase mimic.[40,64] In addition, *bis*(imine) macrocycles with mixed N_3O_2 or N_3O_3 donor groups have never been considered for MRI applications, which is again surprising, given that both Mn^{II} and Gd^{III} are highly oxophilic, so the incorporation of oxygen into the macrocyclic backbone should enhance the stability of the resulting complexes.

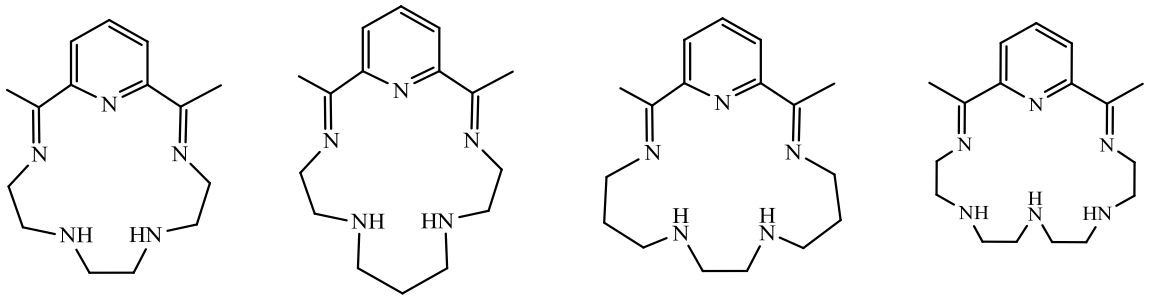

Figure 2.1 N_5 and N_6 Schiff-base macrocycles.[61]

We thus decided to first re-visit the most effective *bis*(imine) system described in the 1992 report, the 15-membered N_5 system **L1**; and subsequently, to investigate for the first

time an expanded family of *bis*(imine) systems with N_3O_2 and N_3O_3 donor sets, **L2**-**L7** (Figure 2.2) as potential MRI contrast agents.

2.1.1 Target family of macrocycles

The target family of Schiff-base macrocycles, **L1**-**L7**, is shown below (Figure 2.2).

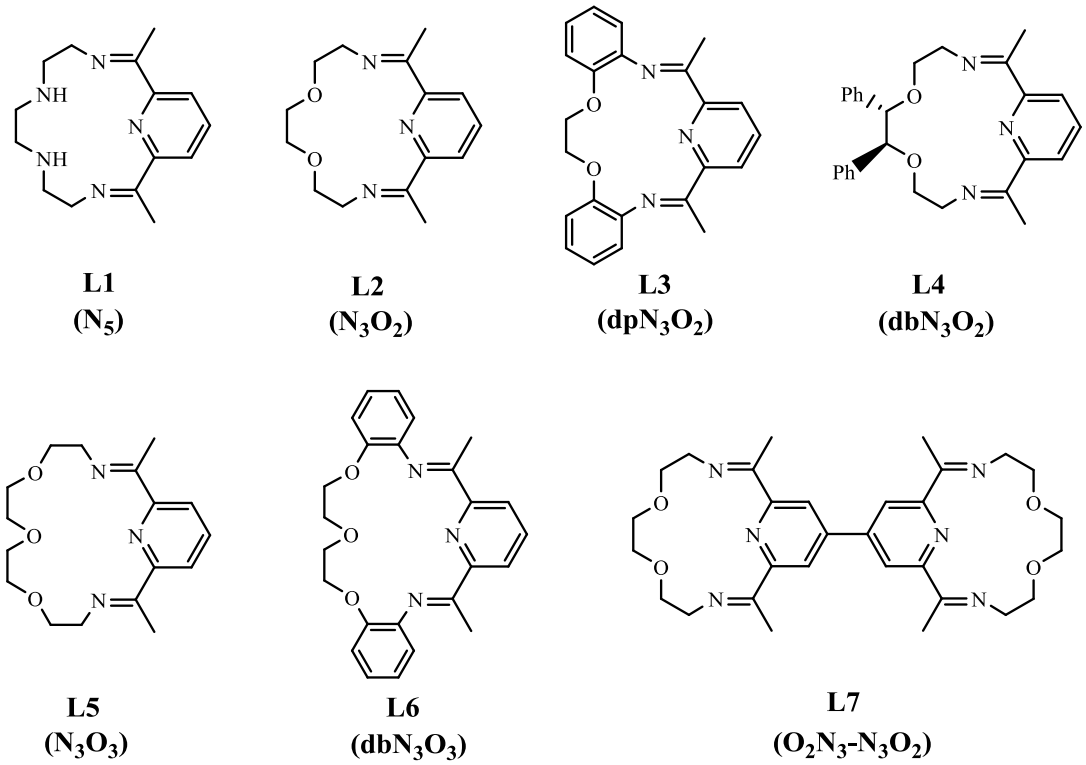

Figure 2.2 Proposed family of macrocycles **L1**-**L7**.

L1 is an N_5 macrocycle, the first of the family to be reported in the literature in any context, and also the only one of the family to have been suggested as a ligand for potential use in MRI contrast agent development. It has a 15-membered macrocyclic backbone. **L2** is the N_3O_2 analogue of **L1**, differing only in the nature of its donor atoms. **L3** and **L4** maintain the size and donor character of the N_3O_2 macrocyclic cavity, but have increased rigidity (**L3**) and steric bulk (**L4**). Additionally, macrocycle **L4** is an

optically active system, with two adjacent chiral centres on the central ethylene linker. **L5** and **L6** have an expanded cavity, with an additional O donor atom and an 18-membered backbone. **L5** is the larger analogue of **L2**, with flexible ethylene linkers, while **L6** is the analogue of the more rigid **L3**. Finally, **L7** is comprised of two covalently-tethered **L2** macrocycles, linked via the pyridine head units. By studying this expanded family of macrocyclic systems, we hoped to be able to investigate the effect of the number and nature of donor atoms, and the cavity size, steric bulk and rigidity on the relaxivities of the resulting complexes. Complex **L7** is particularly noteworthy in that it provides an opportunity to explore how the presence of two metal centers would affect the relaxivity behavior of the complex.

Diacetylpyridine was selected as the diketone building block for macrocycles **L1**-**L6** rather than its dialdehyde analogue diformylpyridine, because Schiff-base macrocycles based on the former have been shown to be more resistant to hydrolysis.[208-213] This is likely because the methyl side-arms of the resulting complexes provide a steric protection.

There were several reasons why we hypothesized that the proposed family of macrocycles would be useful for the formation of contrast agents. Firstly, the planarity of the *bis*(imine) macrocyclic rings allows for the binding of monodentate ligands in the axial position. In aqueous solution, these positions could potentially be filled by aquo ligands, which may undergo unhindered, fast water exchange. Secondly, the known complexes of these Schiff-base macrocycles appear to be very water soluble, which is an important property of an *in vivo* imaging agent. Thirdly, none of the target 15- to 18-membered [1+1] Schiff-base macrocycles had ever been formed or found to exist in the

absence of a metal ion. Thus the metal centers in these templated macrocycles could be less prone to dissociation of the metal ions, leading to complexes with a more favourable toxicity profile than the currently approved agents.

Our short term objectives were therefore ***to template macrocycles*** **L1-L7** ***around*** Mn^{II} ***and*** Gd^{III}***, and study the in vitro relaxivities of any soluble, analytically pure complexes which resulted***. Longer term, our objective was to identify the most promising candidate(s) for further *in vivo* toxicity and imaging studies.

2.2 Organic synthesis: macrocyclic building blocks

As mentioned earlier, complexes of **L1** (N_5) and **L2** (N_3O_2) were formed by the metal-templated Schiff-base condensation of 2,6-diacetylpyridine (**1a**) and a diamine.[126] The diamines used for the preparation of **L1** and **L2** were *tris*(ethylenetetramine) (**1b**) and 2,2′-(ethylenedioxy)*bis*(ethylamine) (**2a**), respectively. All three compounds are commercially available.

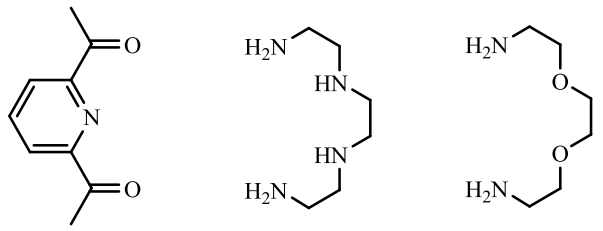

1a **1b** **2a**

Figure 2.3 The organic building blocks required for the synthesis of **L1** and **L2**.

Modifications to the macrocyclic structure may be introduced by altering either the pyridine-based diketone unit, or the ether-containing diamine unit. In order to

synthesize **L3**-**L6**, different diamines were needed, whereas the synthesis of **L7** requires a different ketone unit (Figure 2.4).

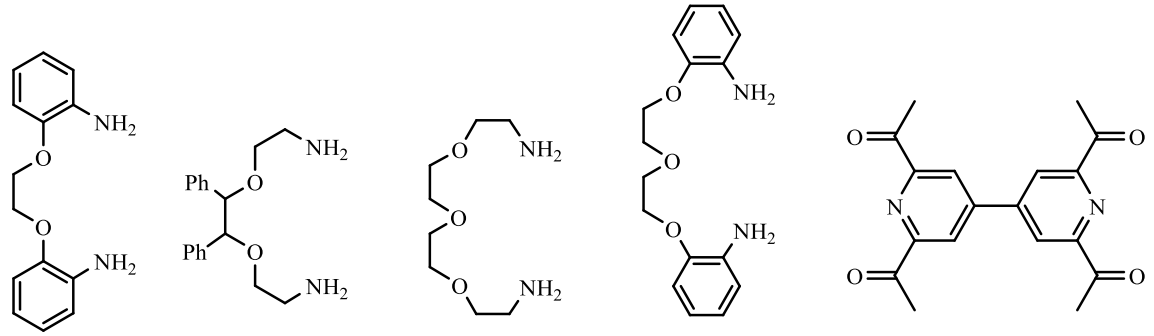

Figure 2.4 Diamines required for the synthesis of **L3**-**L6**, and the tetraketone required for the synthesis of **L7**.

These building blocks are not commercially available, and so were synthesized following a variety of modified literature procedures[214-218] as well as two synthetic pathways developed previously by the Pilkington group.[219-221] Each known organic intermediate and product was characterized by ^{1}H- and ^{13}C-NMR spectroscopy, mass spectrometry and melting point (if solid). In addition, the purity of each final product shown in Figure 2.4 was confirmed via elemental analysis. The success of the metal-templated condensation reaction depends upon the 1:1:1 stoichiometry of the amine/ketone/metal salt (in the case of complexes of **L7**, the ratio would be 2:1:2 amine/ketone/metal salt), so confirmation of the purity of the building blocks was vital. The synthetic pathways utilized are detailed below, followed by a summary of experimental data for the final product in each pathway (Table 2.1).

Diamine **3b** was synthesized following the literature procedure shown in Scheme 2.1.[214] Two equivalents of *p*-nitrophenol were deprotonated using potassium carbonate and refluxed with one equivalent of dibromoethane in a dual Williamson ether synthesis to give the dinitro compound **3a**. The two aryl nitro groups were subsequently reduced to amines in the presence of stannous chloride in acidic conditions, to afford the desired diamine **3b** as a beige solid in 47% yield.

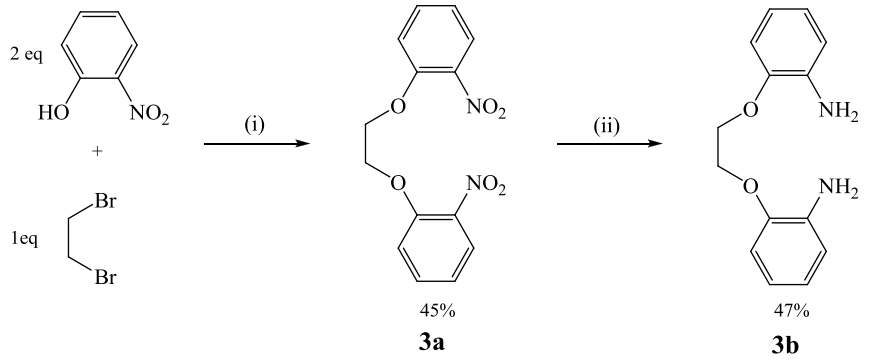

Scheme 2.2 Synthetic pathway for the formation of diamine **3b**.[214] i) K_2CO_3, DMF, reflux, 18 h; ii) $SnCl_2$, HCl/H_2O, reflux, 18 h.

Diamine **4d** was previously unreported in the literature. The synthetic procedure shown in **Scheme 2.3** was developed by the Pilkington group.[219] The commercially available chiral starting material, hydrobenzoin, is available as the *R,R′*-, *S,S′*- or *meso* isomer. For this project, the *R,R′*- isomer was used. For the purposes of this research, the chirality was not of particular interest; the additional bulk conferred by the phenyl groups was the parameter being studied. *R,R′*-hydrobenzoin underwent a Williamson ether synthesis with allyl bromide to form diene **4a**, which was then subjected to Lemieux-Johnson oxidation by reaction with $OsO_4/NaIO_4$ to give diol **4b**. The diol was then

converted to the diphthalimide via the Mitsunobu reaction, namely by reaction with triphenylphosphine, phthalimide and DIAD. Compound **4c** was finally subjected to hydrazinolysis to afford the desired diamine **4d** as an oil in 56% yield.

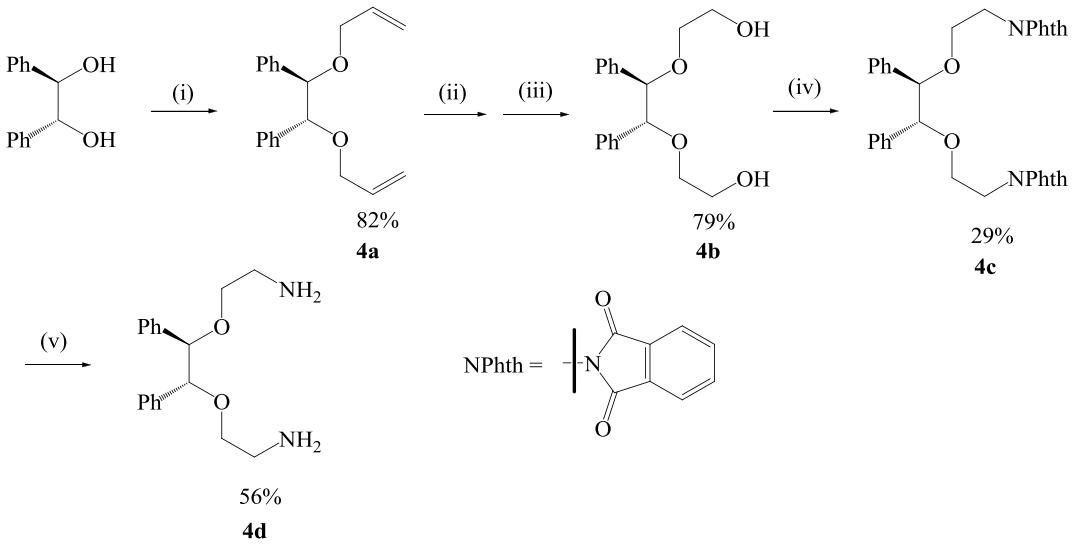

Scheme 2.3 Synthetic procedure for the synthesis of diamine **4d**.[219] i) NaH, allyl bromide, THF, reflux, 18 h; ii) OsO_4, $NaIO_4$, THF/H_2O, r.t., 18 h; iii) $NaBH_4$, DCM/MeOH, r.t., 18 h; iv) PPh_3, phthalimide, DIAD, THF, r.t., 4 d; v) hydrazine monohydrate, EtOH, reflux, 18 h.

The synthesis of **5c** was carried out via the literature procedure shown in Scheme **2.4**.[215,216] Commercially available *tetra*(ethylene)glycol reacted with tosyl chloride to give the ditosyltate **5a**, which then underwent a simple substitution with potassium phthalimide to give **5b** via Gabriel synthesis. Diphthalimide **5b** then underwent hydrazinolysis to afford diamine **5c** as an oil in excellent yield.

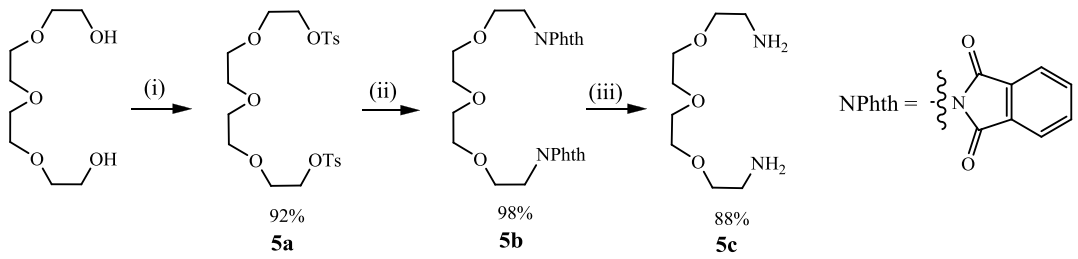

Scheme 2.4 Synthetic procedure for the synthesis of diamine **5c**.[215,216] i) Tosyl chloride, KOH, DMF, 0°C-r.t., 18 h; ii) potassium phthalimide, DMF, 80°C, 18 h; iii) hydrazine monohydrate, THF/MeOH, reflux, 18 h.

Diamine **6c** was synthesized via the pathway given in Scheme 2.4.[217] Amide **6a** was formed from aminophenol and acetic anhydride. Diamide **6b** was synthesized in a dual Williamson ether reaction between *bis*(2-chloroethyl) ether and 2 equivalents of **6a**. The amide groups were then cleaved under basic conditions to give the desired diamine **6c** as a solid in 75% yield.

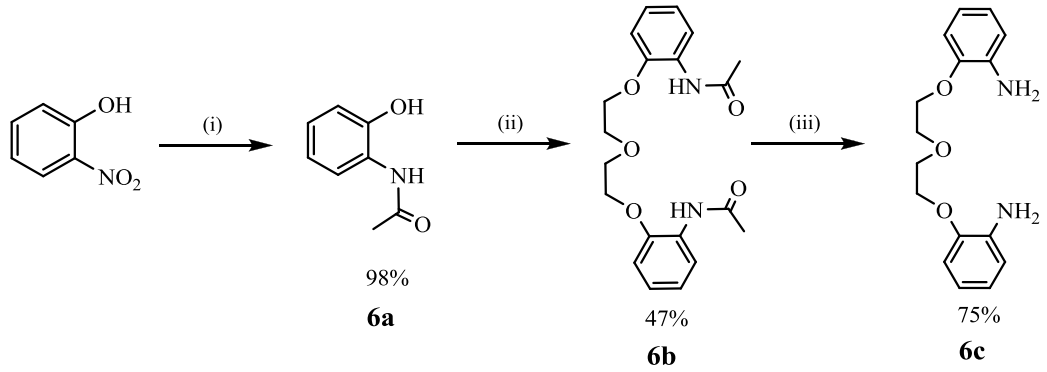

Scheme 2.5 Synthetic procedure for the synthesis of diamine **6c**.[217] i) Acetic anhydride, MeOH/H_2O, r.t., 5 h; ii) *bis*(2-chloroethyl)ether, K_2CO_3, DMF, 80°C, 30 min; iii) NaOH, EtOH/H_2O, reflux, 3 d.

Tetraketone **7d** was formed from the known diacyl chloride **7c**,[220] following a procedure previously published by the Pilkington group (Scheme 2.6).[221] Two

commercially available lutidine precursors were covalently tethered via a reductive coupling with sodium metal to give a non-aromatic anionic intermediate, which after bubbling-through with SO_2 afforded the aromatic tetramethyl species **7a**. This compound was then converted to the tetraacyl chloride **7b** by reaction with thionyl chloride which was activated by DMF. The desired tetraketone **7d** was formed by the reaction of **7c** with deprotonated Meldrum's acid, followed by an acidic work-up.

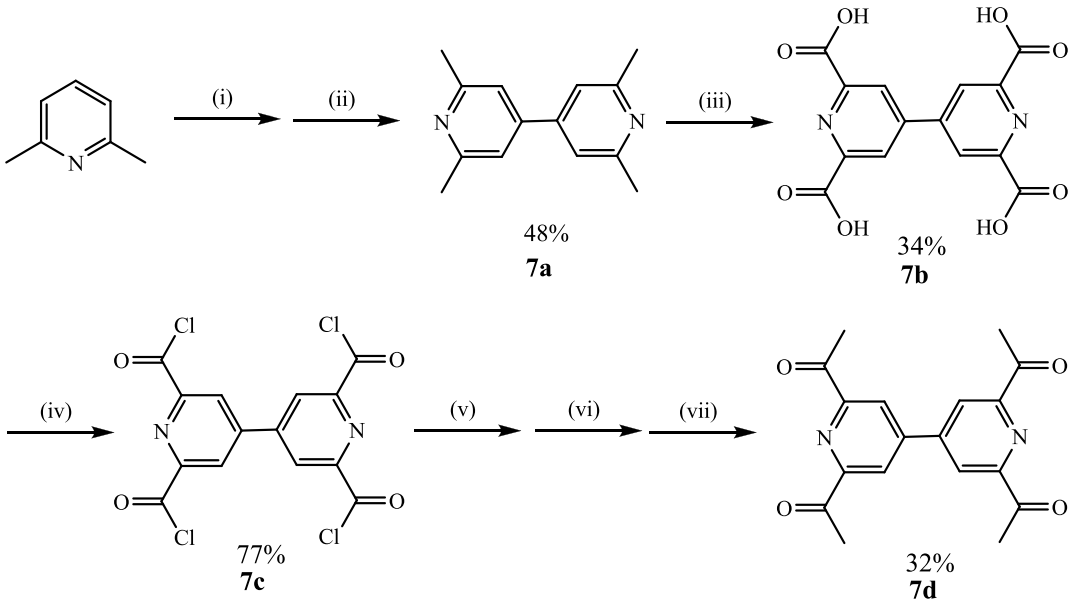

Scheme 2.6 Synthetic procedure for the synthesis of tetraketone **7d** developed by Pilkington and co-workers[220,221] i) Na, THF, r.t., 7 d; ii) SO_2, 0°C, 5 h; iii) CrO_3, H_2SO_4 (conc.), 75°C, 2 h; iv) $SOCl_2$, DMF, reflux, 4 h; v) pyridine, DCM, 0°C-r.t., 2 h; vi) HCl, DCM, 0°C, 5 min; vii) acetic acid, H_2O, reflux, 18 h.

During the course of this project, an alternative synthetic pathway for the formation of **7d** was reported in the literature by Lieb and co-workers, shown in Scheme 2.7.[218]

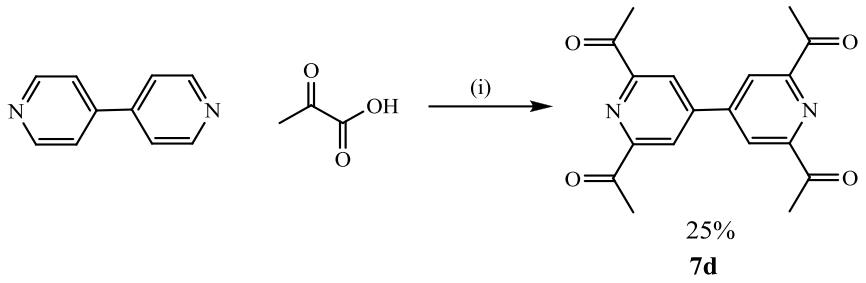

Scheme 2.7 Synthetic procedure for the synthesis of tetraketone **7d** developed by Lieb and co-workers[218] i) Peroxydisulfate, silver nitrate, H_2SO_4 (1 M), r.t., 24 h.

This pathway offers significant advantages over that shown in Scheme 2.6, including reduced overall reaction time (two days for the conversion of 4,4′-biyridine to **7d**, compared with 11 days for the conversion of lutidine to **7d**), milder reagents (Scheme 2.6 involves the use of toxic and corrosive SO_2, CrO_3, and $SOCl_2$), and higher overall yields (overall yield for Scheme 2.6 was 4%, compared with an overall yield of 25% for Scheme 2.7). For these reasons, the latter pathway was subsequently adopted as our preferred method of choice for the synthesis of **7d**.

Experimental data for each of these starting materials, **3b**, **4d**, **5c**, **6c** and **7d**, are summarized in Table 2.1. The relevant numbering scheme is included to aid in interpretation of the NMR data.

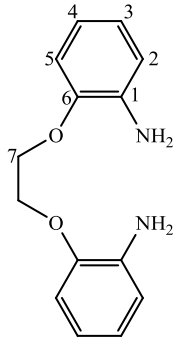

3b

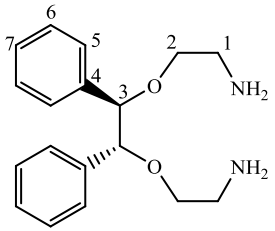

4d

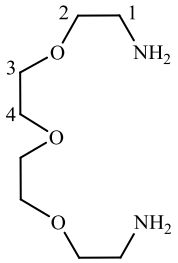

5c

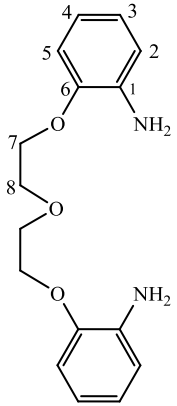

6c

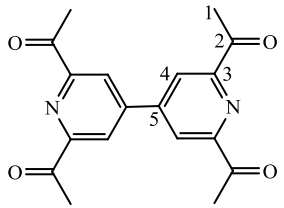

7d

Cmpd.	^{1}H NMR data ($CDCl_3$, 300- 400 MHz)	^{13}C NMR data ($CDCl_3$, 300 - 400 MHz)		C	H	N	Melting point (°C)	FAB-MS data
3b	6.87-6.73 (m, 8H, H_{2-4}), 4.37 (s, 4H, H_7)	146.3 (C_6), 136.9 (C_1), 122.0 (C_3), 118.5 (C_4), 115.5 (C_2), 112.6 (C_5), 67.6 (C_7)	Found Calcd.	65.73 66.09	6.11 6.33	10.82 10.93	126°C (Lit. 129-132°C[214])	*m/z* = 245 $[M+H]^+$ (100%)
4d	7.14-7.03 (m, 10H, H_{5-7}), 4.41 (s, 2H, H_3), 3.46-3.29 (m, 4H, H_2), 2.78 (s, 4H, H_1)	138.6 (C4), 127.9 (C6), 127.6 (C7), 127.5(C5), 86.0 (C3), 71.1 (C2), 41.5 (C1)	Found Calcd.	68.39 67.90	8.04 8.23	8.34 8.80	oil at r.t.	*m/z* = 301 $[M+H]^+$ (27.1%)
5c	3.64 (m, 8H, H_{3-4}), 3.52 (t, *J* = 5.1 Hz, 4H, H_2), 2.87 (t, *J* = 5.9, 4H, H_1)	73.3 (C_2), 70.4 (C_4), 70.7 (C_3), 41.8 (C_1)	Found Calcd.	- -	- -	- -	oil at r.t.	*m/z* = 194 $[M+H]^+$ (2.9%)
6c	6.84-6.69 (m, 8H, H_{2-5}), 4.18 (t, *J* = 4.7 Hz, 4H, H_7), 3.93 (t, *J* = 4.8 Hz, 4H, H_8)	146.4 (C_6), 137.2 (C_1), 122.1 (C_4), 118.5 (C_2), 115.5 (C_5), 113.2 (C_3), 70.0 (C_8), 68.6 (C_7)	Found Calcd.	66.71 66.65	6.82 6.99	9.72 9.53	64°C (Lit. 65°C[217])	*m/z* = 289 $[M+H]^+$ (94.4%)
7d	8.56 (s, 4H, H_4), 2.85 (s, 12H, H_1)	198.8 (C_2), 154.0 (C_3), 146.7 (C_5), 122.3 (C_4), 25.7 (C_1)	Found Calcd.	63.70 63.15	5.37 5.30	7.80 8.18	260°C, decomp. (Lit. 262°C[222])	m/z = 324 $[M]^+$ (28.3%)

Table 2.1 Selected characterization data for the organic building blocks **3b**, **4d**, **5c**, **6c** and **7d**.

2.3 Inorganic synthesis: Mn^{II} and Gd^{III} complexes

Following the synthesis of the required organic building blocks, templation of macrocycles **L1**-**L7** was attempted around Mn^{II} and Gd^{III}. Both of these ions have a large number of unpaired electrons (S = 5/2 and 7/2 respectively), and a long electronic relaxation time, making them the most utilized paramagnetic ions in MRI contrast agent development.

The choice of which salts of these ions to employ as templating agents was influenced by the potential biological applications. Schiff-base macrocycles have been previously templated around chloride, perchlorate, bromide, iodide, triflate, and nitrate salts of metal ions.[126] However, since the contrast agents must be non-toxic, several of these anions were ruled out. For example, perchlorates affect the production and secretion of thyroid hormones;[223] and nitrates are readily reduced to nitrite in the stomach or saliva, which binds with hemoglobin and disrupts its ability to carry oxygen.[224] Chloride was therefore selected as a biologically-present anion, which had previously proven efficient as an anion in the synthesis of other analytically pure Schiff-base macrocyclic complexes.[126] Thus $MnCl_2 \cdot 4H_2O$ and $GdCl_3 \cdot 6H_2O$ were selected as the metal salts around which this family of macrocycles would be templated.

The Mn^{II} chloride complexes of **L1** and **L2** have been well-reported in the literature due to their application as building blocks for magnetically interesting clusters, chains and networks,[126] and the Mn^{II} chloride complex of **L7** was reported previously by the Pilkington group.[221] The Mn^{II} chloride complexes of **L3**-**L6** and the Gd^{III} chloride complexes of all the ligands are unreported to date.

Unless otherwise stated, each complex was synthesized in the following way. One equivalent each of the metal salt, diketone and diamine were refluxed at 85°C for 4-18 h. The solution was cooled, and diethyl ether was added, causing the complex to precipitate out of solution. After the solid was collected by Büchner filtration, it was washed very thoroughly with diethyl ether and allowed to air dry. The complexes were collected as powders in low to good yields (10 – 84%).

2.3.1 Mn^{II} complexes

Our attempts to template **L1**-**L7** around $MnCl_2{\cdot}4H_2O$ resulted in the isolation of six analytically pure complexes with the formula $[Mn(\mathbf{L})Cl_2]\cdot xH_2O$, summarized in Table 2.2, below.

Complex; Abbrev.	Formula		C	H	N	$\nu_{(C=N)}$ (cm^{-1})	λmax (ε) (nm, $L{\cdot}mol^{-1}{\cdot}cm^{-1}$)	$\Lambda_{M\,(aq.)}$ ($S{\cdot}cm^2{\cdot}mol^{-1}$)
1.1* **Mn^{II}-N_5**	$[Mn(\mathbf{L1})Cl_2]\cdot 2H_2O$	Found Calcd.	45.01 45.13	5.88 5.81	17.21 17.54	1649	250 (5110) 300 (3070)	254.3
2.2* **Mn^{II}-N_3O_2**	$[Mn(\mathbf{L2})Cl_2]\cdot 2H_2O$	Found Calcd.	41.19 41.21	5.69 5.76	9.43 9.61	1645	250 (6350) 300 (4240)	194.4
3.1 **Mn^{II}-dbN_3O_2**	$[Mn(\mathbf{L3})Cl_2]\cdot 2H_2O$	Found Calcd.	55.72 55.55	4.65 4.26	8.39 8.45	1617	252 (11060) 284 (7670)	-
4.1 **Mn^{II}-dpN_3O_2**	$[Mn(\mathbf{L4})Cl_2]\cdot 2H_2O$	Found Calcd.	55.15 55.02	5.63 5.64	6.79 7.13	1650	252 (5840) 301 (3240)	293.4
6.1 **Mn^{II}-dbN_3O_3**	$[Mn(\mathbf{L6})Cl_2]\cdot 2H_2O$	Found Calcd.	51.88 52.01	4.98 5.06	7.31 7.28	1618	251 (10520) 282 (6470)	186.2
7.1** **$(Mn^{II}$-$N_3O_2)_2$**	$[Mn_2(\mathbf{L7})Cl_4]\cdot 5H_2O$	Found Calcd.	40.27 40.47	5.49 5.66	9.52 9.44	1647	252 (18060) 311 (3820)	320.4

Table 2.2 Summary of Mn^{II} complex formulae, elemental analyses, IR and UV-visible spectroscopic data, and conductance measurements. Key: *denotes previously reported complexes; **denotes a complex previously reported by the Pilkington group.

In each case, imine formation was confirmed by the key observation of the appearance of a band in the IR spectrum around υ = 1620-1670 cm^{-1}, corresponding to imine (C=N) stretch. Elemental analysis was used to determine the total number of water molecules associated with each complex, both bound and unbound; and conductivity data was employed to establish the hydration number of each complex in aqueous solution. Where possible, X-ray diffraction was used to determine the structure of the complex: in particular, to confirm the planar, equatorially-bound nature of the macrocycle. Additional characterization included FAB mass spectrometry, where in each case a major peak corresponding to $[M\text{-}2H_2O\text{-}Cl]^+$ was observed; and UV-visible spectroscopy, which showed two strong absorption bands in the 250-300 nm, corresponding to π to π^* electronic transitions of the coordinated macrocyclic ligand. A discussion of these factors in relation to each complex is presented below.

As mentioned earlier, complexes **1.1** (Mn^{II}-N_5) and **2.1** (Mn^{II}-N_3O_2) have been reported previously.[139] Macrocyclic formation was confirmed for both complexes by IR spectroscopy, with the appearance of an imine peak at υ = 1649 and 1645 cm^{-1} respectively, and by the absence of a ketone peak. Elemental analysis gave an excellent fit for formulae of $[Mn(\mathbf{L})Cl_2]\cdot 2H_2O$ (**L** = **L1**, **L2**), with maximum differences of 0.33% and 0.14% for Mn^{II}-N_5 and Mn^{II}-N_3O_2 respectively. The largest peak on the FAB-MS spectrum occurred at *m/z* = 363 for Mn^{II}-N_5, and at *m/z* = 365 for Mn^{II}-N_3O_2, corresponding to $[M\text{-}2H_2O\text{-}Cl]^+$ in both cases. The UV-visible spectra of the two systems in methanol were very similar, with each solution absorbing strongly at λ = 250 and 300 nm. The crystal structures of **1.1** (Mn^{II}-N_5) and **2.1** (Mn^{II}-N_3O_2) were previously

characterized by X-ray crystallography.[139] The molecular structures show that in each complex, the Mn^{II} ion is coordinated in a 7-coordinate, *pseudo*-pentagonal bipyramidal geometry. The five donor atoms of the macrocyclic ring (N_5 for **1.1** and N_3O_2 for **2.1**) coordinate in the equatorial plane, with the maximum deviation of a donor atom from the best plane through the donor set in each case equal to 0.083 Å for N(5) of Mn^{II}-N_5 and 0.086 Å for O(3) of Mn^{II}-N_3O_2. Each macrocycle binds to Mn^{II} in an equatorial fashion, with the metal ion offset from the N_3X_2 plane by a negligible distance of 0.003 and 0.001 Å for Mn^{II}-N_5 and Mn^{II}-N_3O_2 respectively.

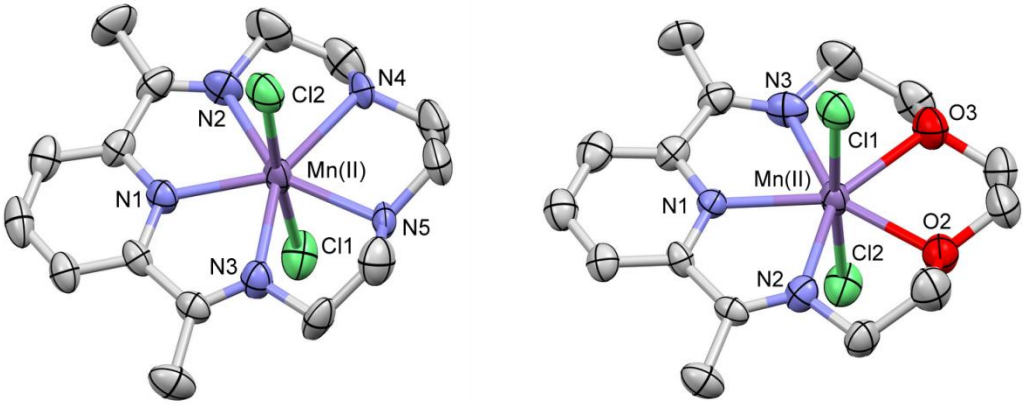

Figure 2.5 View of the molecular structures of complexes **1.1** (Mn^{II}-N_5, left) and **2.1** (Mn^{II}-N_3O_2, right).[139] Hydrogen atoms and water molecules are omitted for clarity. Thermal ellipsoids are shown at 50%.

The published crystal data for **2.1** (Mn^{II}-N_3O_2) was collected on a single crystal grown via evaporation of an ethanol solution in the presence of NaCl.[139] In order to determine whether the presence of excess Cl^- anions in the solution influenced the nature of the axial liagnds, we grew single crystals of **2.1** via the diffusion of diethyl ether into a methanol solution of the complex. The measured X-ray crystal structure was the same as

the literature structure (Figure 2.5), showing that both axial positions are occupied by chloride ions even when crystallization occurs in the absence of excess chloride.

Initial attempts to form **3.1** (Mn^{II}-dbN_3O_2) from diamine **3b** and diacetylpyridine in a refluxing methanolic solution were unsuccessful. The IR spectrum of the isolated product showed amine peaks in the 3300-3400 cm^{-1} region, as well as imine peaks; furthermore, additional bands in the C-O stretch region (around 1100 cm^{-1}) suggested an asymmetric product. When the reaction was carried out in EtOH rather than MeOH, and refluxed for just 4 hours rather than 18 hours, no N-H stretch peaks were visible in the IR spectra. The imine stretch for Mn^{II}-dbN_3O_2 was visible at υ = 1617 cm^{-1}. Intense bands on the UV-visible spectrum at λ = 252 and 284 nm, corresponding to a macrocyclic $\pi \rightarrow \pi^*$ transition. Elemental analysis gave an excellent fit for the formula [Mn(**L3**)Cl_2]·$2H_2O$, and a peak was observed on the FAB-MS spectrum at *m/z* = 461 corresponding to [M-$2H_2O$-Cl]$^+$. However, this complex proved to be completely insoluble in water, so was not pursued further as an MRI contrast agent.

Prior attempts within the Pilkington group to synthesize **4.1** (Mn^{II}-dpN_3O_2) from diamine **4d** and diacetylpyridine in ethanol had not been entirely successful.[219] Red single crystals of the resulting complex were grown from acetonitrile, and showed that although macrocyclization had occurred, half of the complexes were present as a dimer, with one Mn^{II} centre connected to an oxidized Mn^{III} center via a bridging chloride ion; while half were present as the expected monomer.[219] Each unit cell comprised four independent macrocyclic complexes. The resulting compound, with the formula {[Mn(**L4**)Cl_2][Mn(**L4**)-μ-$ClMnCl_3$]}$_2$, is depicted in Figure 2.6.

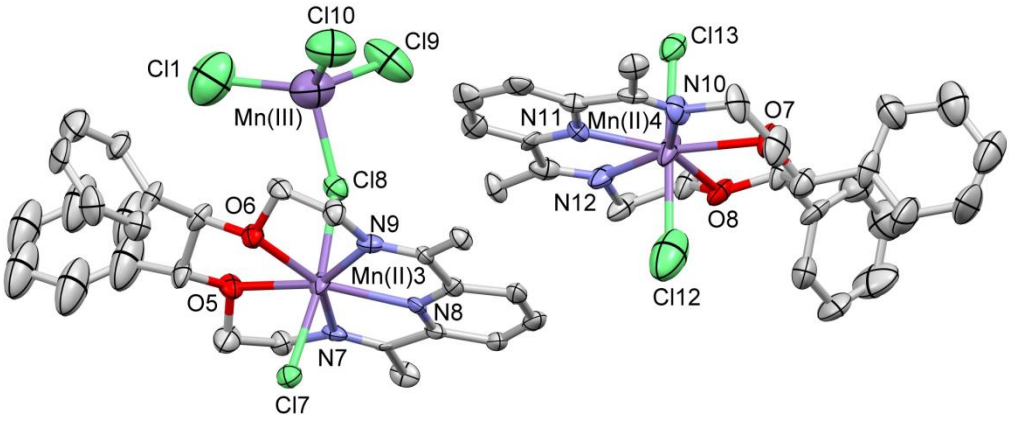

Figure 2.6 View of the asymmetric unit of $\{[Mn(\mathbf{L4})Cl_2][Mn(\mathbf{L4})\text{-}\mu\text{-}ClMnCl_3]\}_2$ (**4.2**).[219] Hydrogen atoms and lattice water molecules are omitted for clarity. Thermal ellipsoids are plotted at 50%.

To prevent oxidation of the Mn^{II} centres, the reaction was repeated under nitrogen using degassed MeOH. Under these conditions, a yellow rather than red product was isolated, and the elemental analysis of the resulting complex was an excellent fit for $[Mn(\mathbf{L4})Cl_2]\cdot 2H_2O$ with a maximum difference of 0.34%. The imine stretch was present in the IR spectrum at υ = 1650 cm^{-1}, the UV-visible absorption maxima occurred at λ = 252 and 301 nm, and the major peak in the mass spectrum at *m/z* = 517 corresponded to $[M\text{-}2H_2O\text{-}Cl]^+$. Repeated attempts were made to crystallize **4.1** (Mn^{II}-dpN_3O_2), but these were unsuccessful; however, a planar, equatorial, pentadentate binding mode may be assigned to this macrocycle, given that this complex likely has a similar structure to the Mn^{II}-dpN_3O_2 units within the structure of the mixed valence system **4.2** (Figure 2.6). Within these units, the macrocycle **L4** (dpN_3O_2) is essentially planar: the maximum

deviation from the N_3O_2 plane of a contributing atom is 0.078 Å, observed for O(8). The Mn^{II} ions binds within the plane of the ring, with a deviation of 0.010 Å.[219]

Attempts were made to template the formation of macrocycle **L5** (N_3O_3) around Mn^{II}, from diamine **5c** and diacetylpyridine. However, only oligomeric products could be obtained, with both ketone (υ = ~1700 cm^{-1}) and amine stretches present in the IR spectra. The increased cavity size of this N_3O_3 system, and the flexibility of its aliphatic backbone, are likely the reasons this macrocycle did not template around the Mn^{II} ion. To the best of my knowledge, there are no structural reports of complexes of this ligand, or its N_6 analogue, in the literature.

Complex **6.1** (Mn^{II}-dbN_3O_3) was successfully prepared from diamine **6c** and diacetylpyridine in the presence of $MnCl_2$. An imine stretch was visible in the IR spectrum at υ = 1618 cm^{-1}, and the elemental analysis was an excellent fit for [Mn(**L6**)Cl_2]·$2H_2O$, with a maximum difference of 0.13% for C. It is interesting to note that the macrocycle **L6** (dbN_3O_3) was able to template around Mn^{II}, while the more flexible macrocycle **L5** (N_3O_3) was not, although the macrocycles have a similar cavity size and the same donor atom set. The enhanced rigidity of **L6** due to the two benzene rings inserted into the backbone presumably facilitates the templation process even around a small ion like Mn^{II}. The FAB-MS spectrum of Mn^{II}-dbN_3O_3 exhibited a 6% peak at *m/z* = 505, corresponding to $[M\text{-}2H_2O\text{-}Cl]^+$; however a much larger peak was visible at *m/z* = 289, corresponding to protonated diamine **6c**. The UV-visible spectrum most closely resembled that of the smaller dibenzo system **3.1** (Mn^{II}-dbN_3O_2): the absorption bands occurred at λ = 251 and 282 nm, with the second band blue shifted when compared to the non-rigid macrocyclic complexes described above (λ = ~300 nm).

Despite repeated attempts, X-ray quality single crystals of **6.1** (Mn^{II}-dbN_3O_3) could not be grown. There are no crystal structures reported for any metal complexes of this macrocycle; however, the formyl derivative f-dbN_3O_3 has been templated around Pb^{II}, with coordinated nitrate counter ions (Figure 2.7).[225] The macrocycle binds in a hexadentate fashion, through all six of its donor atoms; and is fairly planar, with a maximum deviation of a donor atom from the N_3O_3 plane of 0.24 Å; the pyridyl nitrogen and three oxygen atoms lie on one side of the N_3O_3 mean plane, while the imine nitrogens, as well as both benzyl groups, lie on the other. The Pb^{II} ion (ionic radius = 1.49 Å) deviates from the plane by 0.12 Å. Interestingly, in a Cd^{II} (ionic radius = 1.17 Å) complex of the related macrocycle f-dbN_4O_2, the macrocycle binds equatorially in a pentadentate fashion, via the four nitrogen atoms, with axial water ligands bound above and below the plane, giving a seven-coordinate geometry. One oxygen, O(1) remains unbound, and deviates from the pentadentate N_4O donor plane by 1.49 Å.[226] The Cd^{II} ion lies within the plane, with a maximum deviation of 0.14 Å.[226] Although the semi-metals Pb^{II} and Cd^{II} cannot be considered a perfect model for the transition metal Mn^{II}, these structures do confirm that macrocycles with the same cavity size and rigidity can bind equatorially to ions with a larger radius than Mn^{II} (1.04-1.10 Å).

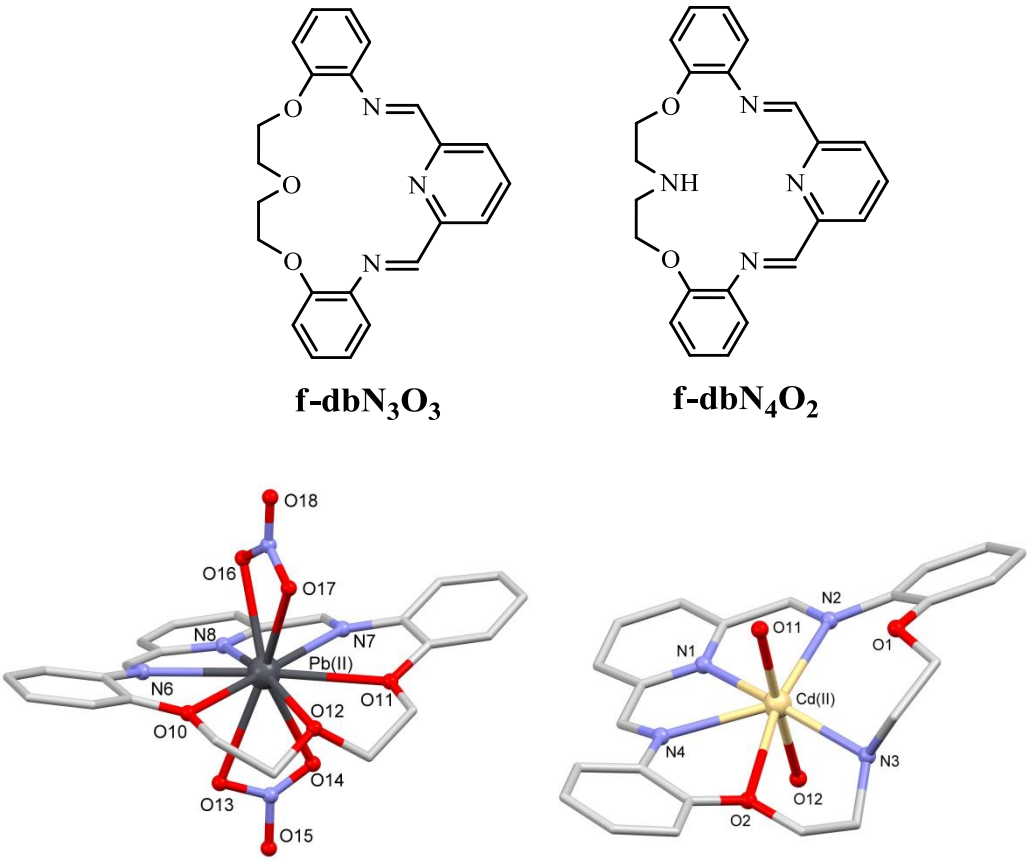

Figure 2.7 Left, molecular structure of Pb^{II}-f-dbN_3O_3;[225] right, molecular structure of Cd^{II}-f-dbN_4O_2.[226]

It is thus uncertain whether the macrocycle binds in a penta- or hexadentate fashion to the Mn^{II} ion in **6.1**. It is, however, probable that the macrocycle binds equatorially, given that the similarly sized Cd^{II} ion and larger Pb^{II} ion are equatorially encapsulated by structurally related macrocycles; leaving the axial positions available for water binding.

As mentioned in Section 1.3, complex **7.1 [**$(Mn^{II}\text{-}N_3O_2)_2$] was first reported several years ago by the Pilkington group.[221] $(Mn^{II}\text{-}N_3O_2)_2$ was synthesized from

$MnCl_2 \cdot 4H_2O$, the tetraketone **7d** and 2,2′-(ethylenedioxy)*bis*(ethylamine) in a 2:1:2 stoichiometric ratio, following the general synthetic method described at the beginning of Section 2.3. Imine formation was confirmed once again by the absence of a ketone peak, and by the presence of an imine stretch at υ = 1647 cm^{-1}. The UV-visible spectrum showed the expected two absorption bands, with a particularly intense peak at λ = 252 nm (ε = 18060 $L \cdot mol^{-1} \cdot cm^{-1}$), and a second weaker absorption at λ = 311 nm (ε = x $L \cdot mol^{-1} \cdot cm^{-1}$), blue shifted when compared to the absorption band associated with the 'half' version of this complex, **1.1** (Mn^{II}-N_3O_2). The elemental analysis data for **7.1** was an excellent fit for the formula $[Mn_2(\mathbf{L7})Cl_4] \cdot 5H_2O$, in agreement with the major peak on the FAB-MS spectrum at *m/z* = 728, corresponding to $[M\text{-}4H_2O\text{-}2Cl]^+$. The crystal structure of $(Mn^{II}\text{-}N_3O_2)_2$ is presented in Figure 2.5.[221] Both macrocyclic rings are almost planar, with maximum donor-atom deviations of 0.099 and 0.097 Å for N(6) and N(2); and the two macrocyclic rings are offset with a dihedral angle of 41.25°. Each Mn^{II} ion is equatorially bound by the macrocycle, with deviations of the metal ions from the pentadentate planes of 0.034 and 0.046 for Mn^{II}(1) and (2) respectively.[221] Interestingly, while the crystal structure of **2.1** (Mn^{II}-N_3O_2) shows that in the solid-state, the axial positions are occupied by chloride ions,[139] the reported crystal structure of **7.1** [(Mn^{II}-$N_3O_2)_2$] shows one chloride anion and one water molecule coordinated to each metal center (Figure 2.5).[221] This is surprising because **L7** [$(N_3O_2)_2$] is simply two covalently tethered **L2** (N_3O_2) macrocycles.

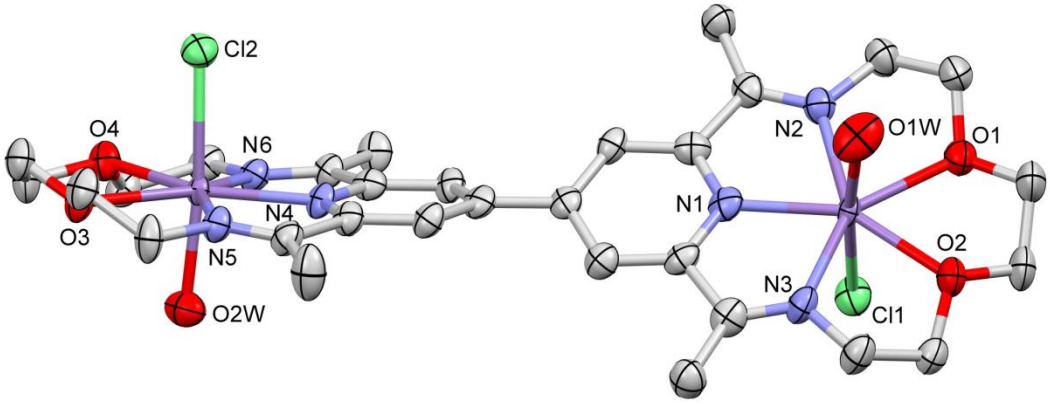

Figure 2.8 Crystal structure of $[Mn_2(\mathbf{L7})Cl_4]\cdot 5H_2O$ (**7.1**).[221] Hydrogen atoms, chloride counter ions and lattice water molecules are omitted for clarity.

Thus six of the seven target macrocycles were successfully templated around $MnCl_2$. Of the resulting complexes, five complexes were water soluble and consequently of interest as potential MRI contrast agents. As discussed above, an examination of the solid-state structures of the previously reported complexes **1.1** (Mn^{II}-N_5), **2.1** (Mn^{II}-N_3O_2) and **7.1** [(Mn^{II}-N_3O_2)$_2$] show that the macrocycles bind in an equatorial, pentadentate fashion, with two axial monodentate ligands. Although solid-state structures of **4.1** (Mn^{II}-dpN_3O_3) and **6.1** (Mn^{II}-dbN_3O_3) could not be measured, the partially dimerized system **4.2** [Mn(**L4**)Cl_2][Mn(**L4**)-μ-$ClMnCl_3$] clearly showed the ability of macrocycle **L4** (dpN_3O_3) to bind in a pentadentate, planar fashion; and a similar equatorial binding mode was assigned to **6.1** (Mn^{II}-dbN_3O_3) based on transition metal structures of related ligands.

These solid-state structures were primarily important in that they confirmed the equatorial nature of the macrocyclic binding, allowing for the presence of axially binding

ligands. Although in each solid-state structure, chloride anions were observed to bind, what is more important for the biological application of these compounds is the nature of the ligands bound to each Mn^{II} center in aqueous solution, as a model for the *in vivo* structure.

In order to investigate the nature of the axial ligands in solution, conductance measurements in aqueous solution were performed on all five complexes. Conductance measurements provide information concerning the electrolytic nature of complexes in solution. The formula unit of each mononuclear complex includes two chloride ions: if both are coordinated in aqueous solution, the complex will be neutral; if one chloride and one water are coordinated, the complex will be a 1:1 electrolyte; and if two water molecules are coordinated and both chloride ions are non-coordinating, the complex will be a 1:2 electrolyte.

Following literature precedence for this family of systems,[208-213] conductance measurements were carried out on 0.5 mM solutions of the complexes in water. Measurements were obtained in triplicate with precision >99%. The recorded values of conductance (G, in μS) were converted to molar conductivity (Λ_M, in $S \cdot cm^2 \cdot mol^{-1}$) via the equation below:

$$\Lambda_M = \frac{G \times K}{c} \qquad \textbf{Eqn. 2.1}$$

where K is the cell constant (1 cm^{-1}) and c is the concentration. The average molar conductivity (Λ_M) of each complex is presented in Table 2.2 and again in Table 2.3, along with the hydration number q.

Complex	Formula	q (solid-state)	Λ_M (H_2O) ($S \cdot cm^2 \cdot mol^{-1}$)	q (solution)
1.1 **Mn^{II}-N_5**	[Mn(**L1**)Cl_2]·2H_2O	0	254.3	2
2.2 **Mn^{II}-N_3O_2**	[Mn(**L2**)Cl_2]·2H_2O	0	194.4	2
4.1 **Mn^{II}-dpN_3O_2**	[Mn(**L4**)Cl_2]·2H_2O	0	293.4	2
6.1 **Mn^{II}-dbN_3O_3**	[Mn(**L6**)Cl_2]·2H_2O	-	186.2	2
7.1 **(Mn^{II}-N_3O_2)$_2$**	[Mn_2(**L7**)Cl_4]·5H_2O	2	320.4	3

Table 2.3 Summary of molar conductivity values ($S \cdot cm^2 \cdot mol^{-1}$) in aqueous solutions at 25°C for the Mn^{II} complexes.

The aqueous molar conductivities of the mononuclear complexes fall in the range 190-290 $S \cdot cm^2 \cdot mol^{-1}$, indicative of 1:2 electrolytic behaviour, which is consistent with the displacement of both coordinated chloride ions by water in aqueous solution. A similar phenomenon was reported by Nelson and co-workers in his series of papers on pentadentate macrocyclic complexes of transition metals in the 1970s.[208-213] With a focus on 7-coordinate, pentagonal bipyramidal complexes of Fe^{II} and Mg^{II}, he found that conductivity measurements in the poorly coordinating solvent acetonitrile were consistent with one or two bound counter ions in the axial positions (1:1 electrolytes or non-electrolytes in solution), while aqueous conductivity measurements indicated complete displacements of both axial ligands by water (1:2 electrolytes in solution).[208-211] The aqueous hydration number of q = 2 observed for the mononuclear complexes in Table 2.3 is higher than that of all the approved agents: 1 for the Mn^{II} agent Teslascan (in solution

only), and 1 for the Gd^{III} complexes. The dinuclear complex **7.1** $(Mn^{II}\text{-}N_3O_2)_2$ exhibited a molar conductivity of 320 $S{\cdot}cm^{2}{\cdot}mol^{-1}$ in aqueous solution, suggesting that one of the two coordinated chloride ions was displaced by a water molecule. It is somewhat surprising that both coordinated chloride ions were not displaced by water, given the complete displacement observed for the mononuclear complexes. Nevertheless, the resulting hydration number of q = 3 is still very high.

Other Mn^{II} complexes with no coordinated waters in the solid state have been shown to exhibit aqueous relaxivity behaviour, by various means. In the case of Teslascan, the solid-state structure shows a hydration number of q = 0. In aqueous solution, and *in vivo*, the observed relaxivity behaviour is due to the complete dissociation of the DPDP ligand (Figure 2.9), yielding small amounts of free Mn^{II}, which becomes fully hydrated; the contrast behaviour of Teslascan is thus due to the species $[Mn(H_2O)_6]^{2+}$.[40,41] A similar full-dissociation is observed for the 8-coordinate, q = 0 complex Mn^{II}-DTPA (Figure 2.9).[40,41] In contrast, the 6-coordinate complex Mn^{II}-DO2A (Figure 2.9) is also coordinatively saturated by the ligand in the solid state with q = 0, but in solution, the ligand remains fully bound, and the coordination sphere transiently increases to 7, as one water binds, giving q = 1 and accounting for the observed relaxivity of this system.[60] Thus full dissociation of a chelating ligand to give hydrated Mn^{II}, and a widening of the coordination sphere to accept a water molecule, have both been described for q = 0 structures. However, the retention of a fully-bound macrocyclic ligand, accompanied by an increase in hydration number *without* increasing the coordination number, due to axial ligand displacement, has not been discussed in the context of contrast agent development.

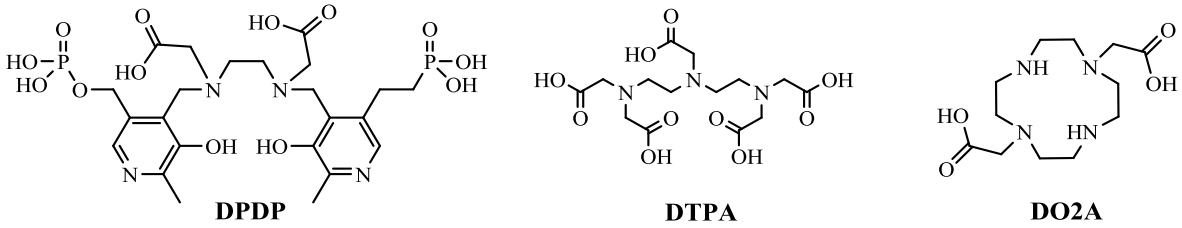

Figure 2.9 Selected ligands which form q = 0 complexes with Mn^{II} in the solid state.

Based on their high water solubility, aqueous hydration numbers of q = 2 and 3, and the planar, equatorial nature of the macrocycles which should allow for ready water exchange, the five Mn^{II} complexes listed above were selected as promising candidates for further investigation as MRI contrast agents.

2.3.2 Gd^{III} complexes

Although small-molecule agent research has focused in recent years on complexes of Mn^{II}, Gd^{III} contrast agents are still of interest: the lanthanide ion has a higher paramagnetic moment and a slower electronic relaxation time than the transition metal – which is why Gd^{III} was the ion which dominated the first 25 years of contrast agent development. In addition, the link between NSF and Gd^{III} has been observed only in patients with already compromised kidney function, which is why Gd^{III}-based agents are still on the market, although more stringent safety measures surrounding their use are in place. The search for Gd^{III}-based agents with non-DOTA or DTPA scaffolds, which have a high relaxivity and an acceptable toxicity profile, is still ongoing.[227]

Our attempts to template **L1**-**L7** around $GdCl_3 \cdot 6H_2O$ resulted in the isolation of five novel, previously unreported complexes with the formula $[Gd(\mathbf{L})Cl_3]\cdot xH_2O$, summarized in Table 2.4. Three of these complexes had a high degree of purity and were

water soluble (complexes **1.2**, **2.2**, and **6.2**), while two were insoluble (**3.2** and **5.2**). This stands in contrast to the ready synthesis of analytically pure complexes of Mn^{II} with all but one of the target macrocycles.

Complex; Abbrev.	Formula		C	H	N	$\nu_{(C=N)}$ (cm^{-1})	λmax (ε) (nm, $L \cdot mol^{-1} \cdot cm^{-1}$)	$\Lambda_M - H_2O$ ($S \cdot cm^2 \cdot mol^{-1}$)
1.2 Gd^{III}-N_5	[Gd(**L1**)Cl_3]·3H_2O	Found Calcd	30.48 30.48	5.21 4.95	11.95 11.85	1631	250 (5860) 281 (4020)	316.7
2.2 Gd^{III}-N_3O_s	[Gd(**L2**)Cl_3H_2O]·6H_2O	Found Calcd	27.89 27.84	5.23 5.14	6.35 6.49	1620	250 (4560) 274 (2730)	-
3.2 Gd^{III}-dbN_3O_2	[Gd(**L3**)Cl_3]·0.5H_2O	Found Calcd	43.71 42.89	4.01 3.44	5.63 6.52	1661	250 (7200) 275 (5160)	-
5.1 Gd^{III}-N_3O_3	[Gd(**L5**)Cl_3]·2H_2O	Found Calcd	32.83 32.98	4.10 4.72	5.95 6.79	1659	251 (10520) 282 (6470)	277.9
6.2 Gd^{III}-dbN_3O_3	[Gd(**L6**)Cl_3]·6H_2O	Found Calcd	38.50 38.14	4.39 4.74	5.14 5.34	1628	254 (8501) 277 (8038)	346.8

Table 2.4 Summary of Gd^{III} complex formulae, elemental analyses, IR and UV-visible spectroscopic data, and conductance measurements.

Gd^{III} readily templated the formation of macrocycles **L1** (N_5), **L2** (N_3O_2) and **L6** (N_3O_3), yielding the pure, soluble complexes **1.2**, **2.2**, and **6.2**. Imine formation was confirmed in each case by appearance of band at υ = 1630, 1620 and 1628 cm^{-1} respectively, corresponding to the imine stretch. Elemental analysis fit for the formulae [Gd(**L**)Cl_3]·$x$$H_2O$, where x = 3 for **l.2** (Gd^{III}-N_5) and x = 6 for **2.2** (Gd^{III}-N_3O_2) and **6.2** (Gd^{III}-dbN_3O_3). In contrast to the FAB mass spectra of the Mn^{II} complexes, in which major peaks corresponding to the intact complex were observed, fragmentation of the Gd^{III} complexes occurred much more readily under FAB, EI and ESI conditions. A small peak at *m/z* = 465 observed for **1.2** corresponding to $[M\text{-}H\text{-}2Cl]^+$, but no peaks

corresponding to the intact complex were observed for **2.2** and **6.2**, only peaks at *m/z* = 297 and 289, corresponding [**L2**+Na]$^+$ (6.6%) and 289 [**L6**+H]$^+$ respectively. All three complexes exhibited similar UV-visible behaviour, with two maxima within the ranges 250-254 and 274-281 nm observed for each. The bands correspond to π to π* electronic transitions or the coordinated macrocycle – comparable to those observed for the Mn^{II} complexes, for which the bands were found at λ = 250-252 and 280-311 nm.

Macrocycles **L3** (dbN_3O_2) and **L5** (N_3O_3) were successfully templated around Gd^{III}, evidenced by imine stretches in their IR spectra at ν = 1661 and 1659 cm^{-1} respectively, and macrocyclic π to π* transitions in their UV-visible spectra at λ = 250 and 275, and 251 and 282 nm respectively. The formation of complex **3.2** (Gd^{III}-dbN_3O_2) was carried out in ethanol rather than methanol, as this macrocycle had proven susceptible to hydrolysis during the formation of the related Mn^{II} complex **3.1**. The successful formation of complex **5.1** (Gd^{III}-N_3O_3) stands in contrast to the inability of macrocycle **L5** to template around Mn^{II} as noted in Section 2.3.1, presumably due to the smaller size of that ion. The best fit for elemental analysis was for complexes of the formulae [Gd(**L**)Cl_3]·$x$$H_2O$, where x = 0.5 for **3.2** and x = 2 for **5.1**. Both complexes were initially formed with a lower degree of purity (maximum difference between observed and calculated C, H, and N elemental analyses was >0.8%); and in spite of repeated attempts to wash and recrystallize the product from methanol and ethanol, a higher degree of purity could not be achieved. Due to their water insolubility, these two complexes are not suitable for development as MRI contrast agents, and so were not pursued further.

An attempt was made to prepare the Gd^{III} complexes of the dimeric macrocycle **L7** [$(N_3O_2)_2$]. However, when the tetraketone **7d** was added to a methanolic solution of Gd^{III}, a precipitate immediately formed, in contrast to all the other systems in which the intermediate metal-ketone species remained in solution. Upon addition of the diamine, the precipitate remained. It was collected and isolated, but the IR spectrum showed the presence of ketone peaks around 1700 cm^{-1}, and the elemental analysis could not be fit to any number of variations of the metal/tetraketone/diamine mixture. It appears that if the dinuclear Gd^{III} complex is to be formed, a suitable solvent must be found in which the intermediate metal-ketone complex is soluble. However, solubility tests on the precipitating species failed to reveal a common solvent in which the compound was soluble.

Although many attempts were made to crystallize each synthesized Gd^{III} complex from a variety of solvents via evaporation, vapour diffusion, and layered systems, no X-ray quality crystals were successfully formed. For this reason, although imine bond formation can be confirmed by IR spectroscopy, and elemental analysis can indicate the formula, the coordination geometry of the metal center and the nature of the anions and water molecules (axially bound, or unbound) could not be definitively determined in the solid state. There is strong literature precedence for this difficulty in growing X-ray quality single crystals of lanthanide complexes of [1+1] Schiff-base macrocycles. Radecka-Paryzek and co-workers attempted to template **L1** (N_5) around the series of lanthanide chloride and perchlorate salts.[137] Only two analytically pure complexes were isolated, template by $LuCl_3$ and $La(ClO_4)_3$. Evidence of macrocycle formation was

observed in the isolated products of the reactions with $LnCl_3$ (Ln = Dy, Tm) and $Ln(ClO_4)_3$ (Ln = Sm, Tm). Bastida and co-workers attempted the synthesis of **L6** (dbN_3O_3) via templation around the whole lanthanide series of nitrate and perchlorate salts. Analytically pure complexes of a number of nitrates (La^{III}, Ce^{III}, Pr^{III}, Nd^{III}, Sm^{III}, Eu^{III}, Gd^{III}, Tb^{III} and Dy^{III}) and two perchlorates (La and Ce) were isolated.[138] In both reports, a range of spectroscopic data, molar conductance values, and thermogravimetric analyses were presented; but the possible coordination numbers and geometries of the metal centers were not speculated upon, and no single crystal structural data was reported.[137,138]

Although X-ray quality crystals of the three complexes of interest (Gd^{III}-N_5, Gd^{III}-N_3O_2 and Gd^{III}-dbN_3O_2) could not be grown, and in fact no rare-earth structures of any of the three macrocycles **L1**, **L2**, or **L6** are known, an examination of related rare earth macrocyclic structures suggests that all three macrocycles bind in an equatorial fashion around the metal ion. Planar, equatorial binding of a *pentadentate* macrocylic ring to a lanthanide was described for the 16-membered analogue of **L1**, p-N_5, which binds to both Yb^{III} and Lu^{III} (Figure 2.10).[228-230] Although p-N_5 is larger than **L1** and **L2** by one $–CH_2$-unit, this macrocycle confirms that a lanthanide ion may be bound within an N_5 donor plane. In addition, 15-membered N_5 and N_3O_2 macrocycles have been reported to bind in a pentadentate fashion to ions with a larger ionic radius than Gd^{III} (1.00 Å when seven-coordinate to 1.11 Å when nine-coordinate), such as Cd^{II}.[231]

Equatorial binding of a related *hexadentate* macrocyclic ring to a rare-earth metal was reported for the La^{III}, Ce^{III}, Pr^{III}, Nd^{III}, and Lu^{III} complexes of the pyridine-functionalized macrocycle f-N_6 (Figure 2.10). In each case, the macrocycle is puckered.

A representative Nd^{III} complex is shown in Figure 2.10, in which the pyridine nitrogen N(1) lies 0.85 Å Ln^{III} away from the mean N_6 plane; the N(1)---N(4) angle is 145.5°. The Nd^{III} ion lies just 0.07 Å out of the macrocyclic plane. These structures provide evidence that a lanthanide ion may be equatorially encapsulated by a hexadentate, 18-membered macrocyclic ring. In addition, as was noted in Section 2.3.1 during a discussion of the Mn^{II} complex of **L6**, ions with a larger ionic radius than Gd^{III} (Pb^{II} and Cd^{II}) are equatorially bound by the rigid hexadentate macrocycles f-dbN_3O_3 and f-dbN_4O_2.[225,226]

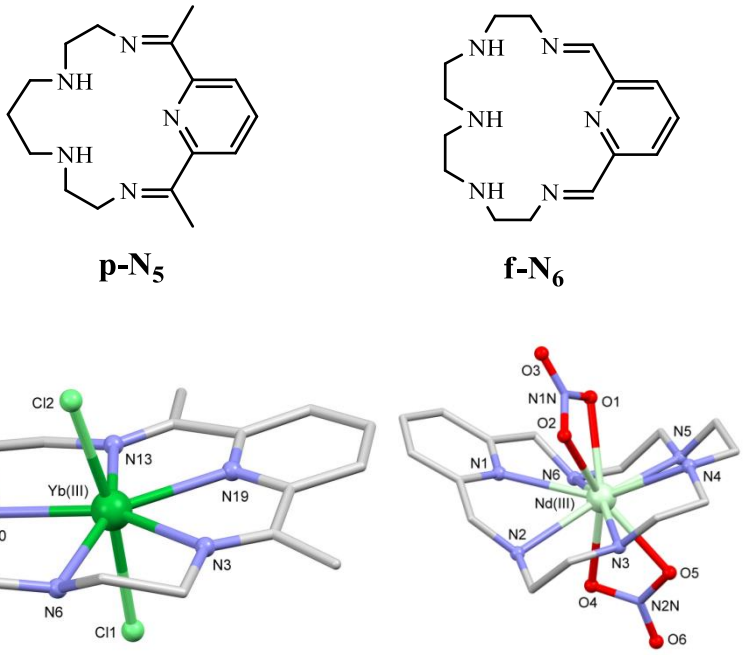

Figure 2.10 Left, molecular structure of the Yb^{III}-p-N_5;[229] right, molecular structure of the Nd-f-N_6 complex.[232]

It can thus be assumed that the pentadentate macrocycles **L1** (N_5) and **L2** (N_3O_2), and the hexadentate macrocycle **L6** (dbN_3O_3), are capable of binding in an equatorial fashion to Gd^{III} via five and six donor atoms respectively. Of the rare earth complexes

with pentadentate and hexadentate macrocyclic ligands, most are at least seven- and eight-coordinate respectively: they have at least two axially-bound ligands.[228,229,233-235]

A detailed discussion of additional rare earth structures is presented in Section 3.2 of Chapter 3, in the context of SMMs for which an understanding of the solid-state structure is very significant. However for the purposes of contrast agent development, as was noted for the Mn^{II} complexes above, the key structural point for this family is that the macrocycles bind in an equatorial fashion, allowing for the potential of fast, unhindered water exchange, and thus efficient (high) relaxivity – as long as at least one water molecule is directly coordinated to the Gd^{III} center in aqueous solution.

As was noted above for the Mn^{II} complexes, information about the nature of the axial ligands may be gleaned from conductance measurements. Conductance measurements were performed in both water and in the poorly coordinating solvent methanol, as the number of unbound chloride ions in methanol may be representative of the number unbound in the solid state.[208-213] The average molar conductivity (Λ_M) of each complex is presented in Table 2.4 and again in Table 2.5, along with the indicated electrolytic behaviour.

Complex	Formula	Λ_M (MeOH) ($S \cdot cm^2 \cdot mol^{-1}$)	electrolytic behaviour (MeOH)	Λ_M (H_2O) ($S \cdot cm^2 \cdot mol^{-1}$)	electrolytic behaviour (H_2O)
1.2 Gd^{III}-N_5	[Gd(**L1**)Cl_3]·3H_2O	95.6	1:1	316.7	1:2-3
2.2 Gd^{III}-N_3O_2	[Gd(**L2**)Cl_3H_2O]·6H_2O	171.9	1:2	277.9	1:2-3
6.2 Gd^{III}-dbN_3O_3	[Gd(**L6**)Cl_3]·6H_2O	164.0	1:2	346.8	1:3

Table 2.5 Summary of molar conductivity values ($S \cdot cm^2 \cdot mol^{-1}$) in aqueous solutions at 25°C for the Gd^{III} complexes.

The *molar conductivity data in methanol* was interpreted in light of the useful review by Geary.[236] This was the paper used by Nelson and Drew in their original series on pentadentate Schiff-base macrocycles, to justify their conclusions regarding the coordination numbers of transition metal complexes in the solid state. Geary gives an expected range of values of 80-115 $S{\cdot}cm^{2}{\cdot}mol^{-1}$ for a 1:1 electrolyte in methanolic solution, 160-220 $S{\cdot}cm^{2}{\cdot}mol^{-1}$ for a 1:2 electrolyte, and 290-350 $S{\cdot}cm^{2}{\cdot}mol^{-1}$ for a 1:3 electrolyte. The Λ_M (MeOH) value for complex **1.1** (Gd^{III}-N_5) is indicative of 1:1 electrolytic behaviour, while the values for **2.2** (Gd^{III}-N_3O_2) and **6.2** (Gd^{III}-dbN_3O_3) suggest a 1:2 electrolyte in solution. This conductance data suggests that in the solid state (represented by methanolic solution), two chloride ions are directly coordinated in **1.2** while one chloride ion is directly coordinated in **2.2** and **6.2**. Given that each complex is likely to be at least seven-coordinate, at least one water molecule is likely bound to the metal centers of **2.2** and **6.2** in the solid state.

Thermogravimetric analysis (TGA) of complex **2.2** (Gd^{III}-N_3O_2) was utilized in order to confirm the reliability of methanolic solution as a model for the solid state structure, and in order to gather further information concerning the nature of the axial ligands (Figure 2.11).

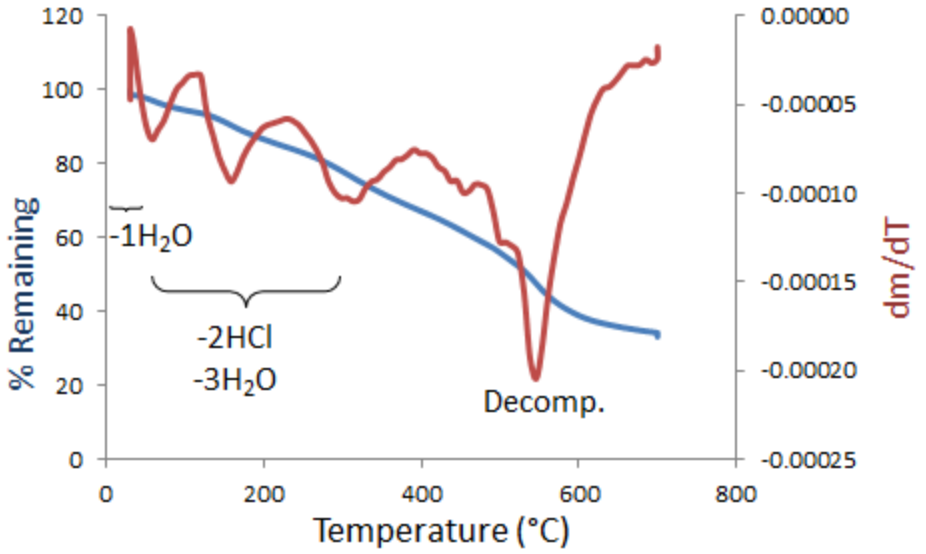

Figure 2.11 TGA plot for complex **2.2** (Gd^{III}-N_3O_2).

Water is present, bound in at least two different ways. An initial water molecule is lost by 60°C, suggesting a weakly bound lattice solvent. Three additional waters are lost by 300°, suggesting strong hydrogen bonding; along with two non-coordinating chloride ions, lost in the form of HCl. Decompositon occurs by ~545°C, and one chloride ion is not observed to leave. Thus the TGA data for **2.2** supports the binding of a single chloride ion to the Mn^{II} centre in the solid state, consistent with the molar conductivity data measured for **2.2** (Gd^{III}-N_3O_2) in methanol.

The *aqueous molar conductivity* data suggested that complexes **1.2** (Gd^{III}-N_5) and **2.2** (Gd^{III}-N_3O_2) are both either 1:2 or 1:3 electrolytes in aqueous solution, while **6.2** (Gd^{III}-dbN_3O_3) acts as a 1:3 electrolyte. That is, in aqueous solution, at the most, one chloride ion is coordinated to **1.2** and **2.2**, and no chlorides are coordinated to the metal center of **6.2**, confirming displacement of axial chloride ligands by water. Again, since

each complex is likely to be at least seven-coordinate, in aqueous solution at least one water molecule is bound to the metal center of **1.2** and **2.2**, and at least two waters are bound to the metal center of **6.2**. Thus the primary requirement for efficient relaxivity behaviour – inner-sphere water molecules – is met by all three soluble, pure Gd^{III} complexes.

2.4 Relaxivity studies

A collaboration was initiated with the STTARR Innovation Centre in Toronto, in order to acquire aqueous relaxivity data on the family of complexes at a clinically relevant magnetic field. Under the guidance of Dr. Warren Foltz, a Bruker minispec mq60 Contrast Agent Analyzer was used to measure the T_1 and T_2 relaxation time constants of all eight pure, water soluble compounds: the Mn^{II} compounds of N_5, N_3O_2, dpN_3O_2, dbN_3O_3, and O_2N_3-N_3O_2; and the Gd^{III} complexes of N_5, N_3O_2, and dbN_3O_3. The measurements were carried out in a magnetic field of 1.4 T (corresponding to a ^1H nuclear resonant frequency of 60 MHz), at 37°C.

Interestingly, although 60 MHz is the most common clinical field utilized in MRI, the relaxivity values of both the approved agents and compounds being investigated as potential agents tend to be reported in a field of 20 MHz. For this reason, the r_1 and r_2 values of the complexes were measured in an additional field of 20 MHz, using a minispec mq20 Contrast Agent Analyzer.

The formulae for the r_1 and r_2 relaxivities are:

$$r_1 = \frac{1/T_1}{c} \qquad \text{and} \qquad r_2 = \frac{1/T_2}{c}$$

In order to calculate the r_1 and r_2 relaxivities of each complex, a series of 5-6 dilutions of each complex were prepared immediately prior to the measurements. The T_1 and T_2 relaxation time constants of each dilution of the 8 analytically pure, water soluble compounds were measured at a temperature of 37°C, as this temperature has the most biological relevance. Then $\frac{1}{T_1}$ or $\frac{1}{T_2}$ (s^{-1}) was plotted against c (mM), to give a series of linear plots, whose slopes gave the values of r_1 and r_2 ($mM^{-1}{\cdot}sec^{-1}$) respectively.

Table 2.6, below, summarizes the clinical field (60 MHz) and low-field (20 MHz) relaxivity results.

Complex	**Formula**	**r_1 (60 MHz)**	**r_2 (60 MHz)**	**r_1 (20 MHz)**	**r_2 (20 MHz)**
1.1	[Mn(**L1**)Cl_2]·$2H_2O$	2.76 ± 0.02	10.7 ± 0.2	3.77 ± 0.02	6.07 ± 0.03
2.1	[Mn(**L2**)Cl_2]·$2H_2O$	2.78 ± 0.03	12.7 ± 0.12	3.58 ± 0.02	6.67 ± 0.06
4.1	[Mn(**L4**)Cl_2]·$2H_2O$	4.00 ± 0.03	23.0 ± 0.2	5.34 ± 0.08	14.8 ± 0.2
6.1	[Mn(**L6**)Cl_2]·$2H_2O$	2.78 ± 0.02	31.1 ± 1.4	7.22 ± 0.12	42.9 ± 0.5
7.1	[Mn_2(**L7**)$Cl_2(H_2O)_2$]Cl_2	7.36 ± 0.05	30.7 ± 0.8	10.0 ± 0.79	26.8 ± 1.5
1.2	[Gd(**L1**)Cl_3]·$6H_2O$	5.58 ± 0.10	6.77 ± 0.04	6.43 ± 0.41	6.85 ± 0.47
2.2	[Gd(**L2**)Cl_3]·$6H_2O$	6.04 ± 0.10	7.67 ± 0.13	-	-
6.2	[Gd(**L6**)Cl_3]·$6H_2O$	2.78 ± 0.23	8.68 ± 0.11	8.05 ± 0.15	8.60 ± 0.27

Table 2.6 Summary of 20 and 60 MHz r_1 and r_2 ($mM^{-1}{\cdot}sec^{-1}$) relaxivity data.

A sample relaxivity plot for **1.1** (Mn^{II}-N_5) at 60 MHz, 37°C is shown in Figure 2.12, below. Relaxivity plots for additional compounds and fields are provided in the Appendix.

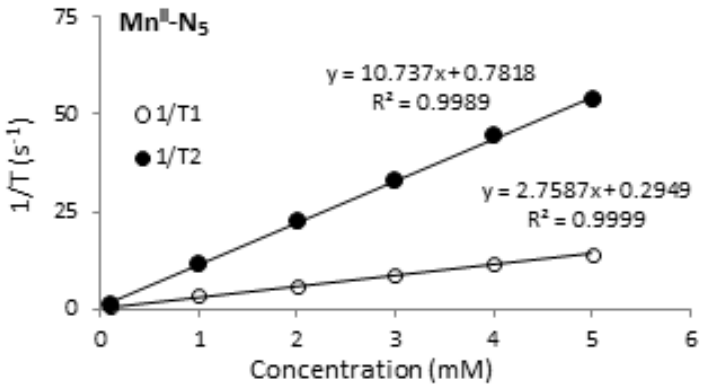

Figure 2.12 Relaxivity plot for **1.1** (Mn^{II}-N_5) at 60 MHz, 37°C, showing an r_1 of 2.76 and an r_2 of 10.7 $mM^{-1}\cdot sec^{-1}$, given by the slopes of the lines.

From this data it can be seen that all eight complexes displayed efficient relaxation of water protons. The measured values of r_1 for the Mn^{II} complexes **6.1** and **7.1** and the Gd^{III} complexes **1.2** and **6.2** are higher than the majority of the r_1 values of the FDA-approved agents at 20 MHz, which tend to be between 3 and 5.5 $s^{-1}\cdot Mm^{-1}$ (see Section 1.1). The r_1 values for the remaining complexes are within the range of the approved agents. All of the r_2 values are remarkably high, in particular those of the Mn^{II} complexes **4.1**, **6.1** and **7.1**, which are above 30 $s^{-1}\cdot Mm^{-1}$. Teslascan, the T_2-reducing Mn^{II}-based agent on the market in the USA, has an r_2 of 3.7 $s^{-1}\cdot Mm^{-1}$. The increased bulk

of **4.1** and **6.1** resulting in slower rotation, and the presence of two metal centers in **7.1**, may be responsible for the extraordinary r_2 values of these systems.

2.5 *In vitro* toxicity study

Following the success of the aqueous relaxivity measurements, an *in vitro* toxicity study was performed in order to evaluate the cytotoxic potential of several of the agents. The primary purpose of this study was to aid in the selection of a test compound for a pilot *in vivo* study, by confirming that at least one of the agents was not significantly more toxic than an agent already approved for use. It is important to note that direct conclusions about *in vivo* toxicity cannot be drawn from *in vitro* toxicity results, chiefly because prior to studies on the biodistribution, pharmacokinetics and excretion timeline/pathway of a compound, it is impossible to say what concentration of the compound would be present in a given tissue or organ at a given time point. However, *in vitro* studies do offer a way to compare a compound approved for human use with one or more test substances, with a view to preventing unnecessary pain and distress on an animal due to unforseen acute toxicity during an *in vivo* study.

The study was performed using primary rat renal proximal tubule epithelial cells (RPTECs), which were chosen because excretion occurs primarily via the kidneys in all but one of the approved small molecule contrast agents.[4,10] Six agents were selected for *in vitro* testing: the Mn^{II} and Gd^{III} complexes of **L1** (N_5), **L2** (N_3O_2) and **L6** (dbN_3O_3); that is, complexes **1.1** and **1.2**, **2.1** and **2.2**, and **6.1** and **6.2**. The compounds were evaluated at seven concentrations (30 mM, 10 mM, 3.3 mM, 1.1 mM, 0.36 mM, 0.12 mM and 0.04 mM) after 2, 4, 10 and 24 hours of treatment in rat RPTECs. The MTT assay was used as

an indicator of viability. MTT, or 3-(4,5-dimethylthiazol-2-yl)-2,5-diphenyltetrazolium bromide, is a yellow tetrazole. Living cells reduce MTT to the purple compound formazan, and thus the proportion of viable cells can be assessed using a spectrophotometer. The cytotoxic potential of the test articles was compared to the toxicity observed in the presence of the approved agent Omniscan (or Gadodiamide, Gd^{III}-DTPA-BMA). The results are summarized in Table 2.7, where the inhibitory concentration (IC50, the concentration resulting in 50% toxicity) was determined by plotting log concentration *vs.* relative viability.

		2 hr	**4hr**	**10 hr**	**24 hr**
1.1	[Mn(**L1)**Cl_2]·$2H_2O$	ND	ND	ND	5.47
2.1	[Mn(**L2)**Cl_2]·$2H_2O$	3.88	2.56	14.66	0.68
6.1	[Mn(**L6)**Cl_2]·$2H_2O$	1.25	0.67	1.39	0.21
1.2	[Gd(**L1)**Cl_3]·$3H_2O$	8.15	3.37	8.53	0.92
2.2	[Gd(**L2)**Cl_3H_2O]·$6H_2O$	9.39	3.65	5.32	1.1
6.2	[Gd(**L6)**Cl_3]·$6H_2O$	2.9	2.19	2.195	1.27
	Omniscan	ND	ND	>30mM	31.05

Table 2.7 Inhibitory concentrations (IC50, mM). ND = not determined due to lack of dose response.

As shown in Table 2.7, following 2 and 4 h of treatment, complex **1.1** and reference article Gadodiamide did not show significant cytotoxicity at the concentrations tested. However, a decrease in viability was observed in the cells which were treated with the other five complexes, suggesting a degree of toxicity at these time points. At the 10 hour time point, complex **1.1** (Mn^{II}-N_5) still did not display significant cytotoxicity. Complexes **1.2** (Gd^{III}-N_5), **2.1** (Mn^{II}-N_3O_2), **2.2** (Gd^{III}-N_3O_2), and **6.1** (Mn^{II}-N_3O_2), exhibited a slight reduction in toxicity, suggesting that the cells might be recovering from

the effects of the test articles. Complex **6.2** (Gd^{III}-N_3O_2) did not show a significant change in toxicity from the 4 to the 10 h time point. Reference article Gadodiamide showed more toxicity after 10 hours of treatment than at earlier time points. Following 24 hours of treatment, all six test articles and the reference article showed some level of toxicity, with **1.1** (Mn^{II}-N_5) and Gadodiamide exhibiting the least cytotoxic effects. It should be noted that the most of the approved small-molecule contrast agents have a clearance time of under 2 hours, so the 10 and 24 hour time points may not be relevant to the *in vivo* toxicity of the test compounds if they are excreted with similar efficiency.

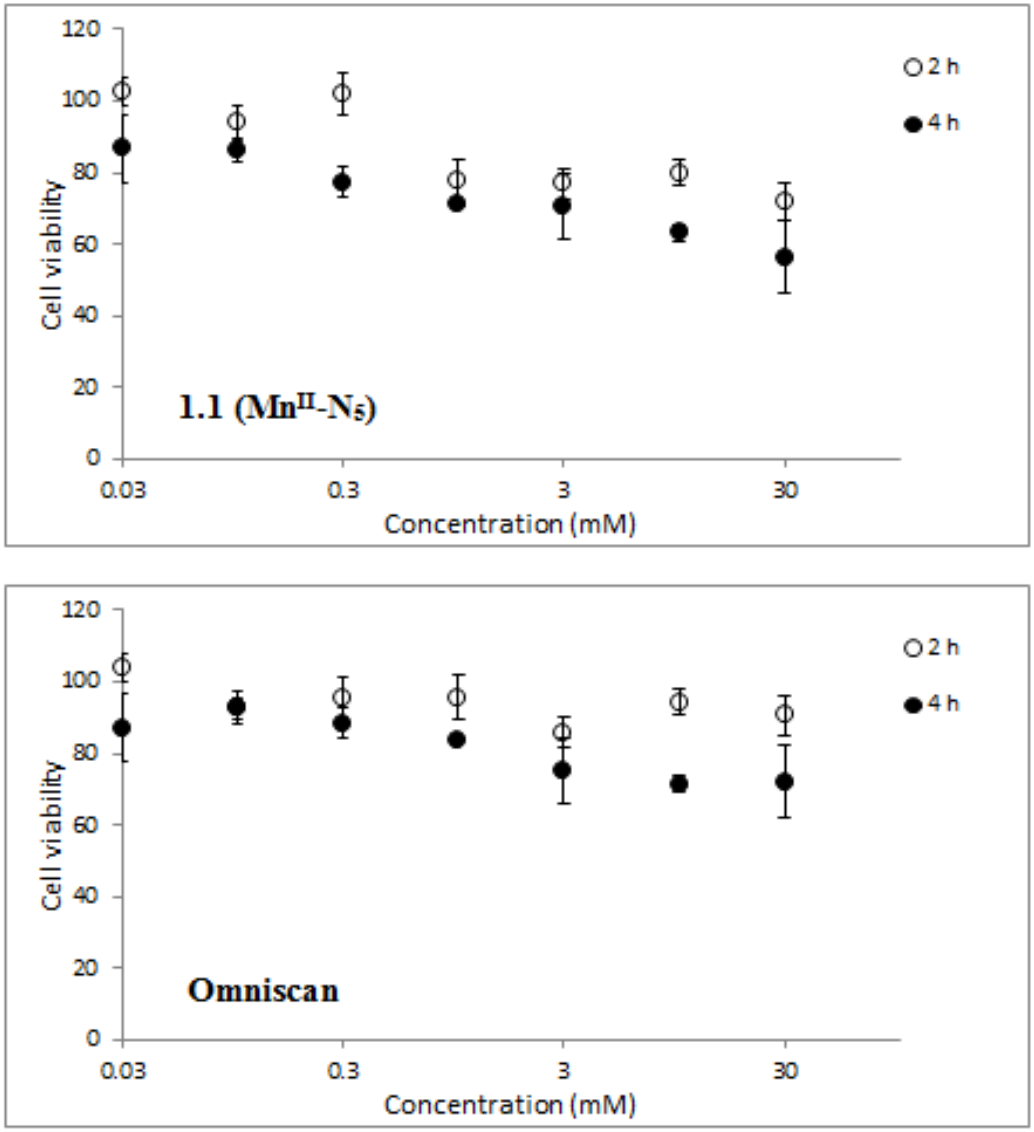

Figure 2.13 Cell viability plots for **1.1** (Mn^{II}-N_5) and Omniscan at the 2 and 4 hour time points, showing high cell viability over the studied concentration range.

Based on the results described above, **1.1** (Mn^{II}-N_5) was selected as the initial agent for *in vivo* testing because it displayed the least cytotoxic activity in rodents RTEPCs. In addition, as was discussed in Section 1.1, there is a current focus on Mn^{II}-

based small molecule agents, due to the recent discovery of the link between Gd^{III}-based agents and the disorder NSF.[26] Since the one Mn^{II}-based agent Teslascan was removed from the market, there is a clear need for alternatives to Gd^{III} for patients with compromised renal function. For this additional reason, the Mn^{II} compounds in our family were of particular interest.

In the approved agents, the *in vivo* stability and thus the toxicity is limited by acid-assisted dissociation of the metal ions.[4,10] In contrast, we were anticipating that the *in vivo* stability of our templated Schiff-base macrocyclic complexes would be limited by the kinetics of the cleavage of the imine bonds. However, although the addition of water, methanol and ethanol to the imine bonds of transition metal complexes of Schiff-base macrocycles has been reported in the literature, these reactions are not necessarily or even usually accompanied by a change in the coordination sphere of the metal ion.[237,238] For instance, the base-catalysed addition of water to the imine bonds of complex **1.1** (Mn^{II}-N_5) was reported as part of a study on Mn^{II} complexes as superoxide dismutase mimics, and UV-visible measurements indicated no change in the Mn^{II} coordination sphere during the addition.[64] Thus even if a certain amount of imine bond cleavage were to occur *in vivo*, the Mn^{II} or Gd^{III} ions would potentially remain coordinated to the now-amine nitrogens of the macrocycle until excreted. It is also important to note that high stability constants are not a representative measure of *in vivo* non-toxicity.[239] The overall *in vivo* toxicity of small-molecule agents is determined by numerous factors, including the concentration and nature of the dose administered; the biodistribution, excretion pathway and excretion time; as well as interactions with biological molecules and ions to give free Mn^{II} or Gd^{III}, and/or degradation products with their own toxicity profiles. For

these reasons, preliminary acute toxicity studies were amongst the earliest data reported for the now-approved Gd^{III}-based agents.[240] Thus a pilot *in vivo* acute toxicity study on representative compounds from our family was an important next step.

2.6 *In vivo* study

Small-scale pilot *in vivo* toxicity and imaging studies were performed first on complex **1.1** (Mn^{II}-N_5) and then on **7.1** [$(Mn^{II}$-$N_3O_2)_2$] as part of a collaboration with the Animal Resource Centre (ARC) and STTARR Innovation Centre in Toronto. Compound **1.1** (Mn^{II}-N_5) was selected due to its particularly low cytotoxicity as noted above, and following the success of that initial study, **7.1** [$(Mn^{II}$-$N_3O_2)_2$] was chosen because it displayed the highest r_1 relaxivity and one of the highest r_2 relaxivity values; and because as a dinuclear system, it is the most novel of the complexes. Compound **2.1** (Mn^{II}-N_3O_2) was also included in the imaging portion of the study, for comparison as a mononuclear analogue of **7.1**.

2.6.1 Acute toxicity

The acute toxicities of **1.1** (Mn^{II}-N_5) and **7.1** [$(Mn^{II}$-$N_3O_2)_2$] were studied in 8 week old male Sprague-Dawley rats. The toxicity of **1.1** was studied over a period of 14 days, in four rats; while the toxicity of **7.1** [$(Mn^{II}$-$N_3O_2)_2$] was studied over a period of 8 days, in 8 rats. Compound **1.1** was injected intravenously at a dosage of 0.02 mmol/kg (c = 12.5 mM), while **7.1** was injected at a dosage of 0.01 mmol/kg (c = 6.25 mM). These dosages were chosen because the dosage for the only Mn^{II}-based compound approved in North America, Teslascan, was 0.005 mmol/kg; and we were anticipating a lower degree of toxicity.

We were excited to find that based on clinical observations, hematology, and gross and microscopic examination, complex **1.1** at the studied dosage can be considered minimally- to non-acutely toxic to rats over the initial two week period post-dose. No clinical signs of toxicity were observed throughout the period of the study, and healthy weight gain by all four rats was recorded. Blood was collected and analyzed on study days 7 and 14. There were no statistically significant deviations in the hematological and biochemical parameters measured on days 7 and 14 in comparison to the baseline measurements taken prior to the study.

Following euthanasia on day 14, necropsy was performed. The heart, lungs, liver, kidneys, spleen, thyroid and pituitary glands of each rat were observed to be grossly unremarkable. A very small adhesion between the ling and thoracic wall was observed in one rat, possibly reflecting a previous localized pleural inflammation. A small degree of variation was found among the organ weight for the four rats, and in comparison to the organ weights reported in a historical database.[241] Tissue samples from the brain, heart, lungs, liver, kidneys, spleen and thymus were examined histopathologically. Renal tubular necrosis was evident in kidney tissue harvested from three of the four rats, attributable to the administration of compound **1.1**. The necrosis spared the epithelial basement membrane of the affected tubules, allowing for repair by re-epithelialization instead of fibrosis and scarring, a characteristic typical of nephrotoxic injury. The amount of injury was very minimal, with less than approximately 1-2% of the renal tubules affected (Figure 2.14)

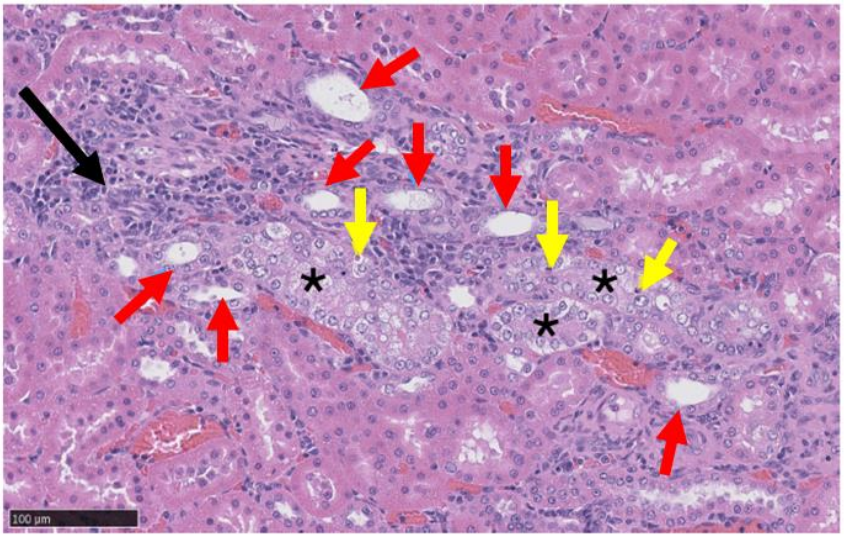

Figure 2.14 Evidence of renal cortical tubular necrosis and regeneration in a kidney of a rat following euthanasia 14 days after administration of compound **1.1**. The cortical tubules are lined with attenuated epithelial cells (red arrows) or large epithelial cells with open nuclei (asterisks). Individual dead epithelial cells (yellow arrows) are interspersed and the surrounding interstitium is expanded by a small number of lymphocytes and plasma cells (black arrow).

Like complex **1.1**, complex **7.1** displayed minimal to no acute toxicity during the first 8 days post-dosage, with no clinical observations of toxicity and no significant hematological or biochemical deviations noted during blood analysis on study days 1 and 8 in comparison to the baseline values recorded pre-study. Following euthanasia on day 8, necropsy was performed. The heart, liver, kidneys, spleen, thyroid and pituitary glands of each rat were observed to be grossly unremarkable. Six of the eight rats displayed minor pulmonary lesions: areas of subtle depression which were red/purple in colour, consistent with atelectasis, or partial lung collapse. However, these lesions may have

resulted from the euthanasia process: during exsanguination under isoflurane anesthesia, respiration is slow and shallow. Histopathological analysis of the tissue samples from the liver, kidneys, lungs, spleen and brain of two rats were examined histopathologically. No significant lesions were observed in the liver, spleen and brain samples. Renal tubular necrosis was evident in kidney tissue harvested from one of the two rats, similar in scope (1-2%) to that observed after administration of compound **1.1**; and similar epithelial regeneration had occurred

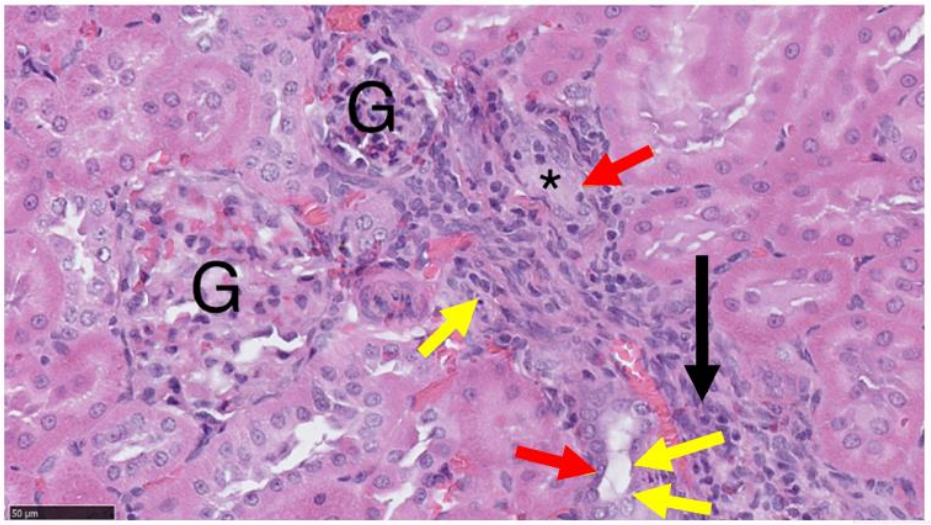

Figure 2.15 Evidence of renal cortical tubular necrosis and regeneration in a kidney of a rat #8, following euthanasia 8 days after administration of compound **7.1**. The cortical tubules are lined with attenuated epithelial cells (red arrows) and some contain luminal protein (asterisk). A few dead epithelial cells (yellow arrows) are interspersed and a small number of lymphocytes and macrophages expand the surrounding intertitium (black arrow). (G = glomeruli.)

2.6.2 Imaging

The *in vitro* contrast potential of **1.1** (Mn^{II}-N_5), **2.1** (Mn^{II}-N_5) and **7.1** $(Mn^{II}\text{-}N_3O_2)_2$ were studied via the collection of fast-spin-echo images for 30-45 minutes immediately following injection of an aqueous solution of each complex. The dosage chosen for **1.1** was 0.02 mmol/kg (c = 12.5 M) while the dosage chosen for **2.1** and **7.1** was 0.01 mmol/kg (c = 6.25 mM).

Predominantly T_1-weighted scans with some T_2-weighting were performed on two rats injected with **1.1** (Mn^{II}-N_5). The compound was observed to appear in the bladder within 5 minutes (Figure 2.16). A slow increase in the renal cortical signal was apparent over the first 45 minutes (

Figure **2.17**), along with a gradual liver hypoenhancement (darkening), reflecting an increase in T_2 relaxivity in this organ.

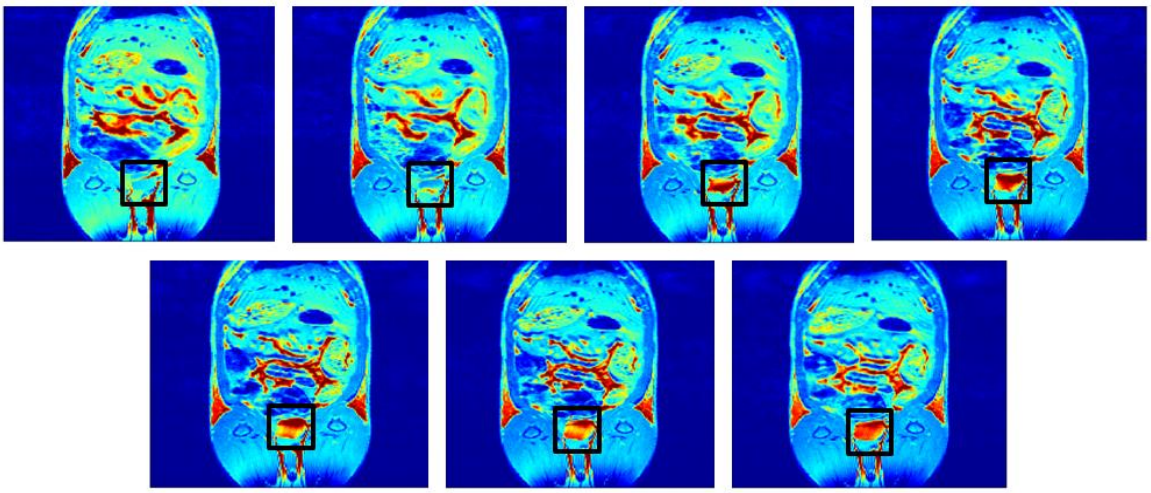

Figure 2.16 Coronal slices at the level of the bladder, showing enhancement due to complex **1.1** (Mn^{II}-N_5). Top left to right: 0, 2, 10, 15; bottom left to right: 20, 30, 45 mins.

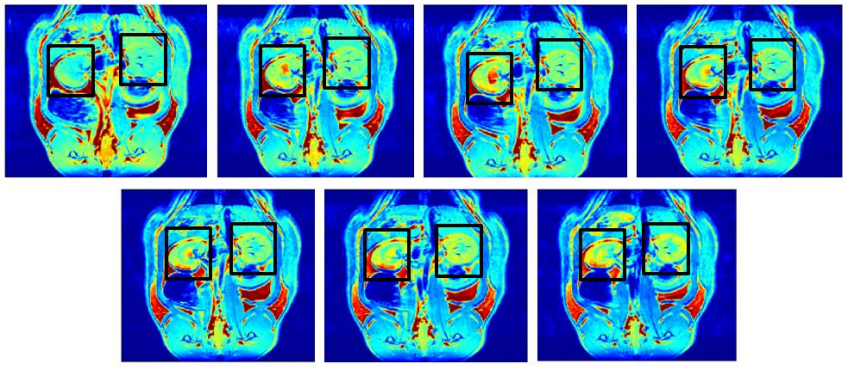

Figure 2.17 Coronal slices at the level of the kidneys, showing enhancement due to complex complex **1.1** (Mn^{II}-N_5). Top left to right: 0, 2, 10, 15; bottom left to right: 20, 30, 45 mins.

The signal alteration can be quantified by the mean voxel intensities measured in each tissue. The time point at which the maximum intensity difference was observed is bolded in Table 2.9, along with the change as a percentage of the initial intensity. The signal alteration is also visually represented in Figure 2.18.

Minutes	**-10**	**2**	**10**	**20**	**30**	**45**	**Max. intensity change**
Renal cortex	579.1	635.2	683.4	717.0	775.4	**804.1**	***39%***
Renal medulla	480.8	**608.9**	561.8	502.9	512.6	520.6	***27%***
Renal pelvis	465.7	881.1	**920.7**	733.9	704.7	666.1	***98%***
Liver	498.6	458.8	436.2	424.5	398.0	**369.8**	***-26%***
Bladder	414.3	454.3	1093.1	1046.4	970.1	1030.1	***177%***
Skeletal muscle	432.1	358.5	354.3	337.5	**330.6**	351.0	***-23%***

Table 2.8 Change in MRI signal intensity (arbitrary units of voxel intensity) in various tissues following injection of **1.1** (Mn^{II}-N_5).

Figure 2.18 Change in MRI signal intensity over the first 45 minutes post-injection of **1.1** (Mn^{II}-N_5). The baseline scan was collected at t = 10 mins.

Scans collected 3 hours post-injection showed no evidence of **1.1** (Mn^{II}-N_5) being retained by any tissue or organ at this time point, indicating rapid excretion.

Both T_1- and T_2-weighted scans were performed on two rats injected with **2.1** (Mn^{II}-N_3O_2) and its dimeric analogue **7.1** [(Mn^{II}-N_3O_2)$_2$] respectively.

T_1-weighted scans showed both compounds appearing in the bladder within 10 minutes, with **2.1** (Mn^{II}-N_3O_2) appearing before **7.1** [(Mn^{II}-N_3O_2)$_2$], suggesting slightly faster excretion of this monomeric system. Interestingly, while both complexes cause an increase in signal intensity in the renal medulla (Figure 2.20, Figure 2.19), compound **2.1** (Mn^{II}-N_3O_2) causes an enhancement in the renal cortex and has negligible effect on liver and lean muscle tissue; while **7.1** [(Mn^{II}-N_3O_2)$_2$] causes a decrease in signal intensity in

all three of these tissues. These results are summarized in Table 2.9 – Table 2.10 and Figure 2.21 – Figure 2.22.

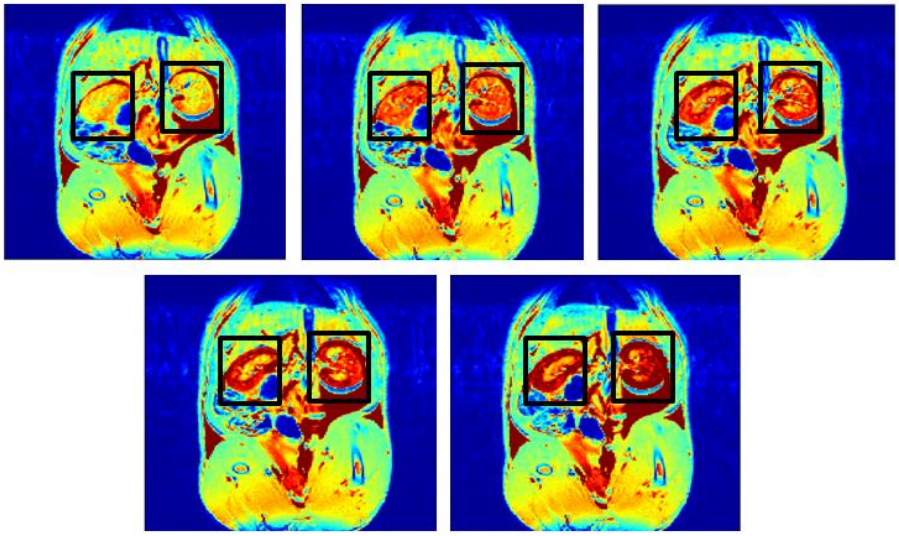

Figure 2.19 Coronal slices at the level of the kidneys, showing enhancement of the T_1-weighted MRI signal due to complex **2.1** (Mn^{II}-N_3O_2). Top left to right: -10, 0 15; bottom left to right: 30, 44 mins.

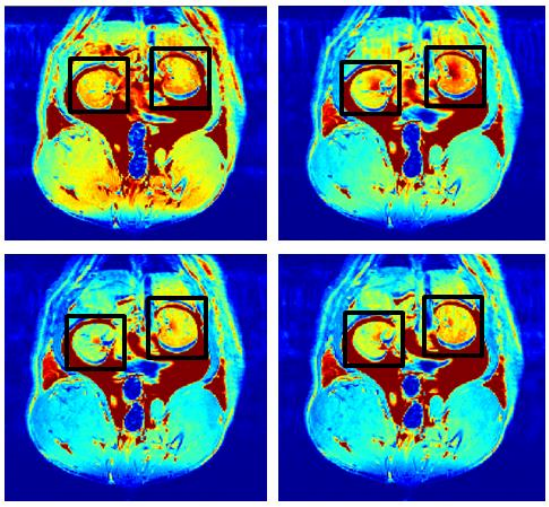

Figure 2.20 Coronal slices at the level of the kidneys, showing enhancement of the T_1-weighted MRI signal due to complex **7.1**[(Mn^{II}-N_3O_2)$_2$]. Top left to right: -10, 1; bottom left to right: 16, 29 mins.

Minutes	-10	1	15	30	45	Max. intensity change
Renal cortex	8005	9368	10144	10702	**11485**	***43%***
Renal medulla	7725	**9169**	8472	7969	8615	***19%***
Liver	7276	7568	7385	**7812**	7683	***7%***
Bladder	5085	5155	**16182**	11996	13104	***218%***
Lean muscle	5640	**5841**	5696	5569	5574	***3%***
Fat	14509	15671	15845	15745	**15860**	***9%***

Table 2.9 Change in T_1-weighted MRI signal intensity (arbitrary units of voxel intensity) in various tissues following injection of **2.1** (Mn^{II}-N_3O_2).

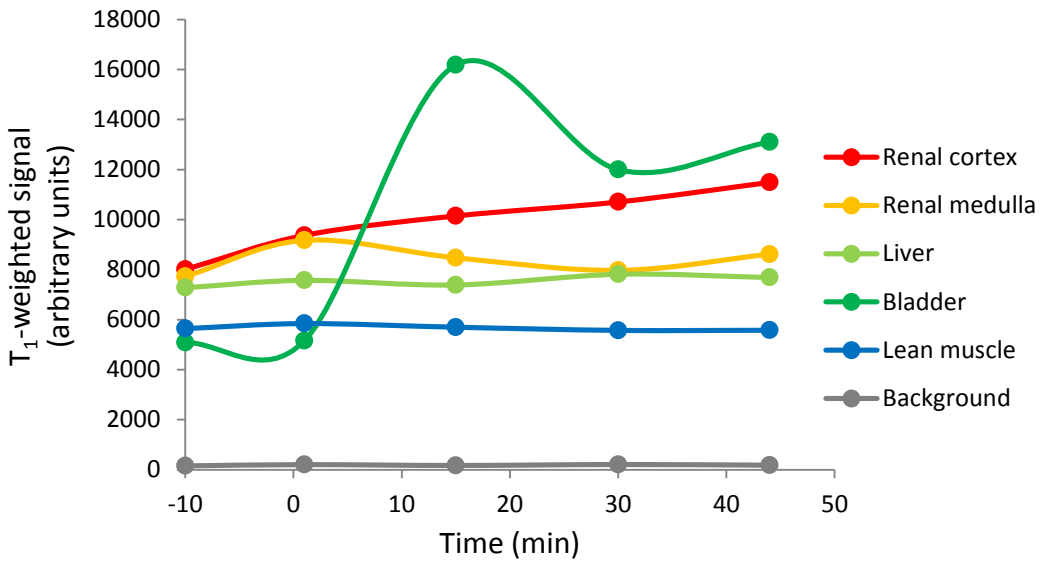

Figure 2.21 Change in T_1-weighted MRI signal intensity over the first 45 minutes post-injection of **2.1** (Mn^{II}-N_3O_2). The baseline scan was measured at t = 10 mins.

Minutes	-10	1	16	29	Max. intensity change
Renal cortex	8324	7160	**6355**	7030	***-24%***
Renal medulla	7439	**9222**	7008	7345	***24%***
Liver	7948	6234	**5508**	5838	***-31%***
Bladder	6374	4991	8171	**10143**	***59%***
Lean muscle	6710	4720	4284	**4095**	***-39%***
Fat	16614	**12834**	13248	13001	***-23%***

Table 2.10 Change in T_1-weighted MRI signal intensity (arbitrary units of voxel intensity) in various tissues following injection of **7.1**[$(Mn^{II}\text{-}N_3O_2)_2$].

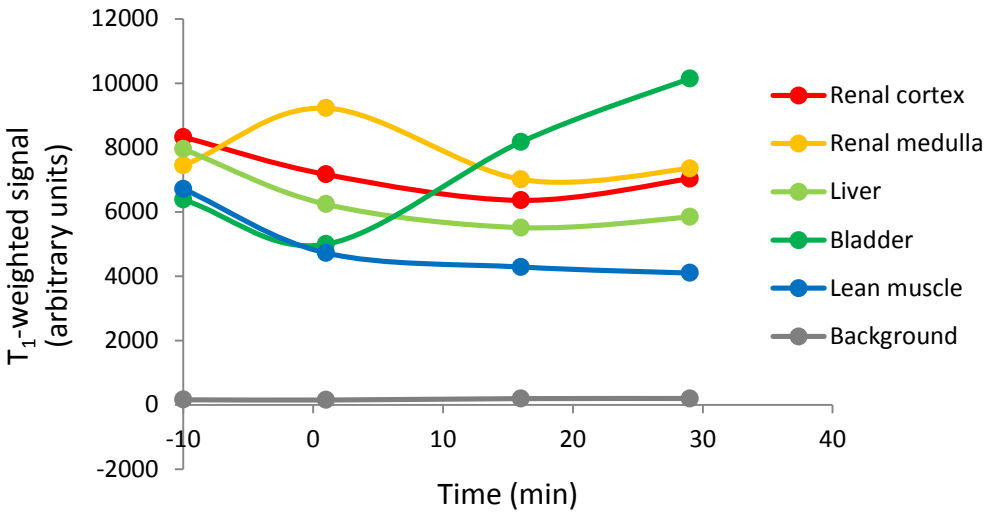

Figure 2.22 Change in T_1-weighted MRI signal intensity over the first 30 minutes post-injection of **7.1** [$(Mn^{II}\text{-}N_3O_2)_2$]. The baseline scan was measured at t = 10 mins.

T_2-weighted scans showed a decrease in signal intensity in the bladder, as well as kidney, liver and muscle tissue over the 30-40 minutes following injection of each compound (Figure 2.23). The hypoenhancement due to **7.1** [$(Mn^{II}\text{-}N_3O_2)_2$] was greater than that due to **2.1** ($Mn^{II}\text{-}N_3O_2$), unsurprising given that the compounds were administered at equimolar concentrations and **7.1** contains double the number of metal centers (Figure 2.24-Figure 2.25; Table 2.11-Table 2.12)

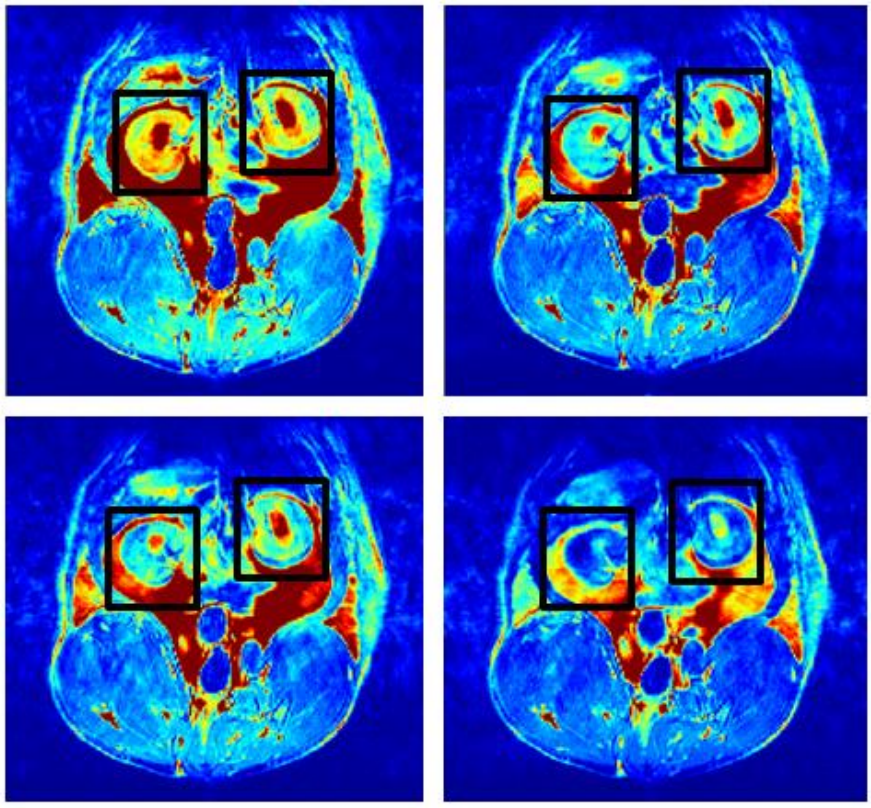

Figure 2.23 Coronal slices at the level of the kidneys, showing hypoenhancement of the T_2-weighted MRI signal due to complex **7.1** [$(Mn^{II}\text{-}N_3O_2)_2$]. Top left to right: -10, 9; bottom left to right: 22, 35 mins.

Minutes	-10	8	22	37	Max. intensity change
Renal cortex	4759	3367	3307	**3034**	***-36%***
Renal medulla	6454	5342	5306	**4215**	***-35%***
Liver	965	788	577	**400**	***-59%***
Bladder	12921	7977	667	**512**	***-96%***
Lean muscle	2673	2386	2451	**2377**	***-11%***
Fat	14834	14550	**12923**	13440	***-13%***

Table 2.11 Change in T_2-weighted MRI signal intensity (arbitrary units of voxel intensity) in various tissues following injection of **2.1** (Mn^{II}-N_3O_2).

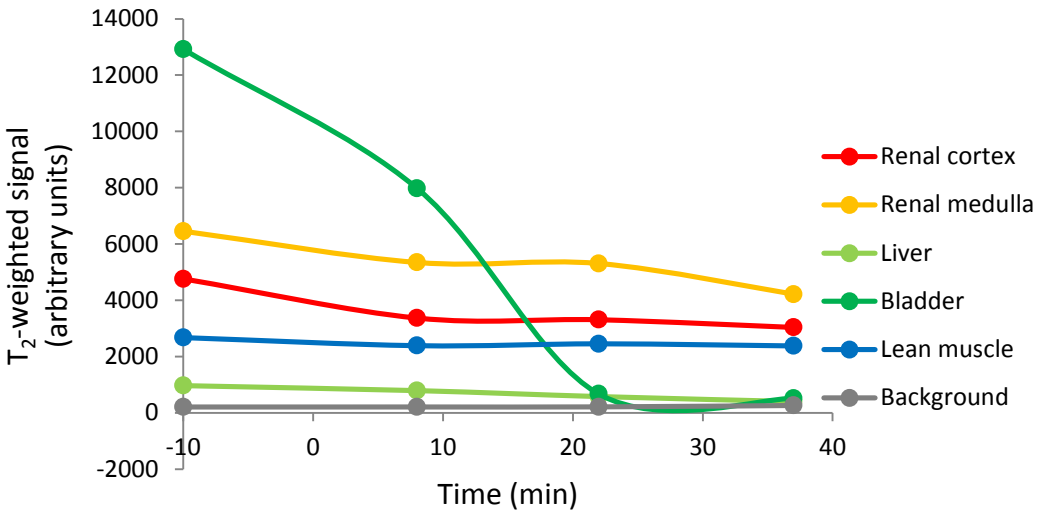

Figure 2.24 Change in T_2-weighted MRI signal intensity over the first 40 minutes post-injection of **2.1** (Mn^{II}-N_3O_2). The baseline scan was measured at t = 10 mins.

Minutes	-10	1	16	29	Max. intensity change
Renal cortex	7718	4270	4640	**2963**	***-62%***
Renal medulla	12041	7869	7063	**2770**	***-77%***
Liver	739	588	498	**408**	***-45%***
Bladder	16247	14484	13169	**10727**	***-34%***
Lean muscle	3053	2707	2399	**2063**	***-32%***
Fat	15094	9718	10027	**8525**	***-44%***

Table 2.12 Change in T_2-weighted MRI signal intensity (arbitrary units of voxel intensity) in various tissues following injection of **7.1** $[(Mn^{II}\text{-}N_3O_2)_2]$.

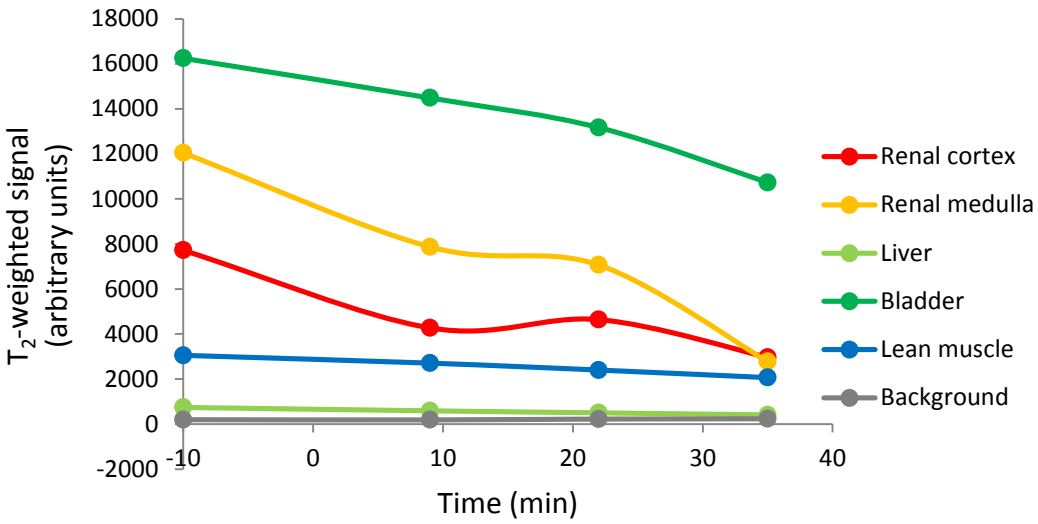

Figure 2.25 Change in T_2-weighted MRI signal intensity over the first 40 minutes post-injection of **7.1** $[(Mn^{II}\text{-}N_3O_2)_2]$. The baseline scan was measured at t = 10 mins.

The results from these small pilot studies on the Mn^{II} complexes **1.1**, **2.1** and **7.1** were very promising, showing negligible toxicity, rapid excretion, and obvious MRI signal enhancement in each case.

2.7 Ongoing and future work

The two clear directions this research will take in the future involve: continuing *in vivo* studies on the extended family of compounds; and pursuing the development of dual-property ('second generation') contrast agents based on this family.

2.7.1 *In vivo* stability studies

To date, a pilot imaging study has been carried out on three of our family of potential agents (Mn^{II}-N_5, Mn^{II}-N_3O_2 and (Mn^{II}-$N_3O_2)_2$), and a pilot toxicity study has been performed on two of these (Mn^{II}-N_5 and (Mn^{II}-$N_3O_2)_2$). These very promising initial investigations confirmed that the complexes can enhance both T_1- and T_2-weighted signals *in vivo*, are rapidly excreted, and are minimally- to non-toxic at a clinical dosage. Similar studies will be performed on the remaining complexes in the family, including the Gd^{III} species, in order to identify the most promising candidates for more detailed study. Larger scale, GLP ('good laboratory practice') studies will then be performed in rodents for a full investigation of the biodistribution, excretion mechanism, and biological interactions / pharmacokinetics of the lead compound(s), as well as the longer term toxicity, and dose-responsive toxicity. In addition, a variety of MRI fields, scanning sequences and parameters will be tried, in order to determine the optimal conditions for the imaging of different tissues and organs

2.7.2 Bio-targeting: development of a model targeted complex

In parallel with pursuing *in vivo* studies, we were intrigued by the possibility of attaching a second functionality to the macrocycle, to allow for a 'second generation' of dual-property agents. Additional functionalities such as a bio-targeting group for directed contrast agent delivery; a therapeutic group, towards a 'theranostic' agent; or a moiety allowing for a second imaging modality, are all of current research interest. Recent examples include contrast agents targeted to specific proteins such as collagen for the detection of fibrosis,[242] serum albumin for angiography,[243] or fibrin for the selective imaging of thrombosis. The recently reported chitosan-functionalized magnetic graphene nanoparticle (CMG) is an example of a theranostic system with the potential to deliver both an iron oxide MRI contrast agent and an anti-cancer drug to a tumor site.[244] Dual-imaging species explored include fluorescence labelled agents,[245] and combination MRI/PET (positron emission tomography) agents.[246]

We proposed that the copper-catalyzed azide-alkyne cycloaddition (CuAAC) reaction could be utilized to attach a bio-active group to the macrocycle. The CuAAC 'click' reaction involves the reaction of an organic azide with a terminal alkyne, in the presence of a Cu^{I} catalyst. The product is a 1,4-substituted-1,2,3-triazole (Scheme 2.8).[247]

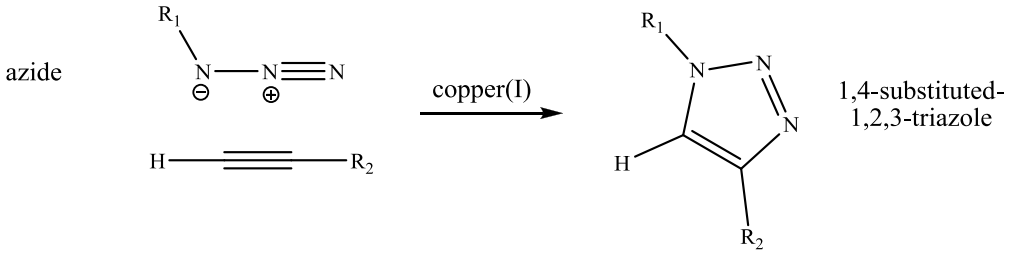

Scheme 2.8 The CuAAC 'click' reaction.

A ‘click’ reaction is a reaction which is powerful and reliable. To be classified as ‘click’, a reaction must be high yielding, stereospecific, and applicable to a wide range of starting materials. Solvents must be easily removable, products must be readily isolated, and there must be no offensive byproducts produced.[248] The CuAAC reaction qualifies as a ‘click’ reaction, and has its own particular advantages. The reaction is applicable to virtually any azide and alkyne pairing, is not affected by the electronic or steric properties of any groups which are attached, and produces a chemically stable triazole product.[247]

The backbone of macrocycles **L1** to **L6** includes a substituted pyridine head-unit. We proposed that if the diacetylpyridine building block could be functionalized with an azide group, then essentially any alkyne-functionalized unit could be ‘clicked’ on via the CuAAC reaction. In order to address these objectives, we developed a strategy for the synthesis of the key intermediate in this process: the novel azide 2,6-diacetyl-4-azidopyridine, **8e** (Scheme 2.9).

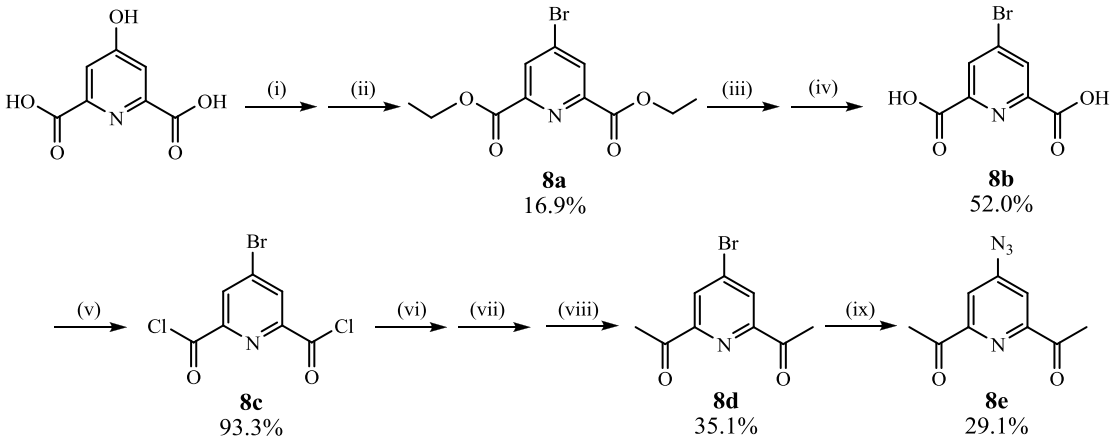

Scheme 2.9 Synthetic procedure for the synthesis of 2,6-diacetyl-4-azidopyridine, **8e**.[249-253] i) Br_2/PBr_3, 90°C, 3 h; ii) EtOH, r.t., 1 h.; iii) NaOH, H_2O, 115°C, 1 h., iv) HCl,

H_2O, r.t., 5 min., v) $SOCl_2$, DMF, reflux, 4 h.; vi) Meldrum's acid, pyridine, DCM, 0°C→r.t., 18 h., vii) HCl, H_2O, 0°C, 5 min., viii) acetic acid, H_2O, 115°C, 18 h., ix) NaN_3, DMF, 85°C, 48 h.

Following literature methodologies, commercially available chelidamic acid was treated with phosphorus pentabromide, formed *in situ* from bromine and phosphorus tribromide.[249] Subsequent treatment with methanol at 0°C yielded the dimethylester **8a**, which was subjected to basic hydrolysis to regenerate the carboxylic acid functionalities in **8b**,[250] which were then activated by conversion to the acyl chloride derivatives via reflux in thionyl chloride to give **8c**. To synthesize the rare bromodiketone **8d** we employed a tri-step procedure involving reaction with Meldrum's acid, HCl and acetic acid (Scheme 2.9)[251,252] which had not previously been applied to this starting material, to give **8d** with an overall yield of 35% after purification via a silica column with pet. ether/ethyl acetate (8:2).

Due to the explosive nature of organic azides, those used in the CuAAC reaction are not usually isolated. Rather, following formation of the azide, the species is reacted *in situ* with the desired terminal alkyne in the presence of a Cu^I catalyst. However, since the desired pyridyl azide **8e** was a new compound, we decided to isolate the species before carrying out the 'click' reaction. Conversion of the bromo-diketone **8d** to the desired azido-diketone **8e** was non-trivial. Formation of an azide for use in the CuAAC reaction is commonly carried out by a simple nucleophilic substitution, by the reaction of a chloro-, bromo- or iodo-species with NaN_3 in DMF. In fact, initially we had searched for a pathway which would allow the attachment of the bromide group to the pyridine head-

unit via an alkyl linker, for this very reason. The 4-position of a pyridine ring is activated with respect to nucleophilic substitution. However, the ketone substituents at the 2- and 6-positions have deactivating effect on this position. A key consideration was the extreme toxicity of sodium azide, as well as the explosive potential of both this species and any organic azides formed. Minimal exposure to heat, pressure, and chlorinated solvents was prioritized. We were able to synthesize the novel azide **8e** via nucleophilic substitution, by carefully heating a small quantity of **8d** with a large excess of sodium azide and monitoring the reaction progress using tlc.[253] The desired product was purified via column chromatography; degeneration on the column was possibly partially responsible for the low yield of 29%.

Preliminary ^{1}H and ^{13}C-NMR data was gathered on the new compound , and the proton and carbon spectra of **8d** and **8e** in d_6-acetone were compared. The singlet peak corresponding to the six ketone protons, H_1, remained at approximately the same chemical shift in both compounds (δ = 2.74 ppm for H_1 of **8d**, δ = 2.64 ppm for H_1 of **8e**). However the singlet corresponding to the aromatic proton H_4 shifted from δ = 8.26 ppm in the spectrum of **8d** to δ = 7.39 ppm in the spectrum of **8e** (deuterated acetone). This upfield shift indicates that the azido group is slightly less electron-withdrawing than the bromo substituent. A similar shift was observed for the peak corresponding to C_5 on each spectrum: the peak occurred at 135.5 ppm for **8d** but was shifted upfield to 126.0 ppm on the spectrum of **8e**.

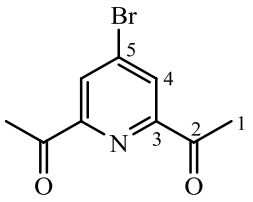

8d

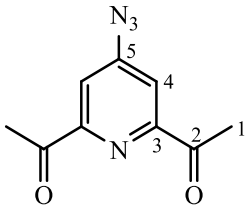

8e

Further characterization techniques were not carried out, due to the very low molecular weight of this azide, and the reported decomposition danger of dry, isolated organic azides with C/N ratios ≤ 3. This new organic azide is an important prescursor for the synthesis of a mononuclear contrast agent functionalized for targeting, therapy or dual-imaging. The next steps will be the 'clicking' on of a model alkyne such as ethynyltoluene (Figure 2.27, left) to establish the conditions necessary for the CuAAC reaction, and to provide proof of principle that the click will work with this building block; followed by the formation of a metal complex, using either Mn^{II} or Gd^{III}, and a diamine. Assuming a model click reaction occurs successfully, the attachment of more complex (bio)molecules will be investigated. For example, ethynylestradiol (Figure 2.27, center) is a commercially available, alkyne-functionalized synthetic estrogen mimic previously employed in click chemistry.[254,255] Functionalization of the macrocyclic backbone by the attachment of this compound should facilitate the passive targeting of breast cancer cells.[256] Other clickable functionalities with targeting potential include protein-targeted imaging probes such a 4,4′-diphenylcyclohexyl moiety which has been shown to bind to albumin for blood pool imaging to detect the presence of albumin in the lymphatics, tumour interstitium and in artherosclerotic plaque;[257,258] and as a fibrin-specific cyclic peptide, important for detecting blood clots.[259] Alkyne-functionalized species for dual-property imaging include commercially available water soluble

fluorescent probes such as boron-dipyrromethene (BODIPY, Figure 2.27, right) derivatives which have been previously appended to Gd^{III}-DOTA.[260]

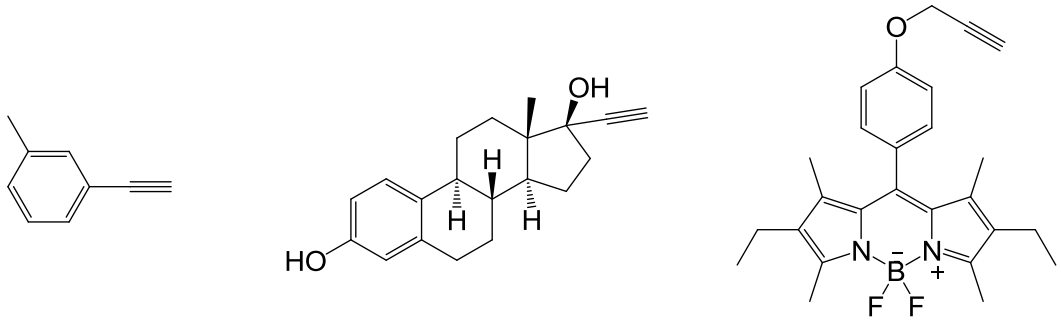

Figure 2.26 Left to right: model alkyne ethynyltoluene; the synthetic estrogen mimic ethynylestradiol; and the fluorescent moiety BODIPY.

2.8 Conclusion

During this project, a family of Mn^{II} and Gd^{III} complexes of N_3X_2 (X = NH, O) and N_3O_3 Schiff-base macrocycles were synthesized, characterized, and analyzed as potential contrast agents for MRI. Of the 8 proposed macrocyclic systems, 6 formed analytically pure complexes with Mn^{II} and 3 formed analytically pure complexes with Gd^{III}. The *in vitro* relaxivities of the soluble, pure complexes were studied at clinical magnetic fields, with very promising results: the Mn^{II} complexes, in particular, displayed relaxivities up to 7x as high as those of the best approved agent. A pilot *in vivo* toxicity and imaging study in rats on Mn^{II}-N_5 indicated that the complex displays negligible toxicity at the studied dosage; effectively enhances the kidneys, bladder and vasculature; and is fully excreted within 3 hours – an extremely encouraging result. Future directions

include ongoing *in vivo* studies, as well as the development of a dual-property agent for targeting, therapy, or bimodal imaging.

3 RESULTS AND DISCUSSION FOR PROJECT 2:

Dy^{III} complexes of Schiff-base macrocycles: towards mononuclear SMMs

3.1 Introduction

My second area of research involves working towards the development of a new family of mononuclear lanthanide single-molecule magnets (Ln-SMMs) with *pseudo-*D_{5h} geometries, formed via the templation of Schiff-base macrocycles around Dy^{III}. SMMs are compounds which exhibit slow relaxation of magnetization due to the presence of a large energy barrier (U_{eff}) between the two orientations of the electronic ground state. As was discussed in Section 1.2.4, the crystal field of a lanthanide ion plays a key role in the splitting of the M_J microstates, and thus in the size of U_{eff} for Ln-SMMs. Emerging principles of rational design in the field of L-SMMs include the simple electrostatic model of Long and co-workers, who postulated that the intrinsic anisotropy of oblate lanthanide ions such as Dy^{III} and Tb^{III} may be enhanced by axially-located charge density; while the anisotropy of prolate lanthanide ions such as Er^{III} may be enhanced by equatorially bound ligand charge density (discussed in more depth in Section 1.2.4).[117]

In addition, the size of U_{eff} is affected in a large way by the presence or absence, and the degree, of quantum tunneling: a phenomenon arising from the overlap of wave functions, which allows magnetic relaxation to occur 'through' rather than thermally 'over' the anisotropy barrier.[261] Suppression of quantum tunneling via structural design remains a key focus of synthetic magneto-chemists. As was succinctly described by Tong and co-workers, certain high-symmetry coordination environments have been

theoretically shown to allow for the control of quantum tunneling by the disappearance of certain terms (B^k_q) in the crystal field Hamiltonian ($\hat{H}_{CF} = \Sigma B^k_q \tilde{O}^k_q$, where $\tilde{O}^k_q$ are the Stephen operators).[104] These high-symmetry cases include $C_{\infty v}$, $D_{\infty h}$, S_8, D_{4d}, D_{5h}, and D_{6d}.[104] The D_{4d} geometry is ubiquitous in the field of Ln-SMMs, with an impressive number of *bis*(phthalocyanine) complexes with this symmetry displaying some of the highest reported energy barriers to date.[113,114]

Of the desirable high-symmetry geometries, one which is extremely rare amongst Ln-SMMs is the 7-coordinate *pseudo*-D_{5h} geometry. To the best of my knowledge there are only four examples in the literature of SMMs containing lanthanide ions in *pseudo*-D_{5h} geometries, including a dinuclear Dy_2 SMM[262] and two $M^{II}_2Dy^{III}$ complexes: a Zn_2Dy trimer and an Fe_2Dy trimer.[104,263] The two Dy^{III} centers in the asymmetric SMM reported by Powell both lie in pentagonal bipyramidal environments (Figure 3.1, right), with N_2O_5 and NCl_2O_4 donor sets respectively. Although at low temperatures, the observed slow relaxation is due to the exchange-coupling interaction between the dimeric centres, bridged by two O donors, at high temperatures, the SMM behaviour is due to the anisotropy of each ion acting individually. The relaxation process due to each ion in the high temperature regime is characterized by a separate relaxation time, and the energy barriers were found to be 198 and 150 K respectively. The Dy^{III} center in the Zn_2Dy complex reported by Tang undergoes a reversible change in coordination geometry upon desolvation, from 7-coordinate *pseudo*-D_{5h} (Figure 3.1, center) to 6-coordinate *pseudo*-O_h. [263] When the Dy^{III} is *pseudo*-D_{5h}, the complex behaves as an SMM with a high energy barrier of 439 K, and after the geometry change, the SMM behaviour is switched off.[263] When the two Zn^{II} ions are replaced with Fe^{II} ions to give an Fe_2Dy trimer, the energy

barrier of the resulting SMM increased to 459 K, due to the change in the immediate environment of the Dy^{III} ion when exchanging diamagnetic for paramagnetic ions.[104] This confirms the vital role that the coordination environment plays in SMM behaviour, as well as the ability of Dy^{III} ions in pentagonal bipyramidal environments to display significant anisotropy barriers. An additional example is a layered Er^{III} phosphonate structure which exhibits field-induced SMM behaviour.[264] The energy barrier U_{eff} was determined to be 34.8 K in an applied dc field of 0.1 T. Unlike the oblate Dy^{III} ion, Er^{III} is prolate, so these results are consistent with the theory of Long described above:[117] that a ligand environment providing equatorial electron density would enhance or confer SMM properties upon an Er^{III} system.

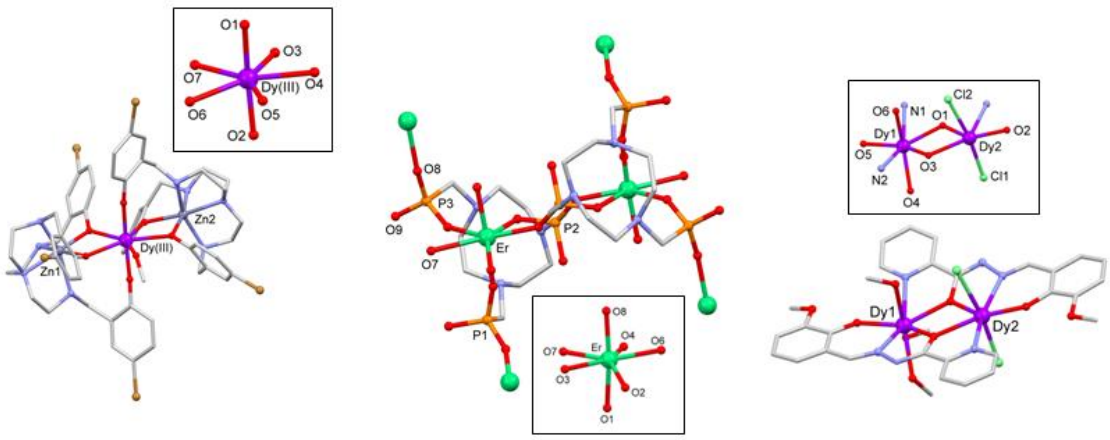

Figure 3.1 Crystal structures of: left, a Zn_2Dy SMM;[263] center, a layered erbium(III) phosphonate complex;[264] and right, a Dy_2 dimer[262] in which the Ln^{III} species have *pseudo*-D_{5h} geometry. Counter ions and non-coordinating solvent molecules are omitted for clarity.

With these exciting but rare examples in mind, we proposed that the templation of equatorially-binding Schiff-base macrocycles around lanthanide ions could confer such high symmetry coordination geometries upon the metal centers, and might afford a new family of mononuclear Ln-SMMs.

Macrocycles **L1** (N_5), **L2** (N_3O_2) and **L6** (dbN_3O_3) were selected as the target macrocycles for this study. The pentadentate macrocycles **L1** and **L2** were chosen due to their potential ability to confer *pseudo*-pentagonal bipyramidal geometry on the resulting complexes. These two macrocycles differ only in the nature of their donor atom sets (N_5 *vs.* N_3O_2), and thus should allow the effect of donor atom strength on the magnetic properties to be examined. The potentially hexadentate macrocycle **L6** was also selected for examination, in order to probe the effect of a larger cavity size and additional steric bulk on the properties of the resulting complex.

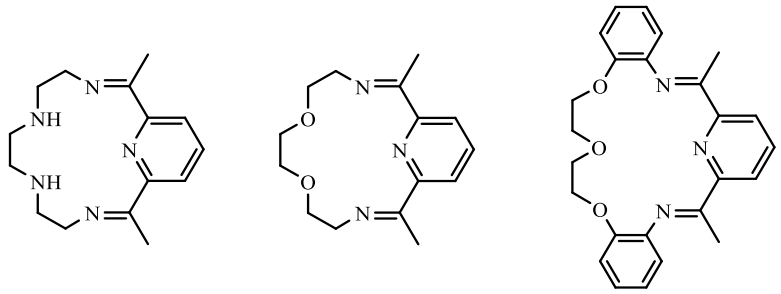

L1 **(N_5)** **L2** **(N_3O_2)** **L6** **(dbN_3O_3)**

Dy^{III} was chosen as the templating cation because it has a large inherent magnetic anisotropy, as well as 5 unpaired electrons, allowing for a high ground state M_J value of 15/2. As well, because it is a Kramers ion with an odd number of unpaired electrons, Dy^{III} always has a doubly degenerate ground state. In addition, the uniaxial anisotropy of

Dy^{III} has been shown to be enhanced by a *pseudo-*D_{5h} crystal field, in the examples given above.

Our objectives were therefore to ***template the formation of selected Schiff-base macrocycles around*** Dy^{III} ***and study the magnetic properties of the resulting complexes, as potential Ln-SMMs.***

3.2 Synthesis and characterization

In light of the successful metal templation reactions using Gd^{III} chloride salts detailed in Chapter 2, $DyCl_3 \cdot 6H_2O$ was chosen as the initial templating agent. The same general synthetic procedure outlined in Section 2.3 described for the synthesis of the Mn^{II} and Gd^{III} complexes was followed: stoichiometric amounts of the metal salt, diketone and diamine were refluxed in methanol, followed by precipitation and copious washing by diethyl ether.

Each of the three macrocycles was successfully templated around $DyCl_3 \cdot 6H_2O$, giving macrocyclic complexes **1.3** (Dy^{III}-N_5), **2.3** (Dy^{III}-N_3O_2) and **6.3** (Dy^{III}-dbN_3O_3) respectively as powders in low to average yields (20 – 50%). Key characterization data for the three complexes are summarized in Table 3.1, below.

Complex; Abbrev.	Molecular Formula		C	H	N	$\nu_{(C=N)}$ (cm^{-1})	λmax (ε) (nm, $L \cdot mol^{-1} \cdot cm^{-1}$)	Λ_M – MeOH ($S \cdot cm^2 \cdot mol^{-1}$)
1.3 **Dy^{III}-N_5**	$[Dy(\mathbf{L1})Cl_3]\cdot 4H_2O$	Found Calcd	29.76 29.33	4.91 5.09	10.87 11.40	1631	250 (6590) 281 (3820)	160.4
2.3 **Dy^{III}-N_3O_s**	$[Dy(\mathbf{L2})Cl_3]\cdot 6H_2O$	Found Calcd	27.94 27.62	4.92 5.10	6.39 6.44	1625	250 (5140) 274 (4050)	180.0
6.3 **Dy^{III}-dbN_3O_3**	$[Dy(\mathbf{L6})Cl_3]\cdot 6H_2O$	Found Calcd	37.94 37.89	4.44 4.71	4.95 5.30	1620	- 276 (4966)	125.6

Table 3.1 Summary of Dy^{III} complex characterization data: complex formulae, elemental analyses, IR and UV-visible spectroscopic data, and conductance measurements. Note: the formulae in Column 2 are not structural formulae denoting the coordination environment of the Dy^{III} centers; but rather, molecular formulae determined via elemental analysis.

The peaks corresponding to an imine stretch in the IR spectrum of each complex were found at ν = 1631 cm^{-1}, 1625 cm^{-1} and 1620 cm^{-1} for **1.3** (Dy^{III}-N_5), **2.3** (Dy^{III}-N_3O_2) and **6.3** (Dy^{III}-dbN_3O_3) respectively, consistent with the values reported for similar rare earth complexes of Schiff-base macrocycles.[137,265] The importance of the IR data cannot be overstated, as it provides evidence for the formation of the macrocyclic ring, templated by the metal ion, and for the absence of amine and ketone starting materials. A representative IR spectrum is presented in Figure 3.2 for the Dy^{III}-N_5 complex **1.3**.

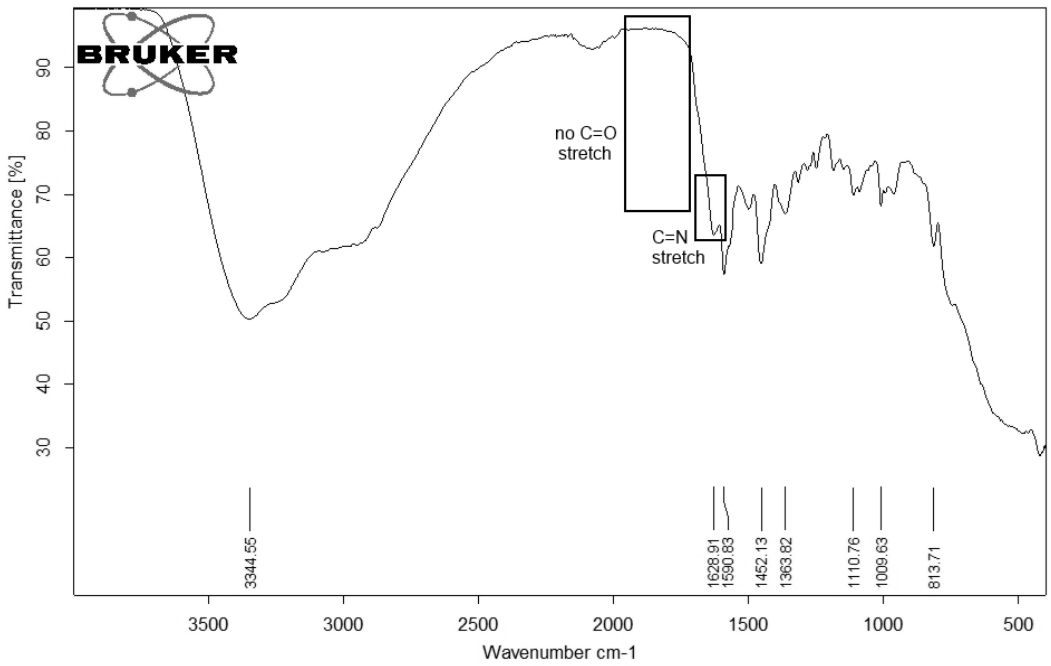

Figure 3.2 IR spectrum of **1.3** (Dy^{III}-N_5), showing the absence of a C=O stretch corresponding to the ketone starting material, and the presence of a C=N stretch for the Schiff-base macrocycle.

The elemental analysis data for **1.3** (Dy^{III}-N_5) fit for the presence of three chloride ions and four H_2O molecules, with a maximum difference of 0.53% for nitrogen. This offers a significant improvement over the attempted synthesis of this complex by Radecka-Paryzek and co-workers in 1998, for which a maximum difference of 2.4% was reported.[137] The elemental analysis data for complexes **2.3** (Dy^{III}-N_3O_2) and **6.3** (Dy^{III}-dbN_3O_3) fit for three chloride ions and six H_2O, and were both within the acceptable +/- 0.4% limit for C, H and N. Both of these complexes are previously unreported.

The mass spectrum of **1.3** (Dy^{III}-N_5) displays a peak at *m/z* = 471 assigned to $[M\text{-}H\text{-}2Cl]^+$. The mass spectrum of **2.3** (Dy^{III}-N_3O_2) displays a peak at *m/z* = 297 assigned to

[**L2**+Na]$^+$, while the most intense peak in the spectrum of **6.3** (Dy^{III}-dbN_3O_3) corresponded to [**L7**+H]$^+$. Similar macrocycle-only peaks were reported in the mass spectra of Ln^{III} complexes of the related 19-membered N_5 Schiff-base macrocycle.[266] The UV-visible spectra of all three complexes show maximum absorption bands at λ = 250-280 nm, once again corresponding to the π to π^* electronic transition of the macrocyclic ligand in each instance. The absorption bands are consistent with those for the corresponding Gd^{III} complexes described in Chapter 2. A representative UV-visible spectrum is shown below (Figure 3.3) for the Dy^{III}-N_5 complex **1.3**.

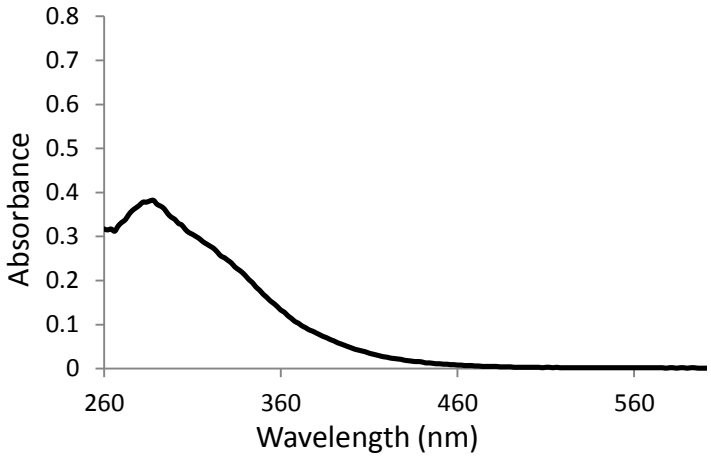

Figure 3.3 UV-visible spectrum of **1.3** in MeOH showing λ_{max} at 288 nm, corresponding to the π to π^* transition of the macrocyclic ligand.

From this data we can therefore conclude that the three Dy^{III} complexes **1.3** (Dy^{III}-N_5), **2.3** (Dy^{III}-N_3O_2) and **6.3** (Dy^{III}-dbN_3O_3) have been successfully isolated as pure solids.

In the field of molecular magnetism, having a specific knowledge of the coordination geometry, bond lengths, and bond angles present in a (para)magnetic

complex is very important, in order to draw conclusions about the relationship between structure and magnetic behaviour. Numerous attempts were made to crystallize the three Dy^{III} complexes described above. Solutions of the complexes in methanol, ethanol, and DCM were used, in various concentrations. Solvents including diethyl ether, pentane, hexane, THF, acetone, toluene, acetonitrile and mixtures of these were layered over the complex solutions, or allowed to vapour-diffuse into the complex solutions at various rates. Vials, test tubes, and H-tubes were utilized. The crystallizations were carried out at room temperature and in the refrigerator.

In spite of my best attempts, no X-ray quality crystals of these complexes have yet been grown. For this reason we decided to template the macrocycles around alternative Dy^{III} salts, thinking that different anions might favour the growth of single crystals due to a more efficient solid state packing of the anions in the crystal lattice. Following this methodology, perchlorate, triflate and nitrate salts of Dy^{III} were also employed to template the formation of each macrocycle. Templating the macrocycles around these salts resulted in solids which were much more difficult to isolate as pure samples: the only compound which could be isolated pure was $[Dy(\mathbf{L6})(OTf)_3]\cdot 6H_2O$ (**6.4**), the triflate derivative of Dy^{III}-dbN_3O_3 (**6.3**). As previously described, the complex was characterized first by IR spectroscopy and displayed the characteristic imine stretch at 1653 cm^{-1}. The elemental analysis of **6.4** (Dy^{III}-dbN_3O_3-OTf) indicated the presence of three triflate anions and six H_2O molecules within the acceptable +/-0.4% difference. The mass spectrum showed a peak at *m/z* = 289 corresponding to $[\mathbf{L6}+H]^+$. Unfortunately, attempts to crystallize **6.4** also met with no success; thus, our attention remained focused on the original three complexes Dy^{III}-N_5 (**1.3**), Dy^{III}-N_3O_2 (**2.3**) and Dy^{III}-dbN_3O_3 (**6.3**).

As was discussed in Chapter 2 (Section 2.3.2), crystal structures of rare earth complexes of 15- to 18-membered [1+1] Schiff-base macrocycles are extremely rare. Concerted efforts to synthesize rare earth complexes of these macrocycles by two research groups in particular have yielded very few crystalline compounds.[137,138] Given the lack of structural information in the literature, we attempted to examine the crystallinity of our compounds by *powder diffraction*. The diffraction pattern for **1.3** (Dy^{III}-N_5) is shown in Figure 3.4, and reveals no well-resolved features out to 33.5°, consistent with its amorphous nature. The powder patterns for complexes **2.3** (Dy^{III}-N_3O_2) and **6.3** (Dy^{III}-dbN_3O_3) were very similar, and we thus concluded that all three complexes were amorphous, which accounts for the difficulties faced when trying to grow single crystals of this family of complexes.

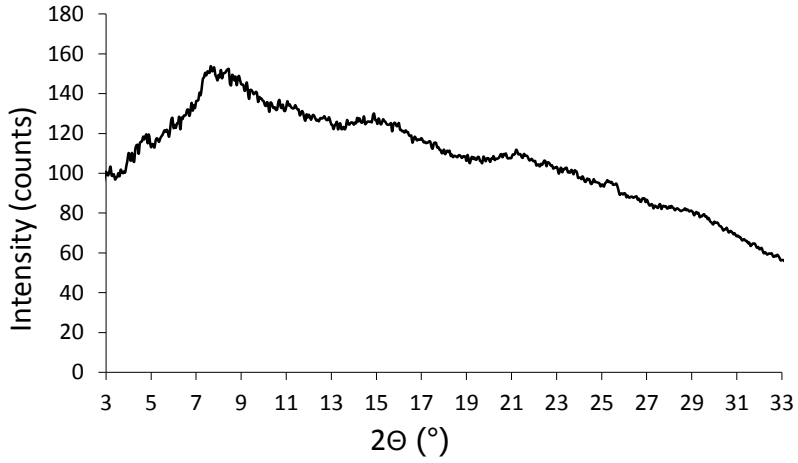

Figure 3.4 Powder diffraction pattern for **1.3** (Dy^{III}-N_5), showing the amorphous nature of the complex. Data were collected at room temperature in the range $2.5 < 2\theta < 33.5^{\circ}$, and were recorded in 0.05° steps using Cu-Kα_1 radiation (λ = 1.54187 Å) with the tube operating at 40 kV and 40 mA with an initial beam diameter of 0.5 mm.

In Chapter 2, our key structural concern was confirming the ability of the macrocycles to bind in an equatorial fashion around Mn^{II} and Gd^{III}, allowing for axially-bound waters and high relaxivity. For the Dy^{III} complexes in this chapter, our structural concern is determining whether the two pentadentate macrocycles N_5 and N_3O_2 give rise to *pseudo*-pentagonal bipyramidal complexes when coordinated to Dy^{III}; and to gain insight into the potential coordination environment of Dy^{III} in the larger, rigid macrocycle dbN_3O_3. We thus turned our attention once again to an analysis of related structures in the literature.

As noted earlier, two related lanthanide complexes for which the crystal structures have been measured are the Lu^{III} and Yb^{III} complexes of the 16-membered N_5 macrocycle p-N_5 (Figure 3.5, left), formed from a mixture of the chloride and perchlorate salts of each ion.[228-230] In both cases, the lanthanide ions adopt a 7-coordinate, pseudo-D_{5h} geometry, with the macrocycle coordinating in the equatorial plane, and two axially bound chloride ions. The flat nature of the macrocycle is confirmed by the near co-planarity of the N_5 donor set, and each lanthanide ion is very slightly displaced from the N_5 plane by 0.114(2) and 0.104(2) Å for Yb^{III} and Lu^{III} (Figure 3.5, right) respectively.

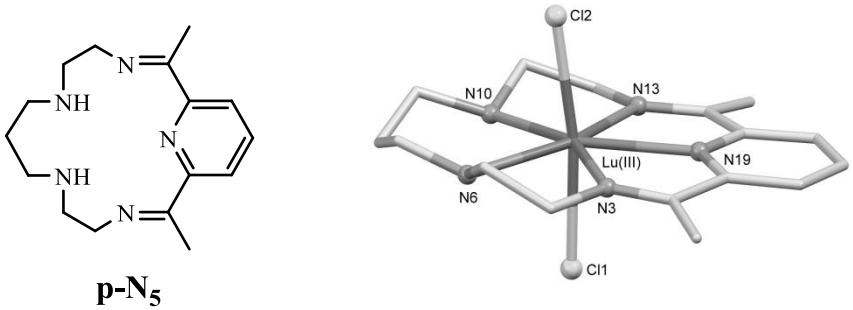

p-N_5

Figure 3.5 Left, 16-membered N_5 macrocycle; right, the crystal structure of the 7-coordinate Lu^{III} complex.[228]

This literature evidence confirmed that a lanthanide ion could accept an equatorial N_5 donor set, along with at least two axial ligands. In addition, a crystal structure of a *pseudo*-D_{5h} Cd^{II} complex in which the metal ion is bound to a 15-membered N_5 macrocycle[231] indicates that an even larger cation than Dy^{III} can coordinate in the plane of a macrocycle of this size. We thus propose that macrocycles **L1** and **L2** coordinate equatorially, via their full N_5 and N_3O_2 donor sets, acting as pentadentate ligands.

However, the coordination of the dbN_3O_3 macrocycle **L6** is less straightforward. There are no published crystal structures of complexes of **L6**, and the few reports of complexes of this macrocycle refrain from postulating on the binding mode of the macrocycle.[138] However, a search of the literature yields several related complexes which shed some light on this question.

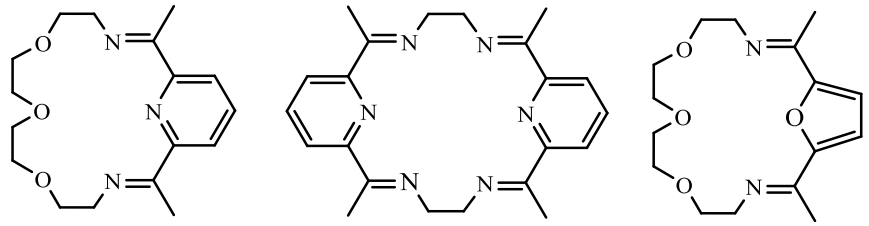

Figure 3.6 Macrocycles discussed in this section.

There are a number of hexadentate macrocyclic ligands, with 18-membered backbones, which coordinate in a planar fashion to lanthanide ions, as well as alkali earth metals with larger ionic radii than Dy^{III}. The $La(NO_3)_3$ complex of **L5**, the flexible analogue of **L6**, has been reported (Figure 3.7, left).[233] The macrocycle coordinates in a hexadentate fashion, and although it binds equatorially, the macrocycle is puckered:

dihedral angle between the planes defined by the three N donors and La, and the three O donors and La, is 135.38º. The remaining 6 positions of the lanthanum coordination sphere are filled with donor O atoms from the three nitrate counter ions. Although **L6** is more rigid than **L5**, due to the substituent benzo groups, so is unlikely to pucker in the same way, this demonstrates that an 18-membered N_3O_3 Schiff-base macrocycle can coordinate to a lanthanide equatorially. Further evidence for this was provided by Hursthouse and co-workers, who reported lanthanide complexes of an 18-membered N_6 macrocycle, **[2+2]N_6** (Figure 3.6) .[234] The La^{III}, Ce^{III} and Nd^{III} complexes of this [2+2] Schiff-base macrocycle were described (Figure 3.7, center). In each case, the macrocycle binds in a hexadentate fashion. Again, the macrocycle is puckered, with a fairly large interplanar angle of 26.7 – 73.9° observed between each N_3-Ln plane. The angle increases as the ionic radii of the lanthanide decreases, presumably in order to optimize the Ln-N bond lengths. Since this is a [2+2] Schiff-base macrocycle, it is not completely analogous to **L6**, but does serve to suggest that to the extent that puckering is possible in the more rigid **L6** macrocycle, this macrocycle will likely fold slightly to accommodate the smaller Dy^{III} ion.[234]

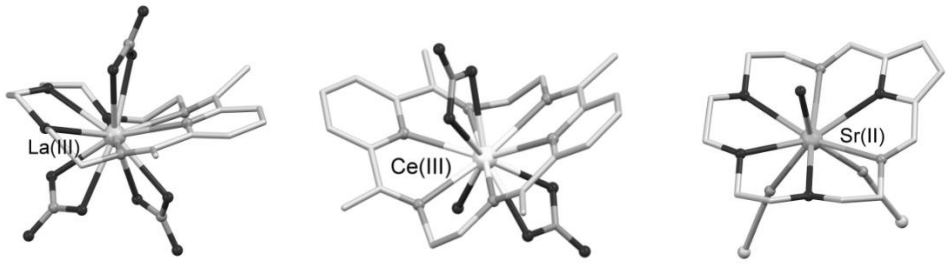

Figure 3.7 Left, the La^{III} complex of **L5**;[233] center, the Ce^{III} complex of **[2+2]N_6**;[234] right, the Sr^{II} complex of **f-N_2O_4**.[235]

Fenton and co-workers report structures of the 18-membered N_2O_4 furan-based analogue of **L5**: **f-N_2O_4** (Figure 3.6).[235] The macrocycle is templated around the alkali earth metals Ca^{II}, Sr^{II} and Ba^{II}, in each case binding in a hexadentate fashion. Interestingly, Ca^{II} (1.00 Å)[267] lies in the plane of the ring, and the two thiocyanates bind in a 'trans' conformation, occupying the two axial positions affording an 8-coordinate geometry. In contrast, the larger Sr^{II} and Ba^{II} cations (1.16 and 1.36 Å respectively)[267] lie very slightly out of the plane of the macrocyclic ring, and the two thiocyanate ions bind in a 'cis' conformation on the out-of-plane side of the cation, with a water bound in the other axial position, conferring 9-coordinate geometry on the cations (Figure 3.7, right).[235] This report further demonstrates that ions with larger radii than Dy^{III} may still be equatorially bound by 18-membered, hexadentate [1+1] Schiff-base macrocycles. Hence it seems probable that the full N_3O_3 donor set of **L6** coordinates equatorially to the Dy^{III} in complex **6.3**.

In light of these related structures, we are confident that the N_5 (**L1**) and N_3O_2 (**L2**) macrocyclic systems can support a pentagonal bipyramidal geometry by binding in a pentadentate, equatorial fashion to Dy^{III}. The larger macrocycle dbN_3O_3 is also likely to bind equatorially, in a hexadentate fashion. In order to shed more light on the proposed 7-coordinate geometry of Dy^{III}-N_5 and Dy^{III}-N_3O_2, and to gain further information about the structure of Dy^{III}-dbN_3O_3, several techniques were employed.

Given the intrinsic problem of a lack of single crystal data, we turned to other means to aid in the structural elucidation. Although imine bond formation was confirmed via IR measurements, and the formulae were elucidated by elemental analysis, these

techniques do not allow for a determination of the number and nature of axial ligands bound to the metal centre. Several additional techniques were thus employed to elucidate the coordination geometries of the three complexes, including thermogravimetric analysis, conductance measurements, and Raman and far-IR spectroscopy.

Thermogravimetric analysis or TGA, was utilized in order to glean information concerning the nature of the chloride anions and water molecules (coordinating *vs.*non-coordinating) determined to be part of the formula unit by elemental analysis. TGA data was gathered on the two pentadentate systems: **1.3** (Dy^{III}-N_5) and **2.3** (Dy^{III}-N_3O_2), and is presented in Figure 3.8.

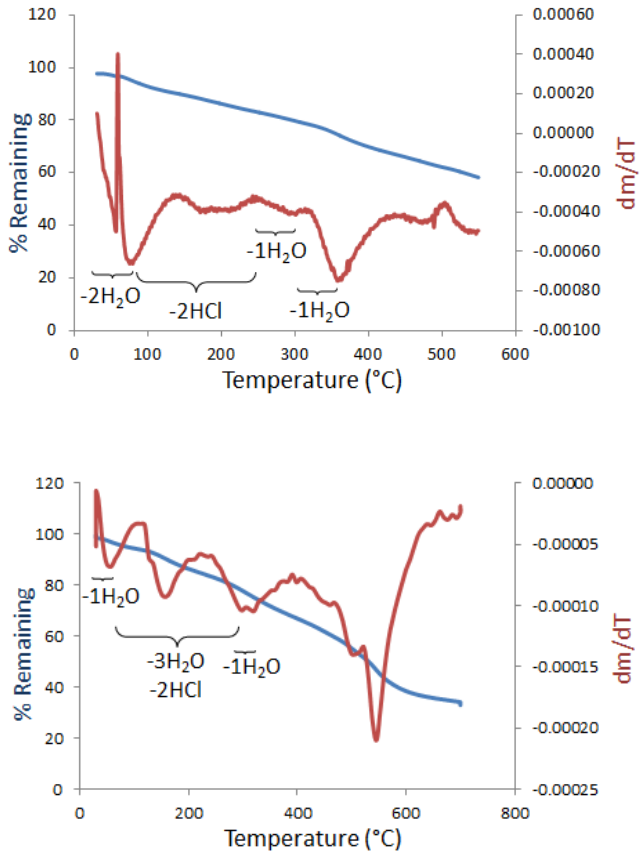

Figure 3.8 TGA plots for complex **1.3** (Dy^{III}-N_5, top) and **2.3** (Dy^{III}-N_3O_2, bottom).

The TGA plot for complex **1.3** (Dy^{III}-N_5) shows the loss of three water molecules and two chloride ions (as HCl) below 300°C, suggesting non-coordination of these species. The varying temperatures at which the water molecules leave may correspond to weakly bound lattice solvent *vs.* strongly hydrogen-bonded water molecules. An additional water molecule is lost by 400°C, which we postulate to indicate coordination of this molecule. The third chloride ion is not observed to leave, again indicative of coordination. The TGA plot for complex **2.3** (Dy^{III}-N_3O_2) shows very similar behaviour: four water molecules and two chloride ions (as HCl) are lost below 300°C, with an additional water molecule, likely to be coordinated, lost by 350°C, and one chloride ion not observed to leave. Thus the TGA data is consistent with the present of one bound chloride and one bound water molecule in each complex.

Conductance measurements have historically been utilized to gain insight into the number of bound versus unbound counter ions in coordination complexes, particularly before X-ray crystallography became routine as a characterization method. In their original series on pentadentate Schiff-base macrocycles, Nelson and Drew utilized conductance measurements in poorly coordinating organic solvents to justify their conclusions regarding the coordination geometry of the complexes, under the assumption that the electrolytic behaviour of a complex in such a solvent would reflect its structure in the solid state.[208-213] In particular, conductance has been very successfully employed to help determine the 7-coordinate geometry of transition metal complexes; an important example is the predicted pentagonal bipyramidal geometry of the Fe^{II} complex studied in

detail for its spin crossover properties;[132] a postulation which was proven correct decades later by single crystal X-ray diffraction.[133]

Following literature precedence for this family of systems,[208-213] conductance measurements were carried out on 0.5 mM solutions of the complexes in both water and methanol. The average molar conductivities (Λ_M) of the three complexes in each solution are presented in Table 2.3.

Complex	Formula	Λ_M (MeOH)	Λ_M (H_2O)
1.3 Dy^{III}-N_5	[Dy(**L1**)Cl_3]·4H_2O	160.4	313.8
2.3 Dy^{III}-N_3O_2	[Dy(**L2**)Cl_3]·6H_2O	180.0	319.6
6.3 Dy^{III}-dbN_3O_3	[Dy(**L6**)Cl_3]·6H_2O	125.6	300.6

Table 3.2 Summary of molar conductivity values ($S \cdot cm^2 \cdot mol^{-1}$) in MeOH and aqueous solutions at 25°C for the Dy^{III} complexes.

As noted in Chapter 2, Geary gives an expected range of values of 80-115 $S \cdot cm^2 \cdot mol^{-1}$ for a 1:1 electrolyte in methanol, 160-220 $S \cdot cm^2 \cdot mol^{-1}$ for a 1:2 electrolyte, and 290-350 $S \cdot cm^2 \cdot mol^{-1}$ for a 1:3 electrolyte.[236] The Λ_M values for complexes **1.3** (Dy^{III}-N_5) and **2.3** (Dy^{III}-N_3O_2) in methanol are indicative of 1:2 electrolytic behavior, consistent with the presence of one bound and two unbound chloride ions. The molar conductivity of **6.3** (Dy^{III}-dbN_3O_3) in MeOH was between the range expected for a 1:1 electrolyte and a 1:2 electrolyte, so a definite determination of the number of bound chloride ions was not clear in this case. In contrast, the molar conductivities observed for

the aqueous solutions range from 300-320 $S \cdot cm^{2} \cdot mol^{-1}$, consistent with 1:3 electrolytes in solution, due to the displacement of the one bound chloride ion (or possible two, in the case of **6.3**) by water.

The conductance data thus indicates that in the solid state (represented by methanolic solution), one chloride ion is directly coordinated to the Dy^{III} center of **1.3** (Dy^{III}-N_5) and **2.3** (Dy^{III}-N_3O_2), in excellent agreement with the TGA data; and either one or two chloride ions are coordinated to **6.3** (Dy^{III}-dbN_3O_3).

Raman and Far-IR spectroscopy are very useful techniques for determining the presence of M-O and M-Cl bonds in coordination complexes. Like conductance, these methods were commonly employed for the characterization of such complexes before X-ray crystallography became so routine.[268] Raman and FT-IR spectroscopic data were collected to provide further information concerning the ligands coordinated to the metal center, in order to corroborate the conclusions drawn from the conductivity and TGA measurements, and to confirm that conductance measurements in MeOH are in fact a valid model for the electrolytic nature of a compound in the solid state.

For complex **1.3** (Dy^{III}-N_5), the presence of a coordinated chloride ion, as predicted by both conductance and TGA, is confirmed by the observation of a strong Raman peak at 257 cm^{-1} corresponding to the *ν*(Dy-Cl) stretching mode (Figure 3.9). In addition, a medium intensity band is visible in the far-IR spectrum at 207 cm^{-1} is attributed to the same stretching mode (Figure 3.10). A complex band in the Raman spectrum between 300-380 cm^{-1} is consistent with the presence of at least one coordinated water molecule.[269]

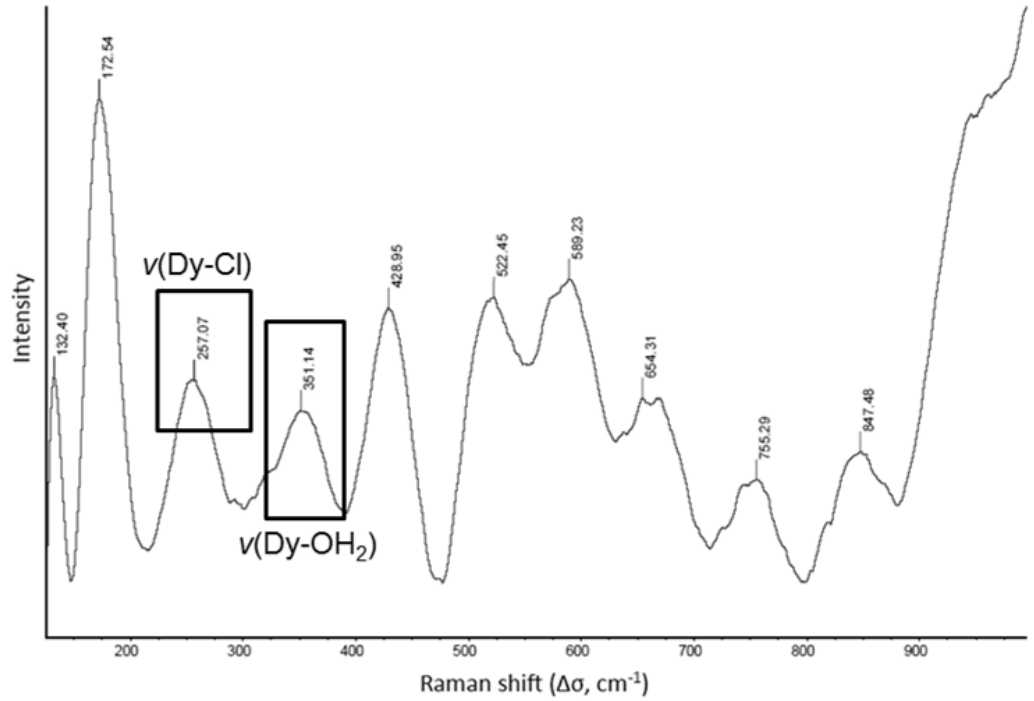

Figure 3.9 Raman spectrum for **1.3** (Dy^{III}-N_5).

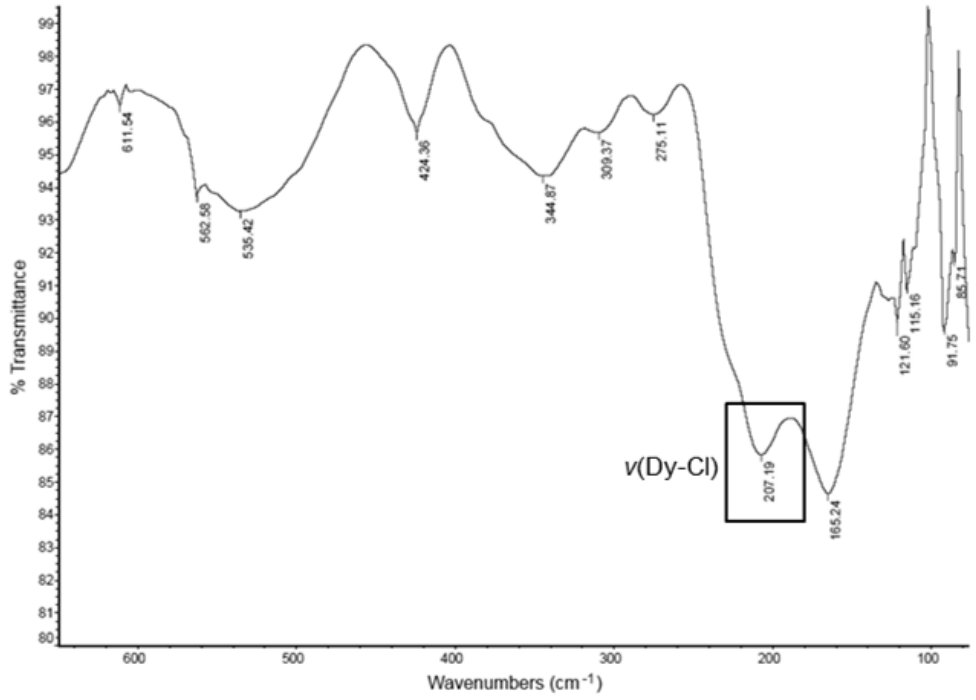

Figure 3.10 Far-IR for **1.3** (Dy^{III}-N_5).

Although literature concerning low-frequency IR and Raman spectra of Ln^{III}-chloride bonds is scarce,[269-271] the observed data do support the assignment of a 7-coordinate environment to the Dy^{III} center of **1.3** (Dy^{III}-N_5). For instance, the far-IR spectrum of the tentatively 7-coordinate Schiff-base complex $[DyCl_3(LH_2)]$ (where LH_2 = diethyl(ethylenebis-β-aminocrotonate) exhibits IR ν(Dy-Cl) bands between 230-240 cm^{-1}, while the far-IR spectrum of the complex $[DyCl_2(H_2O)_6]Cl$ shows ν_{as}(Dy-Cl) and ν_s(Dy-Cl) peaks at 219 and 162 cm^{-1} on the far-IR spectrum, and at 243 and 169 cm^{-1} on the Raman spectrum, respectively.[269] The latter complex also exhibits a complex peak in the Raman spectrum between 290-360 cm^{-1}, corresponding to the ν(Ln–O) stretching mode.[269] Thus the observed Raman and FT-IR data for **1.3** (Dy^{III}-N_5) support the presence of a bound chloride ion and a bound water molecule to a Dy^{III} center; in agreement with the conductivity and TGA data.

Unfortunately, complex **2.3** fluoresced too intensely for the assignment of any useful bands. Like complex **2.3**, complex **6.3** fluoresced intensely; but visible peaks in the Raman spectrum were present: a peak at 242 cm^{-1} may be attributed to the *ν*(Dy-Cl) stretching mode, in agreement with the 1-2 chloride ions predicted to be bound via conductance measurements; while the complex contour on the spectrum between 290-340 cm^{-1} corresponds to the *ν*(Dy-O) stretch of coordinated water.[269]

Based on the above evidence, we thus propose that complexes Dy^{III}-N_5 (**1.3**) and Dy^{III}-N_3O_2 (**2.3**) are 7-coordinate, *pseudo*-pentagonal bipyramidal systems, with the pentadentate macrocycle bound in the equatorial plane, and a coordinated chloride ion and water molecule filling the axial positions; although without a crystal structure, this

cannot be conclusively proven. The third complex, Dy^{III}-dbN_3O_3 (**6.3**), likely has geometry between 8-coordinate and 10-coordinate, with the potentially hexadentate macrocycle bound equatorially, and at least one water and one chloride bound axially. The conferral of anisotropy on a Dy^{III} ion via the equatorial binding of a pentadentate or hexadentate macrocycle has never before been explored, and thus the magnetic properties of these three complexes are of great interest.

3.3 Magnetic studies

Following the synthesis of complexes **1.3** (Dy^{III}-N_5), **2.3** (Dy^{III}-N_3O_2), and **6.3** (Dy^{III}-dbN_3O_3), direct current (dc) and alternating current (ac) susceptibility measurements were carried out on each complex in order to probe their magnetic properties.

Dc magnetic data was collected using a Quantum Design MPMS system. Measurements were performed on a powder sample of each complex, in an applied field of 0.1T, from 300-2 K. The parameters of interest are the room temperature χT value, which should equal the Curie constant (C); and the Weiss constant (θ). The former values can be compared to the theoretical value for an isolated Dy^{III} ion; and the latter value indicates whether or not any weak intermolecular interactions are present. The χT *vs.* T and $1/\chi$ *vs.* T plots for each complex are presented in Figure 3.11, below.

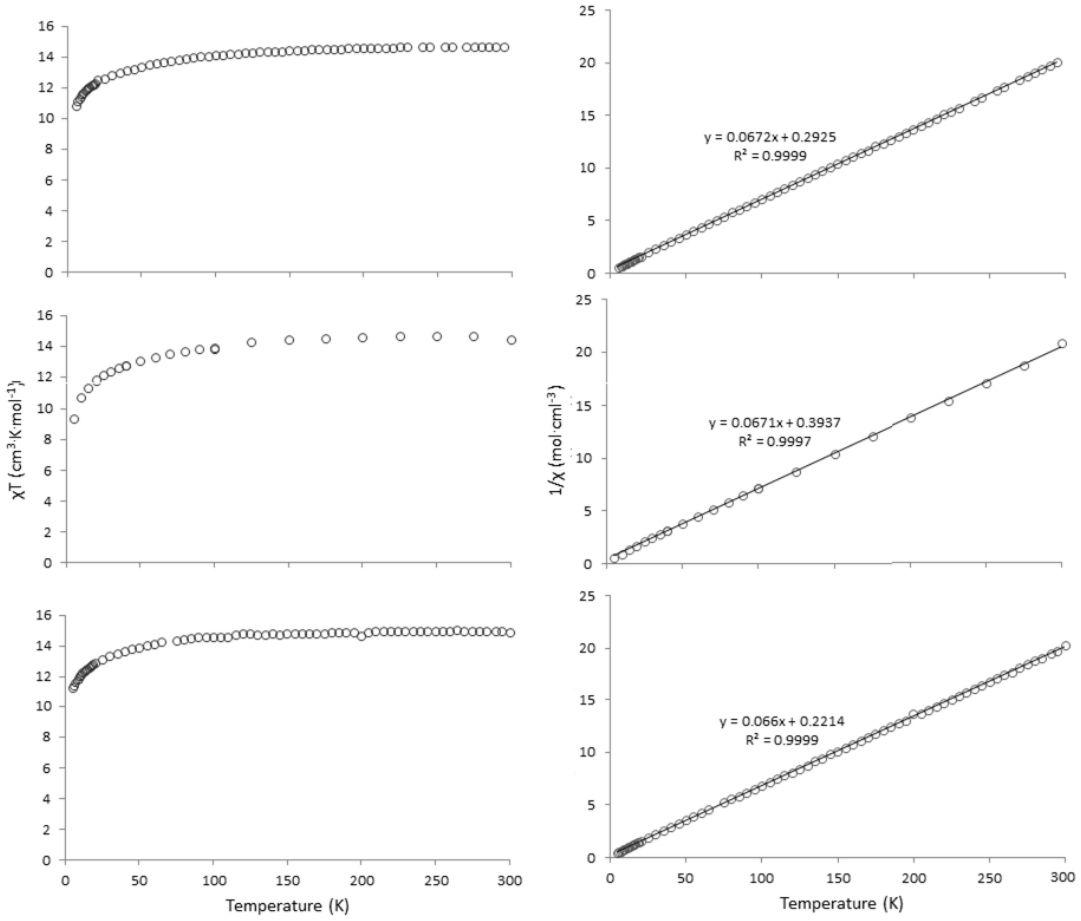

Figure 3.11 χT *vs.* T (left) and 1/χ *vs.* T (right) plots for **1.3** (top), **2.3** (center), and **6.3** (bottom).

The Curie and Weiss constants determined for each complex are summarized in Table 3.4, below.

Complex	Abbreviation	C ($cm^3 \cdot K \cdot mol^{-1}$)	θ (K)
1.3	Dy^{III}-N_5	14.88 ± 0.02	-4.35 ± 0.20
2.3	Dy^{III}-N_3O_2	14.89 ± 0.06	-5.86 ± 0.53
6.3	Dy^{III}-dbN_3O_3	15.15 ± 0.01	-3.35 ± 0.16

Table 3.3 Summary of the parameters describing the dc magnetic susceptibility behaviour of **1.3**, **2.3** and **6.3**.

The theoretical value of χT for a non-interacting Dy^{III} ion ($^6H_{15/2}$, S = 5/2, L = 5, g = 4/3) is 14.17 $cm^3 \cdot K \cdot mol^{-1}$, which is close to the high-temperature values observed for the three complexes (Figure 3.11, left). In each χT *vs.* T plot, the χT value remains constant as temperature decreases, until ~70 K, where the line begins to decrease, reaching a minimum value at 2 K. This decrease at low temperatures is most likely due to the depopulation of the Stark sublevels of each Dy^{III} center.[272] The Curie constant, calculated from the inverse of the slope of each $1/\chi$ *vs.* T plot, should also equal 14.17 $cm^3 \cdot K \cdot mol^{-1}$ for a mononuclear Dy^{III} complex which displays Curie-Weiss behaviour. The Curie constants for the three complexes were in reasonable agreement with the expected value (Table 3.4). The Weiss constants, calculated from the *x*-intercept of the same plot, were all low negative values, due to either the presence of weak antiferromagnetic interactions at low temperatures, or to the single-ion anisotropy of the Dy^{III} ions.

Alternating current (ac) measurements were carried out on each complex at low temperatures (2-15 K), in an oscillating field of 3.5 Oe, over a range of frequencies between 25 and 10,000 Hz. As mentioned in Chapter 1, the rationale behind performing such ac measurements is that the magnetization of an SMM will lag behind an alternating current, so the measured magnetic susceptibility will incorporate a phase shift, φ. The 'in-phase' or 'real' component of magnetic susceptibility is given by $\chi' = \chi\cos\varphi$, while the 'out of phase' or 'imaginary' component is given by $\chi'' = \chi\cos\varphi$.[111] SMM behavior is usually identified by observing that the out-of-phase response has a frequency-dependence, exhibited in a χ'' *vs.* T or χ'' *vs.* frequency plot.

Initially, measurements on each complex were carried out in zero applied dc field. In-phase and out-of-phase susceptibility *vs.* temperature plots are given in Figure 3.12.

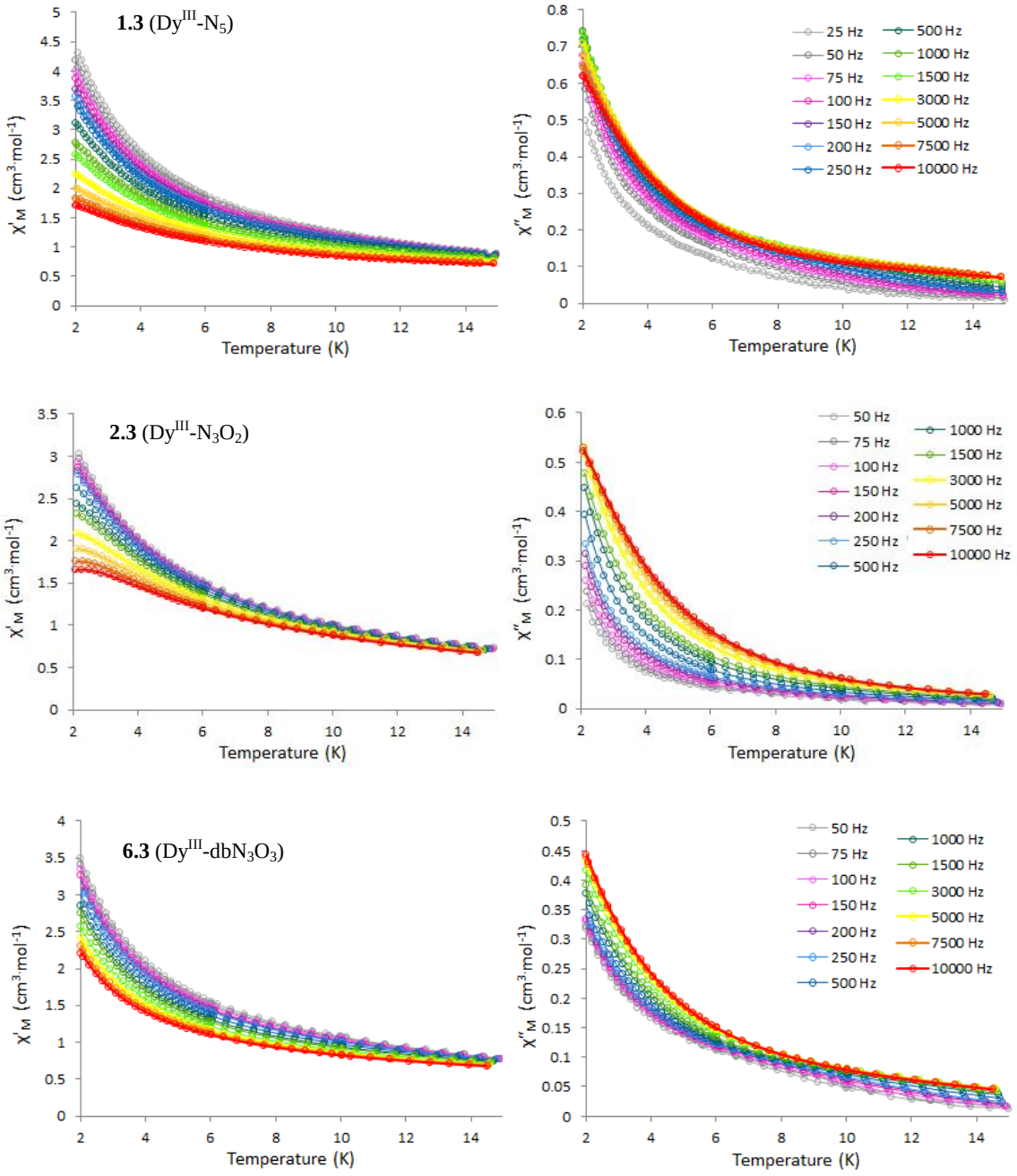

Figure 3.12 In-phase (left) and out-of-phase (right) susceptibility as a function of temperature for **1.3**, **2.3**, and **6.3** from 2-15 K, in zero dc field.

Although a large number of 'field-induced' SMMs have been reported, compounds which display slow relaxation of magnetization in the absence of a static field are of primary interest.[111] We were excited to observe that all three of the Dy^{III} complexes exhibit frequency-dependent magnetization, even in the complete absence of an applied dc field. In each set of χ' and χ'' *vs.* temperature plots (Figure 3.12) a clear separation between the susceptibility curves for each frequency is observed at low temperatures.

While most SMM materials display a clear maximum in the out-of-phase component of the ac data, systems with a distribution of relaxation pathways may not show such well-defined behaviour.[273,274] The absence of the typical maximum in χ'' can be due to the presence of quantum tunneling, and has been observed for other lanthanide complexes including the Er^{III} polyoxometalate-based SMM $[Er(\beta_2\text{-}SiW_{11}O_{39})2]^{13-}$.[275]

In an attempt to resolve the emerging maxima in the χ'' *vs.* T plots (Figure 3.12, right), we collected further ac susceptibility data, in the presence of a series of applied dc fields ranging from zero to 0.5 T. Applying a static dc field serves to quench quantum tunneling processes by slightly altering the energies of the M_J microstates via the Zeeman effect, and removing the degeneracy of the spin states between which tunneling is occurring. It is desirable to use as small a dc field as possible to quench the tunneling, so that the M_J sublevels are shifted as little as possible, in order that any effective barrier U_{eff} calculated in the presence of a static field may be a good representation of the barrier U in zero field. In addition, using a small dc field helps to ensure that the magnetic response observed in the presence of a field is not due to any long-range ordering. Figure 3.13, below, shows the resolution of a maximum in the χ'' *vs.* T data for **1.3** (Dy^{III}-N_5). The 0.5 T data shows that the maximum is best-resolved at lower frequencies (<500 Hz). At

higher frequencies, the maximum shifts to higher temperatures, and a shoulder to the left of the maximum emerges, suggesting the beginning of a second peak due to the presence of more than one relaxation pathway. Similar dynamic ac behaviour has been reported for various polynuclear and mononuclear SMMs, some in the absence and some in the presence of applied dc fields.[275-278]

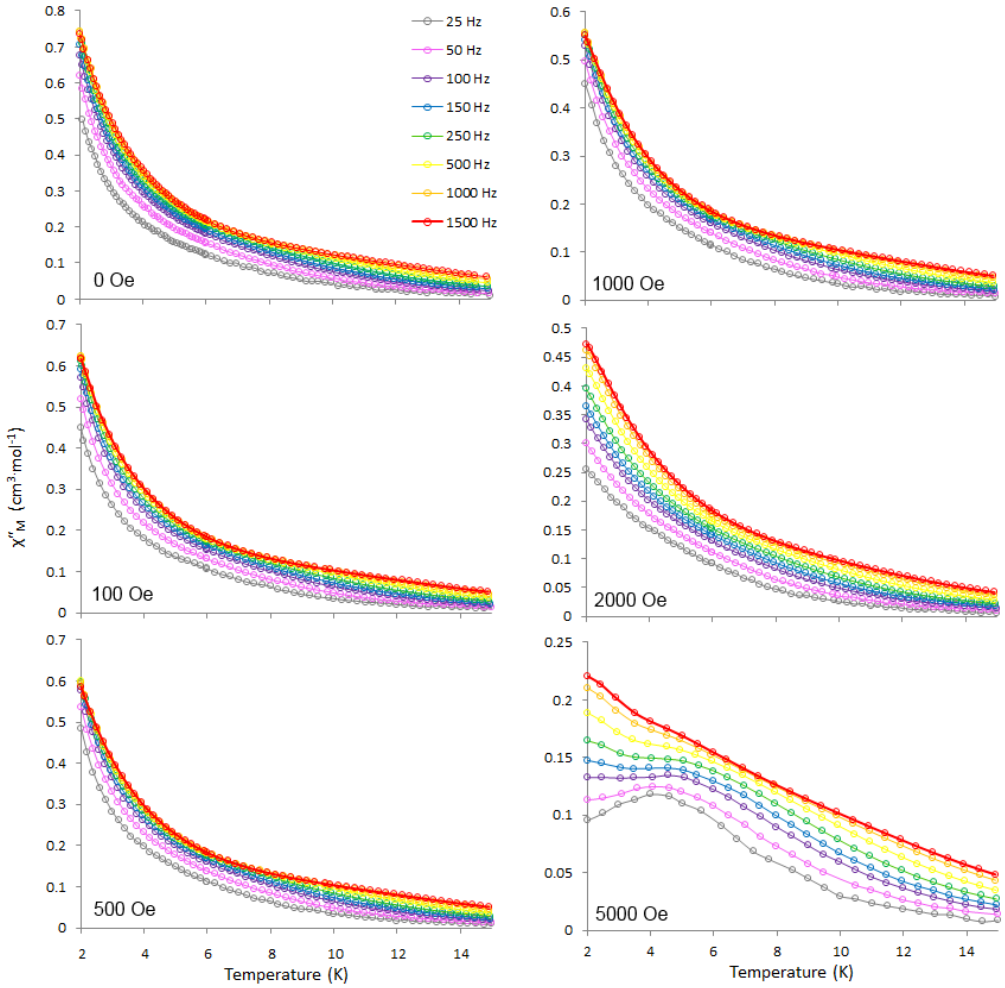

Figure 3.13 χ'' *vs.* T data for **1.3** (Dy^{III}-N_5) from 2-15 K in a series of applied dc fields from 0 to 0.5 T.

Complexes **2.3** (Dy^{III}-N_3O_2) and **6.3** (Dy^{III}-dbN_3O_3) display a similar but smaller change over the series of applied dc fields. In static fields of increasing magnitude, a broad, shallow maximum resolves in the χ'' *vs.* T data for **6.3** (Figure 3.14, bottom right), but is barely detectable even in a field of 0.5 T for **2.3** (Figure 3.14, top right). Like **1.3**, both complexes exhibit a shoulder or upswing as the temperature approaches 2 K.

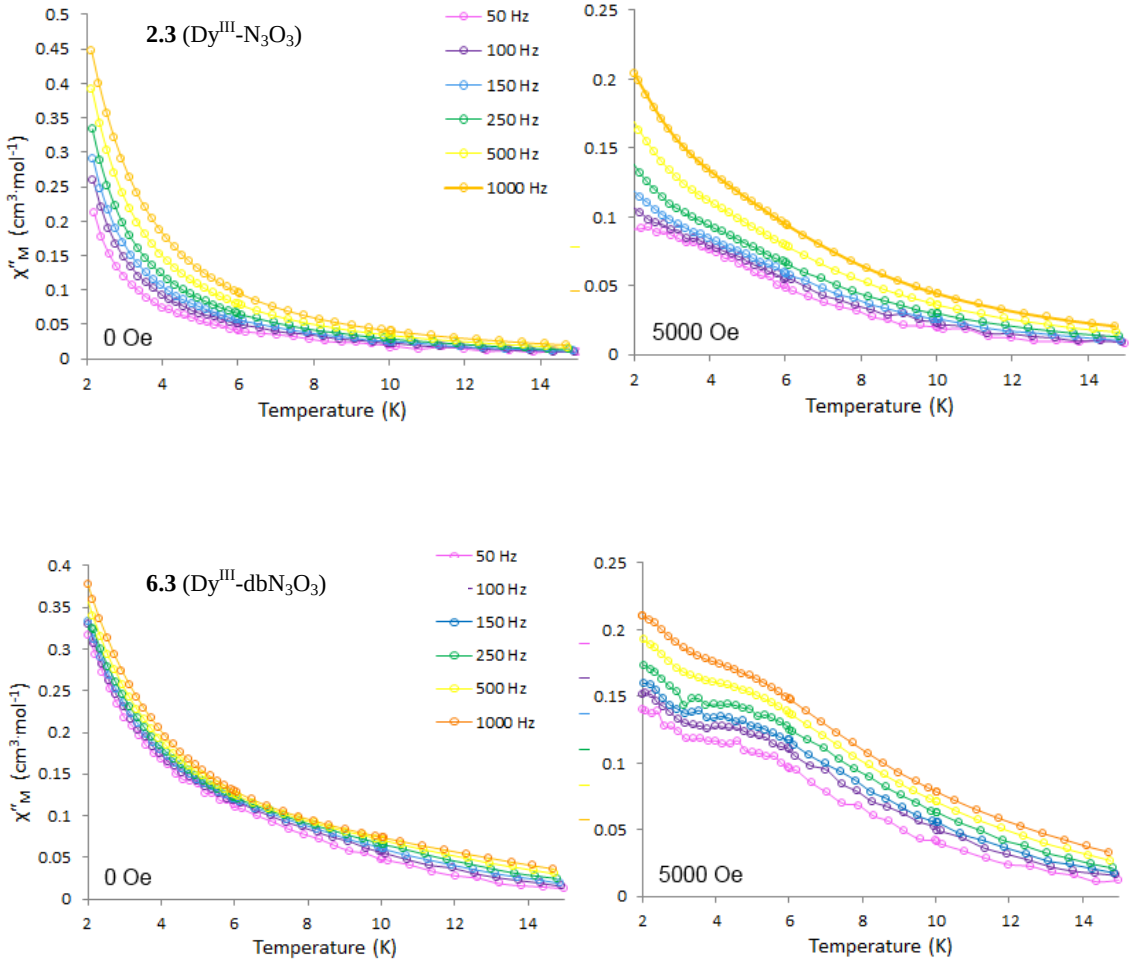

Figure 3.14 χ'' *vs.* T data for **2.3** and **6.3** from 2-15 K in applied dc fields of 0 (left) and 0.5 T (right).

The frequency dependence of the out-of-phase susceptibility is further evidenced when χ'' is plotted as a function of frequency. The χ'' *vs.* frequency plots are shown in Figures 3.15-3.17, below.

Resolved maxima are apparent at both low (2-5 K) and 'high' (11-15 K) temperatures for complex **1.3** (Dy^{III}-N_5, Figure 3.15). In each temperature regime, the position of the maximum shifts slightly, but distinctly between adjacent temperature curves, confirming the frequency-dependent nature of the response.

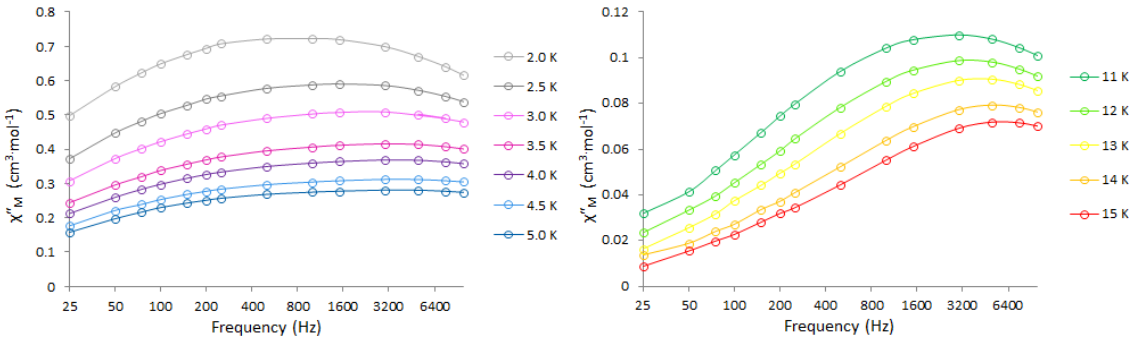

Figure 3.15 χ'' *vs.* frequency data for **1.3** (Dy^{III}-N_5) in zero applied dc field, at low temperatures (2-5 K, left), and 'high' temperatures (11-15 K, right).

For complex **2.3** (Dy^{III}-N_3O_2) maxima are only resolved below ~4 K (Figure 3.16, left), although there is a visible frequency-dependence to the out-of-phase response in the 'high' temperature regime also (Figure 3.16, right).

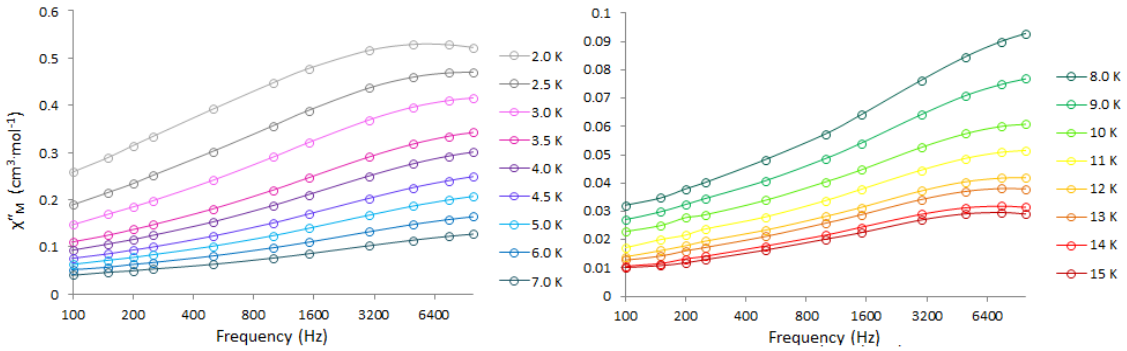

Figure 3.16 χ'' *vs.* frequency data for **2.3** (Dy^{III}-N_3O_2) in zero applied dc field, at low temperatures (<7 K, left), and 'high' temperatures (8-15 K, right).

In contrast, complex **6.3** (Dy^{III}-dbN_3O_3) exhibits resolved maxima only in the 'high' temperature regime, above ~11 K (Figure 3.17, right).

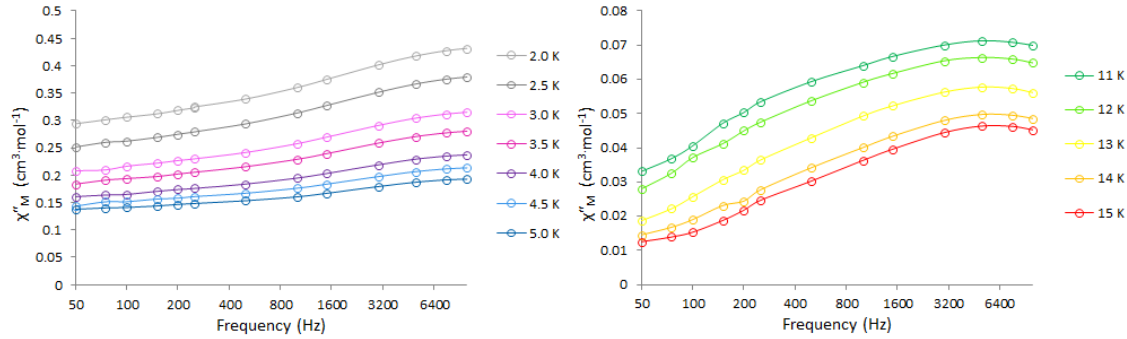

Figure 3.17 χ'' *vs.* frequency data for **6.3** (Dy^{III}-dbN_3O_3) in zero applied dc field, at low temperatures (2-5 K, left), and 'high' temperatures (11-15 K, right).

The χ' and χ'' *vs.* frequency data for a system may be used to determine the parameters describing the mechanisms of relaxation, by a fit of this data to the Cole-Cole equations. The Cole-Cole model describes ac susceptibility as:

$$\chi(\omega) = \chi_S + \frac{\chi_0 - \chi_S}{1+(i\omega\tau_c)^{1-\alpha}} \qquad \textbf{Eqn. 3.1}$$

where $\omega = 2\pi f$, χ_0 is the isothermal susceptibility, χ_S is the adiabatic susceptibility, τ_c is the temperature-dependent relaxation time, and α is a measure of the dispersivity of relaxation times.[273] Dividing this equation into its real and imaginary parts gives:

$$\chi' = \chi_S + \frac{(\chi_0 - \chi_S)}{2}\left\{1 - \frac{\sinh[(1-\alpha)\ln(\omega\tau_c)]}{\cosh[(1-\alpha)\ln(\omega\tau_c)]+\cos[{}^1/_2(1-\alpha)\pi]}\right\} \qquad \textbf{Eqn. 3.2}$$

$$\chi'' = \frac{(\chi_0 - \chi_S)}{2}\left\{1 - \frac{\sin[{}^1/_2(1-\alpha)\pi]}{\cosh[(1-\alpha)\ln(\omega\tau_c)]+\cos[{}^1/_2(1-\alpha)\pi]}\right\} \qquad \textbf{Eqn. 3.3}$$

At a given temperature point, the experimental or observed values of χ' and χ'' may be modelled using these equations, by assigning values to each of the four parameters (χ_0, χ_S, α and τ_c) which minimize the error between the experimental and calculated values of χ' and χ'' at each frequency for that temperature. Subsequently, the Arrhenius equation may be used to determine the tunneling rate, τ_0, and the effective energy barrier, U_{eff}. The Arrhenius equation relates relaxation time τ_c to temperature T, and is given by:

$$\tau_c = \tau_0 e^{U_{eff}/k_B T} \qquad \textbf{Eqn. 3.4}$$

When the natural log of τ_c is plotted against the inverse of temperature ($\ln\tau_c$ *vs.* 1/T), the energy barrier U_{eff} (K) is given by the slope of the line, and the tunneling rate τ_0 (s) is given by exp(y-intercept).[273]

It is not uncommon for different relaxation domains to dominate in different temperature regimes. In addition, several relaxation pathways may contribute to a relaxation domain characterized by a single U_{eff} and τ_0.

In order to successfully use the Cole-Cole equations to model χ' and χ'' data at a given temperature point, a resolved maximum must be observable in the χ'' *vs.* frequency plot at that temperature (which will also mean a resolved maximum in the χ' *vs.* χ'' plot at that temperature). Thus, consistent with the χ'' *vs.* frequency plots above (Figures 3.15-3.17), we were able to model both the high and low temperature regimes of the zero field χ' *vs.* χ'' data for complex **1.3** (Dy^{III}-N_5), the low temperature regime for **2.3** (Dy^{III}-N_3O_2), and the high temperature regime for **6.3** (Dy^{III}-dbN_3O_3). An inability to utilize the Cole-Cole and Arrhenius equations to extract the energy barrier and tunneling rate in the remaining temperature regimes does not mean that slow magnetic relaxation is not occurring; simply that the collected data does not lend itself to characterization via this method.

The Cole-Cole plots for each complex may be seen below (Figures 3.18-3.20).

As mentioned above, both the low and high temperature regimes may be modelled for complex **1.3** (Dy^{III}-N_5, Figure 3.18).

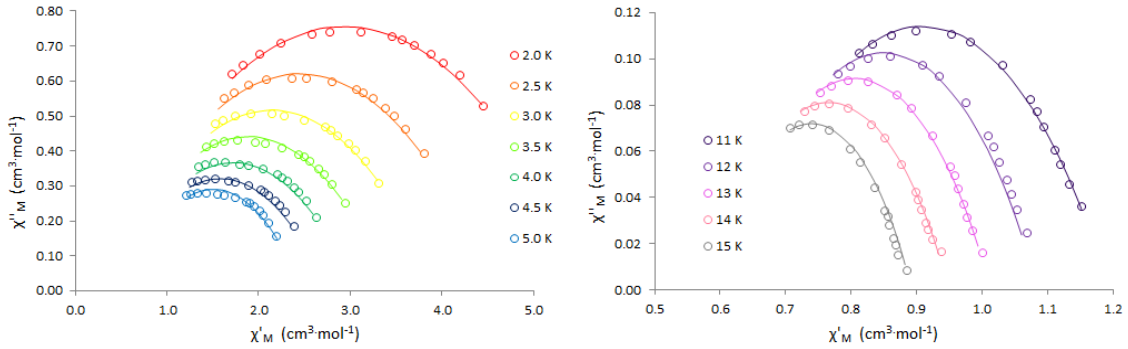

Figure 3.18 χ'' *vs.* χ' plot for **1.3** (Dy^{III}-N_5) in zero dc field from 2-5 K (left) and 11-15 K(right), over the frequency range 25-10,000 Hz. Circles correspond to experimental data, lines correspond to a best fit to the Cole-Cole equation.

Figure 3.19 depicts the χ″ *vs.* χ′ data for **2.3** (Dy^{III}-N_3O_2). The low temperature regime (left) was successfully modelled using the Cole-Cole equations; while the experimental-only χ″ *vs.* χ′ data above 5 K (right) shows the lack of resolved maxima at higher temperatures which was also observed in the χ″ *vs.* frequency data.

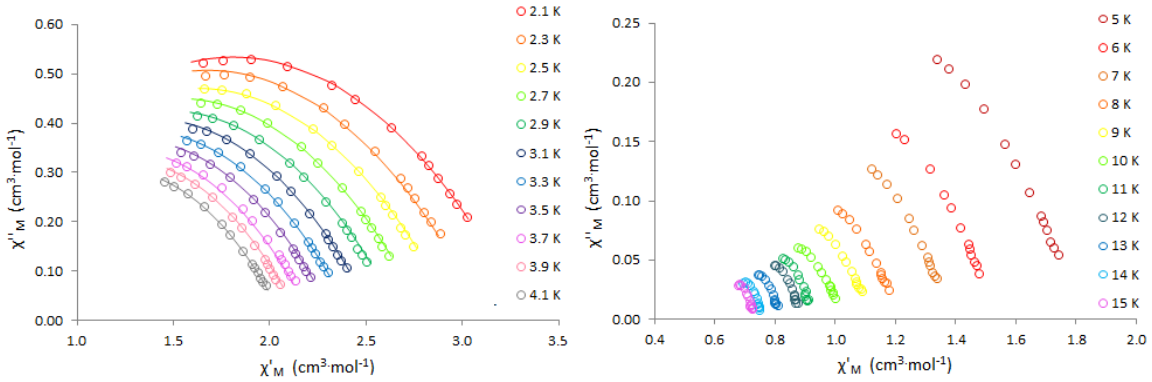

Figure 3.19 χ″ *vs.* χ′ plot for **2.3** (Dy^{III}-N_3O_2) in zero dc field over the frequency range 25-10,000 Hz. Left, temperature range 2-4 K; circles correspond to experimental data, lines correspond to a best fit to the Cole-Cole equation. Right, temperature range 5-15 K; circles correspond to experimental data only.

Complex **6.3** (Dy^{III}-dbN_3O_3) presents an interesting case. As was indicated by the χ″ *vs.* frequency data, the low temperature region may not be modelled with ease, due to the lack of resolved maxima. This absence of resolved maxima is also apparent in the χ″ *vs.* χ′ data (Figure 3.20, left). However, the χ″ *vs.* χ′ curves do display a slight but distinct kink, corresponding to the presence of two separate relaxation domains contributing to the relaxation behaviour at each temperature. For similarly kinked but better resolved data, a fit to the two-component Debye equation allows for the determination of a U_{eff}

and τ_0 parameter for each of the two domains; however, the lack of resolution prevented successful modelling of the low temperature data in this case.

The high temperature (11-15 K) region is readily modelled using a one-component Cole-Cole equation, as shown in Figure 3.20, right.

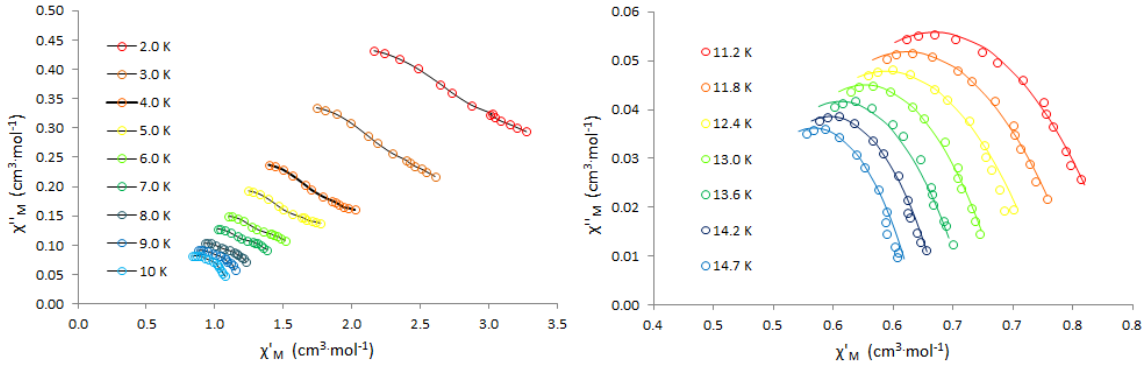

Figure 3.20 χ'' *vs.* χ' plot for **6.3** (Dy^{III}-dbN_3O_3) in zero dc field over the frequency range 25-10,000 Hz. Left, temperature range 2-10 K; circles correspond to experimental data, black lines are guide for the eyes only. Right, temperature range 11-15 K; circles correspond to experimental data only, lines correspond to a best fit to the Cole-Cole equation.

For each modelled temperature regime of each complex, a fit of the temperature dependence of the τ_c values to the Arrhenius equation allowed the energy barriers and tunneling rates to be determined. The Arrhenius plots are shown below (Figure 3.21), and the parameters describing their relaxation behaviour are presented in Table 3.5.

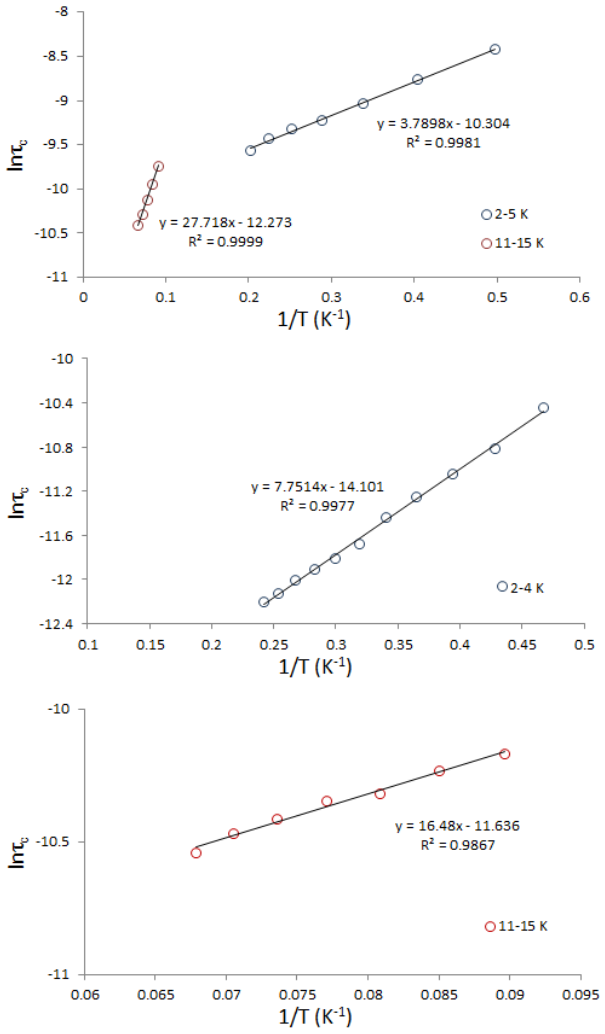

Figure 3.21 Arrhenius plots for (top to bottom) complexes **1.3**, **2.3** and **6.3**. Circles correspond to calculated values, black lines are a best fit to the Arrhenius equation.

Complex	Temperature	U_{eff} (K)	τ_0 (s)	α
1.3 (Dy^{III}-N_5)	2 – 5 K	3.79 ± 0.07	$(3.35 \pm 0.08) \times 10^{-5}$	0.63-0.66
	11 – 15 K	27.7 ± 0.2	$(4.68 \pm 0.07) \times 10^{-6}$	0.44-0.47
2.3 (Dy^{III}-N_3O_2)	2 – 4 K	7.75 ± 0.12	$(7.52 \pm 0.31) \times 10^{-7}$	0.57
6.3 (Dy^{III}-dbN_3O_3)	11 – 15 K	16.5 ± 0.9	$(8.84 \pm 0.59) \times 10^{-6}$	0.49-0.58

Table 3.4 The energy barriers (U_{eff}) and tunelling rates/pre-exponential factors (τ_0) for the modelled regions of the ac susceptibility data for complexes **1.3**, **2.3** and **6.3**.

Thus it can be seen that all three complexes exhibit slow relaxation of magnetism in the absence of an applied magnetic field: they are zero field Ln-SMMs.

Complex **1.3** ($Dy^{III}N_5$) displays two clear relaxation domains or processes: a high and low temperature domain. The relaxation barriers calculated for **1.3** (shown in Table 3.5: 4.13 and 23.7 K) and are very comparable to those of other Dy^{III} SMMs displaying two well-defined relaxation processes.[272,273,279] In keeping with literature observations, we have tentatively assigned the high-temperature domain of the relaxation behaviour of **1.3** to a predominantly thermal pathway, via classical crossing of the energy barrier. In the low temperature domain, the proportion of molecules able to overcome this energy barrier is small, and the dominant relaxation pathway is likely a temperature-independent pathway, such as quantum tunneling mechanism, 'through' the energy barrier.[280]

Only the 2-4 K temperature regime could be modelled for complex **2.3** (Dy^{III}-N_3O_2): a relatively low energy barrier of 7.25 K was calculated for this domain, again assigned to a quantum tunneling pathway. It was not visibly clear from the susceptibility plots (Figure 3.14 top, and Figure 3.16 right) whether a different relaxation process, or the same process, was occurring at temperatures above 4 K.

Complex **6.3** (Dy^{III}-dbN_3O_3) exhibits a well-defined, readily modelled process in the high temperature region with an energy barrier of 16.5 K, comparable to that of complex **1.3**, and probably also due to a classical thermal process. In the low temperature region, two separate relaxation domains are present as mentioned earlier, evidenced by the visibly kinked χ'' *vs.* χ' data (Figure 3.14, left); although the energy barriers and

tunnelling rates could not be extracted for the two low temperature domains, each is likely due to a mixture of temperature-independent and temperature-dependent processes in different proportions.

Within each domain for each complex, multiple overlapping pathways contribute to the observed relaxation behaviour. This distribution of relaxation pathways is evidenced by the large α values given in Table 5, ranging from 0.44 to 0.66. An α value of 0 corresponds to one Debye-like relaxation pathway with a single relaxation time τ_c, while a value of 1 indicates an infinitely wide range of relaxation pathways, characterized by an infinitely wide dispersion of τ_c values. Clear visual evidence for the multiple pathways can be seen in the 0.5 T χ'' *vs.* T data for **1.3** (Dy^{III}-N_5, Figure 3.22), where at low temperatures the low frequency data displays a maximum corresponding to one pathway, and the higher frequency data begins to rise due to a second (or multiple) additional pathway(s).

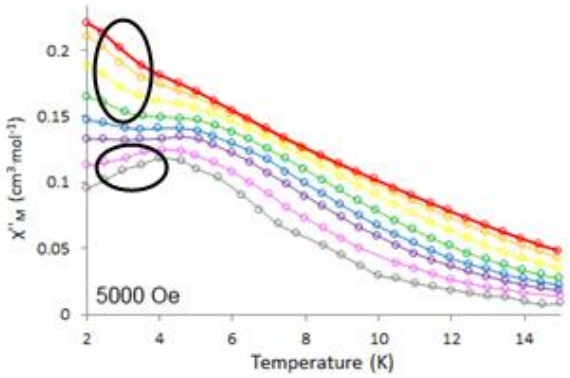

Figure 3.22 χ'' *vs.* T data for **1.3** (Dy^{III}-N_5) in 0.5 T dc field, with (at least) two separation relaxation pathways circled. Lines are a guide for the eye only.

Unfortunately, for this system the lack of single crystal data makes it impossible to carry out detailed magneto-structural correlations in order to rationalize further the differences in the energy barriers and relaxation rates for the three complexes. However, in comparison to the four literature examples detailed at the beginning of this chapter (Section 3.1), our compounds are proposed to be unique in the use of equatorially-binding *macrocycles* to control the geometry. Although our energy barriers do not represent an improvement on those of the compounds described above, our strategy for anisotropy enhancement is a novel one.

3.4 Conclusion and future work

To conclude, we have successfully synthesized three new mononuclear Dy^{III} Ln-SMMs. Mono-cyclic mono-lanthanide SMMs such as these are a rarity, in a field saturated with bi-cyclic sandwich complexes and acyclic chelating ligands. Importantly, complexes **1.3** (Dy^{III}-N_5) and **2.3** (Dy^{III}-N_3O_2) represent the first example of the exploitation of equatorially-binding pentadentate macrocycles to introduce anisotropy into an SMM system via the conferral of *pseudo*-pentagonal bipyramidal geometry. We have thus demonstrated a novel approach for the rational design of mononuclear SMMs, an area at the forefront of the field of molecular magnetism.

Due to the difficulties posed by the amorphous nature of the compounds in the project, future work involving the same design principles will involve a search of the Cambridge Structural Database in order to find macrocycles reported to bind to Ln^{III} ions in a pentadentate fashion, which are also well-known to confer crystallinity upon the resulting complexes. For instance, [1+1] Schiff-base macrocycles of the form below have

been reported to bind to various lanthanides, including Dy^{III}.[281] The two-compartment macrocycle where R = phenol has been reported to bind Dy^{III} in a pentagonal bipyramidal environment, with a sodium cation in the second binding pocket (Figure 3.23, right).[281] An array of structures based on this crystalline, double-pocket system could be synthesized and examined as potential Ln-SMMs.

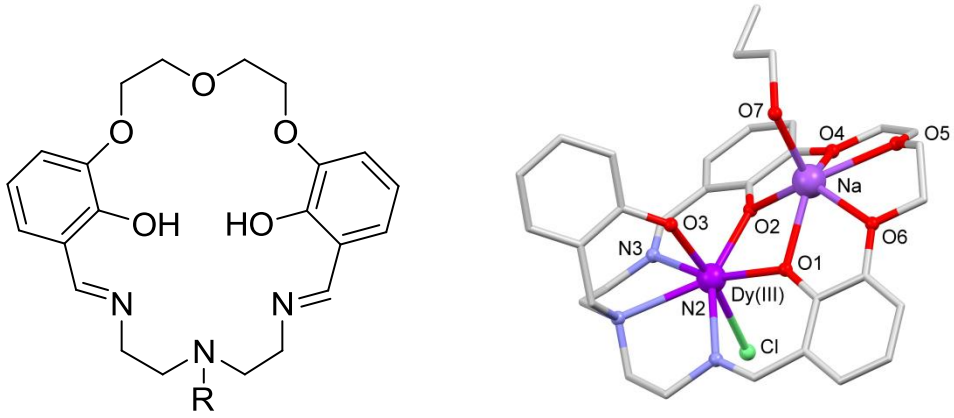

Figure 3.23 Left, general structure of the two-compartment Schiff-base macrocycle; right, the DyNa dimer reported by Tamburini and co-workers.[281]

In addition, an extension of this project involves the utilization of complexes Dy^{III}-N_5 and Dy^{III}-N_3O_2 as building blocks for the synthesis of higher-order magnetic structures. As was discussed in detail in Section 1.3, transition metal complexes of **L1** (N_5) and **L2** (N_3O_2) have been exploited for use in chains, clusters and networks of varying topologies and magnetic properties. The majority of these structures were formed using layering and H-tube diffusion techniques, involving solutions of the macrocyclic complex and a bridging moiety such as a polycyanometalate. Utilizing similar techniques, attempts will be made to incorporate lanthanide complexes of these macrocycles into chains and clusters, with the aim of synthesizing novel higher-order

magnetic structures; including dual-property materials; such as the photomagnetic chain recently reported by Clerac′ and co-workers, in which SMM units were linked via mononuclear spin-crossover (SCO) complexes of [Fe(**L1**)(CN_2)].[157]

4 RESULTS AND DISCUSSION FOR PROJECT 3:

Ln^{III} complexes of crown ethers: towards mononuclear SMMs

4.1 Introduction

In Chapter 2, a family of mononuclear Dy^{III}-SMMs were successfully prepared, demonstrating for the first time the use of equatorially-binding macrocycles to control the geometry, and thus enhance the intrinsic anisotropy of the Dy^{III} ion. However, the persistent amorphous nature of these complexes prevented a full magneto-structural correlation.

We thus turned our attention toward a family of macrocycles well-known to confer crystallinity upon their complexes: the crown ethers. Crown ethers are a commercially available class of macrocyclic ligands in which both the cavity size and number of donor atoms can be structurally tuned. Surprisingly, crown ethers have thus far remained unexplored for the synthesis of Ln-SMMs.

In this project, with a view to forming complexes with the 'sandwich'-type geometries so ubiquitous in SMM chemistry, the 12-crown-4 (12C4) and 15-crown-5 (15C5) macrocycles with cavity diameters between 1.2 and 2.2 Å were employed. For comparison, the larger 18-crown-6 macrocycle, with its cavity diameter of 2.7 Å, has also been utilized for the preparation of a family of complexes in which the macrocycle is equatorially-bound.

A detailed introduction to the modest number of Ln^{III}-crown ether complexes which have been structurally reported is presented in Section 1.4.2. The smaller crown

ether ligands, 12C4 and 15C5, tend to bind axially to the lanthanides. Predominantly half-sandwich topologies have been reported for Ln^{III} complexes of 12C4, including a series of the form $[Ln(12C4)(H_2O)_5]Cl_3 \cdot nH_2O$ (Ln = every trivalent lanthanide but Pm^{III}) reported by Rogers and co-workers in the 1980s.[178] The slightly larger 15C5 macrocycle is also reported to bind in an axial fashion. Three distinct topologies have been described for Ln^{III} complexes of 15C5 to date (Figure 4.1): half-sandwich,[181-183] full-sandwich,[184,185] and *pseudo*-sandwich structures,[187] with coordination numbers ranging from 8 to 11. Ln^{III} complexes of the larger 18C6 macrocycle show in-plane, equatorial binding, with three additional axial ligands bounds.[175,177,188,189]

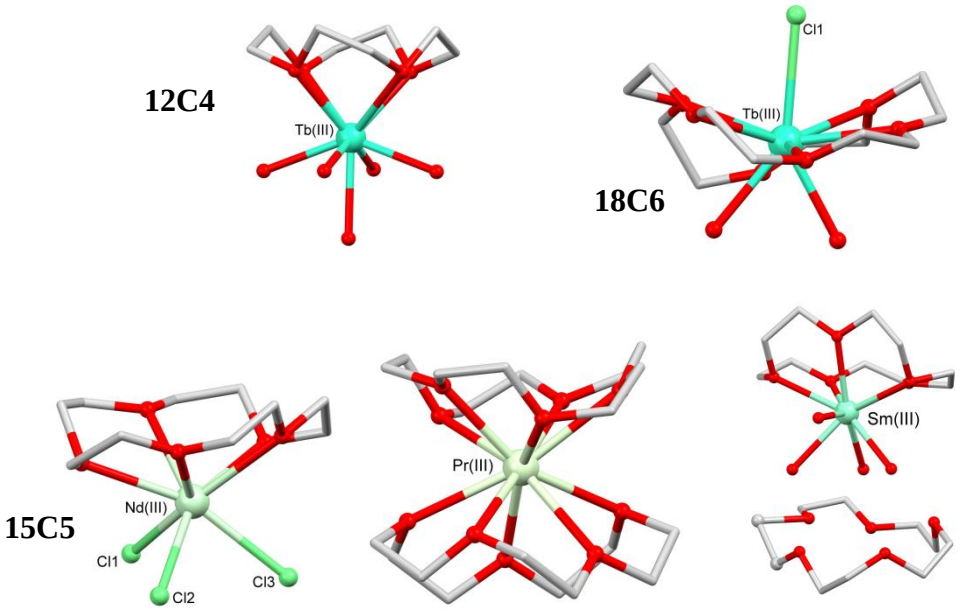

Figure 4.1 Representative topologies for Ln^{III}-crown ether complexes. Top left: a Tb^{III}-12C4 half-sandwich;[178] top right: a Tb^{III}-18C6 equatorial complex;[175] bottom: a Nd^{III}-15C5 half-sandwich,[183] a Pr^{III}-15C5 full-sandwich,[186] and a Sm^{III}-15C5 *pseudo*-sandwich.[187] Hydrogen atoms, lattice water molecules and non-coordinating counter ions are omitted for clarity.

The lanthanide ions selected for study were Tb^{III}, Dy^{III}, Ho^{III} and Er^{III}. To date, there are no structural reports of 15C5 complexes of lanthanides in the Tb^{III}-Er^{III} series; or of 18C6 complexes of Ho^{III}-Er^{III}. As a family, these ions provide a unique opportunity for observing the change in magnetic behaviour along the later lanthanides. All share similar preferences for high coordination geometries, as well as very similar, though slightly decreasing ionic radii (Table 4.1).[267] All have high ground state *J* values, ranging from 6 to 8. However, their electron density distributions differ: Tb^{III}, Dy^{III} and Ho^{III} are oblate ions, while Er^{III} is prolate.[95] The degeneracy of the ground state also differs: Dy^{III} and Er^{III} are Kramers ions, while Tb^{III} and Ho^{III} are non-Kramers ions.

Ln^{III}	Config.	Ground state term symbol ($^{2S+1}L_J$)	Landé g-factor	Distribution of *f* electron density	Radii (Å) Coord. no. 6→9
Tb^{III}	[Xe]$4f^8$	$^7F_6$	3/2	Oblate	0.92-1.10
Dy^{III}	[Xe]$4f^9$	$^6H_{15/2}$	4/3	Oblate	0.91-1.08
Ho^{III}	[Xe]$4f^{10}$	$^5H_8$	5/4	Oblate	0.90-1.07
Er^{III}	[Xe]$4f^{11}$	$^4I_{15/2}$	6/5	Prolate	0.89-1.06

Table 4.1 Selected parameters for Tb^{III}-Er^{III}.[95,267]

The magnetic properties of the selected crown ether complexes of these lanthanide ions are of particular interest due to the differing location of the ligand-centered electron density: predicted to be axially located for the 12C4 and 15C5 complexes, and equatorially centered in the 18C6 complexes. According to Long's crystal field model, presented in Section 1.2.4, equatorial electron density is expected to enhance the anisotropy of the prolate Er^{III} ion, while axial electron density should serve to enhance the anisotropy of the oblate Tb^{III}, Dy^{III} and Ho^{III} ions.[117]

Our primary objective was therefore to ***utilize crown ethers as macrocyclic ligands for the formation of a 'tuneable' family of mononuclear SMMs based on Tb^{III}, Dy^{III}, Ho^{III} and Er^{III}.***

4.2 Lanthanide perchlorate series: structural elucidation

With the above goal in mind, a sequence of reactions was devised by which the later lanthanide series of perchlorates ($Ln(ClO_4)_{3\ (aq)}$, where Ln^{III} = Tb^{III}, Dy^{III}, Ho^{III} and Er^{III}) were reacted in succession with 12-crown-4, 15-crown-5, and 18-crown-6 ligands. The perchlorate salts of the lanthanides were chosen because perchlorate is a non-coordinating anion, unlike chloride; and the larger size of the anion may afford well-separated complexes in the solid state, a prerequistite for SMM behaviour. With a view to forming sandwich-type complexes, the lanthanide salts were combined with 12C4 and 15C5 in both 1:1 and 1:2 Ln/crown ratios; while the lanthanide salts were reacted with the 18C6 in 1:1, 2:1 and 3:1 Ln/crown ratios, in an effort to determine whether the larger crown would bind to more than one Ln^{III} center.

Each reaction was carried out under the same set of conditions, based on a series of papers published by Rogers and co-workers in the 1980s.[175-178] The aqueous lanthanide perchlorate salt and crown ether were combined in a 3:1 mixture of acetonitrile and methanol, and stirred vigorously at 55°C for 3 – 18 hours, followed by pipette filtration and slow evaporation of the reaction mixture. Each reaction was carried out in triplicate at least, allowing for several different rates of evaporation to be utilized for each Ln/crown type and ratio. The various combinations of reagents are summarized in Table 4.2, along with the products of the 28 reactions types. Efforts were focussed on reactions

which yielded X-ray quality single crystals, since the goal of the project was, in part, to investigate the magneto-structural correlation of the resulting complexes.

	Ln:crown	$Tb(ClO_4)_{3(aq)}$	$Dy(ClO_4)_{3(aq)}$	$Ho(ClO_4)_{3(aq)}$	$Er(ClO_4)_{3(aq)}$
12C4	1:1	×	**half-sandwich (9.1)** 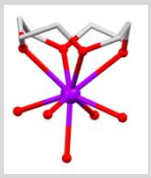	**half-sandwich (9.2)** 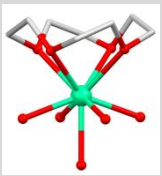	×
	1:2	×	×	×	×
15C5	1:1	*pseudo-sandwich (10.3)* 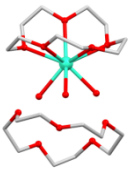	**pseudo-sandwich (10.1)** 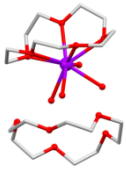	×	**half-sandwich (10.2)** 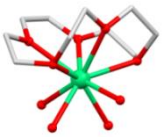
	1:2	×	×	*pseudo-sandwich (10.4)* 	×
18C6	1:1	×	×	×	×
	2:1	**eq. complex (11.1)** 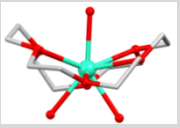	**eq. complex (11.2)** 	**eq. complex (11.3)** 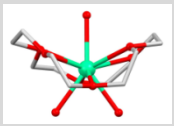	**eq. complex (11.4)** 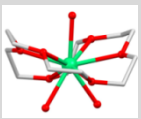
	3:1	×	×	×	×

Table 4.2 The products of the reactions of the Ln^{III} series Tb^{III}-Er^{III} with 12-crown-4, 15-crown-5 and 18-crown-6. Hydrogen atoms, perchlorate counter ions and lattice solvent molecules are omitted for clarity.

In the table above, the symbol × indicates that no X-ray quality single crystals were isolated from the given reaction type. Complexes which were analytically pure in bulk are presented in bold, italicized complexes were structurally characterized via X-ray diffraction, but were not analytically pure in bulk.

Single crystals of ten complexes were successfully obtained from this reaction series and their molecular structures were characterized by X-ray diffraction. In this context, isolation of the products of these reactions for X-ray crystallography involved storing the crystals in their mother liquor before measurement and then mounting the crystals in paraffin oil and flash cooling to 150 K on the X-ray diffractometer to prevent any decomposition of the crystals due to loss of solvent. The isolation of samples for characterization by elemental analysis and mass spectrometry was performed by the selection of individual single crystals from the crystallization vials, followed by washing with hexane and diethyl ether and then gently blotting dry with filter paper.

4.2.1 Ln^{III}-12C4 complexes

Reaction of 1:1 and 2:1 mixtures of 12C4 with the lanthanide perchlorate salts described above resulted in the isolation of single crystals of two analytically pure complexes: the Dy^{III} complex $[Dy(12C4)(H_2O)_5](ClO_4)_3 \cdot H_2O$ (**9.1**), and the Ho^{III} complex $[Ho(12C4)(H_2O)_5](ClO_4)_3 \cdot H_2O$ (**9.2**) (Figure 4.2). Unfortunately, under the reaction conditions described above, no single crystals of Tb^{III} or Er^{III} complexes with 12C4 were isolated. Selected characterization data is presented in Table 4.3, below.

Complex		C	H	N	ν (cm^{-1})	λmax (ε) (nm, $L \cdot mol^{-1} \cdot cm^{-1}$)	MS (*m/z*)
9.1 **Dy^{III}-12C4**	Found Calcd.	12.90 12.89	3.79 3.78	0.00 0.00	3405, 2970, 1050, 1027, 929, 618	269 (119)	FAB: 538 $[M\text{-}6H_2O\text{-}ClO_4]^+$ (100%).
9.2 **Ho^{III}-12C4**	Found Calcd. (+0.1CH_3CH)	12.56 12.80	3.69 3.97	0.18 0.18	3405, 2970, 1026, 929, 616	248 (37)	MALDI-TOF: 441 $[M\text{-}5H_2O\text{-}2ClO_4\text{-}H]^+$ (100%).

Table 4.3 Selected characterization data for complexes **9.1** (Dy^{III}-12C4) and **9.2** (Ho^{III}-12C4). Calcd. formulae are based on the structures determined via single crystal X-ray diffraction.

The molecular structures of both complexes were characterized by X-ray crystallography. The complexes are isostructural, crystallizing in the monoclinic space group $P2_1/c$, with one independent molecule in the asymmetric unit. The O_9 coordination geometry of each Ln^{III} center comprises four oxygen atoms of the tetradentate crown ether ligand (O1 to O4) and five water molecules (O5 to O9), to afford a half-sandwich type structural topology (Figure 4.2). Selected bond lengths and angles for complex **9.1** (Dy^{III}-12C4) are presented in Table 4.4.

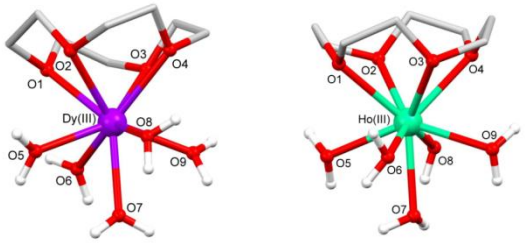

Figure 4.2 View of the molecular structures of **9.1** (Dy^{III}-12C4) and **9.2** (Ho^{III}-12C4) showing their half-sandwich structural topologies. Hydrogen atoms bound to carbon atoms, perchlorate counter ions and lattice water molecules are omitted for clarity.

Atom	Atom	Length (Å)
Dy1	O1	2.513(6)
Dy1	O2	2.420(6)
Dy1	O3	2.495(5)
Dy1	O4	2.457(6)
Dy1	O5	2.446(6)
Dy1	O6	2.337(6)
Dy1	O7	2.386(6)
Dy1	O8	2.372(6)
Dy1	O9	2.344(5)

Atom	Atom	Atom	Angle (˚)
O2	Dy1	O1	62.74(19)
O3	Dy1	O1	118.23(19)
O3	Dy1	O2	62.79(18)
O4	Dy1	O1	129.5(2)
O4	Dy1	O2	121.6(2)
O4	Dy1	O3	64.66(19)
O5	Dy1	O1	65.2(2)
O5	Dy1	O2	87.0(2)
O5	Dy1	O3	85.2(2)
O5	Dy1	O4	65.0(2)
O6	Dy1	O1	66.8(2)
O6	Dy1	O2	90.2(2)
O6	Dy1	O3	138.1(2)
O6	Dy1	O4	147.8(2)
O6	Dy1	O5	127.1(2)
O7	Dy1	O1	117.2(2)
O7	Dy1	O2	74.0(2)
O7	Dy1	O3	71.7(2)

Atom	Atom	Atom	Angle (˚)
O7	Dy1	O4	111.2(2)
O7	Dy1	O5	154.93(18)
O7	Dy1	O6	70.3(2)
O8	Dy1	O1	141.5(2)
O8	Dy1	O2	142.2(2)
O8	Dy1	O3	100.0(2)
O8	Dy1	O4	70.0(2)
O8	Dy1	O5	126.9(2)
O8	Dy1	O6	81.9(2)
O8	Dy1	O7	68.5(2)
O9	Dy1	O1	79.3(2)
O9	Dy1	O2	141.8(2)
O9	Dy1	O3	143.0(2)
O9	Dy1	O4	79.0(2)
O9	Dy1	O5	72.68(19)
O9	Dy1	O6	77.9(2)
O9	Dy1	O7	132.13(19)
O9	Dy1	O8	72.5(2)

Table 4.4 Selected bond lengths and angles for **9.1** (Dy^{III}-12C4). Additional crystallographic data for **9.1** and **9.2** (Ho^{III}-12C4) are presented in the Appendix.

The geometries of the Dy^{III} center of **9.1** and the Ho^{III} center of **9.2** were determined by calculating continuous shape measures (CSMs).[282] The deviation from ideal C_{4v} symmetry was described by CSMs of 0.52 and 0.51 for $Dy^{III}_{9.1}$ and $Ho^{III}_{9.2}$ respectively (Table 4.5), indicating a very small deviation from a capped square antiprismatic polyhedron in each case (Figure 4.3).

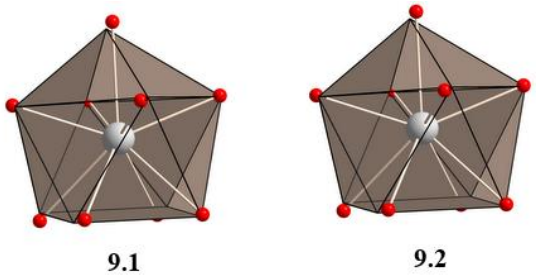

Figure 4.3 Coordination spheres of (left) $Dy^{III}_{9.1}$, and (right) $Ho^{III}_{9.2}$. Colour code: grey = Ln^{III}, red = O, beige = idealized polyhedra.

Polyhedron	$Dy^{III}_{9.1}$	$Ho^{III}_{9.2}$
EP-9	36.27	36.39
OPY-9	23.11	23.28
HBPY-9	18.48	18.48
JTC-9	16.09	16.04
JCCU-9	7.30	7.30
CCU-9	6.22	6.22
JCSAPR-9	1.37	1.35
CSAPR-9	**0.52**	**0.51**
JTCTPR-9	2.69	2.63
TCTPR-9	**1.49**	**1.49**
JTDIC-9	12.72	12.78
HH-9	11.73	11.67
MFF-9	**1.13**	**1.14**

Table 4.5 Continuous shape measures (CSMs) of the 9-coordinate Ln^{III} coordination polyhedra in complexes **9.1** and **9.2**. The values in red indicate the closest polyhedra for

each complex according to the CSMs. Abbreviations: EP-9, Enneagon; OPY-9, Octagonal pyramid; HBPY-9, Heptagonal bipyramid; JTC-9, Johnson triangular cupola J3; JCCU-9, Capped cube J8; CCU-9, Spherical-relaxed capped cube; JCSAPR-9, Capped square antiprism J10; CSAPR-9, Spherical capped square antiprism; JTCTPR-9, Tricapped trigonal prism J51; TCTPR-9, Spherical tricapped trigonal prism; JTDIC-9, Tridiminished icosahedron J63; HH-9, Hula-hoop; MFF-9, Muffin.

The crown ether ligand adopts a gauche conformation in both complexes, with all four O atoms of the crown lying on the same side of the ring. The Ln^{III} ion is displaced out of the best plane through the four crown ether oxygen atoms by 1.645 Å and 1.637 Å for Dy^{III} and Ho^{III} respectively.

The five coordinated water molecules, one uncoordinated water molecule, and three perchlorate counter ions form an extended, 3-D hydrogen-bonded network (Figure 4.4). The hydrogen bonds for both complexes are in the range of 2.700 - 2.980 Å, the shortest being between the proton of the bound water O6 and the oxygen atom of a neighbouring solvent water molecule, O22. For complex **9.1,** the shortest intermolecular $Dy^{III}\cdots Dy^{III}$ distances are 8.8750(5) Å, and for complex **10.1** the shortest $Ho^{III}\cdots Ho^{III}$ distances are 8.831(3) Å (Figure 4.4).

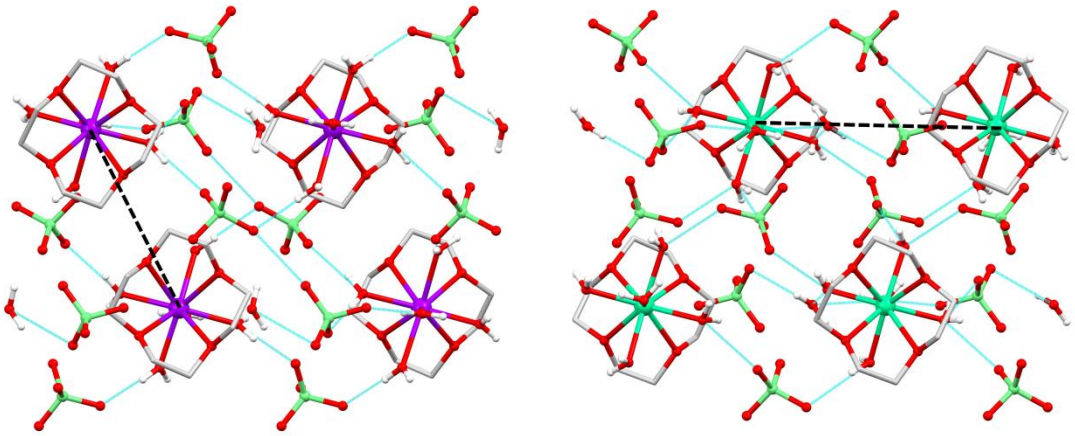

Figure 4.4 Crystal packing of **9.1** (left) and **9.2** (right). View down the *b*-axis, showing H-bonds as blue dashed lines. The shortest Dy···Dy distance of 8.8750(5) Å and the shortest Ho···Ho distance of 8.831(3) Å are shown as black dashed lines. Right: Colour code: purple = Dy^{III}, seafoam = Ho^{III}, grey = C, green = Cl, red = O.

4.2.2 Ln^{III}-15C5 complexes

Reaction of 15C5 with aqueous $Ln(ClO_4)_3$ salts (Ln^{III} = Tb^{III}, Dy^{III}, Ho^{III} and Er^{III}) under the previously described experimental conditions afforded single crystals of four different complexes. Reaction of Tb^{III} and Dy^{III} with 15C5 in a 1:1 ratio afforded the *pseudo*-sandwich structures $[Tb(15C5)(H_2O)_4](ClO_4)_3 \cdot (15C5) \cdot H_2O$ (**10.3**) and $[Dy(15C5)(H_2O)_4](ClO_4)_3 \cdot (15C5) \cdot H_2O$ (**10.1**) respectively. Reaction of Ho^{III} with 15C5 in a 1:1 ratio yielded no X-ray quality crystalline products; but the 2:1 ratio resulted in a similar *pseudo*-sandwich structure, $[Ho(15C5)(H_2O)_4](ClO_4)_3 \cdot (15C5) \cdot H_2O$ (**10.4**). In contrast to the *pseudo*-sandwich complexes observed for Tb^{III}-Ho^{III}, the 1:1 reaction of Er^{III} with 15C5 afforded a half-sandwich complex with the formula $[Er(15C5)(H_2O)_4](ClO_4)_3 \cdot H_2O$ (**10.2**). Unfortunately, we were unable to isolate analytically pure samples of complexes **10.3** (Tb^{III}-15C5) and **10.4** (Ho^{III}15C5).

Nevertheless, the crystal structures of the major products from these reactions were characterized by X-ray diffraction, and a summary of selected structural data for all four complexes is presented in Table 4.6.

	10.1 (Dy^{III}-15C5)	**10.2** (Er^{III}-15C5)	**10.3** (Tb^{III}-15C5)	**10.4** (Ho^{III}-15C5)
Topology	*pseudo*-sandwich	half-sandwich	*pseudo*-sandwich	*pseudo*-sandwich
Space group	Monoclinic $P2_1/n$	Orthorhombic Pbcn	Monoclinic $P2_1/n$	Monoclinic $P2_1/n$
a	15.8533(14)	17.6319(11)	15.8302(11)	15.7919(7)
b	14..6908(14)	14.7648(8)	14.7294(11)	14.6637(6)
c (Å)	16.4867(15)	9.5931(6)	16.4864(12)	16.4443(7)
α	90	90	90	90
β	99.409(4)	90	99.488(4)	99.3610(17)
γ (°)	90	90	90	90
Volume ($Å^3$)	3788.1(6)	2497.4(3)	3791.5(5)	3757.26

Table 4.6 Summary of parameters describing complexes **10.1** – **10.4**. Additional structural data are presented in the Appendix section of the thesis.

Characterization data as well as a detailed discussion of the molecular structures of the Dy^{III} *pseudo*-sandwich and Er^{III} half-sandwich complexes **10.1** and **10.2** are presented below.

Complex		**C**	**H**	**N**	***v*** **(cm^{-1})**	**λmax (ε) (nm, $L \cdot mol^{-1} \cdot cm^{-1}$)**	**MS (*m/z*)**
10.1 Dy^{III}-15C5	Found Calcd. (+4.5H_2O)	22.64 22.40	5.82 5.54	0.00 0.00	3355, 3241, 2930, 2886, 1050, 1028, 939, 619	250 (19)	FAB: 582 [M-4H_2O-ClO_4-15C5]$^+$ (47%)
10.2 Ho^{III}-15C5	Found Calcd. (+0.1CH_3CH)	14.16 14.79	3.65 4.22	0.00 0.00	3395, 2947, 1051, 951, 932, 620	246 (55)	MALDI-TOF: 676 [M-2H_2O-ClO_4]$^+$ (68%)

Table 4.7 Selected characterization data for complexes **9.1** (Dy^{III}-12C4) and **9.2** (Ho^{III}-12C4).

The Dy 15C5 complex **10.1** crystallizes in the monoclinic space group $P2_1/n$ with one Dy^{III} ion and two unique 15-crown-5 molecules in the asymmetric unit: one directly coordinated, and one unbound. The Dy^{III} ion adopts a 9-coordinate pseudo-capped square antiprismatic geometry with the O_9-donor set comprising five oxygen atoms from the bound pentadentate 15-crown-5 ether ligand, O1 to O5, along with four water molecules, O6 to O9. The bound crown adopts a puckered conformation, with an O5-Dy-O2 angle of 86.82°.[37] Three of the bound water molecules, O6, O7 and O8 are H-bonded to the five O atoms of the second, uncomplexed, crown, to afford a *pseudo*-sandwich type structure.[35] The Dy^{III}-crown complex is off-set from the hydrogen-bonded crown, enabling the coordinated water molecules O6 and O8 to form hydrogen-bonds to a perchlorate counter ion. The final coordinated water molecule O9, which is not H-bonded to the uncoordinated crown, is involved in two H-bonding interactions, the first to a free water molecule and the second to a perchlorate counter ion (O9···O1S and O9···O3 respectively). Selected bond lengths and angles for this complex are summarized in Table 4.8.

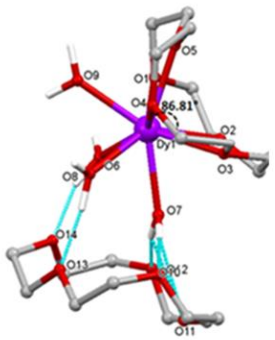

Figure 4.5 View of the molecular structure of **10.1** (Dy^{III}-15C5) showing the H-bonding interactions to the uncoordinated crown ether ligand as dashed blue lines.

Atom	Atom	Length (Å)
Dy01	O1	2.4739(19)
Dy01	O2	2.515(2)
Dy01	O3	2.480(2)
Dy01	O4	2.551(2)
Dy01	O5	2.343(2)
Dy01	O6	2.317(2)
Dy01	O7	2.435(2)
Dy01	O8	2.378(2)
Dy01	O9	2.335(2)

Atom	Atom	Atom	Angle (˚)
O1	Dy01	O2	64.33(7)
O1	Dy01	O3	96.51(7)
O1	Dy01	O4	64.80(6)
O2	Dy01	O4	99.25(7)
O3	Dy01	O2	64.88(6)
O3	Dy01	O4	63.78(7)
O5	Dy01	O1	69.20(7)
O5	Dy01	O2	79.90(7)
O5	Dy01	O3	144.66(7)
O5	Dy01	O4	128.61(7)
O5	Dy01	O7	70.36(7)
O5	Dy01	O8	140.64(7)
O6	Dy01	O1	131.30(7)
O6	Dy01	O2	69.92(7)
O6	Dy01	O3	78.04(8)
O6	Dy01	O4	140.91(7)
O6	Dy01	O5	87.59(8)
O6	Dy01	O7	69.72(7)

Atom	Atom	Atom	Angle (˚)
O6	Dy01	O8	82.12(8)
O6	Dy01	O9	140.67(8)
O7	Dy01	O1	132.44(7)
O7	Dy01	O2	130.12(7)
O7	Dy01	O3	131.05(7)
O7	Dy01	O4	130.61(7)
O8	Dy01	O1	141.64(7)
O8	Dy01	O2	130.09(7)
O8	Dy01	O3	69.48(7)
O8	Dy01	O4	77.16(7)
O8	Dy01	O7	70.42(7)
O9	Dy01	O1	78.91(7)
O9	Dy01	O2	142.62(7)
O9	Dy01	O3	129.38(7)
O9	Dy01	O4	69.10(7)
O9	Dy01	O5	80.98(8)
O9	Dy01	O7	70.99(7)
O9	Dy01	O8	83.35(8)

Table 4.8 Selected bond lengths and angles for **10.1** (Dy^{III}-15C5). Additional crystallographic data for complexes **10.1** and **10.2** (Ho^{III}-12C4) are presented in the Appendix section.

Examining the crystal packing reveals that molecules of **10.1** are organized in a monoclinic space group, in a hexagonal arrangement with layers of Dy^{III} complexes separated by the hydrogen-bonded crowns (Figure 4.6 right). The shortest intermolecular Dy···Dy contacts are 8.880(8) Å (Figure 4.6 left).

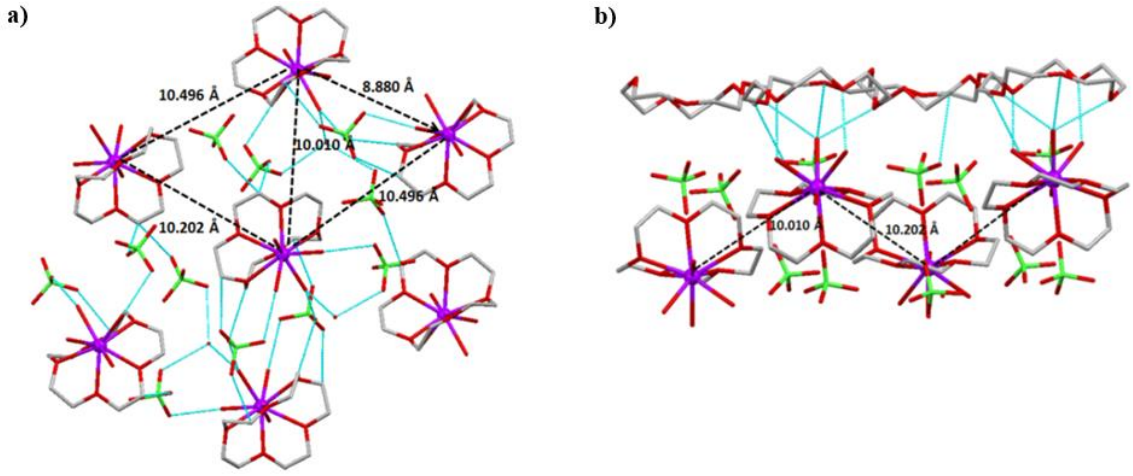

Figure 4.6 a) View of the crystal packing of **10.1** down the b(1/2a+1/2c) plane, showing $Dy^{III}\cdots Dy^{III}$ distances as black dashed lines; b) view of the crystal packing down the *b*-axis, showing the alternating layered arrangement of Dy^{III}-bound crown ether ligands, free H-bonded crowns, ClO_4^- counterions and lattice H_2O molecules. Hydrogen bonds are shown as dashed blue lines. Colour code: purple = Dy^{III}, grey = C, green = Cl, red = O.

In contrast, complex **10.2** (Er^{III}-15C5) crystallizes as a half-sandwich structure in the orthorhombic space group Pnma. The lanthanide ion is nine coordinate, bound to the five oxygens of the crown ether, and four water molecules. The crown ether is puckered, with an O1-Er-O3 angle of 82.62(9)°. Due to the symmetric nature of the puckering (Figure 4.7), the asymmetric unit of the complex consists of an Er^{III} bound only to three of the oxygens of the crown ether, while there are four half-sandwiches in the unit cell.

The crystal packing of **10.2** reveals an extended 3-D hydrogen-bound network, with each of the coordinated water molecules hydrogen-bonded to three different perchlorate anions. The shortest Er···Er distance is 8.22769(4) Å. Selected bond lengths and angles for the complex are presented in Table 4.9.

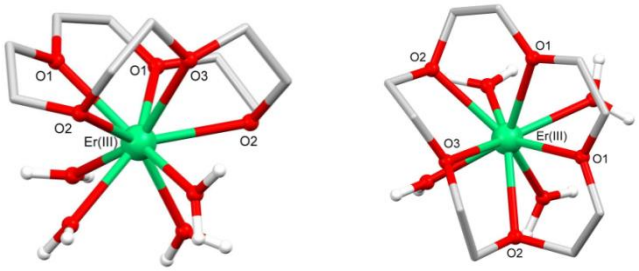

Figure 4.7 View of the molecular structure of **10.2** (Er^{III}-15C5) showing the symmetrically puckered nature of the 15-crown-5 ligand.

Atom	Atom	Atom	Angle (˚)
O1	Er1	O2	64.16(7)
O1	Er1	O3	82.62(9)
O1	Er1	O41	72.96(9)
O1	Er1	O42	142.06(7)
O1	Er1	O43	139.77(9)
O1	Er1	O1	64.48(7)
O1	Er1	O2	121.89(7)
O1	Er1	O42	96.53(7)
O2	Er1	O3	65.70(8)
O2	Er1	O41	114.66(9)
O2	Er1	O42	141.35(7)
O2	Er1	O43	76.58(8)
O2	Er1	O1	121.89(7)
O2	Er1	O2	129.30(7)
O2	Er1	O42	68.75(7)
O3	Er1	O41	151.0(1)
O3	Er1	O42	129.49(8)
O3	Er1	O43	73.2(1)

Atom	Atom	Atom	Angle (˚)
O3	Er1	O1	82.62(9)
O3	Er1	O2	65.70(8)
O3	Er1	O42	129.49(8)
O41	Er1	O42	70.01(9)
O41	Er1	O43	135.8(1)
O41	Er1	O1	72.96(9)
O41	Er1	O2	114.66(9)
O41	Er1	O42	70.01(9)
O42	Er1	O43	76.12(8)
O42	Er1	O1	96.53(7)
O42	Er1	O2	68.75(7)
O42	Er1	O42	78.49(7)
O43	Er1	O1	139.77(9)
O43	Er1	O2	76.58(8)
O43	Er1	O42	76.12(8)
O1	Er1	O2	64.16(7)
O1	Er1	O42	142.06(7)
O2	Er1	O42	141.35(7)

Atom	Atom	Length (Å)
Er1	O1	2.437(2)
Er1	O2	2.443(2)
Er1	O3	2.408(3)
Er1	O41	2.392(3)
Er1	O42	2.333(2)
Er1	O43	2.316(3)

Table 4.9 Selected bond lengths and angles for **10.2** (Er^{III}-15C5).

The geometries of the lanthanide ions in **10.1** (Dy^{III}-15C5) and **10.2** (Er^{III}-15C5) were further investigated by calculating continuous shape measures (CSMs).[282]

Polyhedron	$Dy^{III}_{10.1}$	$Er^{III}_{10.2}$
EP-9	35.21	36.43
OPY-9	24.16	23.53
HBPY-9	14.51	15.77
JTC-9	15.58	16.39
JCCU-9	7.52	8.97
CCU-9	6.38	7.78
JCSAPR-9	2.57	2.43
CSAPR-9	**1.78**	**1.52**
JTCTPR-9	3.69	3.04
TCTPR-9	2.59	**1.70**
JTDIC-9	10.68	12.55
HH-9	9.81	11.21
MFF-9	**1.27**	**1.10**

Table 4.10 Continuous shape measures (CSMs) of the 9-coordinate Ln^{III} coordination polyhedra in complexes **10.1** and **10.2**.[282] The values in red indicate the closest polyhedra for each complex according to the CSMs.

The Dy^{III} center in complex **10.1** is closer to a muffin polyhedron with a CSM of 1.27 than to a pseudo capped square antiprismatic topology, which has a larger CSM of 1.78 (Table 4.10, Figure 4.8). The Er^{III} ion in complex **10.2** also most closely resembles a muffin-shaped polyhedron, with a CSM of 1.10, compared to CSMs of 1.52 and 1.70 for capped square antiprismatic and tri-capped trigonal prismatic geometries respectively (Table 4.10, Figure 4.8).

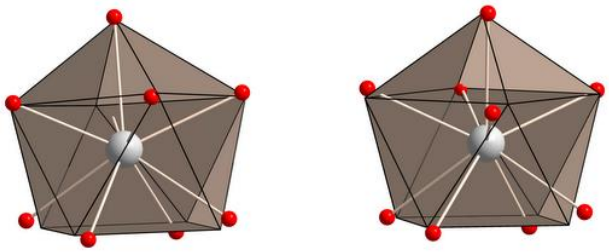

Figure 4.8 Coordination spheres of (left) $\mathbf{Dy^{III}_{10.1}}$, and (right) $\mathbf{Er^{III}_{10.2}}$. Colour code: grey = Ln^{III}, red = O, beige = idealized polyhedra.

As anticipated, based on the reported Ln^{III}-12C4 and Ln^{III}-15C5 structures, [178,181-185,187] both 12C4 and 15C5 coordinate in an axial fashion to the lanthanide ions in the series Tb^{III}-Er^{III}, yielding half- and *pseudo*-sandwich topologies in which the Ln^{III} ions lie above the crown ether cavity. The presence of coordinating water molecules in each structure is due to the aqueous nature of the $Ln(ClO_4)_3$ salts used. In contrast, these ions would be expected to lie within the cavity of the larger 18C6 macrocycle, which should bind in an equatorial fashion.[175,177,188,189]

4.2.3 Ln^{III}-18C6 complexes

The 18C6 macrocycle readily forms mononuclear complexes with the perchlorate salts of all four lanthanide ions, yielding complexes **11.1**-**11.4** (Table 4.11).

Complex		C	H	N	*v* (cm^{-1})	λmax (ε) (nm, $L \cdot mol^{-1} \cdot cm^{-1}$)	MS (*m/z*)
11.1 Tb^{III}**-18C6**	Found Calcd.	17.92 18.16	3.94 4.06	0.00 0.00	3406, 2956, 1049, 1030, 950, 931, 619	250 (29)	MALDI-TOF: 621 $[M\text{-}4H_2O\text{-}ClO_4]^+$ (100%)
11.2 Dy^{III}**-18C6**	Found Calcd.	18.04 18.08	3.90 4.05	0.00 0.00	3422, 2951, 1050, 1030, 952, 931, 619	248 (46)	MALDI-TOF: 626 $[M\text{-}4H_2O\text{-}ClO_4]^+$ (100%)
11.3 Ho^{III}**-18C6**	Found Calcd.	18.06 18.44	3.92 3.87	0.00 0.00	3397, 2955, 1049, 1029, 951, 931, 619	250 (57)	MALDI-TOF: 627 $[M\text{-}4H_2O\text{-}ClO_4]^+$ (100%)
11.4 Er^{III}**-18C6**	Found Calcd.	14.55 17.97	4.004. 02	0.150.00	3422, 2951, 1050, 1030, 952, 931, 619	247 (62)	MALDI-TOF: 630 $[M\text{-}4H_2O\text{-}ClO_4]^+$ (100%)

Table 4.11 Selected characterization data for complexes **11.1**-**11.4**.

X-ray quality single crystals were obtained and the molecular structures of all four complexes were determined by X-ray crystallography (Table 4.12).

	11.1 (Tb^{III}-18C6)	**11.2** (Dy^{III}-18C6)	**11.3** (Ho^{III}-18C6)	**11.4** (Er^{III}-18C6)
Space group	Hexagonal P61	Orthorhombic Pbcn	Monoclinic Pc	Monoclinic $P2_1/c$
# Complexes in unit cell	1	1	2	1
a, b, c (Å)	9.9031(5), 9.9031(5), 44.999(4)	13.4884(9), 22.4361(16), 16.9130(12)	9.7970(8), 17.8698(15), 14.8669(12)	9.8027(6), 17.8702(13), 14.8422(11)
α, β, γ (°)	90, 90, 120	90, 90, 90	90, 100.228(3), 90	90, 100.180(3), 90
Volume ($Å^3$)	3821.87	5118.33	2561.39	2559.07
Min. Ln···plane (Å)	0.265	0.247	0.272	0.272
Min. Ln···Ln (Å)	8.501	8.573	8.878	8.868
Min. Ln-O-Ln (°)	102.9(2)	104.7(1)	98.3(2)	98.0(1)
$Ln\cdots O_{water}$ (Å)	2.356(5)-2.365(4)	2.349(3)-2.377(3)	2.327(5)-2.357(8)	2.316(3)-2.336(3)
$Ln\cdots O_{crown}$ (Å)	2.431(7)-2.545(4)	2.435(4)-2.487(3)	2.397(7)-2.496(6)	2.397(4)-2.468(4)

Table 4.12 Summary of parameters describing the crystal structures of **11.1** – **11.4**. Additional structural data are presented in the Appendix section.

Somewhat surprisingly, each complex crystallizes in a different unit cell. Although the unit cells and volumes are different, the structural topologies of the four complexes are very similar. In each case, the Ln^{III} ion is 9-coordinate, bound to the six oxygen atoms of the equatorially-coordinating 18-crown-6 ligand, as well as three axially bound water molecules: one above, and two below the equatorial plane (Figure 4.9 and Figure 4.10).The crown ether is puckered in each complex, with minimum O-Ln-O angles in the range of 98.0(1) – 104.7(1)°. The Ln^{III} lies in the mean plane formed by the 6 crown ether oxygen atoms, with small deviations from the best plane in the range 0.247 – 0.272 Å, Figure 4.9.

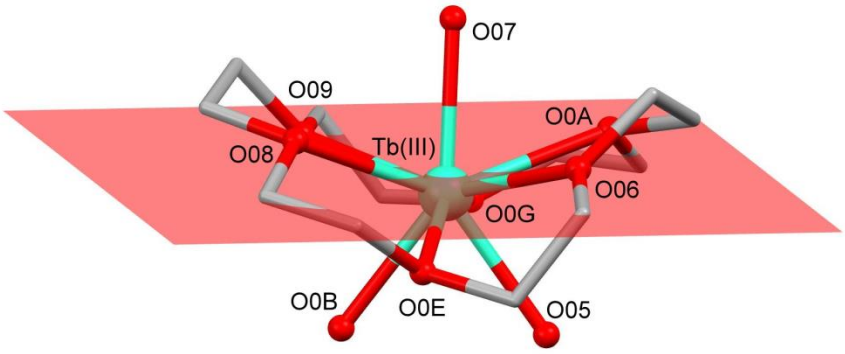

Figure 4.9 View of the molecular structures of **11.1** (Tb^{III}-18C6), showing the very slight deviation of Tb^{III} from the mean plane formed by the crown ether oxygen atoms O(A), O(6), O(E), O(8), O(9), and O(G). Hydrogen atoms are omitted for clarity.

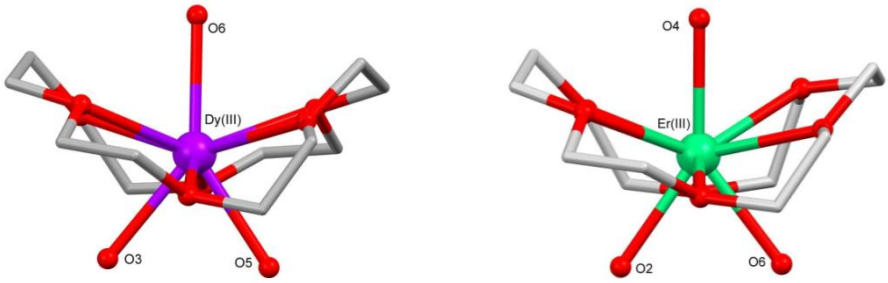

Figure 4.10 View of the molecular structures of **11.2** (Dy^{III}-18C6, left) and **11.4 (**Er^{III}-18C6, right**)**. Hydrogen atoms and perchlorate counter ions are omitted for clarity.

Complexes **11.1 (**Tb^{III}-18C6), **11.2 (**Dy^{III}-18C6), and **11.4 (**Er^{III}-18C6) contain one unique complex in each unit cell (Figure 4.9 and Figure 4.10), while the Ho^{III} complex **11.3** has two independent complexes in the unit cell (Figure 4.11). Examining the crystal packing of each complex reveals that the molecules pack in a 3-D network,

with the directly coordinating water molecules hydrogen-bonded to perchlorate counter ions. The hydrogen bonds for all four complexes are in the range of 2.693-3.031 Å.

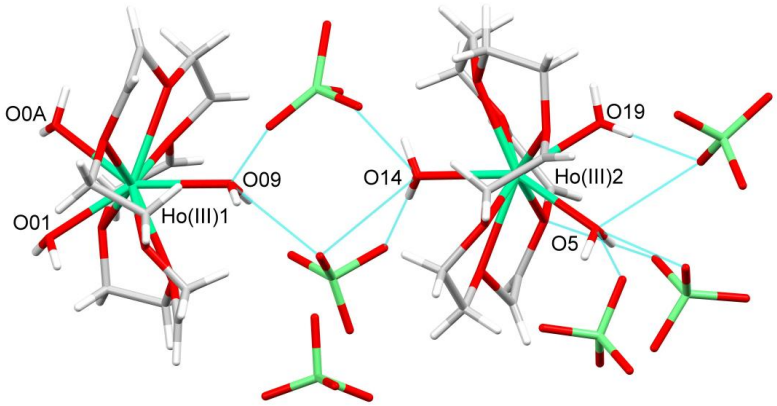

Figure 4.11 View of the molecular structure **11.3**, showing the two complexes of the unit cell, hydrogen-bonded via perchlorate counter ions, with O···O distances ranging from 2.750 Å (O14···OJ) to 3.031 Å (O0B···O0M).

The coordination geometry of each Ln^{III} center was investigated using CSMs, and the coordination sphere of each of the four complexes most closely resembled a muffin geometry (CSMs = 1.13 – 1.62, Table 4.13). The Ho^{III} and Er^{III} complexes **11.3** and **11.4** display a smaller deviation from the higher symmetry capped square antiprismatic geometry than the Tb^{III} and Dy^{III} complexes **11.1** and **11.2** (CSMs = 1.75 and 1.59 *vs.* 2.26 and 2.12 respectively).

Polyhedron	$Tb^{III}_{11.1}$	$Dy^{III}_{11.2}$	$Ho^{III}_{11.3}$	$Er^{III}_{11.4}$
EP-9	32.49	33.32	34.44	34.30
OPY-9	22.50	22.65	22.54	22.98
HBPY-9	16.67	16.07	16.91	17.04
JTC-9	13.89	14.55	14.91	15.10
JCCU-9	7.63	8.86	7.18	7.84
CCU-9	6.61	7.60	6.13	6.69
JCSAPR-9	3.22	3.06	2.81	2.67
CSAPR-9	2.26	2.12	**1.75**	**1.59**
JTCTPR-9	3.36	4.08	3.21	3.20
TCTPR-9	3.16	3.02	2.25	2.35
JTDIC-9	11.7	12.66	12.78	12.38
HH-9	6.26	6.41	7.48	7.66
MFF-9	**1.62**	**1.60**	**1.32**	**1.13**

Table 4.13 Continuous shape measures (CSMs) of the 9-coordinate Ln^{III} coordination polyhedra in complexes **11.1-11.4**. The values in red indicate the closest polyhedra for each complex according to the CSMs.

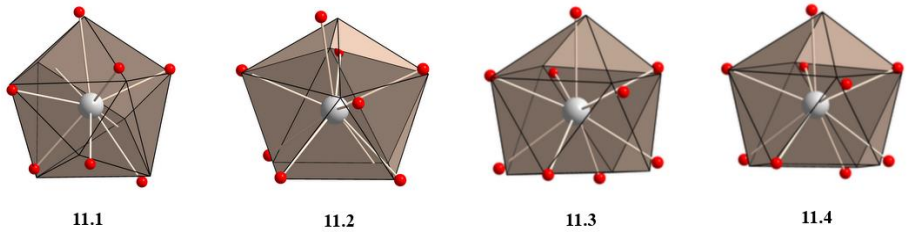

Figure 4.12 Coordination spheres of (left to right): $Tb^{III}_{11.1}$, $Dy^{III}_{11.2}$, $Ho^{III}_{11.3}$, and $Er^{III}_{11.4}$. Colour code: grey = Ln^{III}, red = O, beige = idealized polyhedra.

Following the structural characterization of an array of Ln^{III}-crown ether complexes, our next objective was to probe how turning the size of the macrocyclic cavity affects their electronic and magnetic properties. Given the observed structural topologies, we carried out physical studies in two parts: first, the magnetic and electronic properties of the half- and *pseudo*-sandwich structures **9.1** (Dy^{III}-12C4) and **10.1** (Dy^{III}-15C5) were studied and compared; and secondly, the magnetic properties of the four

'equatorial' complexes **11.1** – **11.14** prepared from 18C6 and the later lanthanides Tb^{III}-Er^{III} were studied. These two families are pictorially summarized in Table 4.14.

	$Tb(ClO_4)_{3(aq)}$	$Dy(ClO_4)_{3(aq)}$	$Ho(ClO_4)_{3(aq)}$	$Er(ClO_4)_{3(aq)}$
12C4	-	half-sandwich (9.1) 	-	-
15C5	-	pseudo-sandwich (10.1) 	-	-
18C6	eq. complex (11.1) 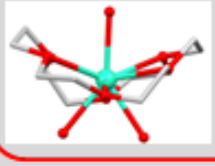	eq. complex (11.2) 	eq. complex (11.3) 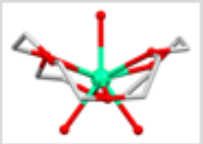	eq. complex (11.4) 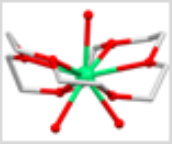

Table 4.14 The two families of Ln^{III}-crown ether complexes selected for detailed analysis.

4.3 Magnetic, electronic and luminescence studies on 9.1 and 10.1

4.3.1 Magnetic studies on 9.1 and 10.1

Both dc and ac magnetic measurements were performed on the 'axial' family of complexes: the half-sandwich **9.1** (Dy^{III}-12C4) and the *pseudo*-sandwich **10.1** (Dy^{III}-15C5).

Dc susceptibility measurements were carried out in an applied field of 0.1 T, over the temperature range 5 – 300 K. Above 100 K, χT values of 14.30 and 13.77 $cm^3 \cdot K \cdot mol^{-1}$ were observed for **9.1** (Dy^{III}-12C4) and **10.1** (Dy^{III}-15C5) respectively (Figure 4.13). These values are in good agreement with the theoretical χT value of 14.17 $cm^3 \cdot K \cdot mol^{-1}$ for a non-interacting Dy^{III} ion ($^6H_{15/2}$, S = $^5/2$, L = 5, g = $^4/3$). The value of χT decreases rapidly below 40 K for complex **9.1** and 25 K for **10.1**, due to thermal depopulation of the M_J sub-levels of the $^6H_{15/2}$ ground multiplet.

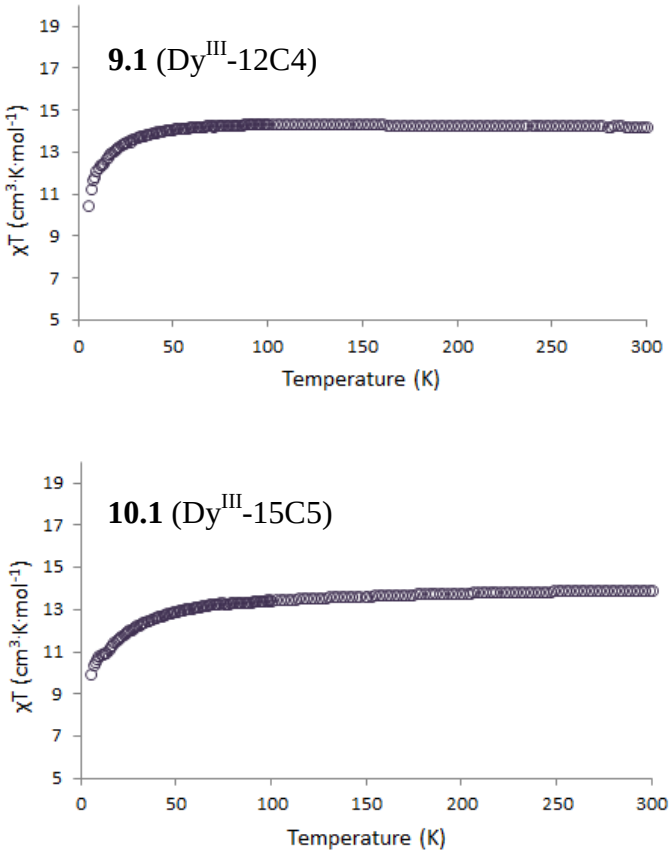

Figure 4.13 Plots of χT *vs.* temperature for **9.1** (top) and **10.1** (bottom) in a field of 0.1 T from 5 - 300 K.

Plots of $1/\chi$ *vs.* temperature were fit to the Curie-Weiss law, giving C = 14.33 ± 0.01 $cm^3 \cdot K \cdot mol^{-1}$ and C = 14.11 ± 0.01 $cm^3 \cdot K \cdot mol^{-1}$ for **9.1** and **10.1** respectively.

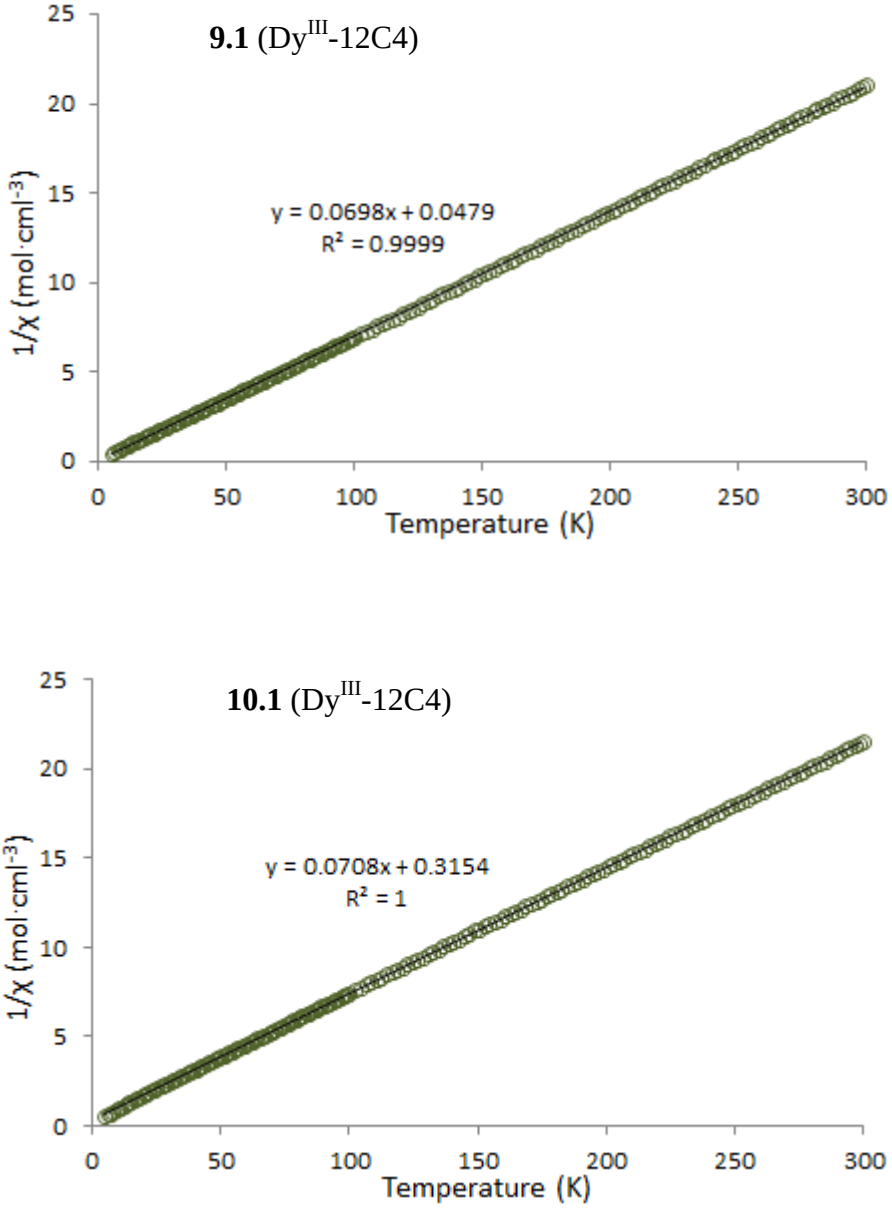

Figure 4.14 Plots of $1/\chi$ *vs.* temperature for **9.1** (top) and **10.1** (bottom) in a field of 0.1 T from 5 - 300 K. Black lines are a best fit to the Curie-Weiss equation.

In order to study the dynamic magnetic properties of the two half-sandwich complexes, *ac susceptibility measurements* were performed using an oscillating field of 3.5 Oe in various applied static fields ranging from 0 to 5 kOe. Measurements were carried out from 2–15 K, over 10–17 frequencies ranging from 5–10,000 Hz. The *pseudo*-sandwich complex **10.1** (Dy^{III}-15C5) displayed a frequency-dependent χ'' signal in zero dc field, characteristic of an SMM. However, full maxima in the plot of χ'' *vs.* temperature were not observed (Figure 4.15).

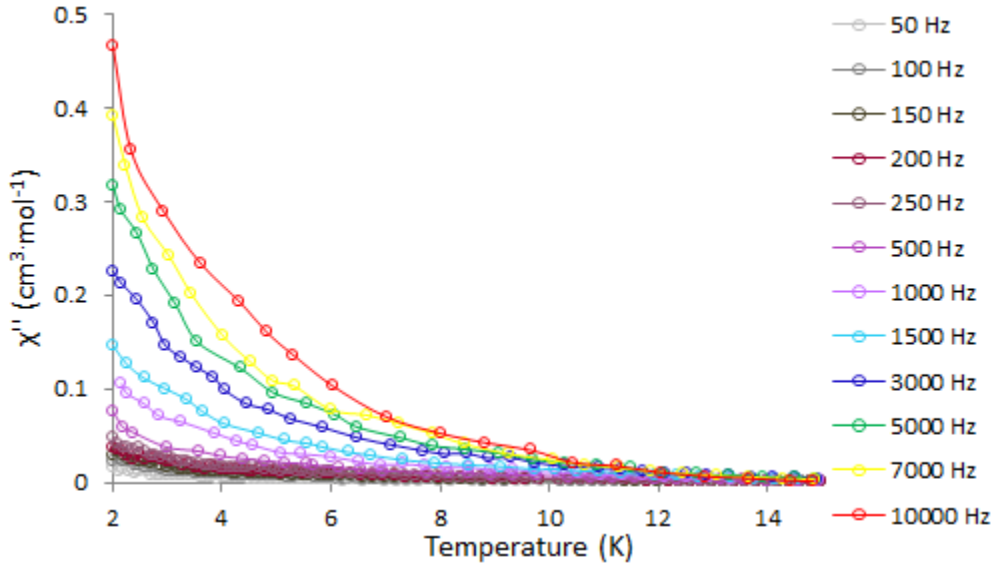

Figure 4.15 χ'' versus temperature for **10.1** (Dy^{III}-15C5) in zero applied dc field, from 2-15 K.

In order to resolve the maximum by removing the degeneracy of the M_J states between which quantum tunnelling might occur, a small static field of 300 Oe was applied. The frequency- and temperature-dependence of the out-of-phase component of the ac susceptibility is shown in Figure 4.16 and 4.17. The complex displayed classic

SMM behaviour below 15 K, with complete maxima emerging (Figure 4.16). Both the in-phase (χ′, Figure 4.16 top) and out-of-phase (χ″, Figure 4.16 bottom and Figure 4.17) components of the susceptibility show frequency dependence, consistent with slow relaxation of the magnetization.

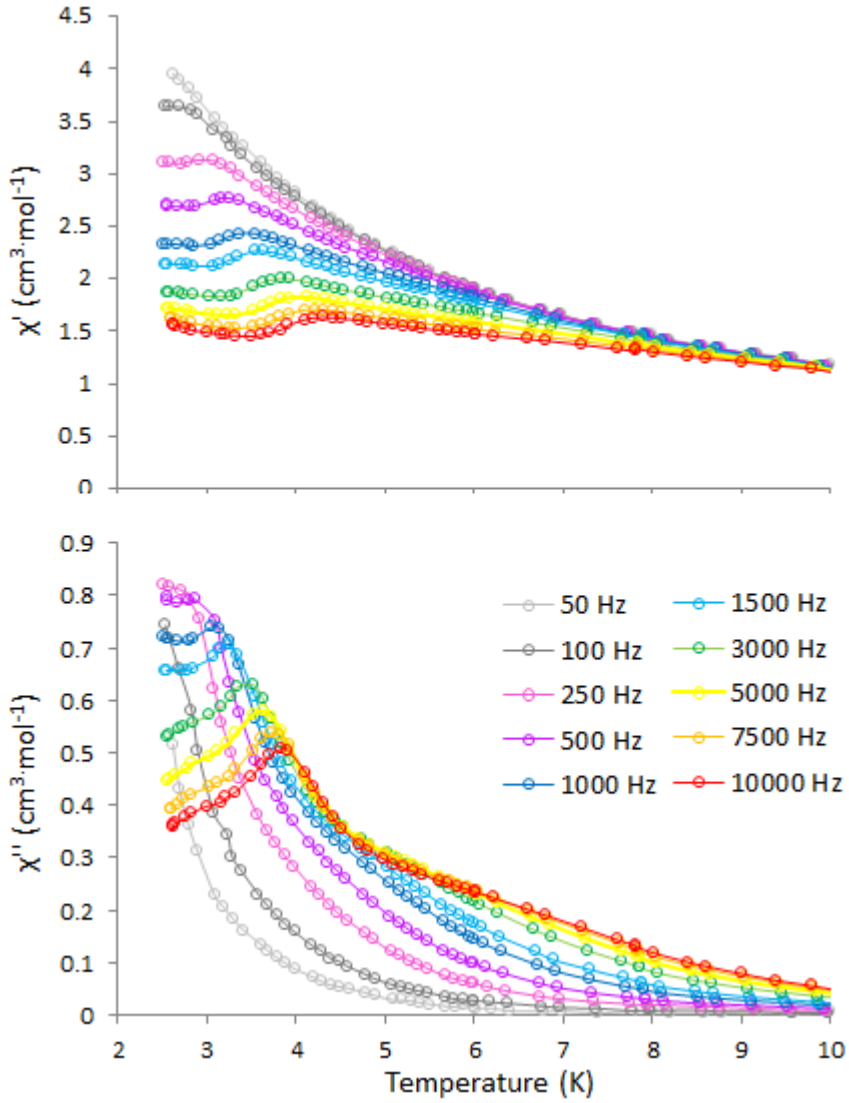

Figure 4.16 χ′ (top) and χ″ (bottom) versus temperature for **10.1** (Dy^{III}-15C5) in 300 Oe applied dc field, below 10 K.

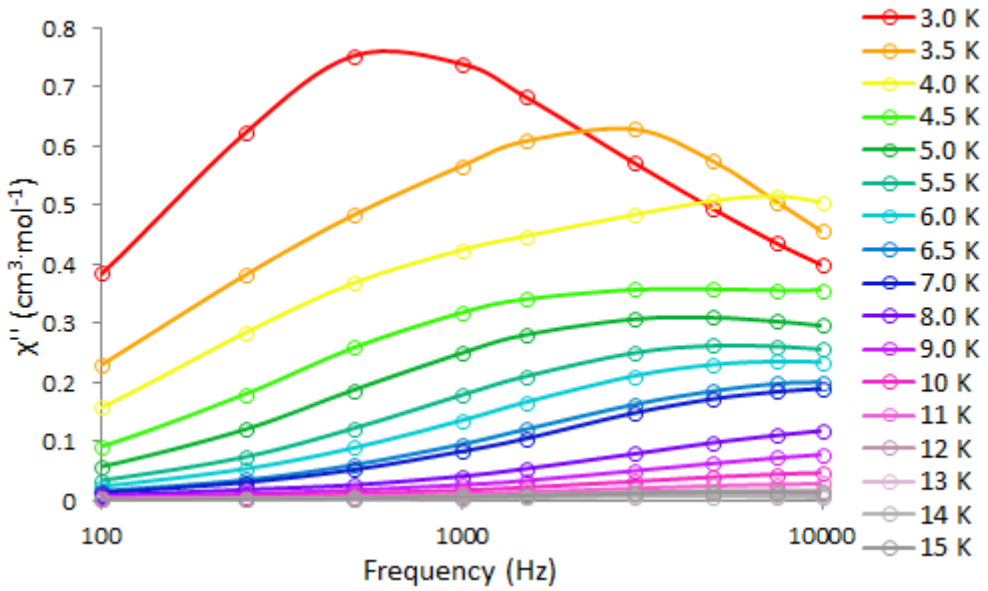

Figure 4.17 χ'' versus frequency for **10.1** (Dy^{III}-15C5) in 300 Oe applied dc field, from 3-15 K.

In order to probe the mechanisms of relaxation of the complex, the χ' *vs* χ'' data in a 300 Oe static field were examined. Below 5 K, several of the χ' *vs* χ'' semicircles are visibly kinked (Figure 4.18), indicative of two partially merged arcs, each corresponding to a distinct relaxation domain. That is, the sharp peak at low temperatures in χ'' (Figure 4.16) comprises contributions from two relaxation pathways. As was discussed in Chapter 3, a single relaxation domain may be fit to the Cole-Cole model, which describes ac susceptibility as:

$$\chi(\omega) = \chi_S + \frac{\chi_T - \chi_S}{1 + (i\omega\tau_c)^{1-\alpha}}$$

where $\omega = 2\pi f$, χ_T is the equilibrium susceptibility, χ_S is the adiabatic susceptibility, τ_c is the temperature-dependent relaxation time, and α is a measure of the dispersivity of

relaxation times. In the case of complex **10.1**, the susceptibility behaviour below 5 K is due to contributions from two distinct relaxation domains. The relaxation in this temperature region can thus be described by the sum of two combined, modified Debye functions:[273]

$$\chi(\omega) = \chi_{S1} + \frac{\chi_{T1} - \chi_{S1}}{1 + (i\omega\tau_{c1})^{1-\alpha1}} + \chi_{S2} + \frac{\chi_{T2} - \chi_{S1}}{1 + (i\omega\tau_{c2})^{1-\alpha2}}$$

The χ' *vs* χ'' data within 0.5 K of the sharp maximum at 4.0 K (10,000 Hz) was modelled using the above equation (Figure 4.18).

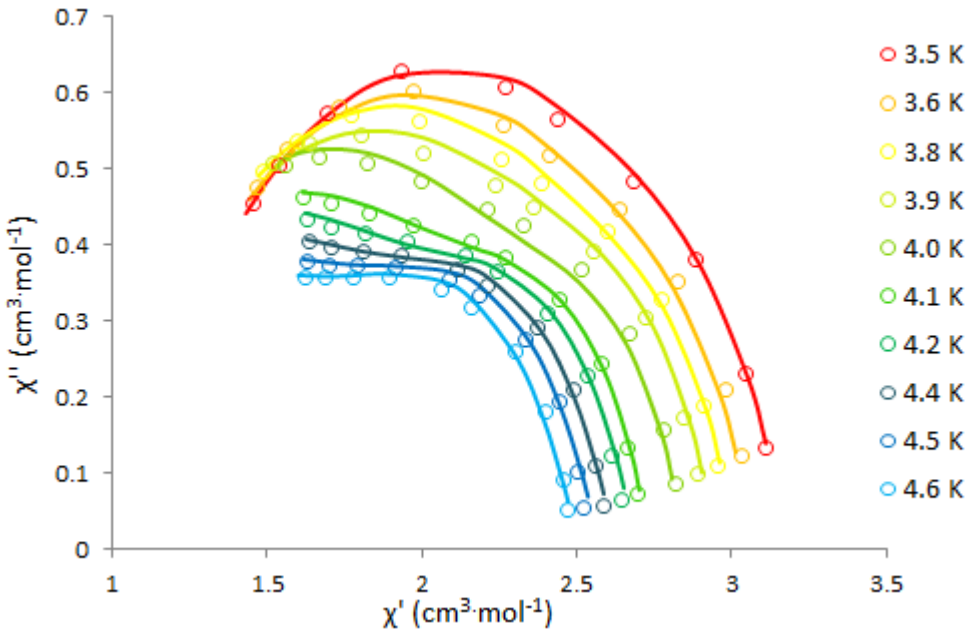

Figure 4.18 χ' versus χ'' for **10.1** in a 300 Oe dc field below 5 K. Open circles represent the observed data, while lines are the best-fit to a generalized two-component Debye model (see text).

The resulting calculated temperature-dependent relaxation times, τ_c, were subsequently fit to the Arrhenius equation, in order to extract the parameters describing each pathway.

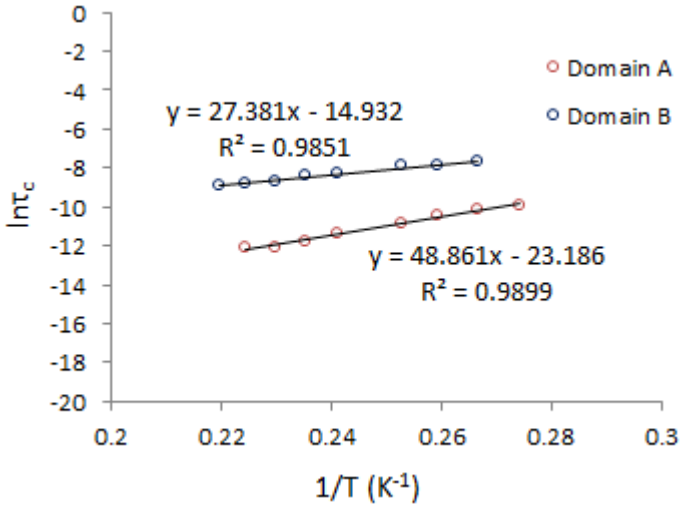

Figure 4.19 Plot of 1/T *vs.* τ_c for **10.1** (Dy^{III}-15C5) below 5 K, under a static field of 300 Oe and an oscillating field of 3.5 Oe. Points are calculated from experimental values, while lines are a best fit to the Arrhenius equation.

The two components of the magnetic relaxation comprise one domain with U_{eff} = 48.9 ± 2.0 K (34.0 ± 1.4 cm^{-1}) and τ_0 = (8.52 ± 4.26) x 10^{-11} s (domain A), and a second domain with U_{eff} = 27.4 ± 1.4 K (19.0 ± 1.0 cm^{-1}) and τ_0 = (3.27 ± 1.09) x 10^{-7} s (domain B). The clear temperature dependence of both pathways shown in Figure 4.19 indicates that each domain has a thermal component; neither may be assigned to a pure quantum tunneling mechanism. The small α parameter for domain B (0.08) suggests that a single mechanism is at play within this domain, while an α value of 0.36 for domain A would indicate the presence of multiple overlapping relaxation mechanisms within this domain.

Above 5 K, the magnetic behaviour may be modelled using a single-component Cole-Cole equation (Figure 4.20).

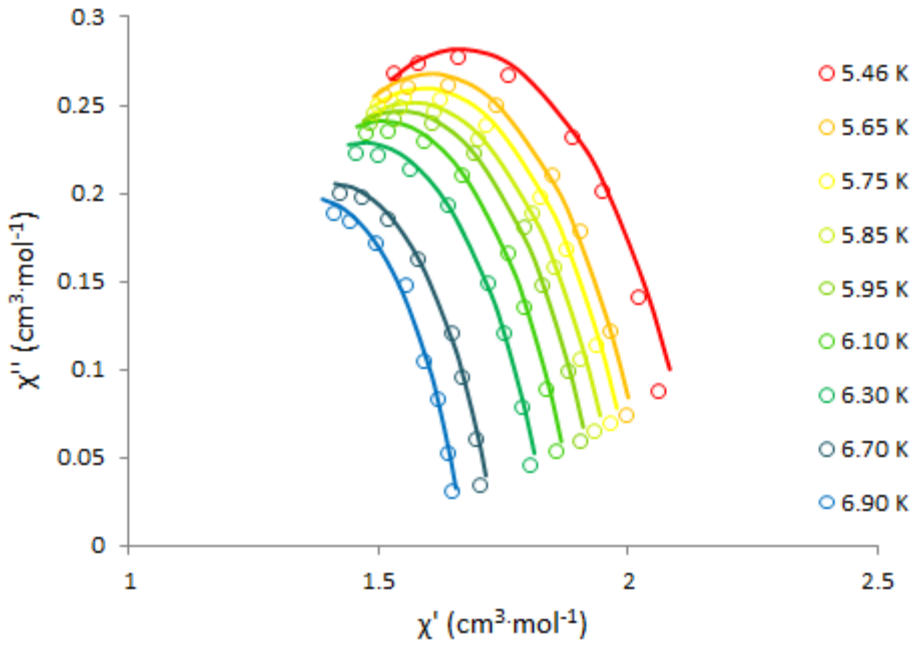

Figure 4.20 χ' versus χ'' for **10.1** (Dy^{III}-15C5) in a 300 Oe dc field, above 5 K. Open circles represent the observed data, while lines are the best-fit to the Cole-Cole equation.

A fit of the 1/T *vs.* τ_c data to the Arrhenius equation (Figure 4.21) yielded an energy barrier of 21.2 ± 0.4 K (14.7 ± 0.3 cm^{-1}) and a pre-exponential factor of (6.57 ± 0.49) × 10^{-7} s. An α value of 0.30 indicates that once again, several pathways are contributing to the observed magnetic behaviour characterized by these values.

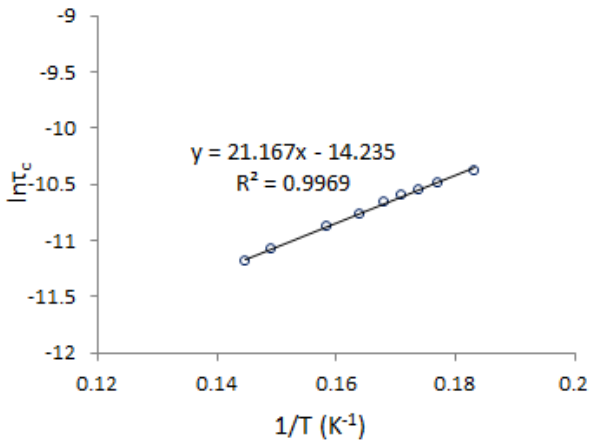

Figure 4.21 Plot of 1/T *vs.* τ_c for **10.1** (Dy^{III}-15C5) above 5 K, under a static field of 300 Oe and an oscillating field of 3.5 Oe. Points are calculated from experimental values, while lines are a best fit to the Arrhenius equation.

The ac magnetic susceptibility response of complex **10.1** (Dy^{III}-15C5) is summarized in Table 4.15.

Temperature	Domain	U_{eff} (cm^{-1})	τ_0 (s)	α
3.5 – 4.5 K	A	34.0 ± 1.4	(8.52 ± 4.26) x 10^{-11}	0.36
	B	19.0 ± 1.0	(3.27 ± 1.09) x 10^{-7}	0.08
5.5 – 7 K	-	14.7 ± 0.3	(6.57 ± 0.49) × 10^{-7}	0.30

Table 4.15 Summary of the parameters describing the slow relaxation of the magnetization of complex **10.1** (Dy^{III}-15C5).

The values suggest that the dominant pathway above 5 K is the same pathway present in domain B below 5 K, while domain A is 'switched off' above 5 K. The observation of two distinct, well-resolved pathways for magnetic relaxation at a single temperature, seen below 5 K for **10.1** (Dy^{III}-15C5), was first reported by Long in 2010,[283]

and remains a rarity among mononuclear SMMs,[125,272,284-286] although similar divergent behaviour was observed for the family of Ln-POM SMMs which were magnetically characterized by Coronado and co-workers.[275,287,288]

To our surprise, the half-sandwich complex **9.1** (Dy^{III}-12C4) displayed very different behaviour. The out-of-phase response of the ac susceptibility in the absence of an applied dc field appeared almost negligible (Figure 4.22) with no evidence of the maximum in χ'' which would be expected for an SMM. In order to investigate how various static fields might affect the magnetic response, dc fields between 300 – 5000 Oe were applied. In an applied field of 800 Oe, a strong out-of-phase response is observed below 6 K, which resolves to give maxima in applied fields greater than 1500 Oe (Figure 4.23).

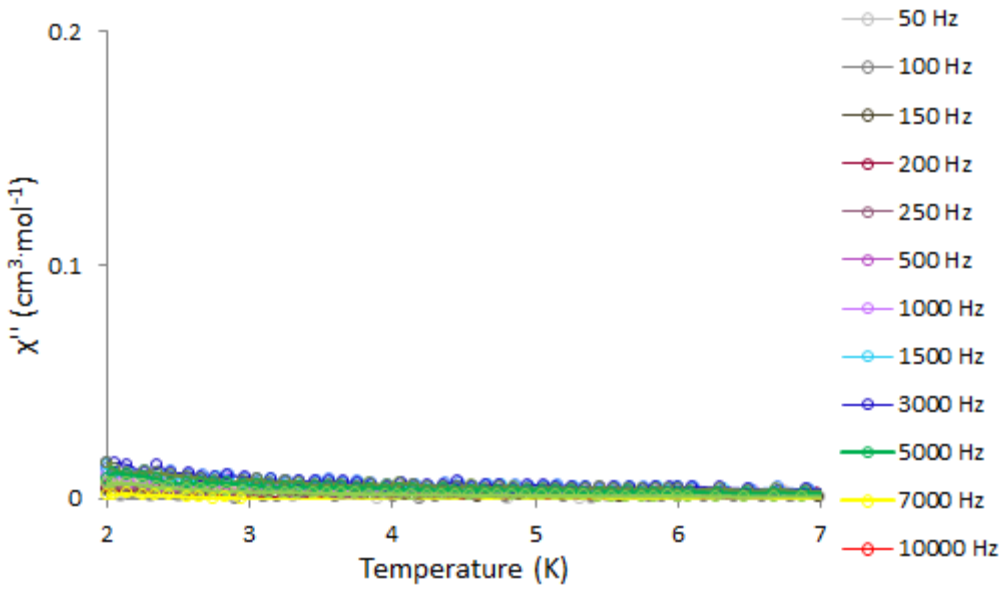

Figure 4.22 χ'' versus temperature for **9.1** (Dy^{III}-12C4) in zero applied dc field, below 7 K.

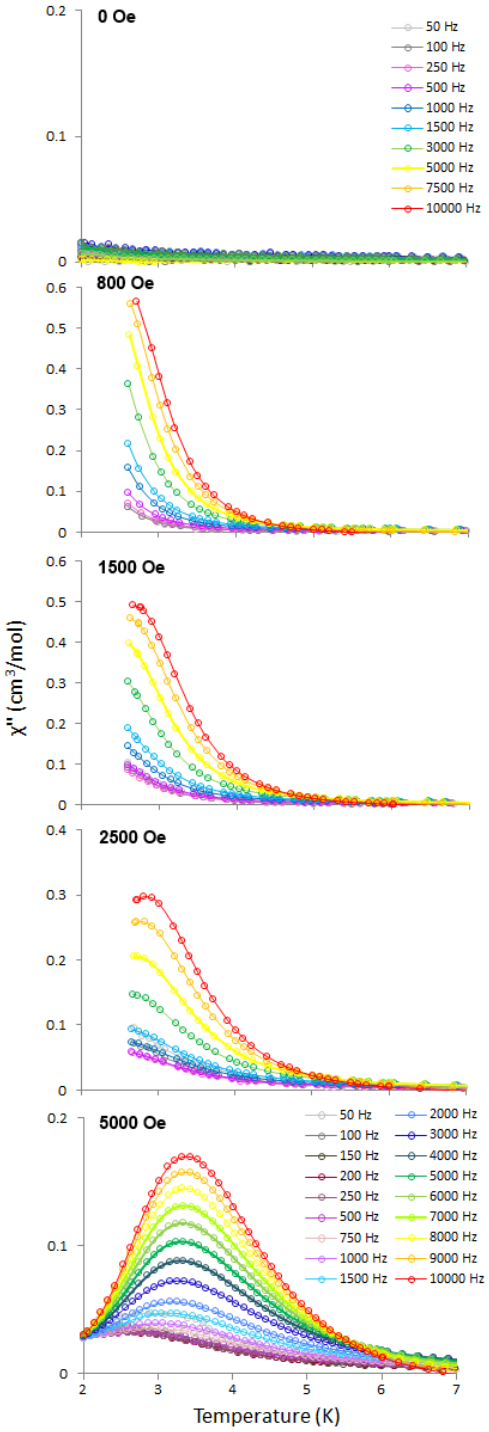

Figure 4.23 χ'' *vs.* temperature plots for **9.1** (Dy^{III}-12C4) in various applied dc fields, below 7 K.

Although the magnitude of the out-of-phase response increases significantly at higher frequencies, the temperature at which the maximum occurs is only very slightly frequency dependent, which is more characteristic of long range magnetic order than SMM-like behaviour. In order to rule out the presence of long-range ordering, zero-field heat capacity measurements were performed from 2-50 K, and showed no sign of any abrupt λ-type anomaly (Figure 4.24). In addition, M *vs.* H measurements were carried out at 3 K, and no hysteresis was observed, confirming the absence of ferromagnetic order.

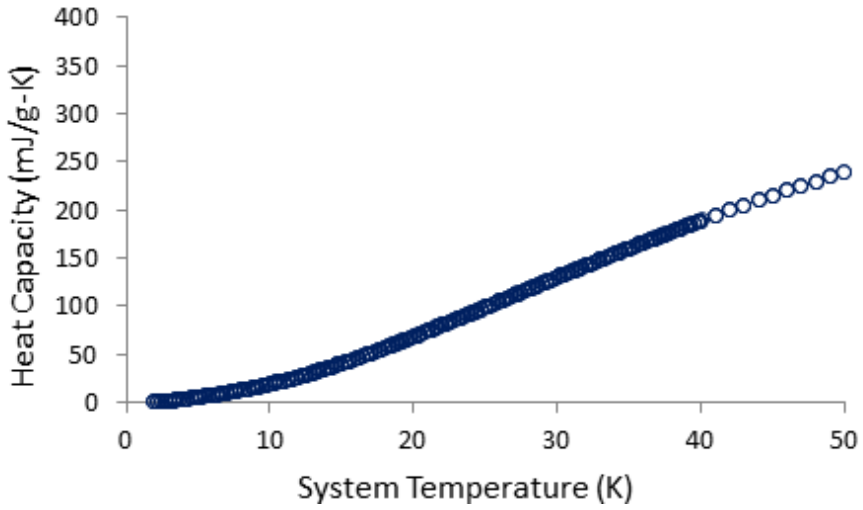

Figure 4.24 Plot of heat capacity *vs.* temperature for **9.1** (Dy^{III}-12C4). The smooth increase in heat capacity upon warming is associated with the phonon (lattice) contribution to the specific heat.

As was described above, a strong out-of-phase susceptibility response with a frequency-dependent magnitude is observed as increasing dc fields are applied to **9.1** (Dy^{III}-12C4). However, the in-phase susceptibility displays no frequency dependence even in an applied field of 5 kOe, and a plot of χ' *vs.* χ'' at various temperatures (Figure 4.25) does not fit the Cole-Cole relaxation model traditionally applied to SMMs.

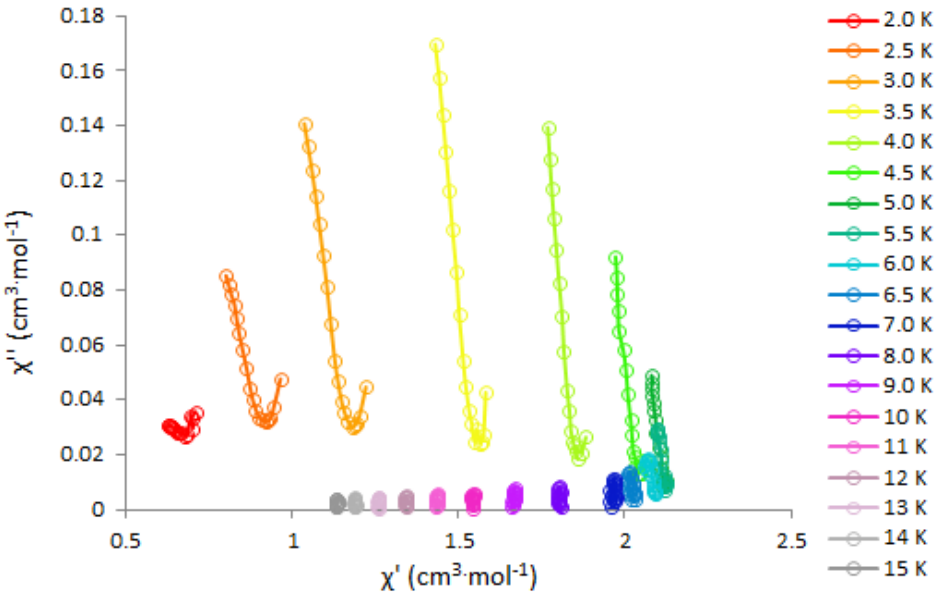

Figure 4.25 χ' *vs* χ'' for **9.1** (Dy^{III}-12C4) in a 5 kOe dc field, from 2-15 K. Lines are a guide for the eyes only.

In light of these experimental observations we assign the unusual temperature independent behaviour of χ'' as being due to a quantum tunnelling mechanism that is very fast in comparison to what is usually observed for SMMs from Cole-Cole plots. Since the mechanism is a non-thermal process, the parameters describing the relaxation pathway are not temperature dependent; that is, a single value for the tunnelling rate τ_c characterizes the whole regime. In addition, when a single tunnelling mechanism is at play, the dispersivity variable α will equal 0. Given that the out-of-phase susceptibility may be described by the Cole-Cole function as:

$$\chi''(\omega) = (\chi_T - \chi_S)\frac{(\omega\tau_c)^{1-\alpha}\sin(\alpha\pi/2)}{1+(\omega\tau_c)^{2\alpha}},$$

since τ_c is fixed, and $\alpha = 0$, the temperature dependence of χ'' depends solely on the temperature dependence of χ_T and χ_S. Whilst the adiabatic susceptibility χ_S does not

change significantly, the equilibrium susceptibility, χ_T, tends to follow Curie-like behaviour and we can approximate $\chi'' \propto \chi_T \propto 1/T$. In light of this, the zero-field ac data, in which only pure quantum tunnelling appears to occur, was re-examined. Although the out-of-phase signal is very small, a good linear fit to the experimental zero field χ'' *vs.* 1/T data was observed (Figure 4.26), consistent with rapid relaxation via a single temperature-independent pathway.

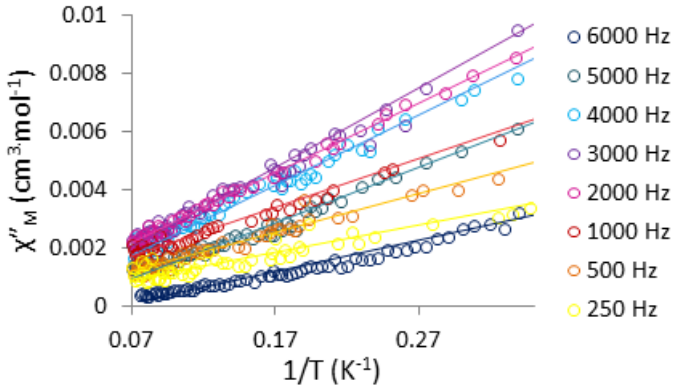

Figure 4.26 χ'' versus1/T for **9.1** (Dy^{III}-12C4) at various frequencies in zero applied dc field, showing the linear, Curie-like relationship between χ'' and 1/T. Lines are a guide for the eyes only.

In addition, the slope of each χ'' and 1/T plot ($d\chi''/d(1/T)$) was plotted as a function of frequency. The turning point of the plot at 3000 Hz corresponds to the point at which $\omega\tau_c = 1$. From this, the τ_c value for the pure quantum tunnelling mechanism of **9.1** (Dy^{III}-12C4) in zero field was determined: τ_c = ~0.3 ms. This value is comparable to those reported by Coronado and co-workers for a series of polyoxometallate SMMs.[24]

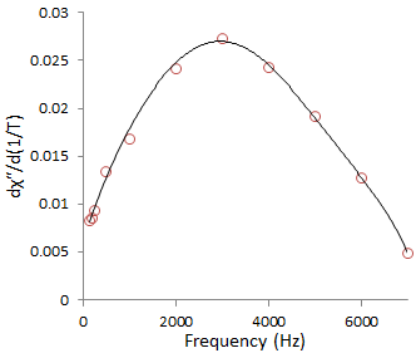

Figure 4.27 Plot of dχ″/d(1/T) *vs* frequency for **9.1** (Dy^{III}-12C4). Line is a guide for the eyes only.

In order to determine whether the relaxation in **9.1** (Dy^{III}-12C4) is assisted by dipolar interactions between neighbouring Dy^{III} ions, complex **9.1** was doped into the analogous diamagnetic Y^{III} lattice in a ratio of Dy/Y = 12:88, as determined by ICP-MS measurements. The isostructural nature of the Dy^{III} complex **9.1**, the analogous Y^{III} complex **9.3**, and the doped Dy^{III}/Y^{III} sample **9.1b** was confirmed by X-ray diffraction measurements (Table 4.16).

	9.1	**9.3**	**9.1b**
Crystal system	monoclinic	monoclinic	monoclinic
Space group	$P2_1/c$	$P2_1/c$	$P2_1/c$
***a*/Å**	13.1195(7)	13.139(1)	13.10
***b*/Å**	10.2129(6)	10.2303(7)	10.19
***c*/Å**	17.5681(10)	17.5916(14)	17.55
α/°	90	90	90
β/°	93.941(2)	93.866(3)	93.72
γ/°	90	90	90
Volume/Å^3	2348.4(2)	2359.2(3)	2342

Table 4.16 Comparison of unit cell dimensions for **9.1**, the yttrium^{III} analogue of **9.1** (**9.3**), and the doped sample of **9.1** (**9.1b**).

Ac susceptibility measurements were performed on the doped sample in a range of dc fields. Similar behaviour to that recorded for the undiluted sample of **9.1** (Dy^{III}-12C4) was observed, indicating that the magnetic response of **9.1** is associated with the behaviour of the single ion. A negligible out-of-phase response was observed in the absence of an applied static field, while a single strong response was induced by the application of a small static dc field (Figure 4.28). The lack of any observed frequency-dependence in the magnetic response of the diluted sample suggests that the QTM is not assisted by dipolar interactions in the crystal lattice. In contrast, although identical ac susceptibility behaviour was recently reported for a mononuclear Dy^{III}-tetramethyl-aluminate complex, for that complex, dilution experiments suggest that dipolar interactions assisted the QTM.[116,289]

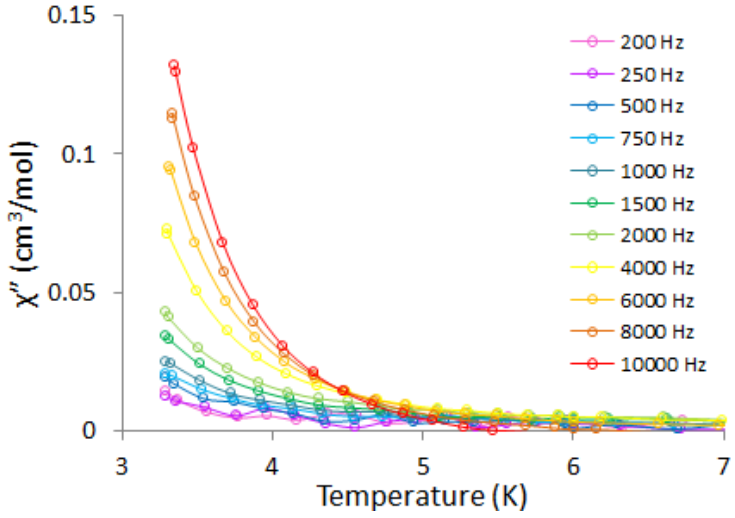

Figure 4.28 χ'' *vs* temperature plot for a magnetically diluted sample of **9.1** (**9.1b**, Dy/Y = 12:88) in a 1500 Oe applied dc field, below 7 K.

4.3.2 Ab initio studies on 9.1 and 10.1

As described above, ac magnetic measurements were used to experimentally determine the parameters surrounding the relaxation behaviour of **9.1** (Dy^{III}-12C4) and **10.1** (Dy^{III}-15C5) In particular, in zero dc field, no slow relaxation of magnetization was observed for **9.1**, while two relaxation processes were observed for **10.1** below 5 K.

In order to further understand the relaxation behaviour of these complexes, and confirm the experimental results, *ab initio* calculations were carried out on **9.1** and **10.1** using MOLCAS 7.8.[290] The following methods were implemented, in order to determine the components of the g-tensors and the relative energies of the Kramers doublets in the $^6H_{15/2}$ ground state of the Dy^{III} ions: SEWARD was used to compute the required one- and two-electron integrals; RASSCF was used to perform multi-configurational complete active space self-consistent field (CASSCF) calculation for the determination of the spin-free eigenstates; RASSI was used to mix the RASSCF wavefunctions; and finally SINGLE_ANISO was used to determine the anisotropic magnetic properties for each mononuclear system.

The coordinates of the atoms in **9.1** and **10.1** as the input for SEWARD were determined crystallographically, and were used without further geometry optimization. The active space for both systems was chosen to be the 9 electrons in the 7 4f-orbitals of the Dy^{III} ion. 'Relativistic Atomic Natural Orbital' (RCC-ANO) basis sets were selected to include the scalar relativistic terms where the dysprosium ions were treated at the VQZP level (9s8p6d4f3g2h), the coordinating oxygen atoms were treated at the VTZP level (4s3p2d1f) and all other atoms were treated at the VDZ level (3s2p for O and C, 4s3p for Cl, and 2s for H) for all models. The Dy^{III} ions were assigned the pseudo-spin S

= ½ for the calculations of the g-tensors of the eight Kramers doublets, and the main magnetic axes.

In order to determine an accurate representation of the electronic structure of each complex within the crystal lattice, several models were investigated. For complex **9.1** (Dy^{III}-12C4), the first model (9.1A. Figure 4.30) was the immediate coordination sphere: the coordinated 12-crown-4 and five water molecules. The second model (9.1B, Figure 4.30) involved the immediate coordination sphere as well as the three perchlorate anions and one water molecule in the asymmetric unit.

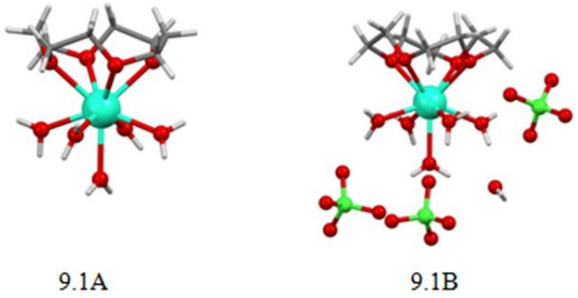

Figure 4.29 The two models investigated for complex **9.1** (Dy^{III}-12C4).

For complex **10.1** (Dy^{III}-15C5), the first model (10.1A, Figure 4.30) was again the immediate coordination sphere: the coordinated 15-crown-5 and four water molecules. The second model (10.1B, Figure 4.30) involved the immediate coordination sphere along with a second crown ether, one hydrogen-bonded water molecule and three hydrogen-bonded perchlorate anions. The third model (10.1C, Figure 4.30) comprised the asymmetric unit of the crystal structure: the immediate coordination sphere, a second 15-crown-5, and a lattice water molecule.

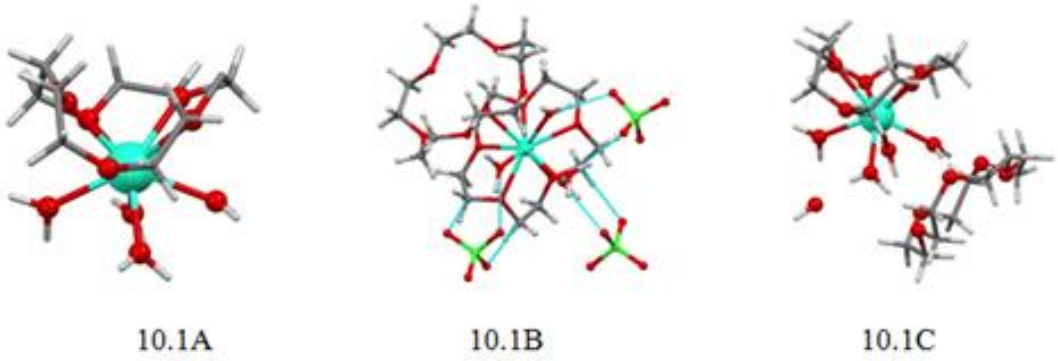

Figure 4.30 The three models investigated for complex **10.1** (Dy^{III}-15C5).

For the calculations of models 9.1A, 9.1B, 10.1A and 10.1B, only the sextets were considered (that is, $S_{Dy} = {}^{5}/_{2}$; $2S_{Dy}+1 = 6$), with 21 roots and no mixing from the quadruplets and doublets. However, in the calculations of the full model 10.1C, mixing of the quadruplets ($S_{Dy} = {}^{3}/_{2}$; $2S_{Dy}+1 = 4$) was considered also, with the quadruplets given 128 roots. No significant difference was observed in the energies of the 8 Kramers doublets calculated with and without the inclusion of quadruplets.

The Kramers doublets of the three lowest-lying energy states calculated for each of the models for **9.1** (Dy^{III}-12C4) and **10.1** (Dy^{III}-15C5) are presented in Table 4.9. Energies are given in wavenumbers.

J	9.1A	9.1B	10.1A	10.1B	10.1C
	0.000	0.000	0.000	0.00	0.000
15/2	34.386	33.083	20.560	58.224	45.528
	67.185	66.942	59.050	68.724	77.849
	98.283	89.758	104.802	112.954	110.527
	137.295	131.235	146.372	177.132	180.244
	153.553	159.251	172.515	234.354	239.466
	211.099	198.393	236.856	268.554	276.889
	269.128	245.699	319.435	369.180	376.751
	3016.365	3011.050	3013.524	3525.412	3002.778
13/2	3048.317	3049.813	3050.661	3578.595	3067.240
	3058.381	3067.427	3080.949	3627.942	3113.915
	3063.738	3091.087	3096.328	3647.843	3134.278
	3118.191	3107.826	3135.303	3680.367	3171.549
	3145.341	3129.249	3156.140	3699.792	3189.595
	3169.155	3152.617	3205.383	3776.225	3263.081
	5576.992	5575.112	5575.344	6071.999	5586.414
11/2	5617.031	5617.497	5624.523	6116.250	5637.116
	5647.751	5650.674	5656.378	6175.548	5699.984
	5684.009	5671.289	5689.806	6189.807	5726.415
	5717.813	5709.507	5740.490	6215.591	5756.563
	5751.463	5733.642	5779.931	6292.237	5835.245

Table 4.17 Energies (cm^{-1}) of the microstates of the three lowest lying *J* electronic states for the three models of complexes **9.1** and **10.1.**

The main components of the g-tensors for the 8 Kramers doublets of the $^{6}H_{15/2}$ level are shown below (Table 4.18). The values were calculated with strong spin-orbit coupling, for models 9.1A – 9.1B and 10.1A – 10.1C.

Doublet	9.1A	9.1B	10.1A	10.1B	10.1C
	0.617	0.903	0.809	0.599	0.258
1	1.316	1.156	5.858	0.190	0.516
	18.190	17.819	13.131	17.727	17.492
	0.539	1.189	1.522	0.201	0.835
2	1.783	1.871	2.714	0.729	3.085
	16.314	16.377	13.384	17.301	15.442

3	3.601 5.139 10.402	8.115 6.635 3.002	8.824 5.784 1.877	10.261 4.959 2.439	0.000 2.252 9.949
4	1.708 2.829 14.332	0.486 2.176 14.629	1.982 4.355 10.132	1.522 5.821 8.527	9.133 6.306 3.036
5	0.912 4.937 11.328	1.515 3.111 10.822	9.021 6.266 2.874	0.730 3.320 12.314	0.708 3.468 11.625
6	11.379 5.819 0.046	10.089 7.735 0.391	0.219 1.340 16.586	0.329 1.234 17.749	0.330 1.122 17.521
7	2.268 2.499 12.527	7.600 5.636 3.587	1.668 2.223 16.001	1.125 1.567 16.293	1.285 1.985 15.943
8	0.528 1.726 17.426	0.817 2.785 16.888	0.286 0.790 18.669	0.214 0.509 18.774	0.182 0.424 18.781

Table 4.18 Main components of the g-tensors for the 8 Kramers doublets of the $^{6}H_{15/2}$ level.

The magnetic moments of both the ground (1) and first (2) excited states significantly depart from the Ising limit of $g_z = 20$ with $g_x = g_y = 0$, thus displaying some transverse anisotropy, supporting the ac magnetic data which reveals fast quantum tunneling processes in both species. The angles (°) between the main magnetic axes (Z_m) of successive states for the full models 9.1B and 10.1B are given in Table 4.19. The electronic ground state is denoted by 1, while 2, 3, 4 etc. refer to subsequent excited electronic states.

State	1	2	3	4	5	6	7	8
9.1	---	72.5	86.7	95.3	77.1	106.3	21.5	122.1
10.1	---	55.5	54.0	32.4	114.2	56.3	65.0	66.2

Table 4.19 The angles between successive electronic states for **9.1** and **10.1**.

The theoretically determined orientation of the magnetic moments for both the ground and first excited states of **9.1** (Dy^{III}-12C4) and **10.1** (Dy^{III}-15C5) are shown below (Figure 4.31).

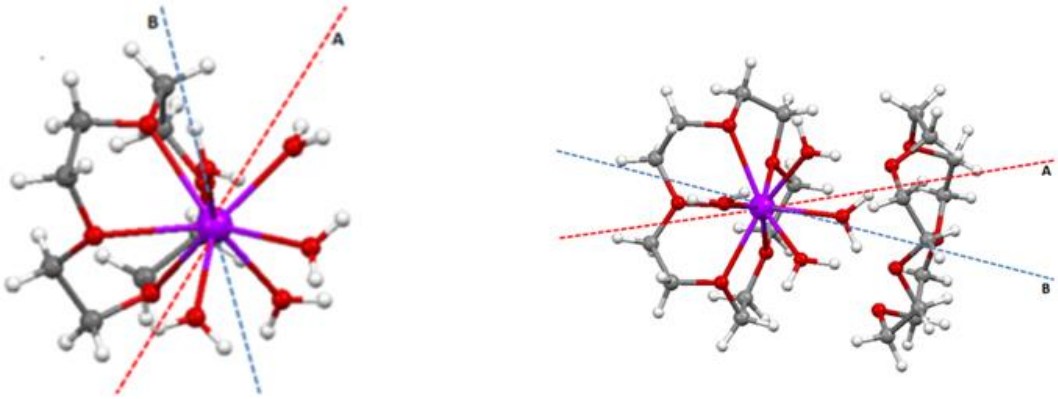

Figure 4.31 Calculated orientations of the principle magnetic axes of the Dy^{III} ions for the ground (A) and first excited (B) Kramers doublets for (left) **9.1** and (right) **10.1**. The values of the components of the relevant g-tensors are given in Table 4.19.

From the data presented in Table 4.18 and Table 4.19, it is clear that a consideration of species beyond the immediate coordination environment must be considered for an accurate representation of the electronic structure of the Dy^{III} centers within the crystal lattice. In the case of the *pseudo*-sandwich complex **10.1** (Dy^{III}-15C5), the model which best accounts for the experimental data is that which includes the

hydrogen-bonded water and perchlorate anions, as well as the second crown ether, since the Dy^{III} center is essentially encapsulated between the two crown ether ligands. For the half-sandwich complex **9.1** (Dy^{III}-12C4), it becomes particularly important to include the perchlorate anions in the model, since they are tightly hydrogen-bonded to the coordinated water molecules.[125] Thus models 9.1B and 10.1B most accurately describe the two complexes, and are thus considered to aid in the interpretation of the experimental magnetic data.

As Table 4.17 shows, the first excited state for the Dy^{III} ion in the *pseudo*-sandwich complex **10.1** (Dy^{III}-15C5), the ground state (1±) and the first (2±) and second (±3) excited states are well separated, consistent with the experimental observations of SMM behaviour. The theoretically calculated 1± → 2± energy gap of 58 cm^{-1} is larger than the magnetically-derived effective anisotropy barrier of 34.0 cm^{-1} for domain A of complex **10.1**, but this discrepancy is consistent with the observations of Sessoli and co-workers for the Dy^{III}-DOTA complex, and is accounted for by the fact that a small applied dc field changes the energies of the M_J microstates; and in addition, the *ab initio* calculations do not take into account quantum tunneling.[291] As previously discussed, complex **10.1** (Dy^{III}-15C5) displays multiple relaxation pathways. The *ab initio* results described above support the propositions that the two closely spaced relaxation processes below 5 K are consistent with quantum tunneling and Orbach mechanisms likely involving both the ground and first excited state Kramers doublets (Figure 4.32).[292] The much smaller 1± → 2± energy gap of calculated for the Dy^{III} ion in the half-sandwich

complex **9.1** (Dy^{III}-12C4) is consistent with the observation that this complex is not an SMM in zero dc field.

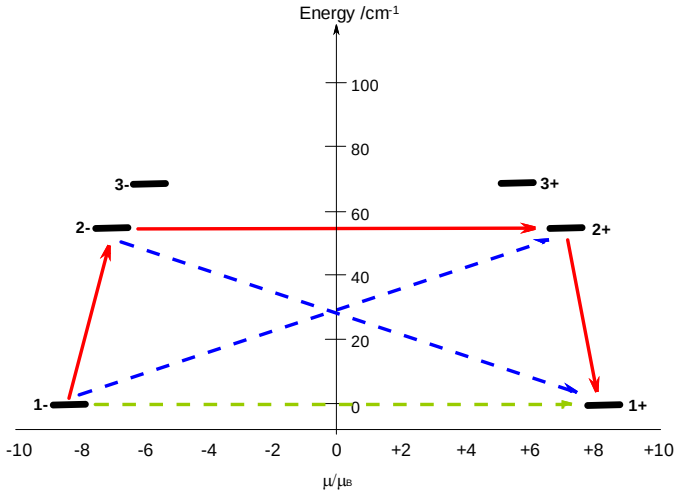

Figure 4.32 The low lying electronic structure for **10.1**, showing the lowest three Kramers doublets for the Dy^{III} ion and possible relaxation pathways (representative energies). The thick black lines represent the Kramers doublets as a function of their magnetic moment along the main axes of anisotropy. The green dashed line corresponds to quantum tunneling between the ground state doublets, while the solid red lines correspond to thermally assisted-QTM via the first and second excited state Kramers' doublets. Dashed blue lines show possible Orbach processes.

4.3.3 Luminescence properties of 9.1 and 10.1

The transitions of particular interest in lanthanide luminescence are the 4*f* - 4*f* transitions, because these transitions produce extremely sharp, narrow emission bands characteristic of a given metal. Although 4*f* - 4*f* transitions are 'forbidden' (highly improbable) by the Laporte parity selection rule, they can still occur in the presence of a ligand field which disrupts the orbital symmetry. As was discussed in depth in Section

1.4.3, the commercial applications of lanthanides exploit the sharp emission bands corresponding to transitions between electronic terms or levels (a change in L or J).[201] But lanthanide emission can also provide information regarding the energy differences between electronic M_J microstates: in theory, the fine splitting of the highest energy $f - f$ transition in the emission spectrum of a lanthanide can be modelled to provide a direct picture of the splitting of the ground J multiplet.

However, examples of mononuclear SMMs for which the fine structure of the f - f transition is resolved well enough to extract this information are scarce in the literature. In the ground-breaking paper mentioned previously, Sessoli and co-workers reported a remarkably detailed magnetic and structural study of a Dy^{III} complex of tetraaza-cyclododecanetetraacetate (DOTA).[293] The complex displays SMM behavior, with an anisotropy barrier of 42 cm^{-1} calculated from the magnetic data. The luminescence emission spectrum of the complex showed well-resolved peaks at 20800, 17500, and 15200 cm^{-1}, corresponding to $^4F_{9/2} \rightarrow {}^6H_J$ where J = 15/2, 13/2 and 11/2 respectively. The highest energy band shows well-resolved fine structure, corresponding to the Stark splitting of the ground state $^6H_{15/2}$ multiplet. Importantly, the energy gap between the two highest energy peaks is 53 ± 8 cm^{-1}, which is in reasonable agreement with the experimentally determined U_{eff} barrier of 42 cm^{-1}. This unprecedented correlation between the anisotropy barrier and Stark splitting confirmed that population of the first excited doublet would be sufficient to reverse the magnetization.[293] More recently, Long and coworkers synthesized a Dy^{III} complex incorporating a Zn^{II}-Schiff base antenna to enhance the luminescence.[294] The complex displayed SMM behavior, with U_{eff} = 27.38 cm^{-1} calculated from the ac magnetic data. The fine structure in the high-energy

luminescence band was assigned to transitions between the Stark sublevels of the $^4F_{9/2}$ and $^6H_{15/2}$ multiplets. The energy barrier to relaxation predicted from the sublevel separation was 44.1 $\pm$ 3.0 cm^{-1}. Long postulated that the difference between the magnetically-calculated and spectrally-observed energy barriers indicates that quantum tunneling or dipolar interactions are occurring.[294] Following this work, Long and co-workers reported an additional chiral, ferroelectric Zn^{II}/Dy^{III} complex displaying a rare combination of magnetism, Dy^{III} luminescence, and optical activity.[295]

With these examples in mind, the luminescence properties of complexes **9.1** (Dy^{III}-12C4) and **10.1** (Dy^{III}15C5) were studied via collaboration with Dr. Rute Ferreira. Emission spectra of each complex excited at 280 and 340 nm were collected at room and low temperatures (300 and 14 K). The spectra are presented in Figure 4.33, and reveal the characteristic luminescence of Dy^{III} ions, assigned to the $^4F_{9/2} \rightarrow {}^6H_{15/2\text{-}11/2}$ transitions.

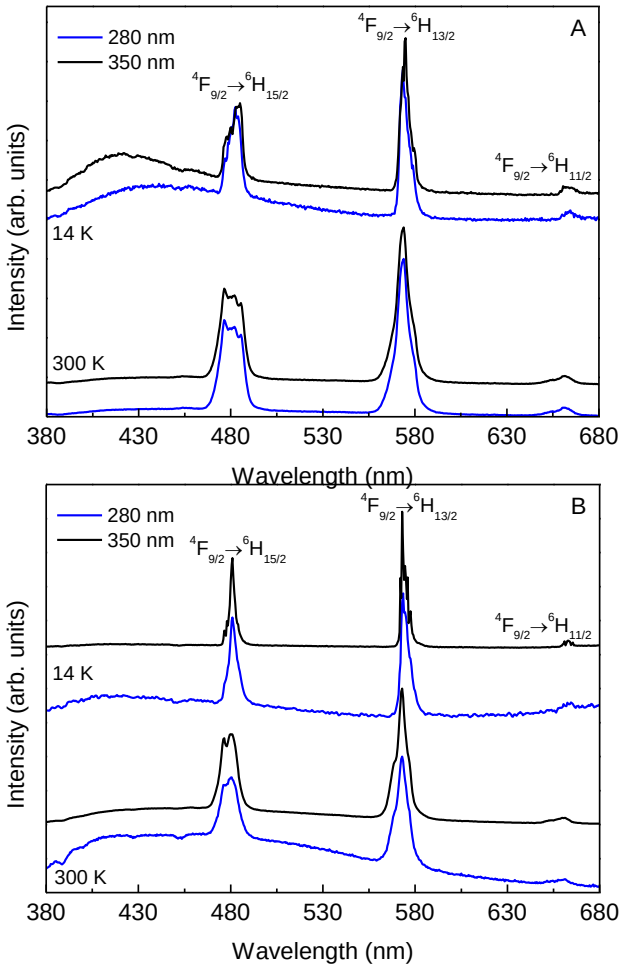

Figure 4.33 Emission spectra measured at 14 and 300 K for (A) **10.1** and (B) **9.1** excited at 280 nm and 350 nm.

In order to experimentally investigate the crystal field splitting of the ground state of the Dy^{III} ions in **9.1** (Dy^{III}-12C4) and **10.1** (Dy^{III}15C5), a low temperature (14 K) emission spectra was acquired on single crystals of each complex in the spectral region of the $^6F_{9/2}\rightarrow{}^6H_{15/2}$ transition (Figure 4.34, Figure 4.35). The $^6H_{15/2}$ level may undergo Stark splitting due to the crystal field to give a maximum of 8 microstates; this makes an unambiguous fit of the components of the transition difficult. For this reason, just the

high-energy region of the transition (20900-21100 cm^{-1}) was analysed, in order to estimate the energy difference between the ground level and the first excited state. Using a multi-Gaussian function fit, this spectral region was fit to two Stark components (labelled A_1 and A_2 in Figures 4.35 and 4.36) which are ascribed to transitions from the first excited $^4F_{9/2}$ Stark sublevel to the two lowest Stark levels of the $^6H_{15/2}$ multiplet. A 'hot' band (labelled A*) involving a microstate of the $^7F_{9/2}$ level is also detected in each spectrum.

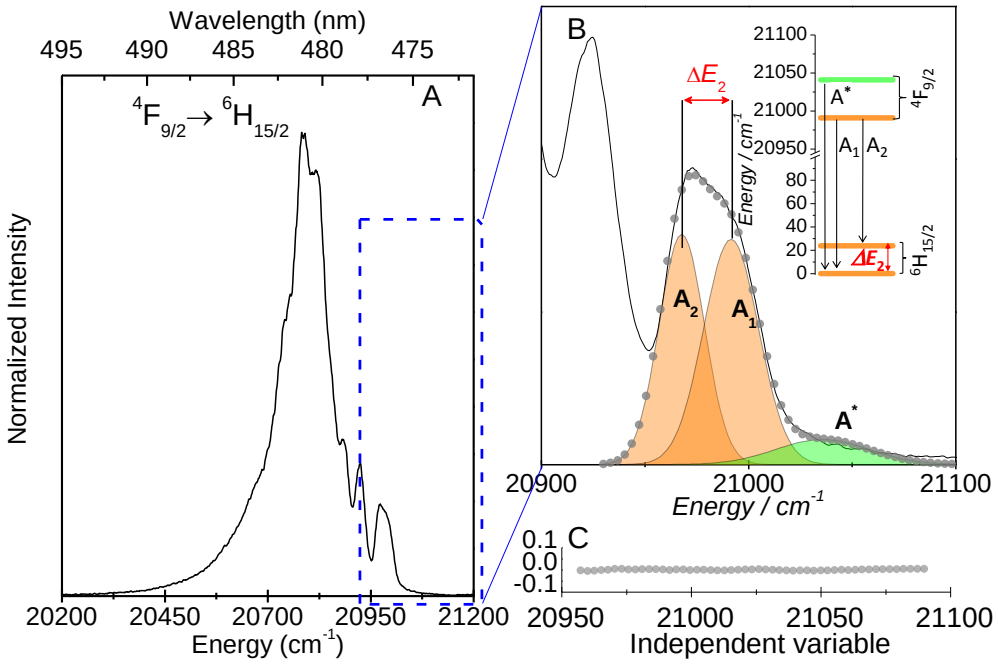

Figure 4.34 (A) High-resolution emission spectra (14 K) for **9.1** excited at 351 nm. (B) Magnification of the $^4F_{9/2} \rightarrow {}^6H_{15/2}$ transition and multi-Gaussian functions envelope fit (solid circles) and the components arising from the first $^4F_{9/2}$ Stark sublevel to the $^6H_{15/2}$ multiplet in the energy interval 20950-21100 cm^{-1}. (C) Regular residual plot (R^2~0.98) for a better judgment of the fit quality.

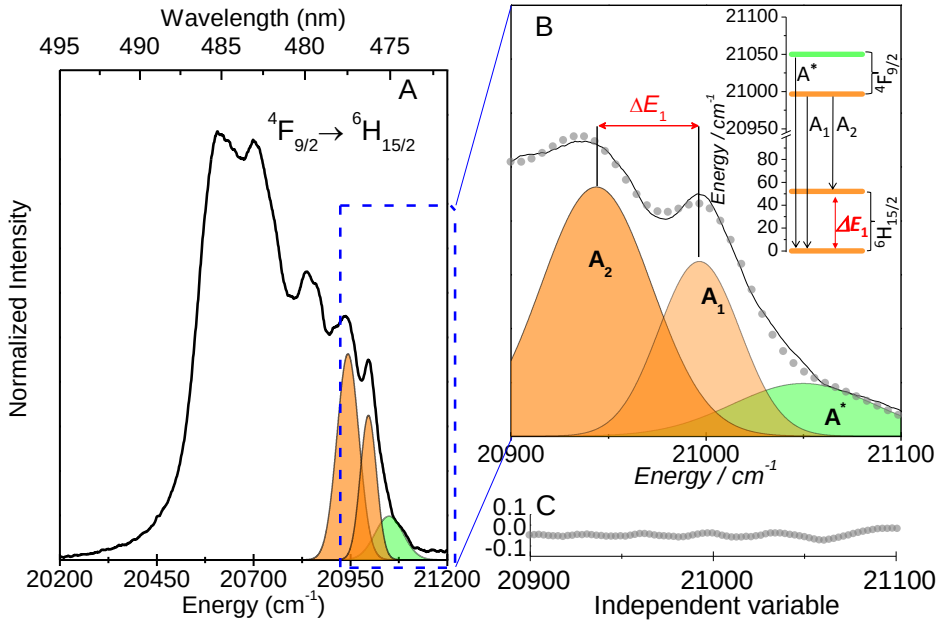

Figure 4.35 (A) High-resolution emission spectra (14 K) for **10.1** excited at 350 nm; (B) Magnification of the $^4F_{9/2} \rightarrow {}^6H_{15/2}$ transition and multi-Gaussian functions envelope fit (solid circles) and the components arising from the first $^4F_{9/2}$ Stark sublevel to the $^6H_{15/2}$ multiplet in the energy interval 20900-21100 cm^{-1}. (C) Regular residual plot (R^2~0.98) for a better judgment of the fit quality.

From this data, the energy gap $\Delta E_{\mathbf{10.1}}$ between the ground and first excited state of the Dy^{III} ion in **10.1** (Dy^{III}-15C5) was calculated to be $\Delta E_{\mathbf{10.1}} = 58 \pm 3$ cm^{-1}. This value is in excellent agreement with the energy gap determined from the *ab initio* calculations, but ~24 cm^{-1} higher than the value determined from magnetic measurements. As previously mentioned, there are two contributions to this disagreement: 1) the magnetically-determined parameters were calculated from data collected in the presence of a small dc field, which alters the energies of the M_J microstates; and 2) the *ab initio* and luminescence methods do not take quantum tunnelling into account. As was

mentioned earlier, similar discrepancies have been noted before for both $[DyDOTA]^{3+}$ and $[Zn(L)Dy]^{3+}$ SMMs.[24,44]

For **9.1**, the luminescence-derived energy gap between the first and second excited state of the Dy^{III} ion was much lower, determined to $\Delta E_{9.1} = 30 \pm 3\ cm^{-1}$, which again is in excellent agreement with the $1\pm \rightarrow 2\pm$ energy gap of 33 cm^{-1} predicted from the *ab initio* calculations. This smaller energy barrier ($\Delta E_{9.1} < \Delta E_{10.1}$) is qualitatively consistent with the lack of SMM behaviour for this compound.

As this work shows, luminescence can be used to probe the electronic structure of lanthanide centers in SMMs, providing information on the Stark splitting of the electronic ground state, as well as the relationship between this splitting energy and the magnetic relaxation behaviour. It should be emphasized that for **9.1** (Dy^{III}-12C4), the lack of ac response prevents the experimental determination of the zero-field energy barrier from magnetic susceptibility data, highlighting the importance of photoluminescence data to experimentally probe the energies of the ground and low lying excited states in Ln-based SMMs. The importance of magneto-electronic correlation was highlighted in a recent *Nature* review, in which Murugesu emphasized that studies such as these are vitally important in helping to understand and control the 'elusive' magnetism of SMMs, towards application in the technologies of tomorrow.[296]

4.4 Magnetic studies on the 18C6 complexes 11.1-11.4

Dc magnetic measurements were performed on each of **11.1-11.4** between 5 and 300 K, in small fields of 1-2 kOe. In each case, the χT *vs.* T plots showed a low-temperature decrease in susceptibility, consistent with a slight depopulation of the Stark sublevels.

The decrease was slight for complex **11.1** (Tb^{III}-18C6) occurring below 40 K, and more marked in the other three complexes, occurring in a gradual fashion below 100 K (Figure 4.36 left).

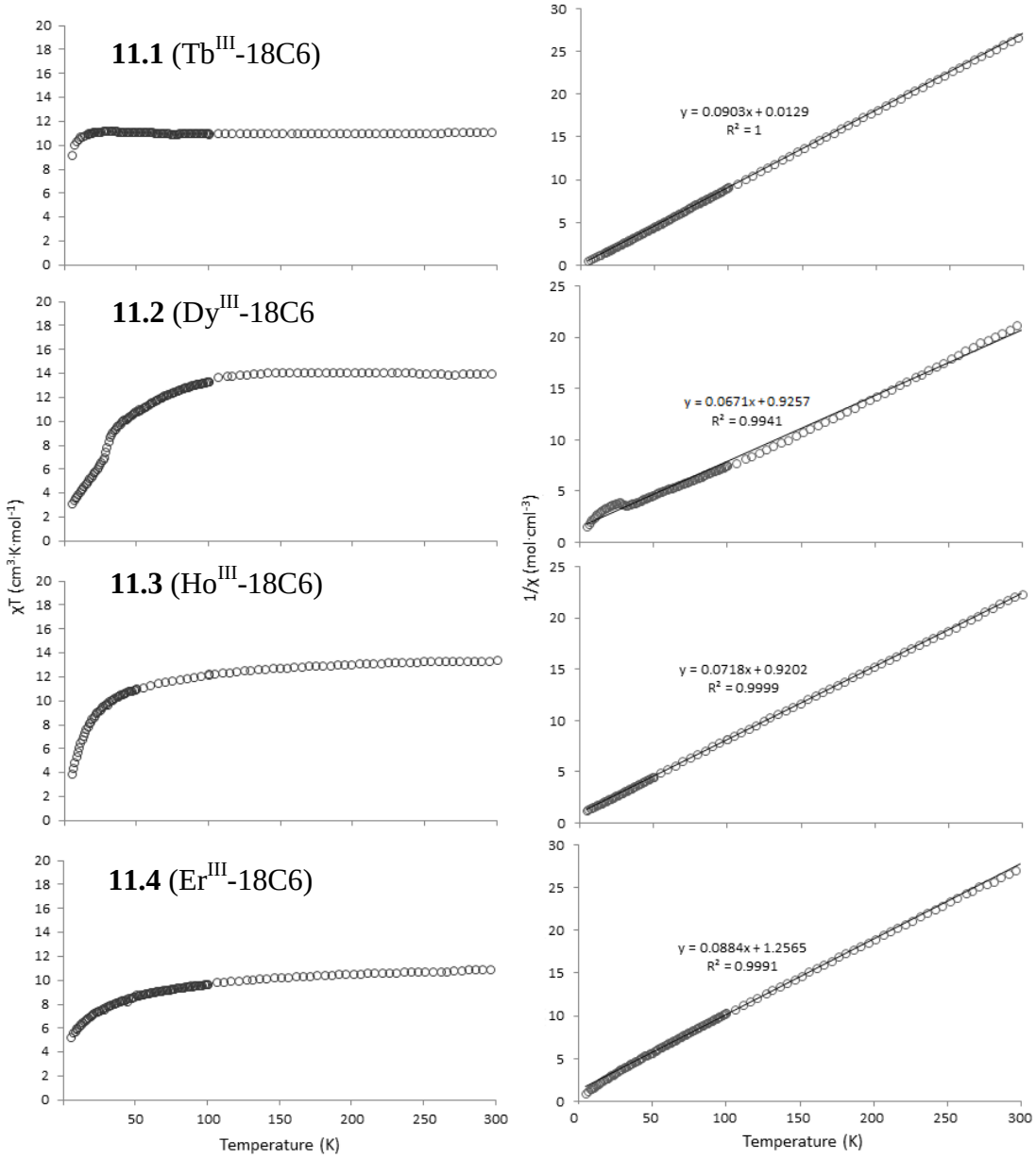

Figure 4.36 χT *vs.* T (left) and 1/χ *vs.* T (right) for: (top to bottom) **11.1**-**11.4** in a field of 0.1 T from 5 - 300 K.

The parameters extracted from the dc data are summarized below in Table 4.20.

Complex	Abbrev.	Expected χ_T (300 K, $cm^3 \cdot K \cdot mol^{-1}$)	C ($cm^3 \cdot K \cdot mol^{-1}$)	θ (K)
11.1	Tb^{III}-18C6	11.82	11.07 ± 0.01	-0.14 ± 0.05
11.2	Dy^{III}-18C6	14.17	14.89 ± 0.07	-13.9 ± 0.8
11.3	Ho^{III}-18C6	14.07	13.93 ± 0.01	-12.8 ± 0.1
11.4	Er^{III}-18C6	11.48	11.31 ± 0.03	-14.2 ± 0.4

Table 4.20 Summary of the parameters describing the dc magnetic susceptibility behaviour of **11.1**-**11.4**.

The theoretical and experimental χT and C values, as well as the Weiss constants, are summarized in Table 4.20. The Curie constants, calculated from the inverse of the slope of each 1/χ *vs.* T plot (Figure 4.36 right), were in reasonable agreement with the theoretical values for each isolated Ln^{III} centre. The Weiss constants, calculated from the *x*-intercept of the same plot, were all small negative values (Table 4.20), indicating the presence of weak antiferromagnetic interactions at low temperatures. In the case of the Tb^{III} complex, the Weiss constant was negligible, indicating almost ideal Curie behaviour even at low temperatures.

Preliminary ac susceptibility measurements were carried out on polycrystalline samples of **11.1**-**11.4**. An oscillating field of 3.5 Oe was applied, at various frequencies from 50 to 10,000 Hz, over the temperature range 2.8 – 15 K.

All four complexes displayed a negligible out-of-phase susceptibility response in zero dc field. It is perhaps unsurprising that **11.1**-**11.3** are not zero field SMMs, given that the intrinsic anisotropy of oblate metal ions is not enhanced by an equatorially-bound ligand field. Following the unremarkable zero field measurements, ac susceptibility data

was collected in the presence of static fields ranging from zero to 5 kOe. Upon initial inspection, there appeared to be a frequency-dependent out-of-phase susceptibility response in the ac data of all four complexes, in the presence of a 5 kOe field (Figure 4.37).

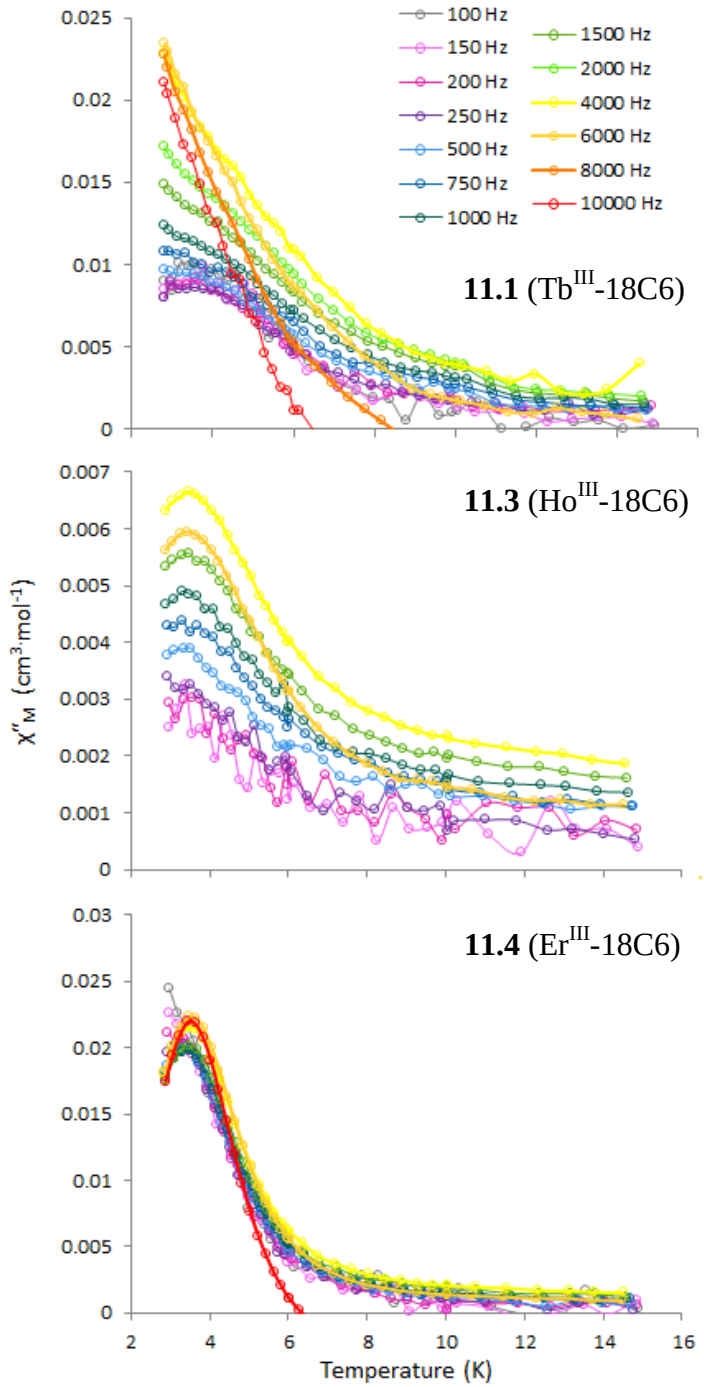

Figure 4.37 χ'' versus temperature for (top to bottom) **11.1**, **11.3**, and **11.4** in a 5 kOe applied dc field, from 2-15 K.

However, as can be seen by a glance at the *y*-axes of the plots in Figure 4.37, the scale on which each response occurs is so miniscule, that in effect the observed responses of **11.1** (Tb^{III}-18C6), **11.3** (Ho^{III}-18C6), and **11.4** (Er^{III}-18C6) in a 5 kOe field can be called negligible.

Of the four later lanthanide 18C6 complexes, the Dy^{III} complex **11.2** alone displayed a strong field-induced susceptibility response. In applied dc fields of increasing strength, a single fully resolved maximum appeared by 5 kOe (Figure 4.38).

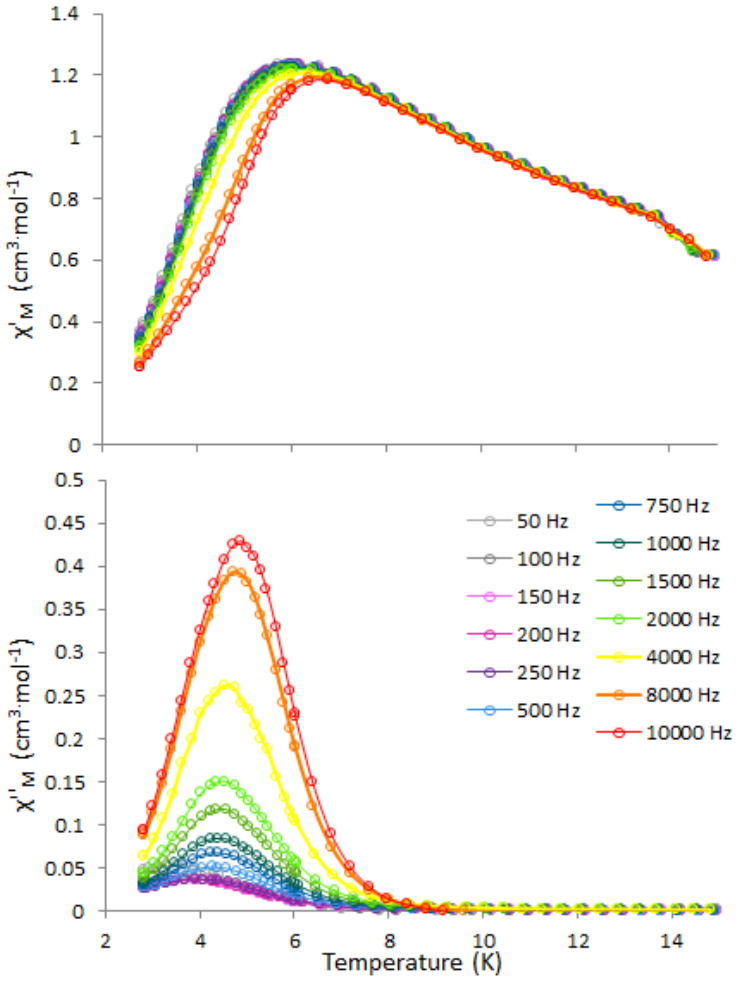

Figure 4.38 χ'' versus temperature for **11.2** in a 5 kOe applied dc field, from 2-15 K.

The frequency-independence of the position of the maximum is reminiscent of the Dy^{III}-12C4 structure **9.1**, and again was assigned to a rapid relaxation pathway such as QTM. Assuming the same Curie-like relationship discussed earlier, that $\chi'' \propto 1/T$, the slopes of the lines in a plot of χ'' *vs.* 1/T were plotted as a function of frequency (Figure 4.39).

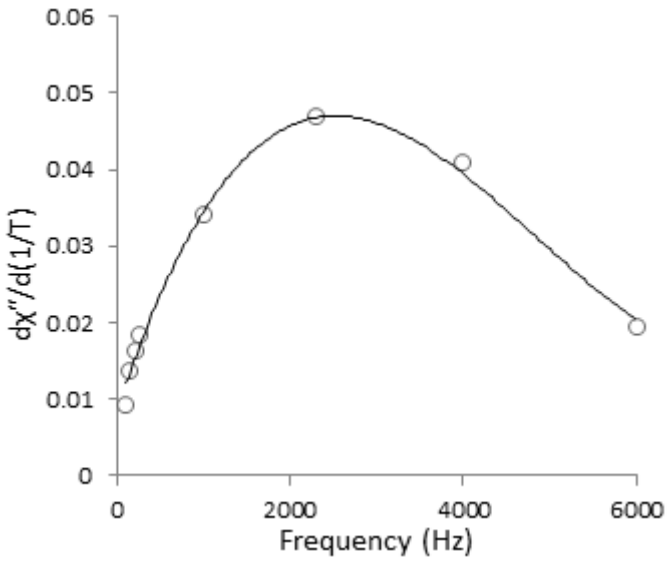

Figure 4.39 Plot of $d\chi''/d(1/T)$ versus frequency for **11.2** (Dy^{III}-18C6), based on the zero field ac susceptibility data. Line is a guide for the eyes only.

The turning-point occurs at ~2300 Hz, which corresponds to the point at which $\omega\tau_c = 1$. This allows the determination of τ_c ~0.43 ms from the frequency dependent zero field data.

The observation of a temperature-independent quantum tunnelling process for **11.2** (Dy^{III}-18C6) in the presence of an applied field is of interest in the context of the

previously discussed complexes **9.1** (Dy^{III}-12C4) and **10.1** (Dy^{III}-15C5). All three of these complexes have Dy^{III} ions in O_9 coordination environments.

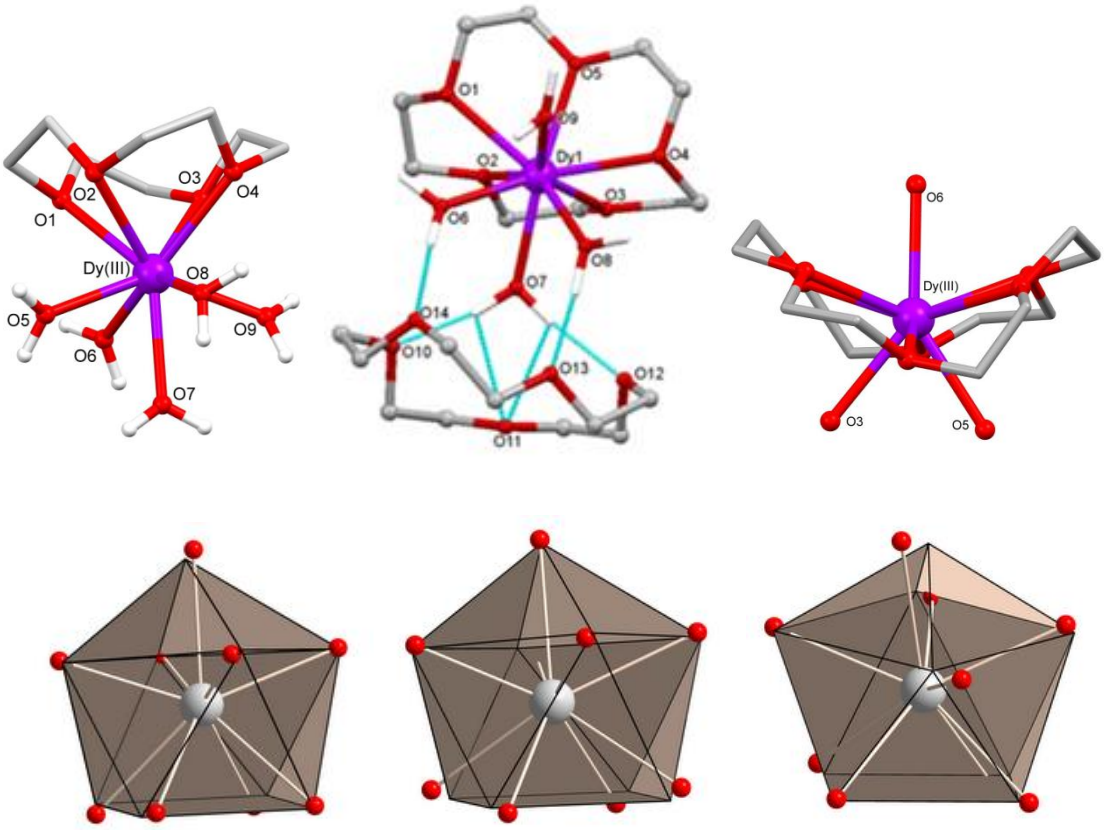

Figure 4.40 The immediate coordination spheres (top) and idealized polyhedra (bottom) for **9.1** (Dy^{III}-12C4), **10.1** (Dy^{III}-15C5) and **11.2** (Dy^{III}-18C6).

Complexes **9.1** (Dy^{III}-12C4) and **10.1** (Dy^{III}-15C5) are most similar to one another in terms of their immediate coordination environment, with axially-bound crowns contributing 4 and 5 of the coordinated oxygens respectively. Geometrically, **10.1** (Dy^{III}-15C5) and **11.2** (Dy^{III}-18C6) are most similar, with slightly distorted muffin-shaped topologies, in contrast to **9.1** (Dy^{III}-12C4) which exhibits only a small deviation from a

capped square antiprismatic geometry. Yet magnetically, complex **9.1** (Dy^{III}-12C4) closely resembles **11.2** (Dy^{III}-18C6), with no magnetic relaxation observed in zero field, and the induction of QTM in the presence of a dc field. These observations point to the significant role that crystal packing plays in the magnetic behaviour of mononuclear lanthanide complexes. In the Dy^{III}-DOTA SMM described by Sessoli and co-workers with similar capped square-antiprismatic geometry, the outer coordination sphere had an unexpectedly large effect on the axis of anisotropy.[125] Additionally, the drastic effects of modifications to the peripheral ligand sphere in a family of Er^{III} SIMs was recently reported by Waldmann.[297] It is increasingly clear that a systematic study of the effects of structural modification on magnetic and other properties is a necessary step towards the rational design of functional SMMs. In addition, it is apparent that while the electrostatic Long model is helpful in explaining the observed magnetic properties of many reported Dy^{III} and Tb^{III} 'sandwich' structures, the presence or absence of axial ligand electron density will not necessarily determine the presence or absence of slow magnetic relaxation.

4.5 Conclusion

To conclude, reaction of the later lanthanides (Tb^{III}, Dy^{III}, Ho^{III} and Er^{III}) with the aliphatic crown ethers 12C4, 15C5 and 18C6 resulted in the formation of a number of new structures. Two families of compounds (the half- and *pseudo*-sandwich structures **9.1** and **10.1**, and the equatorial complexes **11.1**-**11.4**) were analyzed as potential single molecule magnets. The correlation between the magnetic, electronic and spectroscopic properties in **9.1** (Dy^{III}-12C4) and **10.1** (Dy^{III}-15C5) was discussed, which is a rare

approach in the ongoing conversation concerning Ln-SMMs. Complex **10.1** (Dy^{III}-15C5) represents the first mononuclear Ln-SMM based on a crown ether, and displays dual properties: slow magnetic relaxation and photoluminescence.

4.6 Future directions

Future work in this vein will include the use of rigorously dry conditions. Given the propensity for the oxophilic lanthanides to coordinate to water, a logical next step would be the exclusion of water from the reaction conditions. Although the lanthanide perchlorate salts are commercially available only as aqueous solutions, the *in situ* synthesis of anhydrous $Ln(ClO_4)_3$ from $LnCl_3$ and $NaClO_4$ in a dry, poorly coordinating solvent under glove-box conditions is possible. The reaction of the resulting anhydrous perchlorate salts with the various crowns would ideally result in full-sandwich topologies, which would provide an intriguing comparison to the half- and *pseudo*-sandwich structures analyzed thus far.

In addition, other classes of oxophilic macrocycle will be explored. The usefulness of the MOLCAS program has been demonstrated and will enable us to calculate the energy levels of coordination complexes prior to investing time and effort in the synthesis.

Finally, as mentioned above, the magneto-electronic-luminescence correlation work described herein is still rare for mononuclear lanthanide complexes. This approach to an examination of the relationship between molecular structure, electronic properties, and magnetic susceptibility behaviour will continue to be employed for the systems which emerge during the continuation of this project.

5 EXPERIMENTAL

5.1 General Information

All reagents were purchased from Sigma-Aldrich or Alfa Aesar and used without further purification. Anhydrous solvents were obtained from a Puresolve PS MD-4 solvent purification system. Silica gel (75-250 mesh, 60 Å) and activated neutral alumina powder used for column chromatography were purchased from Desican Inc.

5.2 Instrumentation

Elemental analysis: Measurements were performed by Atlantic Microlab Inc.

Mass spectrometry: Data was recorded on a Carlo Erba / Kratos EC/ms acquisition system and processed at a SPARC workstation. Samples were introduced through a direct inlet system, with *tris*(perflouroheptyl-S-triazine) as the internal standard.

NMR spectroscopy: ^{1}H- and ^{13}C-NMR spectra were recorded at 300 MHz on a Bruker Advance AV 300 Digital NMR spectrometer in deuterated solvents. Data was analyzed using the Bruker TOPSPIN 2.1 PL6 software.

Infrared spectroscopy: Infrared spectra were recorded on a Bruker Alpha FT-IR spectrometer.

Far-IR spectroscopy: Far-IR spectra were collected on a Nicolet 6700 system equipped with the solid substrate beam splitter and a polyethylene detector, resolution 4 cm^{-1}. The

system was purged with dry nitrogen gas before use and the data was smoothed during processing.

Raman spectroscopy: Raman spectra were measured on a Renshaw in Via Laser Raman spectrometer with an attached Leica microscope and a red solid-state laser (785 nm).

UV-visible spectroscopy: UV-visible data were obtained using a Beckman Coulter DU 720 General-Purpose UV-visible spectrophotometer.

Luminescence measurements: Luminescence data were recorded at 300 K and at 14 K with a modular double grating excitation spectrofluorimeter with a TRIAX 320 emission monochromator (Fluorolog-3, Horiba Scientific) coupled to a R928 Hamamatsu photomultiplier, using a front face acquisition mode. The excitation source was a 450 W Xe arc lamp. The emission spectra were corrected for detection and optical spectral response of the spectrofluorimeter and the excitation spectra were corrected for the spectral distribution of the lamp intensity using a photodiode reference detector. The room temperature time-resolved emission spectra and emission decay curves (10^{-6}-10^{-9} s) were recorded on a Fluorolog TCSPC spectrofluorimeter (Horiba Scientific) coupled to a TBX-04 photomultiplier tube module (950 V), 200 ns time-to-amplitude converter and 70 ns delay. The excitation source was a Horiba-Jobin-Yvon pulsed diode (NanoLED-390, peak at 390 nm, 1.2 ns pulse duration, 1 MHz repetition rate and 150 ns synchronization delay). The emission decay curves (10^{-6}-10^{-2} s) were recorded at room temperature with a Fluorolog TCSPC spectrofluorometer (Horiba Scientific) coupled to a TBX-04 photomultiplier tube module (950 V), 50 μs delay. The exciting source was a Horiba Scientific pulsed diode light source (SpectraLED-355, peak at 356 nm).

ICP-MS: Inductively Coupled Plasma Mass Spectrometry (ICP-MS) measurements were carried out on a PerkinElmer-Sciex ELAN DRC II mass spectrometer. Measurements were carried out in triplicate. Dy and Y standards were made from elemental stock solutions (1000 ppm), manufactured by High-Purity Standards (Charleston, SC, USA). Calibration range: 0-20 ppb. Samples of ca. 8 mg of were digested with 500 μL conc. HNO3 and 200 μL conc. HCl, then diluted with distilled water to a total volume of 10.0 mL.

Conductivity: Conductivity measurements were carried out using an Oakton CON 6+ Handheld Conductivity Meter with cell constant K = 1. The probe was calibrated using standard solutions of KCl at 20°C. Aqueous and methanolic 0.5 mM solutions of the complex were prepared, and measurements were obtained in triplicate with precision < 1%.

X-ray diffraction: Single crystals suitable for X-ray diffraction were mounted on a cryoloop with paratone oil and examined on a Bruker APEX-II CCD diffractometer equipped with a CCD area detector and an Oxford Cryoflex low temperature device. Data were measured at 150(2) K with Mo-Kα radiation (λ = 0.71073 Å) using the APEX-II software.[298] Cell refinement and data-reduction were carried out by SAINT. An absorption correction was performed by the multi-scan method implemented in SADABS.[299] The structures were solved by direct methods (SHELXS-97)[300] and refined using SHELXL-2013 in the Bruker SHELXTL suite and Olex2.[301]

Powder diffraction: Powder X-ray diffraction experiments were performed on a Bruker D8 Discover powder diffractometer equipped with a Hi-Star detector and GADDS

software package. Data were collected at room temperature in the range $2.5 < 2\Theta < 33.5^{\circ}$, and were recorded in 0.05° steps using Cu-Kα_1 radiation (λ = 1.54187 Å) with the tube operating at 40 kV and 40 mA with an initial beam diameter of 0.5 mm.

Magnetic susceptibility measurements: Dc measurements were performed using a Quantum Design SQUID magnetometer MPMS. Temperature scans were performed at applied fields between 0.1 - 0.2 T, from 2 – 300 K. Field scans were performed over the range -5 to 5 T, at temperatures between 3 - 5 K. Ac measurements were carried out using a Quantum Design PPMS, with an oscillating field of 3.5 Oe over multiples frequencies between 25 and 1500 MHz. Static fields ranging from 0 to 0.5 T were applied, from 2 – 15 K.

Computational details: *Ab initio* calculations were performed using the MOLCAS 7.8 quantum chemistry software package.[290,302,303] For all calculations, the multi-configurational CASSCF/RASSI-SO approach was used. The spin-free eigenstates were calculated by the CASSCF method using the Douglas-Kroll-Hess Hamiltonian, followed by mixing via the RASSI-SO method to include spin-orbit coupling. The active space for **9.1** and **9.2** was chosen to be the 9 electrons in the 7 4*f*-orbitals of the Dy^{III} ion. The coordinates of the atoms were determined crystallographically, and were used without further geometry optimization. Relativistic basis sets of the type RCC-ANO were selected to include the scalar relativistic terms where the dysprosium ions were treated at the VQZP level (9s8p6d4f3g2h), the coordinating oxygen atoms were treated at the VTZP level (4s3p2d1f) and all other atoms were treated at the VDZ level (3s2p for O and C, 4s3p for Cl, and 2s for H) for all models. The Dy^{III} ions were assigned the pseudo-spin

S = ½ for the calculations of the g-tensors of the eight Kramers doublets, and the main magnetic axes.

5.3 Organic building blocks

5.3.1 Organic building blocks for L3 (dbN_3O_2)

5.3.1.1 Synthesis of 1,4-bis-(2-nitrophenyl)-1,4-dioxabutane (3a)[214]

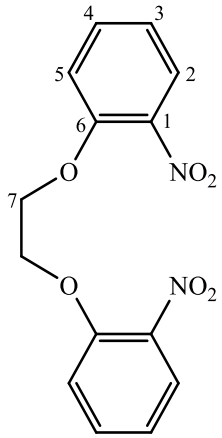

A solution of 2-nitrophenol (2 eq., 20.0 g, 144 mmol) in dry DMF (20 mL) was heated to 80°C. K_2CO_3 (1 eq., 9.93 g, 71.9 mmol) was added portionwise and the resulting bright red mixture was heated to 160°C and stirred for 5 min. 1,2-Dibromoethane (1 eq., 6.22 mL, 71.9 mmol) was added dropwise with stirring over 30 min, after which the mixture was refluxed at 170°C for 2.5 h. The resulting orange mixture was poured into cold H_2O and a granular yellow precipitate formed. The solid was collected by filtration and washed well with dilute $NaOH_{(aq)}$. The product was recrystallized from acetone to give **3a** as a crystalline beige solid (9.72 g, 45%).

M.p.: 170°C (Lit. 169-170°C[214]).

EI-MS:	*m/z* = 304 $[M]^+$ (14%).
^{1}H NMR ($CDCl_3$, 300 MHz) δ (ppm):	7.83 (dd, *J* = 8.2, 1.6 Hz, 2H, H_2), 7.57 (td, *J* = 7.8, 1.7 Hz, 2H, H_4), 7.23 (dd, *J* = 7.8, 0.9 Hz, H_3), 7.08 (td, *J* = 7.7, 1.0 Hz, H_5), 4.54 (s, 4H, H_7)
^{13}C NMR ($CDCl_3$, 300 MHz) δ (ppm):	152.0 (C_6), 134.4 (C_1), 125.7 (C_2), 121.5 (C_3), 116.0 (C_5), 68.8 (C_7)

5.3.1.2 Synthesis of 1,4-bis-(2-aminophenyl)-1,4-dioxabutane (3b)[214]

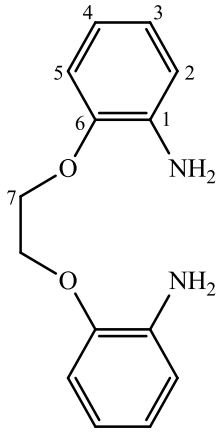

A solution of $SnCl_2$ (10 eq., 24.9 g, 132 mmol) in conc. HCl (20 mL) was heated to 70°C. Compound **3a** (1 eq., 4.00 g, 13.2 mmol) was added and the resulting mixture was refluxed at 110°C for 30 min. After cooling to room temperature, the reaction mixture was neutralized to pH = 7 by the addition of $NaOH_{(aq)}$. The product was extracted into $CHCl_3$ (5 x 50 mL), washed with brine (3 x 50 mL), dried over Na_2SO_4 and concentrated under vacuum to give **3b** as a cream solid (1.52 g, 47%).

M.p.:	126°C (Lit. 129-132°C[214]).
FAB-MS:	*m/z* = 245 $[M+H]^+$ (100%).
^{1}H NMR ($CDCl_3$, 300 MHz) δ (ppm):	6.87-6.73 (m, 8H, H_{2-4}), 4.37 (s, 4H, H_7).
^{13}C NMR ($CDCl_3$, 300 MHz) δ (ppm):	146.3 (C_6), 136.9 (C_1), 122.0 (C_3), 118.5 (C_4), 115.5 (C_2), 112.6 (C_5), 67.6 (C_7).
CHN:	Found C: 65.73, H: 6.11, N: 10.82%; Calcd. for $(C_{14}H_{16}N_2O_2)\cdot 0.1CHCl_3$ C: 66.09; H: 6.33; N: 10.93%.

5.3.2 Organic building blocks for L4 (dpN_3O_2)

5.3.2.1 Synthesis of *R,R*-5,6-diphenyl-4,7-dioxa-1,9-decadiene (4a)[219]

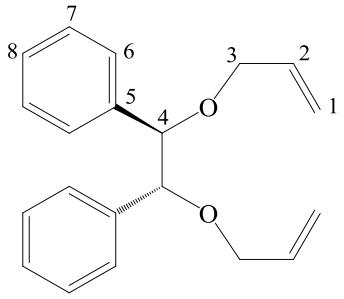

Sodium hydride (3.2 eq., 1.79 g, 74.7 mmol) was added in two portions to a solution of *R,R*-hydrobenzoin (1 eq., 5.00 g, 23.3 mmol) in dry THF (90 mL). The resulting purple/grey mixture was stirred at 30°C for 1 h, after which a solution of allyl bromide (3.5 eq., 6.90 mL, 81.6 mmol) in dry THF (20 mL) was added dropwise. The reaction mixture was stirred at 40°C for 2 h, and then refluxed at 95°C for 18 h. The mixture was cooled to room temperature, and passed through a Buchner funnel to remove the white

precipitate. The yellow filtrate was concentrated under vacuum, and then dissolved in DCM and washed well with H_2O (2 x 50 mL) and brine (2 x 50 mL). The organic layer was dried over $MgSO_4$ and concentrated under vacuum to give **4a** as a yellow oil (5.63 g, 82%).

FAB-MS:	*m/z* = 295 $[M+H]^+$ (16%).
^{1}H NMR ($CDCl_3$, 300 MHz) δ (ppm):	7.18-7.02 (m, 10H, H_{6-8}), 5.92-5.80 (m, 2H, H_2), 5.17 (dd, *J* = 17.1, 1.7 Hz, 4H, H_1), 4.53 (s, 2H, H_4), 3.94 (dd, 4H, *J* = 12.6, 5.1 Hz, H_3).
^{13}C NMR ($CDCl_3$, 300 MHz) δ (ppm):	138.8 (C_5), 135.1 (C_2), 128.0 (C_7), 127.8 (C_8), 127.6 (C_6), 116.6 (C_1), 85.0 (C_4), 70.2 (C_3).

5.3.2.2 Synthesis of *R,R*-4,5-diphenyl-3,6-dioxa-1,8-octanediol (4b)[219]

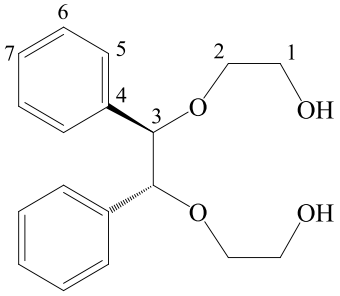

Osmium(IV) tetroxide (0.03 eq., 133 mg, 0.524 mmol) was added to a solution of **4a** (1 eq., 5.14 g, 17.5 mmol) in THF/H_2O (3:1, 200 mL). The dark purple mixture was stirred at room temperature for 2 h, and then sodium metaperiodate (5.8 eq., 21.70 g, 101.5

mmol) was added portionwise over 1 h. The mixture was stirred in the dark at room temperature for 18 h. The resulting creamy white mixture was concentrated under vacuum to give a cream residue, which was taken up into DCM/MeOH (1:1, 200 mL). The white precipitate was removed by Büchner filtration, and the yellow filtrate was cooled to 0°C in an ice bath. Sodium borohydride (6.8 eq., 4.50 g, 119 mmol) was added in two portions, and the reaction mixture was warmed to room temperature and stirred for 18 h. The solvent was removed under vacuum to give a dark brown residue, which was stirred vigorously in distilled H_2O (500 mL) for 1 h. The product was extracted with DCM (3 x 50 mL), and then washed with 1N HCl (3 x 50 mL), H_2O (3 x 50 mL) and brine (3 x 50 mL). The organic layer was dried over $MgSO_4$ and concentrated under vacuum to give **4b** as a brown oil (7.42 g, 79%).

^{1}H NMR ($CDCl_3$, 300 MHz) δ (ppm):	7.17-7.02 (m, 10H, H_{5-7}), 4.47 (s, 2H, H_3), 3.75-3.44 (m, 8H, H_{1-2}).
^{13}C NMR ($CDCl_3$, 300 MHz) δ (ppm):	138.3 (C_4), 128.2 (C_7), 128.0 (C_6), 127.7 (C_5), 86.9 (C_3), 71.2 (C_2), 61.9 (C_1).

5.3.2.3Synthesis of *R,R*-4,5-diphenyl-3,6-dioxa-1,8-octanediphthalimide (4c)[219]

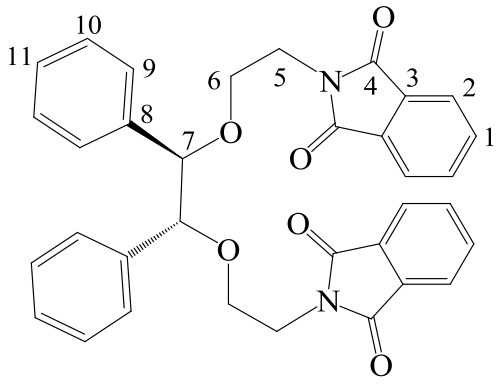

A solution of **4b** (1 eq., 3.72 g, 10.5 mmol) in dry THF (60 mL) was added to triphenylphosphine (2.2 eq., 3.41 g, 23.2 mmol) and phthalimide (2.2 eq., 6.07 g, 23.2 mmol) under N_2. The pale yellow mixture was briefly stirred, and then a solution of DIAD (2.2 eq., 5.05 g, 23.1 mmol) in dry THF (20 mL) was added dropwise. The resulting orange solution was stirred at room temperature for 4 d. The mixture was concentrated under vacuum, and the crude product was purified by silica gel column chromatography in hexane/EtOAc (2:1), followed by passage through a second silica gel column in pet. ether/EtOAc (3:1) to give **4c** as a cream powder (1.70 g, 29%).

M.p.	175°C.
^{1}H NMR ($CDCl_3$, 300 MHz) δ (ppm):	7.75 (ddd, *J* = 36.0, 5.2, 3.2 Hz, 8H, H_{1-2}), 7.00-6.78 (m, 10H, H_{9-11}), 4.39 (s, 2H, H_7), 3.79 (q, *J* = 6.6 Hz, 4H, H_5), 3.58 (t, *J* = 5.8 Hz, 1H, H_6).
^{13}C NMR ($CDCl_3$, 300 MHz) δ (ppm):	168.5 (C_4), 137.9 (C_8), 134.1 (C_1), 133.2 (C_3), 127.8 (C_2), 123.2 (C_{9-11}), 85.7 (C_7), 66.2 (C_6), 37.7 (C_5).

5.3.2.4 Synthesis of *R,R*-4,5-diphenyl-3,6-dioxa-1,8-octanediamine (4d)[219]

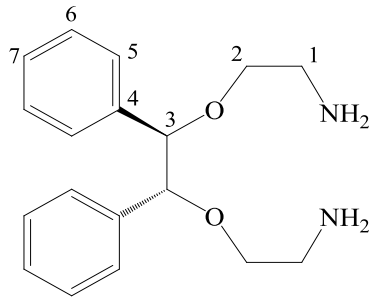

Hydrazine monohydrate (10 eq., 571 μL, 11.7 mmol) was added to a suspension of **4c** (1 eq., 563 mg, 1.17 mmol) in warm EtOH (75 mL). The mixture was refluxed at 80°C for 18 h, and a fluffy white precipitate gradually formed. The mixture was cooled to r.t. and then further cooled to 0°C in the freezer. The precipitate was removed by Buchner filtration, and washed well with cold EtOH (3 x 25 mL) and DCM (3 x 25 mL). The combined organic solutions were concentrated under vacuum, to give a dark yellow residue which was dissolved in DCM (150 mL). The product was was extracted into 2N HCl (3 x 50 mL), and the aqueous phase was then basified to pH = 10 by the addition of $NaOH_{(aq)}$. After briefly stirring, the product was extracted into DCM (3 x 50 mL), washed with H_2O (3 x 50 mL) and brine (3 x 50 mL), dried over Na_2SO_4 and concentrated under vacuum. Toluene (3 x 50 mL) was then added and removed under vacuum to give which was then dissolved in toluene (50 mL) and concentrated again to give **4d** as a yellow oil (196 mg, 56%).

FAB-MS: *m/z* = 301 $[M+H]^+$ (27%).

^{1}H NMR ($CDCl_3$, 400 MHz) δ (ppm):	7.14-7.03 (m, 10H, H_{5-7}), 4.41 (s, 2H, H_3), 3.46-3.29 (m, 4H, H_2), 2.78 (s, 4H, H_1)
^{13}C NMR ($CDCl_3$, 400 MHz) δ (ppm):	138.6 (C_4), 127.9 (C_6), 127.6 (C_7), 127.5(C_5), 86.0 (C_3), 71.1 (C_2), 41.5 (C_1)
CHN:	Found C: 68.39, H: 8.04, N: 8.34%; Calcd. for $(C_{18}H_{24}N_2O_2)\cdot H_2O$ C: 67.90; H: 8.23; N: 8.80%.

5.3.3 Organic building blocks for L5 (N_3O_3)

5.3.3.1 Synthesis of tetra(ethylene glycol)-p-ditosylate (5a)[216]

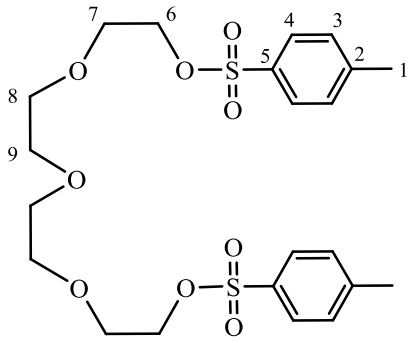

Tosyl chloride (2.2 eq., 86.4 g, 453 mmol) was added to a solution of (tetraethylene)glycol (1 eq., 40.00, 206 mmol) in dry DCM (120 mL). The mixture was cooled to 0°C in an ice bath and KOH (3 eq., 34.7 g, 618 mmol) was added portionwise over 30 min. The resulting beige mixture was stirred at 0°C for 1 h, and then warmed to room temperature and stirred for a further 18 h. DCM (50 mL) and H_2O (200 mL) were then added to the reaction flask, and the mixture was stirred vigorously for 1 min. The

resulting layers were separated, and the aqueous layer was extracted with DCM (2 x 50 mL). The combined organic layers were then washed with H_2O (2 x 50 mL), dried over $MgSO_4$ and concentrated under vacuum to give **5a** as a yellow oil (95.6 g, 92%).

FAB-MS:	*m/z* = 503 $[M+H]^+$ (1.7%).
^{1}H NMR ($CDCl_3$, 300 MHz) δ (ppm):	7.78 (d, *J* = 8.0 Hz, 4H, H_4), 7.33 (d, *J* = 8.2 Hz, 4H, H_3), 4.14 (t, *J* = 4.8, 4H, H_6), 4.15 (t, *J* = 5.5, 4H, H_7), 3.55 (s, 8H, $H_{8\text{-}9}$), 2.43 (s, 6H, H_1).
^{13}C NMR ($CDCl_3$, 300 MHz) δ (ppm):	144.9 (C_5), 133.1 (C_2), 129.9 (C_3), 128.1 (C_4), 70.8 ($C_{8/9}$), 70.7 ($C_{8/9}$), 69.4 (C_7), 68.8 (C_6), 21.8 (C_1).

5.3.3.2 Synthesis of 1,11-diphthalimido-3,6,9-trioxaundecane (5b)[215]

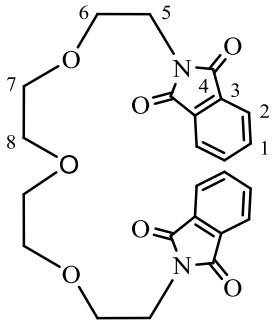

Potassium phthalimide (2.5 eq., 9.73 g. 21.0 mmol) was added to a solution of **5a** (2.5 eq., 26.4 g, 52.5 mmol) in dry DMF (100 mL). The cream reaction mixture was heated to 80°C and stirred for 18 h. After cooling to room temperature, the solvent was removed

under vacuum to give a tan residue. The crude product was purified by passage through a silica gel column in MeOH/$CHCl_3$ (3:1), and concentrated under vacuum to give **5b** as a cream solid (9.56 g, 98%).

M.p.:	102°C (Lit. 104-105°C[304]).
FAB-MS:	*m/z* = 453 $[M+H]^+$ (1.0%).
^{1}H NMR ($CDCl_3$, 300 MHz) δ (ppm):	7.83-7.68 (m, 8H, H_{3-4}), 3.76 (dt, *J* = 2.5 Hz, 5.6 Hz, 8H, H_{7-8}), 3.59-3.50 (m, 8H, H_{5-6}).
^{13}C NMR ($CDCl_3$, 300 MHz) δ (ppm):	168.3 (C_4), 134.0 (C_1), 132.2 (C_3), 123.3 (C_2), 70.7 (C_7), 70.1 (C_8), 68.0 (C_6), 37.3 (C_5).

5.3.3.3 Synthesis of 1,11-diamino-3,6,9-trioxaundecane (5c)[215]

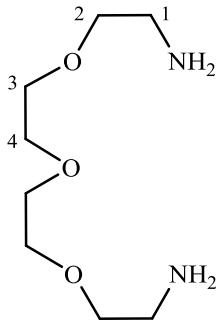

Hydrazine monohydrate (20 eq., 10.5 mL, 214 mmol) was added to a suspension of **5b** (1 eq., 5.01 g, 10.7 mmol) in dry MeOH/THF (1:1. 90 mL). The clear yellow mixture was refluxed at 95°C for 18 h, and a cream precipitate formed. The solvent volume was reduced by evaporation, and the flask was cooled to 0°C. The precipitate was removed by

filtration through a sintered funnel, and washed well with ice-cold MeOH/THF (3 x 10 mL). The clear yellow filtrate was concentrated under vacuum to give **5c** as a thick yellow oil (2.74 g, 89 %).

FAB-MS:	*m/z* = 194 $[M+H]^+$ (2.9%).
^{1}H NMR ($CDCl_3$, 300 MHz) δ (ppm):	3.64 (m, 8H, $H_{3\text{-}4}$), 3.52 (t, *J* = 5.1 Hz, 4H, H_2), 2.87 (t, *J* = 5.9, 4H, H_1).
^{13}C NMR ($CDCl_3$, 300 MHz) δ (ppm):	73.3 (C_2), 70.4 (C_4), 70.7 (C_3), 41.8 (C_1).

5.3.4 Organic building blocks for L6 (dbN_3O_3)

5.3.4.1 Synthesis of 2-(acetylamino)phenol (6a)[217]

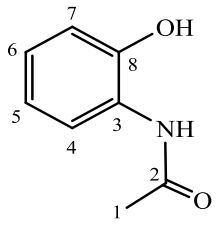

A solution of acetic anhydride (2.3 eq., 60 mL, 636 mmol) in MeOH (40 mL) was added dropwise to a suspension of 2-aminophenol (1 eq., 30.0 g, 275 mmol) in H_2O (200 mL). The resulting mixture was stirred vigorously for 5 h at room temperature. The progress of the reaction was monitored by tlc (hexane/acetone (3:2)) (R_f = 0.2). The precipitate which formed was collected by Buchner filtration and washed well with EtOH to give **6a** as a beige solid (40.7 g, 98%).

M.p.: 210°C (Lit. 209-210°C[305]).

FAB-MS: *m/z* = 152 $[M+H]^+$ (52.2%).

^{1}H NMR (d_6-DMSO, 300 MHz) δ (ppm): 7.67 (d, *J* = 8.3 Hz, 1H, H_4), 7.00-6.72 (m, 3H, H_{5-7}), 2.09 (s, 1H, H_1).

^{13}C NMR (d_6-DMSO, 300 MHz) δ (ppm): 169.0 (C_2), 147.9 (C_8), 126.4 (C_3), 124.6 (C_6), 122.4 (C_5), 119.0 (C_4), 115.9 (C_7), 23.6 (C_1).

5.3.4.2 Synthesis of bis-(2-(2-acetylaminophenoxy)-ethyl) ether (6b)[217]

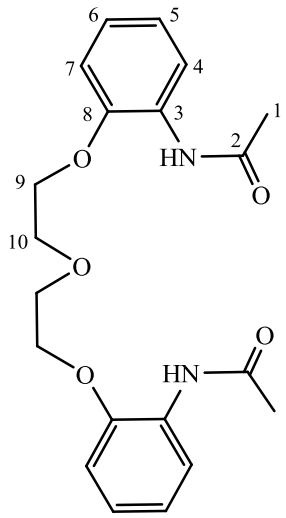

Bis(2-chloroethyl) ether (1 eq., 10.3 g, 71.7 mmol) was dissolved in dry DMF (30 mL). K_2CO_3 (2 eq., 39.6 g, 143 mmol) was added and the resulting suspension was stirred at 80°C for 30 min. A solution of **6a** (2 eq., 21.6 g, 143 mmol) in dry DMF (10 mL) was added dropwise, with the temperature being maintained at 80°C, and the reaction mixture was stirred for a further 18 h. The mixture was then cooled to room temperature and the

inorganic solids were removed by Buchner filtration. The filtrate was concentrated under vacuum to give a dark red/brown liquid which quickly hardened into a brown solid. The product was washed well with acetone to give **6b** as an off-white solid (12.6 g, 47%).

M.p.:	132°C (Lit. 130-134°C[217]).
FAB-MS:	*m/z* = 373 $[M+H]^+$ (41.3%).
^{1}H NMR ($CDCl_3$, 300 MHz) δ (ppm):	8.35-8.32 (m, 2H, H_4), 7.94 (s, 2H, H_6), 7.01-6.90 (m, 6H, $H_{5,7}$), 4.22 (t, *J* = 5.7 Hz, 4H, H_9), 3.90 (t, *J* = 4.6 Hz, 4H, H_{10}), 2.06 (s, 6H, H_1).
^{13}C NMR ($CDCl_3$, 300 MHz) δ (ppm):	168.3 (C_2), 146.8 (C_8), 128.9 (C_6), 123.8 (C_3), 122.4 (C_5), 120.5 (C_4), 113.1 (C_7), 69.5 (C_{10}), 68.9 (C_9), 24.8 (C_1).

5.3.4.3 Synthesis of 1,5-bis(2-amino)-phenoxy-3-oxapentane (6c)[217]

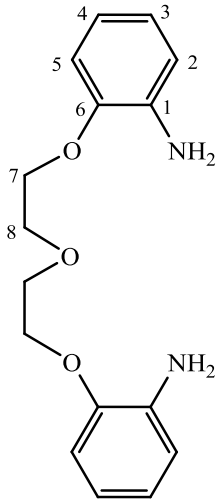

A solution of NaOH (7.1 eq., 7.64 g, 191 mmol) in H_2O (25 mL) was added dropwise to a suspension of **6b** (1 eq., 10.0 g, 26.9 mmol) in EtOH (75 mL). The beige mixture was refluxed at 80°C for 3 d, then cooled to r.t. and concentrated under vacuum. The dark brown residue was dissolved in $CHCl_3$, washed with H_2O (3 x 50 mL), and concentrated under vacuum to give **6c** as a dark brown liquid which solidified after several days into a light brown solid (5.80 g, 75%).

M.p.:	64°C (Lit. 65°C[217]).
FAB-MS:	*m/z* = 289 $[M+H]^+$ (94.4%).
^{1}H NMR ($CDCl_3$, 300 MHz) δ (ppm):	6.84-6.69 (m, 8H, $H_{2\text{-}5}$), 4.18 (t, *J* = 4.7 Hz, 4H, H_7), 3.93 (t, *J* = 4.8 Hz, 4H, H_8).
^{13}C NMR ($CDCl_3$, 300 MHz) δ (ppm):	146.4 (C_6), 137.2 (C_1), 122.1 (C_4), 118.5 (C_2), 115.5 (C_5), 113.2 (C_3), 70.0 (C_8), 68.6 (C_7).
CHN:	Found C: 66.71, H: 6.82, N: 9.72%; Calcd. for $C_{16}H_{20}N_2O_3$ C: 66.65; H: 6.99; N: 9.53%.

5.3.5 Organic building blocks for L7 (O_2N_3-N_3O_2)

5.3.5.1 Synthesis of 2,2',6,6'-tetramethyl-4,4'-bipyridine (7a)[219,221]

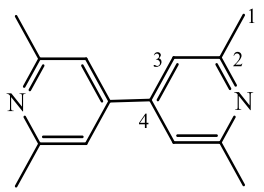

Sodium (2 eq., 3.98 g, 173 mmol) in paraffin oil was washed with hexane (3 x 50 mL) under N_2. Dry THF (120 mL) and 2,6-dimethylpyridine (1 eq., 8.83 g, 82.4 mmol) were added, and the mixture was stirred vigorously for 7 d. The beige reaction mixture was cooled to 0°C, and SO_2 gas was passed over the mixture for 5 h. Ethanol (150 mL) was then poured into the mixture, followed by sat. $NaOH_{(aq)}$ until the pH was ~8. The product was extracted with DCM (3 x 50 mL), dried over $MgSO_4$ and concentrated under vacuum to give an amorphous cream solid, which was vigorously stirred in hot H_2O for 5 min, and then cooled in the freezer. The product was collected by Buchner filtration and washed with water to give (**8.1**) as a white solid (4.24 g, 49%).

M.p.:	151°C (Lit. 149°C[306]).
FAB-MS:	*m/z* = 213 $[M+H]^+$ (82.4%).
^{1}H NMR ($CDCl_3$, 300 MHz) δ (ppm):	7.19 (s, 4H, H_3), 2.62 (s, 12H, H_1).
^{13}C NMR ($CDCl_3$, 300 MHz) δ (ppm):	158.6 (C_2), 146.8 (C_4), 118.2 (C_3), 24.6 (C_1).

5.3.5.2 Synthesis of 2,2',6,6'-tetracarboxylic-4,4'-bipyridine (7b)[221]

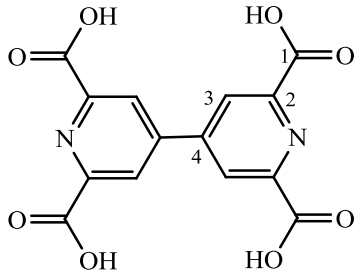

Chromium(VI) trioxide (12.2 eq., 11.0 g, 110 mmol) was added portionwise to a solution of **8.1** (1 eq., 1.91 g, 9.0 mmol) in conc. H_2SO_4 (32 mL). The reaction mixture was stirred

at r.t. for 1 h and then slowly heated to 75°C and stirred for a further 2 h. The mixture was cooled to r.t. and ~50 mL of ice chips were dropped in, with vigorous stirring. The mixture was then poured into ice water (300 mL) and left to cool in the fridge for 18 h. The resulting light green solid was collected by Buchner filtration and washed well with H_2O to give **8.2** as an off-white solid (1.06 g, 34%).

M.p.:	270°C, decomp.(Lit. 270°C[307]).
FAB-MS:	*m/z* = 303$[M+H]^+$ (100%).
^{1}H NMR (d_6-DMSO, 300 MHz) δ (ppm):	13.62 (s, 4H, H_{COOH}), 8.61 (2, 4H, H_3).
^{13}C NMR (d_6-DMSO, 300 MHz) δ (ppm):	165.8 (C_1), 150.1(C_4), 146.7 (C_2), 125.8 (C_3).

5.3.5.3 Synthesis of 2,2′,6,6′-tetrachloroformyl-4,4′-bipyridine (7c)[221]

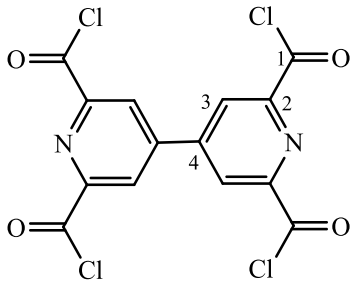

$SOCl_2$ (excess, 8 mL) and dry DMF (1 mL) were added to **8.2** (1 eq., 930 mg, 2.80 mmol) under an atmosphere of N_2. The mixture was heated to 80°C and vigorously stirred for 4 h, during which time it changed colour from green to pink. The solvent was removed by vacuum distillation to give a **8.3** as pale green solid (870 mg, 77%).

M.p.: 204°C (Lit. 205-206°C[307]).

FAB-MS: *m/z* = 406 $[M+H]^+$ (0.4%).

^{1}H NMR (d_6-DMSO, 300 MHz) δ (ppm): 8.58 (s, 4H, H_3).

^{13}C NMR (d_6-DMSO, 300 MHz) δ (ppm): 165.4 (C_1), 149.6 (C_2), 146.4 (C_4), 125.5 (C_3).

5.3.5.4 Synthesis of 2,2',6,6'-tetraacetyl-4,4'-bipyridine (7d)

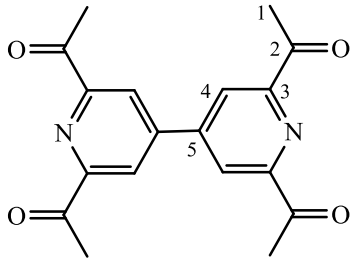

<u>METHOD 1</u>[221]

Meldrum's acid (4.1 eq., 4.45 g, 30.9 mmol) was dissolved in dry DCM (25 mL) and dry pyridine (excess, 6 mL). The mixture was cooled to 0°C, and **8.3** (1 eq., 3.03 g, 7.46 mmol) was added. After stirring for 1 h at 0°C and 1 h at r.t., DCM (40 mL) was added and the solution was poured into 2N HCl (50 mL) containing crushed ice. After vigorous stirring for 5 min, the layers were separated. The aqueous layer was extracted with DCM (3 x 50 mL), and the combined organic layers were washed with 2N HCl (2 x 50 mL), dried over $MgSO_4$ and concentrated under vacuum to give a dark brown solid. The solid was refluxed in acetic acid/H_2O (1:1, 240 mL) at 115°C for 18 h. After the solution was cooled to r.t., H_2O (150 mL) was added, and the product was extracted with DCM (6 x 50

mL), washed with 5% $NaHCO_3$, dried over $MgSO_4$ and concentrated under vacuum to give **8.4** as a light brown solid (770 mg, 32 %).

METHOD 2[218]

4,4′-Bipyridine (1 eq., 1.25 g, 8.0 mmol), pyruvic acid (7 eq., 3.95 mL, 56.0 mmol), and silver nitrate (0.075 eq., 0.102 g, 0.60 mmol) in H_2O (5 mL) were stirred in a solution of H_2SO_3 (0.4 M, 150 mL) for 5 mins. Ammonium persulfate (8 eq., 14.6 g, 54.0 mmol) was added carefully in small portions over 30 min, and the resulting bright yellow mixture was vigorously stirred at r.t. for 18 h. The cream solid which precipitated was collected by filtration, and the same portions of pyruvic acid, silver nitrate, and ammonium persulfate were added to the filtrate again. Conc. H_2SO_4 (5 mL) was added, and the mixture was stirred for a further 18 h. The resulting precipitate was collected by filtration, and the combined precipitates were purified by column chromatography (EtOAc/hexane/DCM 1:2:7) to give **7d** as a cream solid (285 mg, 11%).

M.p.:	260°C, decomp.(262°C[222]).
EI-MS:	*m/z* = 324 $[M]^{\cdot+}$ (28.3%).
^{1}H NMR ($CDCl_3$, 300 MHz) δ (ppm):	8.56 (s, 4H, H_4), 2.85 (s, 12H, H_1).
^{13}C NMR ($CDCl_3$, 300 MHz) δ (ppm):	198.8 (C_2), 154.0 (C_3), 146.7 (C_5), 122.3 (C_4), 25.7 (C_1).
CHN:	Found C: 63.70, H: 5.37, N: 7.80%; Calcd. for $(C_{18}H_{16}N_2O_4)\cdot H_2O$ C: 63.15; H: 5.30; N: 8.18%.

5.3.6 Organic building blocks for targeted complex

5.3.6.1 Synthesis of dimethyl-4-bromopyridine-2,6-dicarboxylate (8a)[308]

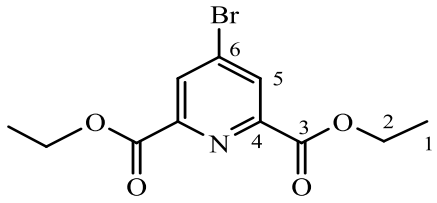

Phosphorus tribromide (3.6 eq., 9.4 mL, 98.3 mmol) was added dropwise to a solution of bromine (3 eq., 4.2 mL, 81.9 mmol) in dry hexane (35 mL). The reaction mixture was vigorously stirred for 1 h, during which time a yellow solid precipitated. The dark red liquid was decanted, and the yellow solid was washed with dry hexane (4 x 50 mL). Chelidamic acid (1 eq., 5.00 g, 27.3 mmol) was added, and the reaction mixture was refluxed at 90°C for 4 h. After cooling to r.t., $CHCl_3$ (75 mL) was added, and the dark purple mixture was passed through a Buchner filter. The brown filtrate was concentrated under vacuum, and then re-dissolved in $CHCl_3$ (100 mL) and cooled in an ice-bath. EtOH (50 mL) was added dropwise, and the resulting brown mixture was allowed to warm to r.t. and stirred for 18 h. The solvent was removed under vacuum to give a thick brown oil. The product was extracted from the oil with hot hexane (6 x 50 mL), and crystallized upon cooling to 0°C. The desired product **8a** was collected by filtration as white needles (1.39 g, 17%).

M.p.:	93°C (Lit. 90-93°C[309]).
ESI-MS:	*m/z* = 245 $[M-2Et+2H]^+$ (4%).

^{1}H NMR ($CDCl_3$, 400 MHz) δ (ppm): 8.42 (s, 2H, H_5), 4.49 (dd, *J* = 14.3, 6.9 Hz, 4 H, H_2), 1.46 (t, *J* = 7.2 Hz, 6H, H_3).

^{13}C NMR ($CDCl_3$, 400 MHz) δ (ppm): 163.7 (C_3), 149.7 (C_4), 135.0 (C_6), 131.21 (C_5), 62.9 (C_2), 14.3 (C_1).

5.3.6.2 Synthesis of 4-bromopyridine-2,6-dicarboxylic acid (8b)[308]

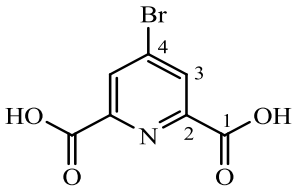

$NaOH_{(aq)}$ (excess, 5M, 60 mL) was added to **9.1** (1 eq., 1.00 g, 3.3 mmol), and the resulting cloudy white mixture was refluxed at 115°C for 1 h. The mixture was cooled to r.t., and then acidified to pH = 2 by the addition of 3N HCl. The cream precipitate was collected by Buchner filtration and allowed to air dry, giving **9.2** as a white solid (420 mg, 52.0%).

M.p.: 211°C, decomp. (Lit. 205-209°C[310]).

EI-MS: *m/z* = 246 $[M]^{\cdot+}$ (4%).

^{1}H NMR (d_6-DMSO, 400 MHz) δ (ppm): 13.72 (s, 2H, H_{COOH}), 8.37 (2, 2H, H_3).

^{13}C NMR (d_6-DMSO, 400 MHz) δ (ppm): 165.0 (C_1), 149.7 (C_2), 134.4 (C_4), 130.2 (C_3).

5.3.6.3 Synthesis of 4-bromopyridine-2,6-dicarboxylic dichloride (8c)[311]

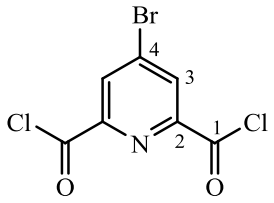

Freshly distilled $SOCl_2$ (excess, 10 mL) was added to **8b** (1 eq., 1.23 g, 5.0 mmol) under N_2. Dry DMF (0.5 mL) was added and the resulting yellow solution was refluxed for 2 h. After the mixture was cooled to r.t., the $SOCl_2$ and DMF were removed by vacuum distillation to give **8c** as a tan solid, which was used without further purification (1.32 g, 93%).

M.p.: 104°C (Lit. 105-108°C[310]).

EI-MS: *m/z* = 283 $[M]^{\cdot+}$ (1%).

^{1}H NMR ($CDCl_3$, 300 MHz) δ (ppm): 8.31 (s, 2H, H_3).

^{13}C NMR ($CDCl_3$, 300 MHz) δ (ppm): 168.7 (C_1), 150.2 (C_2), 148.0 (C_4), 129.0 (C_3).

5.3.6.4 Synthesis of 2,6-diacetyl-4-bromo-pyridine (8d)[312,313]

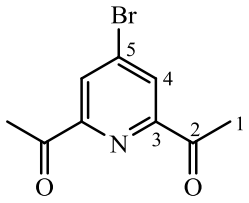

Meldrum's acid (2 eq., 1.15 g, 8.0 mmol) was dissolved in dry DCM (10 mL) and pyridine (excess, 2 mL). The pale yellow solution was cooled to 0°C, and (**8c**) (1eq., 1.13

g, 4.0 mmol) was added in one portion. The resulting mixture was stirred at 0°C for 1 h, and then warmed to r.t. and stirred for a further 18 h. Dry DCM (50 mL) was added, and the mixture was poured onto 2N HCl (60 mL) containing crushed ice. The mixture was vigorously stirred for 5 min, and then the two layers were separated. The aqueous layer was extracted with DCM (3 x 50 mL), and the combined organic layers were washed with 2N HCl (2 x 50 mL), dried over $MgSO_4$ and concentrated under vacuum to give a dark brown solid. The solid was refluxed in acetic acid/H_2O (1:1, 240 mL) at 115°C for 18 h. After the solution was cooled to r.t., H_2O (150 mL) was added, and the product was extracted with DCM (6 x 50 mL), washed with 5% $NaHCO_3$, dried over $MgSO_4$ and concentrated under vacuum. The crude product was purified by a pipette-scale silica column in pet. ether/EtOAc (8:2) to give **8d** as a light brown solid (340 mg, 35%).

M.p.:	92-94°C.
EI-MS:	*m/z* = 241 $[M]^{\cdot+}$ (100%).
^{1}H NMR (d_6-acetone, 400 MHz) δ (ppm):	8.26 (s, 2H, H_4), 2.74 (s, 6H, H_1).
^{13}C NMR (d_6-acetone, 400 MHz) δ (ppm):	198.0 (C_2), 154.6 (C_3), 135.5 (C_5), 128.0 (C_4), 25.5 (C_1).
CHN:	Found C: 45.38, H: 3.44, N: 5.76%; Calcd. for $C_9H_8BrNO_2$ C: 44.66; H: 3.33; N: 5.78%.

5.3.6.5 Synthesis of 2,6-diacetyl-4-azido-pyridine (8e)

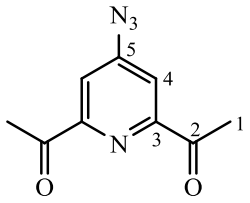

NaN_3 (10 eq., 0.209 g, 3.22 mmol) was added to a vigorously stirred solution of **8d** (1 eq., 0.078 mg, 0.322 mmol) in DMF/H_2O (10 mL, 4:1). The resulting mixture was carefully stirred at 90°C for 48 h. After cooling to r.t., the dark red solution was poured slowly onto ice-cooled water. The product was extracted with EtOAc (6 x 10 mL), and the organic layers were concentrated carefully under vacuum. The crude product was purified via a pipette-scale silica column in pet. ether/EtOAc (8:2), to give the desired product **8e** as a crystalline beige solid (19.4 mg, 29%).

^{1}H NMR (d_6-acetone, 400 MHz) δ (ppm): 7.39 (s, 2H, H_4), 2.64 (s, 6H, H_1)

^{13}C NMR (d_6-acetone, 400 MHz) δ (ppm): 200.0 (C_2), 157.1 (C_3), 138.2 (C_5), 126.0 (C_4), 25.6 (C_1).

5.4 Schiff-base macrocyclic complexes

5.4.1 Complexes of L1

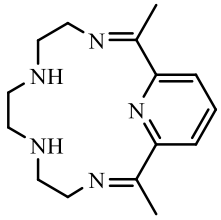

L1
(N_5)

5.4.1.1 Synthesis of $[Mn(L1)Cl_2]\cdot 2H_2O$ (1.1)

Diacetylpyridine (1 eq., 329 mg, 2.01 mmol) was added in one portion to a solution of $MnCl_2\cdot 4H_2O$ (1 eq., 349 mg, 2.01 mmol) in MeOH (30 mL). The solution was heated to 50°C, and then triethyltetramine (1 eq., 300 μL, 2.01 mmol) was added in one portion. The reaction mixture was heated to 85°C and refluxed for 18 h. The solvent volume was reduced by half, and the mixture was cooled to r.t. An excess of Et_2O was added, and the resulting precipitate was collected by Büchner filtration and washed well with cold Et_2O to give **1.1** as a beige solid (530 mg, 60%).

FAB-MS:	*m/z* = 363 $[M\text{-}Cl]^+$ (100%).
CHN:	Found C: 45.01, H: 5.88, N: 17.21%; Calcd. for $C_{15}H_{23}N_5Cl_2Mn)\cdot 2H_2O$ C: 45.13; H: 5.81; N: 17.54%.
IR (KBr, cm^{-1}):	3330 (br, O-H), 3271 (m, N-H) , 2907 (s, C-H), 2853 (s, C-H), 1649 (s, C=N), 1583 (s,

	py), 1457 (s, C-H), 1201 (s, C-N), 1112 (m, C-N), 945 (w, py).
UV-Vis (MeOH, nm):	λ_{max} = 250 (ε = 5110), λ = 300 (ε = 3070).

5.4.1.2 Synthesis of $[Gd(L1)Cl_3]\cdot 3H_2O$ (1.2)

Diacetylpyridine (1 eq., 329 mg, 2.01 mmol) was added in one portion to a solution of $GdCl_3\cdot 6H_2O$ (1 eq., 749 mg, 2.01 mmol) in MeOH (30 mL). The solution was heated to 50°C, and then triethyltetramine (1 eq., 300 μL, 2.01 mmol) was added in one portion. The reaction mixture was heated to 85°C and refluxed for 18 h. The solvent volume was reduced by half, and the mixture was cooled to r.t. After syringe flitration, an excess of Et_2O was added, and the resulting precipitate was collected by Buchner filtration and washed well with cold Et_2O to give **1.2** as a pale yellow solid (144 mg, 12%).

FAB-MS:	*m/z* = 465 $[M-H-2Cl]^+$ (2.9%).
CHN:	Found C: 30.48, H: 5.21, N: 11.95%; Calcd. for $(C_{15}H_{23}N_5Cl_3Gd)\cdot 3H_2O$ C: 30.48; H: 4.95; N: 11.85%.
IR (KBr, cm^{-1}):	3383 (br, O-H, N-H), 2961, (s, C-H), 1631 (s, C=N), 1592 (s, py), 1458 (s, C-H), 1089 (m, C-N), 1011 (w, py).
UV-Vis (MeOH, nm):	λ_{max} = 250 (ε = 5860), λ = 281 (ε = 4020).

5.4.1.3 Synthesis of $[Dy(L1)Cl_3]\cdot 4H_2O$ (1.3)

Diacetylpyridine (1 eq., 329 mg, 2.01 mmol) was added in one portion to a solution of $DyCl_3\cdot 6H_2O$ (1 eq., 759 mg, 2.01 mmol) in MeOH (30 mL). The solution was heated to 50°C, and then triethyltetramine (1 eq., 300 μL, 2.01 mmol) was added in one portion. The reaction mixture was heated to 85°C and refluxed for 18 h. The solvent volume was reduced by half, and the mixture was cooled to r.t. An excess of Et_2O was added, and the resulting precipitate was collected by Buchner filtration and washed well with cold Et_2O to give **1.3** as a beige solid (587 mg, 47.5%).

FAB-MS:	*m/z* = 471 [M-H-2Cl] (6.6%).
CHN:	Found C: 29.76, H: 4.91, N: 10.87%; Calcd. for $(C_{15}H_{23}N_5Cl_3Dy)\cdot 4H_2O$ C: 29.33; H: 5.09; N: 11.40%.
IR (KBr, cm^{-1}):	3345 (br, O-H), 3246 (m, N-H), 1629 (s, C=N), 1591 (m, py), 1492 (m, py), 1111 (w, C-N), 1010 (w, py), 813 (w, O-H).
UV-Vis (MeOH, nm):	λ_{max} = 250 (ε = 6590), λ = 281 (ε = 3820).

5.4.2 Complexes of L2

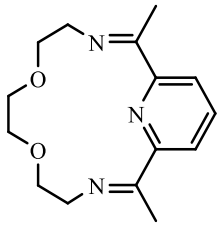

L2
(N_3O_2)

5.4.2.1 Synthesis of $[Mn(L2)Cl_2]\cdot 2H_2O$ (2.1)

Diacetylpyridine (1 eq., 412 mg, 2.53 mmol) was added in one portion to a solution of $MnCl_2\cdot 4H_2O$ (500 mg, 2.53 mmol) in MeOH (30 mL). The solution was heated to 50°C, and then 2,2′-(ethylenedioxy)bisethylamine (1 eq., 370 μL, 2.53 mmol) was added in one portion. The reaction mixture was heated to 85°C and refluxed for 18 h. The solvent volume was reduced by half, and the mixture was cooled to r.t. An excess of Et_2O was added, and the resulting precipitate was collected by Büchner filtration and washed well with cold Et_2O to give **2.1** as a pale yellow solid (875 mg, 79%).

FAB-MS:	*m/z* = 365 [M-2H_2O-Cl] (100%).
CHN:	Found C: 41.19, H: 5.69, N: 9.43%; Calcd. for ($C_{15}H_{21}N_3O_2Cl_2Mn$)·2H_2O C: 41.21; H: 5.76; N: 9.61%.
IR (KBr, cm^{-1}):	3403 (br, O-H), 2923 (s, C-H), 2880 (s, C-H), 1645 (s, C=N), 1586 (m, py), 1110 (m, C-O), 1018 (w, py).

UV-Vis (MeOH, nm):	λ_{max} = 250 (ε = 6350), λ = 300 (ε = 4240).

5.4.2.2 Synthesis of $[Gd(L2)Cl_3]\cdot 6H_2O$ (2.2)

Diacetylpyridine (1 eq., 329 mg, 2.02 mmol) was added in one portion to a solution of $GdCl_3\cdot 6H_2O$ (1 eq., 749 mg, 2.02 mmol) in MeOH (30 mL). The solution was heated to 50°C, and then 2,2′-(ethylenedioxy)bisethylamine (1 eq., 295 μL, 2.02 mmol) was added in one portion. The reaction mixture was heated to 85°C and refluxed for 18 h. The solvent volume was reduced by half, and the mixture was cooled to r.t. An excess of Et_2O was added, and the resulting precipitate was collected by Büchner filtration and washed well with cold Et_2O to give **2.2** as an orange/brown solid (287 mg, 22%).

MS-FAB:	*m/z* = 297 $[\mathbf{L2}+Na]^+$ (6.6%).
CHN:	Found C: 27.89, H: 5.23, N: 6.35%; Calcd. for $(C_{15}H_{21}N_3O_2Cl_3Gd)\cdot 6H_2O$ C: 27.84; H: 5.14; N: 6.49%.
IR (KBr, cm^{-1}):	3386 (br, O-H), 2924 (s, C-H), 1620 (m, C=N), 1595 (m, py), 1460 (m, C=C), 1095 (m, C-O).
UV-Vis (MeOH, nm):	λ_{max} = 250 (ε = 4560), λ = 274 (ε = 3720).

5.4.2.3 Synthesis of $[Dy(L2)Cl_3]\cdot 6H_2O$ (2.3)

Diacetylpyridine (1 eq., 612 mg, 3.76 mmol) was added in one portion to a solution of $DyCl_3\cdot 6H_2O$ (1 eq., 1.41 g, 3.76 mmol) in MeOH (30 mL). The solution was heated to

50°C, and then 2,2′-(ethylenedioxy)bisethylamine (1 eq., 550 μL, 3.76 mmol) was added in one portion. The reaction mixture was heated to 85°C and refluxed for 18 h. The solvent volume was reduced by half, and the mixture was cooled to r.t. An excess of Et_2O was added, and the resulting precipitate was collected by Büchner filtration and washed well with cold Et_2O to give **2.3** as an orange solid (2.36 g, 96%).

MS-FAB:	*m/z* = 297 [**L2**+Na]$^+$ (9.1%).
CHN:	Found C: 27.94, H: 4.92, N: 6.39%; Calcd. for $(C_{15}H_{21}N_3O_2Cl_3Dy)\cdot 6H_2O$ C: 27.62; H: 5.10; N: 6.44%.
IR (KBr, cm^{-1}):	3375 (br, O-H), 3007 (s, C-H), 1625 (m, C=N), 1593 (m, py), 1460 (w, C-H), 1095 (m, C-O), 1017 (m, py).
UV-Vis (MeOH, nm):	λ_{max} = 250 (ε = 5140), λ = 274 (ε = 4050), λ = 315 (ε = 4410).

5.4.3 Complexes of L3

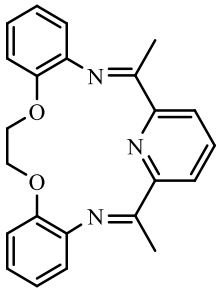

L3
(dpN_3O_2)

5.4.3.1 Synthesis of $[Mn(L3)ClH_2O]Cl \cdot H_2O$ (3.1)

Diacetylpyridine (1 eq., 134 mg 0.82 mmol) was added in one portion to a solution of $MnCl_2 \cdot 4H_2O$ (1 eq., 142 mg, 0.82 mmol) in EtOH (30 mL). The solution was heated to 50°C, and then diamine **3b** (1 eq., 200 mg, 0.82 mmol) was added in one portion. The reaction mixture was heated to 85°C and refluxed for 4 h. The solvent volume was reduced by half, and the mixture was cooled to r.t. An excess of Et_2O was added, and the resulting precipitate was collected by Büchner filtration and washed well with cold Et_2O to give **3.1** as an orange solid (62 mg, 14%).

MS-FAB:	*m/z* = 461 $[M\text{-}2H_2O\ Cl]^+$ (10%).
CHN:	Found C: 55.72, H: 4.65, N: 8.39%; Calcd. for $(C_{23}H_{21}N_3O_2Cl_2Mn) \cdot 2H_2O$ C: 55.55; H: 4.26; N: 8.45%.
IR (KBr, cm^{-1}):	3351 (br, O-H), 3072 (m, C-H ar.), 2968 (s, C-H), 2924 (s, C-H), 1617 (m, C=N), 1592 (m, py), 1503 (m, C=C), 1362 (m, C-H), 1087 (m, C-O).
UV-Vis (MeOH, nm):	λ_{max} = 252 (ε = 11060), λ = 284 (ε = 7670).

5.4.3.2 Synthesis of $[Gd(L3)Cl_3] \cdot 0.5H_2O$ (3.2)

Diacetylpyridine (1 eq., 134 mg, 0.82 mmol) was added in one portion to a solution of $GdCl_3 \cdot 4H_2O$ (1 eq., 304 mg, 0.82 mmol) in EtOH (30 mL). The solution was heated to 50°C, and then diamine **3b** (1 eq., 200 mg, 0.82 mmol) was added in one portion. The

reaction mixture was heated to 85°C and refluxed for 4 h. The solvent volume was reduced by half, and the mixture was cooled to r.t. An excess of Et_2O was added, and the resulting precipitate was collected by Büchner filtration and washed well with cold Et_2O to give **3.2** as a brown solid (58 mg, 11%).

CHN:	Found C: 43.71, H: 4.01, N: 5.63%; Calcd. for $(C_{23}H_{21}N_3O_2Cl_3Gd)\cdot 0.5H_2O$ C: 42.89; H: 3.44; N: 6.52%.
IR (KBr, cm^{-1}):	3342 (br, O-H), 2828 (m, C-H), 1632 (m, C=N), 1597 (s, py), 1503 (m, C=C), 1460 (w, C=C), 1362 (w, C-H), 1082 (m, C-O).
UV-Vis (MeOH, nm):	λ_{max} = 250 (ε = 7200), λ = 275 (ε = 5160).

5.4.4 Complexes of L4

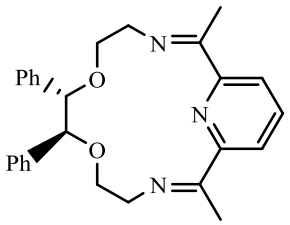

L4
(dbN_3O_2)

5.4.4.1 Synthesis of *R,R*-[Mn(L4)Cl_2]·2H_2O (4.1)

Diacetylpyridine (1 eq., 107 mg, 0.65 mmol) was added in one portion to a solution of $MnCl_2\cdot 4H_2O$ (1 eq., 113 mg, 0.65 mmol) in bubbled MeOH (30 mL) under inert conditions. The solution was heated to 50°C, and then diamine **4d** (1 eq., 196 mg, 0.65 mmol) in MeOH (5 mL) was added in one portion. The reaction mixture was heated to

85°C and refluxed for 18 h under N_2. The solvent volume was reduced by half, and the mixture was cooled to r.t. An excess of Et_2O was added, and the resulting precipitate was collected by Büchner filtration and washed well with cold Et_2O to give **4.1** as a beige solid (102 mg, 27%).

FAB-MS:	*m/z* = 517 $[M\text{-}2H_2OCl]^+$ (100%).
CHN:	Found C: 55.15, H: 5.63, N: 6.79%; Calcd. for $(C_{27}H_{29}Cl_2MnN_3O_2)\cdot 2H_2O$ C: 55.02; H: 5.64; N: 7.13%.
IR (KBr, cm^{-1}):	3371 (br, O-H), 3061 (m, C-H ar.), 2888 (m, C-H), 1650 (m, C=N), 1587 (m, py), 1454 (m, C=C), 1079 (m, C-O), 929 (w, py).
UV-Vis (MeOH, nm):	λ_{max} = 252 (ε = 5840), λ = 301 (ε = 3240).

5.4.5 Complexes of L5

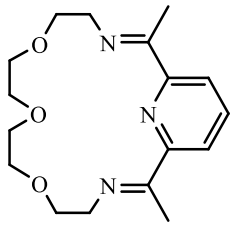

L5
(N_3O_3)

5.4.5.1 Synthesis of $[Gd(L5)Cl_3]\cdot 2H_2O$ (5.1)

Diacetylpyridine (1 eq., 620 mg, 3.80 mmol) was added in one portion to a solution of $GdCl_3\cdot 6H_2O$ (1 eq., 1.412 g, 3.80 mmol) in MeOH (30 mL). The solution was heated to 50°C, and then diamine **5c** (1 eq., 731 mg, 3.80 mmol) in MeOH (5 mL) was added in one portion. The reaction mixture was heated to 85°C and refluxed for 18 h. The solvent volume was reduced by half, and the mixture was cooled to r.t. An excess of Et_2O was added, and the resulting precipitate was collected by Büchner filtration and washed well with cold Et_2O to give **5.1** as a yellow solid (136 mg, 6%).

FAB-MS:	*m/z* = 193 $[\mathbf{L5}+H]^+$ (41%).
CHN:	Found C: 32.83, H: 4.10, N: 5.95%; Calcd. for $(C_{17}H_{25}N_3O_3Cl_3Gd)\cdot 2H_2O$ C: 32.98; H: 4.72; N: 6.79%.
IR (KBr, cm^{-1}):	3289 (br, O-H), 1626 (s, C=N), 1595 (s, py), 14534 (w, C-H), 1361 (m, C-H), 1118 (w, C-O), 1083 (m, C-O), 1012 (w, py), 814 (w, O-H).
UV-Vis (MeOH, nm):	λ_{max} = 251 (ε = 10520), λ = 278 (ε = 7480).

5.4.6 Complexes of L6

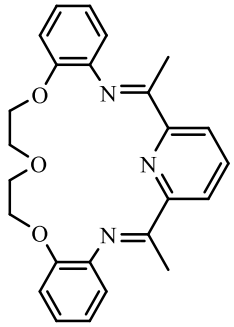

L6
(dbN_3O_3)

5.4.6.1 Synthesis of $[Mn(L6)Cl_2]\cdot 2H_2O$ (6.1)

Diacetylpyridine (1 eq., 417 mg, 2.55 mmol) was added in one portion to a solution of $MnCl_2\cdot 4H_2O$ (1 eq., 505 g, 2.55 mmol) in MeOH (30 mL). The solution was heated to 50°C, and then diamine **6c** (1 eq., 736 mg, 2.55 mmol) was added in one portion. The reaction mixture was heated to 85°C and refluxed for 18 h. The solvent volume was reduced by half, and the mixture was cooled to r.t. An excess of Et_2O was added, and the resulting precipitate was collected by Büchner filtration and washed well with cold Et_2O to give **6.1** as a yellow solid (856 mg, 58%).

FAB-MS:	*m/z* = 289 [**L6**+H]$^+$ (60%), 505 [M-2H2O-Cl]$^+$ (5.9%).
CHN:	Found C: 51.88, H: 4.98, N: 7.31%; Calcd. for $(C_{25}H_{25}N_3O_3Cl_2Mn)\cdot 2H_2O$ C: 52.01; H: 5.06; N: 7.28%.

IR (KBr, cm^{-1}):	3422 (br, O-H), 3069 (m, C-H ar.), 2872 (m, C-H), 1617 (m, C=N), 1586 (s, py), 1492 (s, C=C), 1116 (m, C-O), 1084 (m, C-O), 1011 (w, py), 816 (w, O-H).
UV-Vis (MeOH, nm):	λ_{max} = 251 (ε = 10520), λ = 282 (ε = 6470).

5.4.6.2 Synthesis of $[Gd(L6)Cl_3]\cdot 6H_2O$ (6.2)

Diacetylpyridine (1 eq., 97.9 mg, 0.60 mmol) was added in one portion to a solution of $GdCl_3\cdot 6H_2O$ (1 eq., 223 mg, 0.60 mmol) in MeOH (30 mL). The solution was heated to 50°C, and then diamine **6c** (1 eq., 173 mg, 0.60 mmol) was added in one portion. The reaction mixture was heated to 85°C and refluxed for 18 h. The solvent volume was reduced by half, and the mixture was cooled to r.t. An excess of Et_2O was added, and the resulting precipitate was collected by Büchner filtration and washed well with cold Et_2O to give **6.2** as a brown solid (148 mg, 31%).

FAB-MS:	*m/z* = 289 [**L6**+H]$^+$ (100%).
CHN:	Found C: 38.50, H: 4.39, N: 5.14%; Calcd. for $(C_{25}H_{25}N_3O_3Cl_3Gd)\cdot 6H_2O$ C: 38.14; H: 4.74; N: 5.34%.
IR (KBr, cm^{-1}):	3331 (br, O-H), 2868 (m, C-H), 1628 (m, C=N), 1594 (s, py), 1504 (s, C=C), 1362 (w, C-H), 1127 (m, C-O), 1055 (m, C-O), 957 (w, py), 816 (w, O-H).

UV-Vis (MeOH, nm):	λ_{max} = 254 (ε = 8501), λ = 277 (ε = 8038).

5.4.6.3 Synthesis of $[Dy(L6)Cl_3]\cdot 6H_2O$ (6.3)

Diacetylpyridine (1 eq., 433 mg, 2.65 mmol) was added in one portion to a solution of $DyCl_3\cdot 6H_2O$ (1 eq., 1.00 g, 2.65 mmol) in MeOH (30 mL). The solution was heated to 50°C, and then diamine **6c** (1 eq., 765 mg, 2.65 mmol) was added in one portion. The reaction mixture was heated to 85°C and refluxed for 18 h. The solvent volume was reduced by half, and the mixture was cooled to r.t. An excess of Et_2O was added, and the resulting precipitate was collected by Büchner filtration and washed well with cold Et_2O to give **6.3** as a dark brown solid (390 mg, 19%).

FAB-MS:	*m/z* = 289 [**L6**+H]$^+$ (100%).
CHN:	Found C: 37.94, H: 4.44, N: 4.95%; Calcd. for $(C_{25}H_{25}N_3O_3Cl_3Dy)\cdot 6H_2O$ C: 37.89; H: 4.71; N: 5.30%.
IR (KBr, cm^{-1}):	3318 (br, O-H), 2936 (m, C-H), 1620 (m, C=N), 1594 (m, C=N), 1501 (s, C=C), 1360 (m, C-H), 1117 (m, C-O), 1084 (m, C-O).
UV-Vis (MeOH, nm):	λ_{max} = 276 (ε = 4966).

5.4.7 Complexes of L7

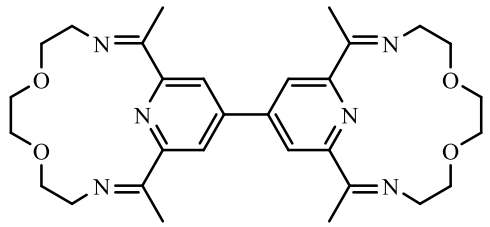

L7
(O_2N_3-N_3O_2)

5.4.7.1 Synthesis of $[Mn_2(L7)Cl_4]\cdot 5H_2O$ (7.1)

To a solution of $MnCl_2\cdot 4H_2O$ (1 eq., 135 mg, 0.783 mmol) in MeOH (20 mL) was added **7d** (1 eq., 127 mg, 0.392 mmol) in one portion. The brown mixture was heated to 50°C, and then 2,2′-(ethylenedioxy)bisethylamine (1 eq., 116 μL, 0.783 mmol) was added. The reaction mixture was heated to 85°C and refluxed for 18 h. The solvent volume was reduced by half and the solution was passed through a syringe filter. An excess of Et_2O was added, and precipitate was collected by Buchner filtration to give **7.1** as a beige solid (190 mg, 54%).

FAB-MS:	*m/z* = 728 $[M\text{-}4H_2O\text{-}2Cl]^+$ (16.4%).
CHN:	Found C: 40.27, H: 5.49, N: 9.52%; Calcd. for $(C_{30}H_{40}N_6O_4Cl_4Mn_2)\cdot 5H_2O$ C: 40.47; H: 5.66; N: 9.44%.
IR (KBr, cm^{-1}):	3385 (br, O-H), 2932 (s, C-H), 1648 (s, C=N), 1596 (m, py), 1378, 1349, 1106 (m, C-O) 1071 (w, C-O).

UV-Vis (MeOH, nm): λ_{max} = 252 (ε = 18060), λ = 311 (ε = 3820).

5.5Crown ether complexes

5.5.1 Complexes of 12-crown-4

5.5.1.1 Synthesis of $[Dy(12C4)(H_2O)_5](ClO_4)_3{\cdot}H_2O$ (9.1)

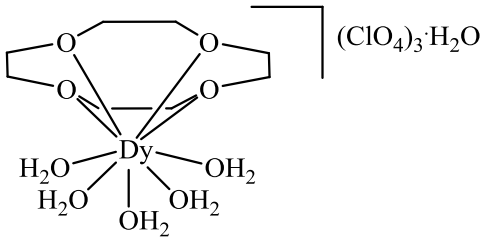

$Dy(ClO_4)_3$(aq) (40% w/w, 847 μL, 1.09 mmol) and 12-crown-4 (173 μL, 1.09 mmol) were vigorously stirred in MeOH/CH_3CN (1:3, 6 mL) at 55 °C for 3 h. The reaction mixture was cooled to room temperature, filtered through cotton wool and left to crystallize by slow evaporation. Clear, colourless block-shaped crystals of 9.1 were isolated after 6 days (77.5 mg, 10%).

FAB-MS: *m/z* = 538 $[M\text{-}6H_2O\text{-}ClO_4]^+$ (100%).

CHN: Found C: 12.90, H: 3.79, N: 0.00 %; Calcd. for $C_8H_{28}Cl_3O_{22}Dy$ C, 12.89; H, 3.79; N, 0.00%.

IR (cm^{-1}): 3405 (br, O-H), 2970 (w, C-H), 1050 (s, Cl-O/C-O), 1027 (s, Cl-O/C-O), 929 (m, Cl-O), 618 (m, Cl-O).

UV-Vis (MeOH, nm): λ_{max} = 269 (ε = 119).

5.5.1.2 Synthesis of Y-doped $[Dy(12C4)(H_2O)_5](ClO_4)_3 \cdot H_2O$ (9.1b)

$Dy(ClO_4)_{3(aq)}$ (50% w/w, 57 μL, 0.098 mmol), $Y(ClO_4)_{3(aq)}$ (50% w/w, 1.00 mL, 1.95 mmol) and 12-crown-4 (326 μL, 2.05 mmol) were vigorously stirred in MeOH/CH_3CN (1:3, 6 mL) at 55 °C for 3 h. Clear, pale yellow block-shaped crystals of **9.1b** were obtained via slow evaporation after 6 days (260 mg, 19%).

CHN: Found C: C: 14.35, H: 3.81, N: 0.00%; Calcd. for $C_8H_{26}Cl_3O_{21}Dy_{0.12}Y_{0.88}$ C, 14.51; H, 3.95; N, 0.00%.

5.5.1.3 Synthesis of $[Ho(12C4)(H_2O)_5](ClO_4)_3 \cdot H_2O$ (9.3)

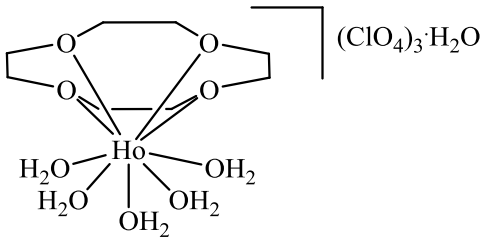

$Ho(ClO_4)_3$(aq) (40% w/w, 1 eq., 250 μL, 0.303 mmol) and 12-crown-4 (1 eq., 48.2 μL, 0.303 mmol) were vigorously stirred in MeOH/CH_3CN (1:3, 6 mL) at 55 °C for 3 h. The reaction mixture was cooled to room temperature, filtered through cotton wool and left to crystallize by slow evaporation. After 3 days, clear pale pink crystals of **9.3** were isolated (132 mg, 58%).

MALDI-TOF-MS:	*m/z* = 441 $[M-5H_2O-2ClO_4-H]^+$ (100%).
CHN:	Found C: C: 12.56, H: 3.69, N: 0.18%; Calcd. for $C_8H_{28}Cl_3HoO_{22}\cdot H_2O\cdot 0.1CH_3CN$ C, 12.80; H, 3.97; N, 0.18%.
IR (cm^{-1}):	3405 (br, O-H), 2970 (w, C-H), 1043 (s, Cl-O/C-O), 1026 (s, Cl-O/C-O), 929 (m, Cl-O), 616 (m, Cl-O).
UV-Vis (MeOH, nm):	λ_{max} = 248 (ε = 37).

5.5.2 Complexes of 15-crown-5

5.5.2.1 Synthesis of $[Dy(15C5)(H_2O)_4](ClO_4)_3\cdot 15C5\cdot H_2O$ (10.1)

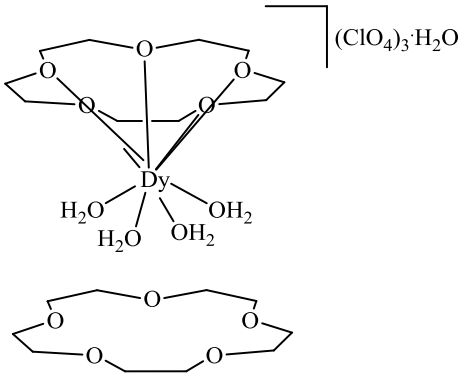

$Dy(ClO_4)_3$(aq) (40% w/w, 847 μL, 1.09 mmol) and 15-crown-5 (215 μL, 1.09 mmol) were vigorously stirred in MeOH/CH_3CN (1:3, 6 mL) at 55 °C for 3 h. The reaction mixture was cooled to room temperature, filtered through cotton wool and left to crystallize by slow evaporation. After 8 days, opaque white crystals of **10.1** were isolated (231 mg, 21%).

FAB-MS:	*m/z* = 582 $[M\text{-}4H_2O\text{-}ClO_4\text{-}15C5]^+$ (47%).
CHN:	Found C: C: 22.64, H: 5.82, N: 0.00%; Calcd. for $C_{10}H_{30}Cl_3O_{22}Dy{\cdot}4.5H_2O$ C, 22.40; H, 5.54; N, 0.00%.
IR (cm^{-1}):	3355 (br, O-H), 3241 (br, O-H), 2930 (w, C-H), 2886 (w, C-H), 1050 (s, Cl-O/C-O), 1028 (s, Cl-O/C-O), 939 (m, Cl-O), 619 (m, Cl-O).
UV-Vis (MeOH, nm):	λ_{max} = 250 (ε = 19).

5.5.2.2 Synthesis of $[Er(15C5)(H_2O)_4](ClO_4)_3{\cdot}3H_2O$ (10.2)

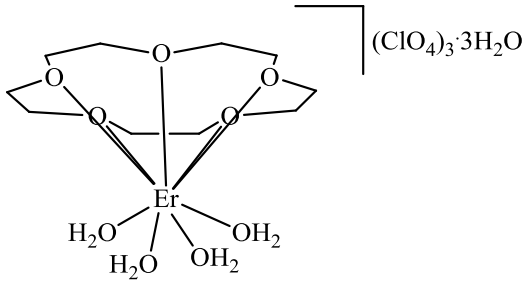

$Er(ClO_4)_3$(aq) (40% w/w, 149 μL, 0.178 mmol) and 15-crown-5 (35.3 μL, 0.178 mmol) were vigorously stirred in MeOH/CH_3CN (1:3, 6 mL) at 55 °C for 18 h. The reaction mixture was cooled to room temperature, filtered through cotton wool and left to crystallize by slow evaporation. After 5 days, pink needle-like crystals of **10.2** were isolated (68 mg, 44%).

MALDI-TOF-MS:	*m/z* = 676 $[M\text{-}2H_2O\text{-}ClO_4]^+$ (68%), 586 $[M\text{-}7H_2O\text{-}ClO_4]^+$ (21%).
CHN:	Found: C: 14.16, H: 3.65, N: 0.00%; Calcd. for $C_{10}H_{34}Cl_3ErO_{24}$ C, 14.79; H, 4.22; N, 0.00%.
IR (cm^{-1}):	3395 (br, O-H), 2947 (w, C-H), 1051 (b, Cl-O/C-O), 951 (m, Cl-O), 932 (m, Cl-O), 620 (m, Cl-O).
UV-Vis (MeOH, nm):	λ_{max} = 246 (ε = 55).

5.5.3 Complexes of 18-crown-6

5.5.3.1 Synthesis of $[Tb(18C6)(H_2O)_3](ClO_4)_3{\cdot}H_2O$ (11.1)

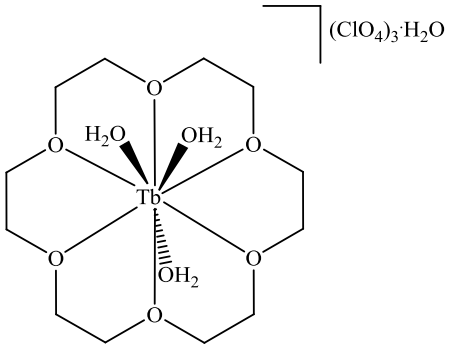

$Tb(ClO_4)_3$(aq) (50% w/w, 2 eq., 547 μL, 0.757 mmol) and 18-crown-6 (1 eq., 100 mg, 0.379 mmol) were vigorously stirred in MeOH/CH_3CN (1:3, 6 mL) at 55 °C for 18 h. The reaction mixture was cooled to room temperature, filtered through cotton wool and left to crystallize by slow evaporation. After 6 days, **11.1** was isolated as clear, pale yellow crystals (232 mg, 77%).

MALDI-TOF-MS:	*m/z* = 621 $[M\text{-}4H_2O\text{-}ClO_4]^+$ (100%)
CHN:	Found: C, 17.92; H, 3.94; N, 0.00%; Calcd. for $C_{12}H_{32}Cl_3O_{22}Tb$: C: 18.16, H: 4.06, N: 0.00%.
IR (cm^{-1}):	3406 (br, O-H), 2956 (w, C-H), 1049 (s, Cl-O/C-O), 1030 (s, Cl-O/C-O), 950 (m, Cl-O), 931 (m, Cl-O), 619 (m, Cl-O).
UV-Vis (MeOH, nm):	λ_{max} = 250 (ε = 29).

5.5.3.2 Synthesis of $[Dy(18C6)(H_2O)_3](ClO_4)_3{\cdot}H_2O$ (11.2)

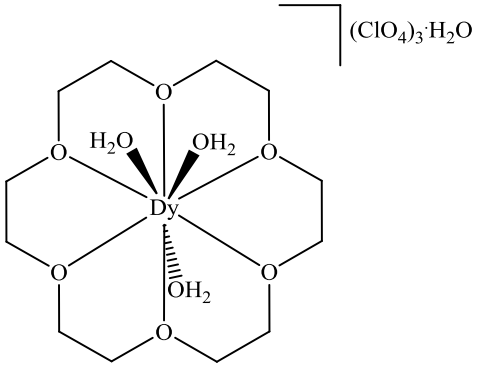

$Dy(ClO_4)_3$(aq) (50% w/w, 3 eq., 468 μL, 0.757 mmol) and 18-crown-6 (1 eq., 67 mg, 0.252 mmol) were vigorously stirred in MeOH/CH_3CN (1:3, 6 mL) at 55 °C for 18 h. The reaction mixture was cooled to room temperature, filtered through cotton wool and left to crystallize by slow evaporation. After 6 days, **11.2** was isolated as clear, colourless crystals (120 mg, 60%).

MALDI-TOF-MS:	*m/z* = 626 $[M\text{-}4H_2O\text{-}ClO_4]^+$ (100%)
CHN:	Found: C: 18.04, H: 3.90, N: 0.00%; Calcd. for $C_{12}H_{32}Cl_3O_{22}Dy$: C, 18.08; H, 4.05; N, 0.00%.
IR (cm^{-1}):	3422 (br, O-H), 2951 (w, C-H), 1050 (b, Cl-O/C-O), 1030 (b, Cl-O/C-O), 952 (m, Cl-O), 931 (m, Cl-O), 619 (m, Cl-O).
UV-Vis (MeOH, nm):	λ_{max} = 248 (ε = 46).

5.5.3.3 Synthesis of $[Ho(18C6)(H_2O)_3](ClO_4)_3$ (11.3)

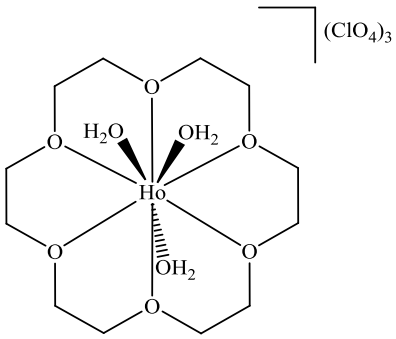

$Ho(ClO_4)_3$(aq) (40% w/w, 3 eq., 601 μL, 0.757 mmol) and 18-crown-6 (1 eq., 67 mg, 0.252 mmol) were vigorously stirred in MeOH/CH_3CN (1:3, 6 mL) at 55 °C for 18 h. The reaction mixture was cooled to room temperature, filtered through cotton wool and left to crystallize by slow evaporation. After 4 days, **11.3** was isolated as pink needle-like crystals (144 mg, 73%).

MALDI-TOF-MS:	*m/z* = 627 $[M\text{-}4H_2O\text{-}ClO_4]^+$ (100%)

CHN:	Found: C: 18.06, H: 3.92, N: 0.00%; Calcd. for $C_{12}H_{30}Cl_3HoO_{21}$: C, 18.44; H, 3.87; N, 0.00%.
IR (cm^{-1}):	3397 (br, O-H), 2955 (w, C-H), 1049 (s, Cl-O/C-O), 1029 (s, Cl-O/C-O), 951 (m, Cl-O), 931 (m, Cl-O), 619 (m, Cl-O).
UV-Vis (MeOH, nm):	λ_{max} = 250 (ε = 57).

5.5.3.4 Synthesis of $[Er(18C6)(H_2O)_3](ClO_4)_3$ (11.4)

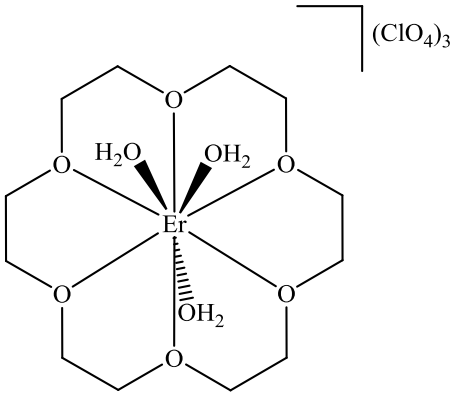

$Er(ClO_4)_3$(aq) (50% w/w, 2 eq., 560 µL, 0.757 mmol) and 18-crown-6 (1 eq., 100 mg, 0.379 mmol) were vigorously stirred in MeOH/CH_3CN (1:3, 6 mL) at 55 °C for 18 h. The reaction mixture was cooled to room temperature, filtered through cotton wool and left to crystallize by slow evaporation. After 6 days, **11.4** was isolated as clear pink crystals (140 mg, 47%).

MALDI-TOF-MS:	*m/z* = 630 $[M\text{-}4H_2O\text{-}ClO_4]^+$ (100%)

CHN:	Found: C: 14.55, H: 4.00, N: 0.15%; Calcd. for $C_{12}H_{30}Cl_3ErO_{21}$: C, 17.97; H, 4.02; N, 0.00%.
IR (cm^{-1}):	3422 (br, O-H), 2951 (w, C-H), 1050 (b, Cl-O/C-O), 1030 (b, Cl-O/C-O), 952 (m, Cl-O), 931 (m, Cl-O), 619 (m, Cl-O).
UV-Vis (MeOH, nm):	λ_{max} = 247 (ε = 62).

5.6 *In vitro* and *in vivo* methods

5.6.1 *In vitro* relaxivity measurements

T_1 and T_2 relaxation times were measured at 300 and 600 MHz using a Bruker Advance AV 300 Digital NMR spectrometer and a Bruker Advance AV 600 Digital NMR spectrometer, with the guidance of Razvan Simionescu. Measurements were carried out on a series of 5-10 aqueous dilutions between 0 – 5 mM, with a deuterated water insert, and processed using Bruker TOPSPIN 2.1 PL6 software. T_1 and T_2 relaxation times were measured at 60 MHz at the STTARR Innovation Centre in Toronto, Canada using a Bruker minispec mq60 Contrast Agent Analyzer, with the guidance of Dr. Warren Foltz. T_1 and T_2 relaxation times were measured at 20 MHz at the Bruker Showroom in Milton, Canada on a model mq20 Contrast Agent Analyzer. At 60 and 20 Hz, measurements were carried out on a series of 6 aqueous dilutions between 0 – 5 mM.

5.6.2 *In vitro* cytotoxicity study

The *in vitro* cytotoxicity study was performed by In Vitro ADMET Laboratories, Columbia, MD.

Reference compound: Gadodiamide (Selleckchem, Lot # 02) was used as the reference compound. It is one of the 8 Gd(III)-based MRI agents approved for use in Canada (trade name: Omniscan).

Preparation of test articles and reference compound: The test articles and reference compound were weighed and dissolved in the incubation medium to give the highest test concentration of 30 mM. The solution was filter sterilized and diluted to the remaining test concentrations of 10 mM, 3.3 mM, 1.1 mM, 0.36 mM, 0.12 mM and 0.04 mM.

Preparation of cells: Cryopreserved primary rat renal proximal tubule epithelial cells (RPTECs) (ScienCell Research Laboratories, Carlsbad, CA) were used for the study. The rat RPTECs were thawed completely at 37ºC, and transferred to epithelial cell medium (ScienCell Research Laboratores, Carlsbad, CA) followed by plating in poly-L-lysine coated 96-well plates. The RPTECs were allowed to recover and grow in a cell culture incubator (37°C, humidified atmosphere of 5% carbon dioxide and 95% air) for 3 additional days with a medium change every alternate day.

Treatment of cells: Following 3 days of plating, the RPTECs were washed once with serum free epithelial cell medium (ScienCell Research Laboratories, Carlsbad, CA) followed by treatment with the test, reference or control articles for 2, 4, 10 or 24 h. All treatments were performed in triplicate.

Quantification of cell viability: Cellular viability and metabolic activity were assessed by using the 3-(4,5dimethylthiazol- 2-yl)-2,5-diphenyl tetrazolium bromid e(MTT)

uptake assay. A 10x stock of the MTT dye was prepared in phosphate buffered saline (PBS). An aliquot of dye was added 2 hrs before the intended time point to achieve a final 1x concentration, after which incubation (37°C, humidified atmosphere of 5% carbon dioxide and 95% air) continued until the desired time point. For the 2 hr time point, the aliquot of dye was added immediately after the test articles. Following incubation, all media was aspirated from the wells and the plates were allowed to dry. The resulting formazan crystals were dissolved in DMSO using an orbital shaker, and the absorbance at 570 nm was measured using a Victor ^{3}V multilabel plate reader (reference wavelength = 650 nm).

Data analysis: The inhibitory concentration (IC_{50}, the concentration resulting in 50% toxicity) was determined by plotting log concentration vs. relative viability, followed by non-linear regression of the curve using Graph Pad Prism 5.0.

5.6.3 *In vivo* methods

Preliminary *in vivo* studies were performed at the Animal Resource Centre and the STTARR Innovation Centre, Toronto, as outlined in UHN AUP 3859.1. Necropsy and histopathology were carried out by Mbed Pathology.

Acute toxicity: Compound **1.1** (aq., 0.0125 mM) was injected intravenously into 4 male rats (Sprague Dawley Crl:SD, 315-340 g) at a dosage of 0.02 mmol/kg following anaesthesia with 5% isoflurane. The animals were observed for a period of 14 days. Body weight measurements and hematology were performed on days 7 and 14. Following euthanasia, the heart, lungs, liver, kidneys, spleen, thyroid and pituitary glands were

grossly examined during necropsy, and samples of the brain, heart, lungs, liver, kidneys, spleen and thymus were microscopically evaluated during histopathological examination.

Imaging: Compound **1.1** (aq., 0.0125 mM) was injected intravenously into 2 male rats (Sprague Dawley Crl:SD, 312-338 g) at a dosage of 0.02 mmol/kg following anaesthesia with 5% isoflurane. Anesthesia was maintained at 2-2.5% isoflurane through a nose cone for the duration of the scans. Fast-spin-echo images were collected for 45 mins. immediately post-injection. The DT1-weighted RARE (Rapid Acquisition Relaxation Enhancement) scans were acquired with an echo time of 10 ms, and a repetition time = respiratory cycle duration (~1100 ms).

6 REFERENCES

[1] Saslow, D.; Boetes, C.; Burke, W.; Harms, S.; Leach, M. O.; Lehman, C. D.; Morris, E.; Pisano, E.; Schnall, M.; Sener, S. *CA - Cancer J. Clin*. **2007**, *57*, 75.

[2] Jack, C. R.; Bernstein, M. A.; Fox, N. C.; Thompson, P.; Alexander, G.; Harvey, D.; Borowski, B.; Britson, P. J.; L Whitwell, J.; Ward, C. *J. Magn. Reson*. **2008**, *27*, 685.

[3] Sabatini, U.; Boulanouar, K.; Fabre, N.; Martin, F.; Carel, C.; Colonnese, C.; Bozzao, L.; Berry, I.; Montastruc, J.; Chollet, F. *Brain* **2000**, 123, 394.

[4] Hermann, P.; Kotek, J.; Kubíček, V.; Lukeš, I. *Dalton Trans*. **2008**, 3027.

[5] Dominik Weishaupt, V. D. K., Borut Marincek How Does MRI Work? An Introduction to the Physics and Functioning of Magnetic Resonance Imaging; Springer: Berlin, Heidelberg, 2006.

[6] Caravan, P. *Chem. Soc. Rev*. **2006**, *35*, 512.

[7] Spencer, A.; Wilson, S.; Harpur, E. *Hum. Exp. Toxicol*. **1998**, *17*, 633.

[8] Spencer, A. J.; Wilson, S. A.; Batchelor, J.; Reid, A.; Pees, J.; Harpur, E. *Toxicol. Pathol*. **1997**, *25*, 245.

[9] Zhao, B.; Chen, X.-Y.; Wang, W.-Z.; Cheng, P.; Ding, B.; Liao, D.-Z.; Yan, S.-P.; Jiang, Z.-H. *Inorg. Chem. Commun*. **2005**, *8*, 178.

[10] Caravan, P.; Ellison, J. J.; McMurry, T. J.; Lauffer, R. B. *Chem. Rev*. **1999**, *99*, 2293.

[11] Chang, C. A.; Francesconi, L. C.; Malley, M. F.; Kumar, K.; Gougoutas, J. Z.; Tweedle, M. F.; Lee, D. W.; Wilson, L. J. *Inorg. Chem*. **1993**, *32*, 3501.

[12] Rohrer, M.; Bauer, H.; Mintorovitch, J.; Requardt, M.; Weinmann, H.-J. *Invest. Radiol*. **2005**, *40*, 715.

[13] Kanal, E.; Maravilla, K.; Rowley, H. *Am. J. Neuroradiol.* **2014**, *35*, 2215.

[14] Shen, Y.; Goerner, F. L.; Snyder, C.; Morelli, J. N.; Hao, D.; Hu, D.; Li, X.; Runge, V. M. *Invest. Radiol*. **2015**, *50*, 330.

[15] Sabach, A. S.; Bruno, M.; Kim, D.; Mulholland, T.; Lee, L.; Kaura, S.; Lim, R. P. *Am. J. Roentgenol*. **2013**, *200*, 1378.

[16] Kumar, K.; Chang, C. A.; Francesconi, L.; Dischino, D.; Malley, M.; Gougoutas, J.; Tweedle, M. *Inorg. Chem*. **1994**, *33*, 3567.

[17] Toth, E.; Kiraly, R.; Platzek, J.; Radüchel, B.; Brücher, E. *Inorg. Chim. Acta* **1996**, *249*, 191.

[18] Imura, H.; Choppin, G.; Cacheris, W.; De Learie, L.; Dunn, T.; White, D. *Inorg. Chim. Acta* **1997**, *258*, 227.

[19] Caravan, P.; Comuzzi, C.; Crooks, W.; McMurry, T.; Choppin, G.; Woulfe, S. *Inorg. Chem*. **2001**, *40*, 2170.

[20] Laurent, S.; Vander Elst, L.; Copoix, F.; Muller, R. N. *Invest. Radiol*. **2001**, *36*, 115.

[21] Raymond, K. N.; Pierre, V. C. *Bioconjugate Chem*. **2005**, *16*, 3.

[22] Xu, J.; Franklin, S. J.; Whisenhunt Jr, D. W.; Raymond, K. N. *J. Am. Chem. Soc*. **1995**, *117*, 7245.

[23] Pierre, V. C.; Melchior, M.; Doble, D. M.; Raymond, K. N. *Inorg. Chem*. **2004**, *43*, 8520.

[24] Cohen, S. M.; Xu, J.; Radkov, E.; Raymond, K. N.; Botta, M.; Barge, A.; Aime, S. *Inorg. Chem*. **2000**, *39*, 5747.

[25] Cacheris, W. P.; Quay, S. C.; Rocklage, S. M. *MRI* **1990**, *8*, 467.

[26] Marckmann, P.; Skov, L.; Rossen, K.; Dupont, A.; Damholt, M. B.; Heaf, J. G.; Thomsen, H. S. *J. Am. Soc. Nephrol*. **2006**, *17*, 2359.

[27] Grobner, T. *Nephrol. Dial. Transplant*. **2006**, *21*, 1104.

[28] Morcos, S. K. *Br. J. Radiol*. **2007**, *80*, 73.

[29] Perazella, M. A. *Curr. Drug Safety* **2008**, *3*, 67.

[30] Boyd, A. S.; Zic, J. A.; Abraham, J. L. *J. Am. Acad. Dermatol*. **2007**, *56*, 27.

[31] Thomsen, H. S.; Morcos, S. K. *Br. J. Radiol*. **2003**, *76*, 513.

[32] Stacul, F.; van der Molen, A.; Reimer, P.; Webb, J. W.; Thomsen, H.; Morcos, S.; Almén, T.; Aspelin, P.; Bellin, M.-F.; Clement, O.; Heinz-Peer, G. *Eur. Radiol.* **2011**, *21*, 2527.

[33] Lauterbur, P.; Mendonca-Dias, M.; Rudin, A. Frontiers of Biological Energetics; Academic Press: New York, 1978, p. 752.

[34] Leopoldini, M.; Russo, N.; Toscano, M. *Chem. Eur. J.* **2009**, *15*, 8026.

[35] Wedler, F. C.; Denman, R. B.; Roby, W. G. *Biochem.* **1982**, *21*, 6389.

[36] Schulz, M.; Schmoldt, A. *Pharmazie* **2003**, *58*, 447.

[37] Crossgrove, J. S.; Yokel, R. A. *Neurotoxicology* **2005**, *26*, 297.

[38] Pal, P. K.; Samii, A.; Calne, D. *Neurotoxicology* **1999**, *20*, 227.

[39] Small, W.; Macchi, D. D.; Parker, J. R.; Bernardino, M. E. Acad. *Radiol.* **1998**, *5*, S147.

[40] Kueny-Stotz, M.; Garofalo, A.; Felder-Flesch, D. *Eur. J. Inorg. Chem*. **2012**, 1987.

[41] Drahoš, B.; Lukeš, I.; Tóth, É. *Eur. J. Inorg. Chem*. **2012**, 1975.

[42] Sahani, D. V.; O'Malley, M. E.; Bhat, S.; Hahn, P. F.; Saini, S. J. *Comput. Assist. Tomogr.* **2002**, 26, 216.

[43] Rofsky, N.; Earls, J. Magnetic Resonance Imaging Clinics of North America **1996**, *4*, 73.

[44] Elizondo, G. *Radiology* **1991**, 178.

[45] Zetter, M. S.; Grant, M. W.; Wood, E. J.; Dodgen, H. W.; Hunt, J. P. *Inorg. Chem*. **1972**, *11*, 2701.

[46] Wolf, G. L.; Burnett, K. R.; Goldstein, E. J.; Joseph, P. M. *Magn. Reson. Annu*. **1985**, 231.

[47] Zhang, Q.; Gorden, J. D.; Beyers, R. J.; Goldsmith, C. R. *Inorg. Chem*. **2011**, *50*, 9365.

[48] Maigut, J.; Meier, R.; Zahl, A.; van Eldik, R. *Inorg. Chem*. **2008**, *47*, 5702.

[49] Aime, S.; Anelli, P.; Botta, M.; Brocchetta, M.; Canton, S.; Fedeli, F.; Gianolio, E.; Terreno, E. *J. Biol. Inorg. Chem*. **2002**, *7*, 58.

[50] Troughton, J. S.; Greenfield, M. T.; Greenwood, J. M.; Dumas, S.; Wiethoff, A. J.; Wang, J.; Spiller, M.; McMurry, T. J.; Caravan, P. *Inorg. Chem*. **2004**, *43*, 6313.

[51] Rolla, G. A.; Tei, L.; Fekete, M.; Arena, F.; Gianolio, E.; Botta, M. *Bioorg. Med. Chem.* **2011**, *19*, 1115.

[52] Moghaddam, M. J.; de Campo, L.; Waddington, L. J.; Drummond, C. J. *Soft Matter* **2010**, *6*, 5915.

[53] Tang, H.-A.; Sheng, Y.; Yang, R.-D. *Inorg. Chem. Commun*. **2003**, *6*, 1213.

[54] Zhang, D.-W.; Yang, Z.-Y.; Zhang, S.-P.; Yang, R.-D. *Transition Met. Chem*. **2006**, *31*, 333.

[55] Geraldes, C. F. G. C.; Sherry, A. D.; Brown, R. D.; Koenig, S. H. *Magnet. Reson. Med.* **1986**, *3*, 242.

[56] Balogh, E.; He, Z.; Hsieh, W.; Liu, S.; Tóth, É. *Inorg. Chem*. **2007**, *46*, 238.

[57] Drahos, B.; Pniok, M.; Havlickova, J.; Kotek, J.; Cisarova, I.; Hermann, P.; Lukes, I.; Toth, E. *Dalton Trans*. **2011**, *40*, 10131.

[58] Baranyai, Z.; Uggeri, F.; Giovenzana, G. B.; Bényei, A.; Brücher, E.; Aime, S. *Chem. Eur. J*. **2009**, *15*, 1696.

[59] Tei, L.; Gugliotta, G.; Fekete, M.; Kalman, F. K.; Botta, M. *Dalton Trans*. **2011**, *40*, 2025.

[60] Wang, S.; Westmoreland, T. D. *Inorg. Chem*. **2009**, *48*, 719.

[61] Jackels, S. C.; Durham, M. M.; Newton, J. E.; Henninger, T. C. *Inorg. Chem.* **1992**, *31*, 234.

[62] Drahoš, B.; Kotek, J.; Hermann, P.; Lukeš, I.; Tóth, E. V. *Inorg. Chem*. **2010**, *49*, 3224.

[63] Drahoš, B.; Kotek, J.; Císařová, I.; Hermann, P.; Helm, L.; Lukeš, I.; Tóth, É. *Inorg. Chem*. **2011**, *50*, 12785.

[64] Dees, A.; Zahl, A.; Puchta, R.; van Eikema Hommes, N. J.; Heinemann, F. W.; Ivanovic-Burmazovic, I. *Inorg. Chem*. **2007**, *46*, 2459.

[65] Kessel, D. *Biochemical Pharmacology* **1984**, 33, 1389.

[66] Chen, C.-w.; Cohen, J. S.; Myers, C. E.; Sohn, M. *FEBS Lett*. **1984**, *168*, 70.

[67] Place, D. A.; Faustino, P. J.; Berghmans, K. K.; van Zijl, P. C. M.; Chesnick, A. S.; Cohen, J. S. *MRI* **1992**, *10*, 919.

[68] Fiel, R. J.; Musser, D. A.; Mark, E. H.; Mazurchuk, R.; Alletto, J. J. *MRI* **1990**, *8*, 255.

[69] Saini, S. K.; Jena, A.; Dey, J.; Sharma, A. K.; Singh, R. *MRI* **1995**, *13*, 985.

[70] Ni, Y.; Marchal, G.; Jie, Y.; Lukito, G.; Petré, C.; Wevers, M.; Baert, A. L.; Ebert, W.; Hilger, C.-S.; Maier, F.-K.; Semmler, W. *Acad. Radiol.* **1995**, *2*, 687.

[71] McMillan, J. H.; Cox, G. G.; Kimler, B. F.; Spicer, J. S.; Batnitzky, S. *MRI* **1991**, *9*, 553.

[72] Schmiedl, U. P.; Nelson, J. A.; Starr, F. L.; Schmidt, R. *Invest. Radiol*. **1992**, *27*, 536.

[73] Bohdiewicz, P. J.; Lavallee, D. K.; Fawwaz, R. A.; Newhouse, J. H.; Oluwolf, S. F.; Alderson, P. O. *Invest. Radiol*. **1990**, *25*, 765.

[74] Takehara, Y.; Sakahara, H.; Masunaga, H.; Isogai, S.; Kodaira, N.; Sugiyama, M.; Takeda, H.; Saga, T.; Nakajima, S.; Sakata, I. *Magnet. Reson. Med*. **2002**, *47*, 549.

[75] Tagami, T.; Foltz, W. D.; Ernsting, M. J.; Lee, C. M.; Tannock, I. F.; May, J. P.; Li, S.-D. *Biomaterials* **2011**, *32*, 6570.

[76] Viglianti, B. L.; Abraham, S. A.; Michelich, C. R.; Yarmolenko, P. S.; MacFall, J. R.; Bally, M. B.; Dewhirst, M. W. *Magnet. Reson. Med*. **2004**, *51*, 1153.

[77] Klaveness, J. *Carbohydr. Res*. **1991**, *214*, 315.

[78] Tan, M.; Wu, X.; Jeong, E.-K.; Chen, Q.; Parker, D. L.; Lu, Z.-R. *Mol. Pharm*. **2010**, *7*, 936.

[79] Maurer, J. A., PhD Thesis: I. Structure-Function Analysis of the Mechanosensitive Channel of Large Conductance. II. Design of Novel Magnetic Materials using Crystal Engineering; California Institute of Technology: 2003.

[80] Miller, J. S.; Epstein, A. J. *Angew. Chem. Int. Ed*. **1994**, *33*, 385.

[81] Molecular Materials; Bruce, D. W. O. H., Dermot; Walton, Richard I., Ed.; Wiley & Sons, Ltd.: West Sussex, United Kingdom, 2010.

[82] Yakhmi, J. V. *Bull. Mater. Sci*. **2009**, *32*, 217.

[83] Miller, J. S.; Calabrese, J. C.; Rommelmann, H.; Chittipeddi, S. R.; Zhang, J. H.; Reiff, W. M.; Epstein, A. J. *J. Am. Chem. Soc.* **1987**, *109*, 769.

[84] Miller, J. S.; Epstein, A. J. *MRS Bull.* **2000**, *25*, 21.

[85] Lines, M.; Jones, E. *Physical Review* **1965**, *139*, A1313.

[86] Kmety, C. R.; Huang, Q.; Lynn, J. W.; Erwin, R. W.; Manson, J. L.; McCall, S.; Crow, J.; Stevenson, K. L.; Miller, J. S.; Epstein, A. J. *Physical Review B* **2000**, *62*, 5576.

[87] Korotin, M.; Anisimov, V.; Khomskii, D.; Sawatzky, G. *Phys. Rev. Lett*. **1998**, *80*, 4305.

[88] Yanase, A.; Siratori, K. *J. Phys. Soc. Jpn.* **1984**, *53*, 312.

[89] Caneschi, A.; Gatteschi, D.; Rey, P.; Sessoli, R. *Inorg. Chem*. **1988**, *27*, 1756.

[90] Yamaguchi, S.; Okimoto, Y.; Tokura, Y. *Phys. Rev. B* **1997**, *55*, R8666.

[91] Baker, W. A.; Bobonich, H. M. *Inorg. Chem*. **1964**, *3*, 1184.

[92] Miller, J. S.; Epstein, A. J. In Crystal Engineering: From Molecules and Crystals to Materials; Springer: 1999, p 43.

[93] Miller, J. S.; Gatteschi, D. *Chem. Soc. Rev.* **2011**, *40*, 3065.

[94] Rawson, J.; Lecture Notes: Molecular Magnetism; University of Windsor: 2012.

[95] Feltham, H. L. C.; Brooker, S. *Coord. Chem. Rev*. **2014**, *276*, 1.

[96] Sessoli, R.; Gatteschi, D.; Caneschi, A.; Novak, M. *Nature* **1993**, *365*, 141.

[97] Lis, T. *Acta Cryst. Sect. B* **1980**, *36*, 2042.

[98] Brooker, S.; Kitchen, J. A. *Dalton Trans*. **2009**, 7331.

[99] Saywell, A.; Magnano, G.; Satterley, C. J.; Perdigão, L. M.; Britton, A. J.; Taleb, N.; del Carmen Giménez-López, M.; Champness, N. R.; O'Shea, J. N.; Beton, P. H. *Nat. Commun*. **2010**, *1*, 75.

[100] Yoshihara, D.; Karasawa, S.; Koga, N. *J. Am. Chem. Soc*. **2008**, *130*, 10460.

[101] Manoli, M.; Johnstone, R. D. L.; Parsons, S.; Murrie, M.; Affronte, M.; Evangelisti, M.; Brechin, E. K. *Angew. Chem. Int. Ed*. **2007**, *119*, 4540.

[102] Rogez, G.; Donnio, B.; Terazzi, E.; Gallani, J. L.; Kappler, J. P.; Bucher, J. P.; Drillon, M. *Adv. Mater*. **2009**, *21*, 4323.

[103] Ako, A. M.; Hewitt, I. J.; Mereacre, V.; Clérac, R.; Wernsdorfer, W.; Anson, C. E.; Powell, A. K. *Angew. Chem. Int. Ed*. **2006**, *45*, 4926.

[104] Liu, J.-L.; Wu, J.-Y.; Chen, Y.-C.; Mereacre, V.; Powell, A. K.; Ungur, L.; Chibotaru, L. F.; Chen, X.-M.; Tong, M.-L. *Angew. Chem. Int. Ed*. **2014**, *53*, 12966.

[105] Blagg, R. J.; Muryn, C. A.; McInnes, E. J. L.; Tuna, F.; Winpenny, R. E. P. *Angew. Chem. Int. Ed*. **2011**, *50*, 6530.

[106] Alexandropoulos, D. I.; Mukherjee, S.; Papatriantafyllopoulou, C.; Raptopoulou, C. P.; Psycharis, V.; Bekiari, V.; Christou, G.; Stamatatos, T. C. *Inorg. Chem*.**2011**, *50*, 11276.

[107] Mazarakioti, E. C.; Poole, K. M.; Cunha-Silva, L.; Christou, G.; Stamatatos, T. C. *Dalton Trans*. **2014**, *43*, 11456.

[108] Milios, C. J.; Vinslava, A.; Wernsdorfer, W.; Moggach, S.; Parsons, S.; Perlepes, S. P.; Christou, G.; Brechin, E. K. *J. Am. Chem. Soc*. **2007**, *129*, 2754.

[109] Harman, W. H.; Harris, T. D.; Freedman, D. E.; Fong, H.; Chang, A.; Rinehart, J. D.; Ozarowski, A.; Sougrati, M. T.; Grandjean, F.; Long, G. J. *J. Am. Chem. Soc*. **2010**, *132*, 18115.

[110] Ganivet, C. R.; Ballesteros, B.; de la Torre, G.; Clemente-Juan, J. M.; Coronado, E.; Torres, T. *Chem. Eur. J.* **2013**, *19*, 1457.

[111] Woodruff, D. N.; Winpenny, R. E. P.; Layfield, R. A. *Chem. Rev*.**2013**, *113*, 5110.

[112] Boca, R. A Handbook of Magnetochemical Formulae; Elsevier: 2012.

[113] Ishikawa, N.; Sugita, M.; Ishikawa, T.; Koshihara, S.-y.; Kaizu, Y. *J. Am. Chem. Soc.* **2003**, *125*, 8694.

[114] Koike, N.; Uekusa, H.; Ohashi, Y.; Harnoode, C.; Kitamura, F.; Ohsaka, T.; Tokuda, K. *Inorg. Chem.***1996**, *35*, 5798.

[115] Tong, Y.-Z.; Gao, C.; Wang, Q.-L.; Wang, B.-W.; Gao, S.; Cheng, P.; Liao, D.-Z. *Dalton Trans*. **2015**. *44(19)*, 9020.

[116] Layfield, R. A. *Organometallics* **2014**, *33*, 1084.

[117] Rinehart, J. D.; Long, J. R. *Chem. Sci*. **2011**, *2*, 2078.

[118] Cavallini, M.; Gomez-Segura, J.; Ruiz-Molina, D.; Massi, M.; Albonetti, C.; Rovira, C.; Veciana, J.; Biscarini, F. *Angew. Chem. Int. Ed*. **2005**, *117*, 910.

[119] Leuenberger, M. N.; Loss, D. *Nature* **2001**, *410*, 789.

[120] Stepanenko, D.; Trif, M.; Loss, D. *Inorg. Chim. Acta* **2008**, *361*, 3740.

[121] Žutić, I.; Fabian, J.; Das Sarma, S. *Rev. Modern. Phys*. **2004**, 76, 323.

[122] Bogani, L.; Wernsdorfer, W. *Nat. Mater*. **2008**, *7*, 179.

[123] Rocha, A. R.; Garcia-Suarez, V. M.; Bailey, S. W.; Lambert, C. J.; Ferrer, J.; Sanvito, S. *Nat. Mater*. **2005**, *4*, 335.

[124] Rinehart, J. D.; Fang, M.; Evans, W. J.; Long, J. R. *Nat. Chem*. **2011**, *3*, 538.

[125] Cucinotta, G.; Perfetti, M.; Luzon, J.; Etienne, M.; Car, P. E.; Caneschi, A.; Calvez, G.; Bernot, K.; Sessoli, R. *Angew. Chem. Int. Ed*. **2012**, *51*, 1606.

[126] Gavey, E. L.; Pilkington, M. *Coord. Chem. Rev*. **2015**, *296*, 125.

[127] Schiff, H. *Justus Liebigs Ann. Chem*. **1864**, *131*, 118.

[128] Fleischer, E.; Hawkinson, S. *J. Am. Chem. Soc*. **1967**, *89*, 720.

[129] Drew, M. G. B. D.; Nelson, S. M. *Acta Cryst. Sect. A* **1975**, *31*, S140.

[130] Cook, D. H.; Fenton, D. E.; Drew, M. G. B.; McFall, S. G.; Nelson, S. M. *J. Chem. Soc., Dalton Trans*. **1977**, 446.

[131] Drew, M. G. B.; bin Othman, A. H..; McFall, S. G.; McIlroy, P. D. A.; Nelson, S. M. *J. Chem. Soc., Dalton Trans.* **1977**, 1173.

[132] Nelson, S. M.; McIlroy, P. D. A.; Stevenson, C. S.; Konig, E.; Ritter, G.; Waigel, J. *J. Chem. Soc., Dalton Trans*. **1986**, 991.

[133] Hayami, S.; Gu, Z.-z.; Einaga, Y.; Kobayasi, Y.; Ishikawa, Y.; Yamada, Y.; Fujishima, A.; Sato, O. *Inorg. Chem*. **2001**, *40*, 3240.

[134] Guionneau, P.; Le, G. F.; Kaiba, A.; Costa, J. S.; Chasseau, D.; Letard, J.-F. *Chem. Commun*. **2007**, 3723.

[135] Radecka-Paryzek, W.; Patroniak-Krzyminiewska, V. *Polyhedron* **1995**, 14, 2059.

[136] Krieck, S.; Görls, H.; Westerhausen, M. *Inorg. Chem. Commun*.**2009**, 12, 409.

[137] Patroniak-Krzyminiewska, V.; Radecka-Paryzek, W. *Collect. Czech. Chem. Commun*. **1998**, *63*, 363.

[138] Bastida, R.; de Blas, A.; Castro, P.; Fenton, D. E.; Macías, A.; Rial, R.; Rodríguez, A.; Rodríguez-Blas, T. *J. Chem. Soc., Dalton Trans.* **1996**, 1493.

[139] Zhang, D.; Wang, H.; Tian, L.; Jiang, J.; Ni, Z.-H. *CrystEngComm* **2009**, *11*, 2447.

[140] Bonadio, F.; Senna, M.-C.; Ensling, J.; Sieber, A.; Neels, A.; Stoeckli-Evans, H.; Decurtins, S. *Inorg. Chem*. **2005**, *44*, 969.

[141] Paraschiv, C.; Andruh, M.; Journaux, Y.; Zak, Z.; Kyritsakas, N.; Ricard, L. *J. Mater. Chem.* **2006**, *16*, 2660.

[142] Zhang, Y.-Z.; Wang, B.-W.; Sato, O.; Gao, S. *Chem. Commun*. **2010**, *46*, 6959.

[143] Tanase, S.; Andruh, M.; Stanica, N.; Mathonière, C.; Rombaut, G.; Golhen, S.; Ouahab, L. *Polyhedron* **2003**, *22*, 1315.

[144] Acha, R. T.; Gavey, E. L.; Wang, J.; Rawson, J. M.; Pilkington, M. *Polyhedron* **2014**, *76*, 122.

[145] Zhang, Y.-Z.; Sato, O. *Inorg. Chem*.**2010**, *49*, 1271.

[146] Dogaru, A.; Pichon, C.; Ababei, R.; Mitcov, D.; Maxim, C.; Toupet, L.; Mathonière, C.; Clérac, R.; Andruh, M. *Polyhedron* **2014**, *75*, 146.

[147] Qian, K.; Huang, X.-C.; Zhou, C.; You, X.-Z.; Wang, X.-Y.; Dunbar, K. R. *J. Am. Chem. Soc.* **2013**, *135*, 13302.

[148] Sra, A. K.; Andruh, M.; Kahn, O.; Golhen, S.; Ouahab, L.; Yakhmi, J. V. *Angew. Chem. Int. Ed.* **1999**, *38*, 2606.

[149] Wang, Q.-L.; Zhang, Y.-Z.; Southerland, H.; Prosvirin, A. V.; Zhao, H.; Dunbar, K. R. *Dalton Trans*. **2014**, *43*, 6802.

[150] Wang, X. Y.; Prosvirin, A. V.; Dunbar, K. R. *Angew. Chem. Int. Ed*. **2010**, *49*, 5081.

[151] Pradhan, R.; Desplanches, C.; Guionneau, P.; Sutter, J.-P. *Inorg. Chem*.**2003**, *42*, 6607.

[152] Venkatakrishnan, T. S.; Sahoo, S.; Brefuel, N.; Duhayon, C.; Paulsen, C.; Barra, A.-L.; Ramasesha, S.; Sutter, J.-P. *J. Am. Chem. Soc*. **2010**, *132*, 6047.

[153] Rombaut, G.; Golhen, S.; Ouahab, L.; Mathonière, C.; Kahn, O. *Dalton Trans.* **2000**, 3609.

[154] Venkatakrishnan, T. S.; Duhayon, C.; Gogoi, N.; Sutter, J.-P. *Inorg. Chim. Acta* **2011**, *372*, 403.

[155] Hayami, S.; Juhasz, G.; Maeda, Y.; Yokoyama, T.; Sato, O. *Inorg. Chem*. **2005**, *44*, 7289.

[156] Zhang, D.; Wang, H.; Chen, Y.; Ni, Z.-H.; Tian, L.; Jiang, J. *Inorg. Chem*. **2009**, *48*, 5488.

[157] Ababei, R.; Pichon, C.; Roubeau, O.; Li, Y.-G.; Bréfuel, N.; Buisson, L.; Guionneau, P.; Mathoniere, C.; Clérac, R. *J. Am. Chem. Soc*. **2013**, *135*, 14840.

[158] Zhang, D.; Wang, H.; Chen, Y.; Zhang, L.; Tian, L.; Ni, Z.-H.; Jiang, J. *Dalton Trans*. **2009**, 9418.

[159] Sra, A. K.; Sutter, J.-P.; Guionneau, P.; Chasseau, D.; Yakhmi, J. V.; Kahn, O. *Inorg. Chim. Acta* **2000**, *300–302*, 778.

[160] Paraschiv, C.; Sutter, J.-P.; Schmidtmann, M.; Müller, A.; Andruh, M. *Polyhedron* **2003**, *22(12)*, 1611.

[161] Madalan, Augustin M.; Voronkova, V.; Galeev, R.; Korobchenko, L.; Magull, J.; Roesky, Herbert W.; Andruh, M. Eur. J. *Inorg. Chem*. **2003**, 1995.

[162] Shao, D.; Zhang, S.-L.; Zhao, X.-H.; Wang, X.-Y. *Chem. Commun*. **2015**, *51*, 4360.

[163] Shatruk, M.; Avendano, C.; Dunbar, K. R. In Progress in Inorganic Chemistry; John Wiley & Sons, Inc.: 2009, p 155.

[164] Pedersen, C. J. *Angew. Chem. Int. Ed*. **1988**, *27*, 1021.

[165] Pedersen, C. J. *J. Am. Chem. Soc*. **1967**, *89*, 7017.

[166] Steed, J. W.; Atwood, J. L. Supramolecular Chemistry; John Wiley & Sons: 2009.

[167] Saji, T.; Kinoshita, I. *J. Chem. Soc. Chem. Commun*. **1986**, 716.

[168] Olsher, U.; Hankins, M. G.; Kim, Y. D.; Bartsch, R. A. *J. Am. Chem. Soc*. **1993**, *115*, 3370.

[169] Landini, D.; Montanari, F.; Pirisi, F. M. *J. Chem. Soc. Chem. Commun*. **1974**, 879.

[170] Cinouini, M.; Colonna, S.; Molinari, H.; Montanari, F.; Tundo, P. *J. Chem. Soc. Chem. Commun.* **1976**, 394.

[171] Hyun, M. H. *Bull. Korean Chem. Soc.* **2005**, *26*, 1153.

[172] Kuhn, R.; Erni, F.; Bereuter, T.; Haeusler, *J. Anal. Chem*. **1992**, *64*, 2815.

[173] Gokel, G. W. *Chem. Soc. Rev*. **1992**, *21*, 39.

[174] Krakowiak, K. E.; Bradshaw, J. S. *Isr. J. Chem*. **1992**, *32*, 3.

[175] Rogers, R. D.; Kurihara, L. K. *Inorg. Chem*. **1987**, *26*, 1498.

[176] Rogers, R. D.; Kurihara, L. K.; Benning, M. M. *Inorg. Chem*. **1987**, *26*, 4346.

[177] Rogers, R. D.; Kurihara, L. K.; Voss, E. J. *Inorg. Chem*. **1987**, *26*, 2360.

[178] Rogers, R. D.; Rollins, A. N.; Benning, M. M. *Inorg. Chem*. **1988**, *27*, 3826.

[179] Nieland, A.; Mix, A.; Neumann, B.; Stammler, H.-G.; Mitzel, N. W., Naturforsch, Z. *Chem. Sci*. **2014**, *69*, 327.

[180] Willey, G. R.; Spry, M. P.; Woodman, T. J.; Drew, M. G. *J. Indian Chem. Soc*. **1998**, *75(5)*, 271.

[181] McIntosh, N. N.; Kahwa, I. A.; Mague, J. T. *Acta Cryst. Sect. E* **2001**, *57*, 21.

[182] Bunzli, J. C. G.; Klein, B.; Chapuis, G.; Schenk, K. J. *Inorg. Chem*. **1982**, *21*, 808.

[183] Rogers, R. D.; Rollins, A. N.; Henry, R. F.; Murdoch, J. S.; Etzenhouser, R. D.; Huggins, S. E.; Nunez, L. *Inorg. Chem.* **1991**, *30*, 4946.

[184] Starynowicz, P. *Dalton Trans*. **2004**, 825.

[185] Starynowicz, P. *Polyhedron* **2003**, *22*, 337.

[186] Nieland, A.; Mix, A.; Neumann, B.; Stammler, H.-G.; Mitzel, N. W. *Dalton Trans*. **2010**, *39*, 6753.

[187] Lee, T.; Sheu, H.-R.; Chiu, T.; Chang, C. *Acta Cryst. Sect. C* **1983**, *39*, 1357.

[188] Bakker, J. M.; Deacon, G. B.; Junk, P. C. *Polyhedron* **2013**, *52*, 560.

[189] Misra, P.; Koner, R.; Nayak, M.; Mohanta, S.; Low, J. N.; Ferguson, G.; Glidewell, C. *Acta Cryst. Sect. C* **2007**, *63*, 440.

[190] Arndt, S.; Zeimentz, P. M.; Spaniol, T. P.; Okuda, J.; Honda, M.; Tatsumi, K. *Dalton Trans*. **2003**, 3622.

[191] Rogers, R. D.; Nunez, L. *Inorg. Chim. Acta* **1990**, *172*, 173.

[192] Bünzli, J.-C. G.; Klein, B.; Wessner, D.; Alcock, N. W. *Inorg. Chim. Acta* **1982**, *59*, 269.

[193] Bünzli, J. C. G.; Wessner, D. Helv. *Chim. Acta* **1981**, *64*, 582.

[194] Shinde, K.; Dhoble, S. J.; Swart, H. C.; Park, K. In Phosphate Phosphors for Solid-State Lighting; Springer: Berlin, Heidelberg, 2012; Vol. 174, p 41.

[195] Bünzli, J.-C. G.; Eliseeva, S. V. In Lanthanide Luminescence; Springer: 2011, p 1.

[196] Armelao, L.; Quici, S.; Barigelletti, F.; Accorsi, G.; Bottaro, G.; Cavazzini, M.; Tondello, E. *Coord. Chem. Rev*. **2010**, *254*, 487.

[197] Moore, E. G.; Samuel, A. P. S.; Raymond, K. N. *Acc. Chem. Res*. **2009**, *42*, 542.

[198] Bünzli, J.-C. G. *Chem. Rev*.**2010**, *110*, 2729.

[199] Nishioka, T.; Fukui, K.; Matsumoto, K. Handbook on the Physics and Chemistry of Rare Earths **2007**, *37*, 171.

[200] Eliseeva, S. V.; Bünzli, J.-C. G. *Chem. Soc. Rev*. **2010**, *39*, 189.

[201] Bünzli, J.-C. G.; Comby, S.; Chauvin, A.-S.; Vandevyver, C. D. B. *J. Rare Earth* **2007**, *25*, 257.

[202] Belian, M. F.; de Sá, G. F.; Alves Jr, S.; Galembeck, A. *J. Lumin*. **2011**, *131*, 856.

[203] Belian, M. F.; De Sá, G. F.; Alves Jr, S.; De Farias, R. F. *J. Coord. Chem*. **2007**, *60*, 173.

[204] Belian, M. F.; Freire, R. O.; Galembeck, A.; de Sá, G. F.; de Farias, R. F.; Alves Jr, S. *J. Lumin*. **2010**, *130*, 1946.

[205] Felinto, M. C. F. C.; Tomiyama, C. S.; Brito, H. F.; Teotonio, E. E. S.; Malta, O. L. *J. Solid State Chem*. **2003**, *171*, 189.

[206] Chen, L.; Wang, J.; Wei, J.-M.; Wernsdorfer, W.; Chen, X.-T.; Zhang, Y.-Q.; Song, Y.; Xue, Z.-L. *J. Am. Chem. Soc*. **2014**, *136*, 12213.

[207] Happ, P.; Plenk, C.; Rentschler, E. *Coord. Chem. Rev*. **2015**, *289-290*, 238-260

[208] Drew, M. G.; Grimshaw, J.; Mcllroy, P. D.; Nelson, S. M. *J. Chem. Soc., Dalton Trans*. **1976**, 1388.

[209] Drew, M. G.; bin Othman, A. H.; McFall, S. G.; Mcllroy, P. D.; Nelson, S. M. *J. Chem. Soc., Dalton Trans*. **1977**, 438.

[210] Cook, D. H.; Fenton, D. E.; Drew, M. G.; McFall, S. G.; Nelson, S. M. *J. Chem. Soc., Dalton Trans*. **1977**, 446.

[211] Drew, M. G.; bin Othman, A. H.; McFall, S. G.; Mcllroy, P. D.; Nelson, S. M. *J. Chem. Soc., Dalton Trans*. **1977**, 1173.

[212] Drew, M. G.; bin Othman, A. H.; Mcllroy, P. D.; Nelson, S. M. *J. Chem. Soc., Dalton Trans*. **1975**, 2507.

[213] Drew, M. G.; bin Othman, A. H.; Nelson, S. M. *J. Chem. Soc*., **1976**, 1394.

[214] Cannon, R. D.; Chiswell, B.; Venanzi, L. M. *J. Chem. Soc. A* **1967**, 1277.

[215] Numata, M.; Koumoto, K.; Mizu, M.; Sakurai, K.; Shinkai, S. *Org. Biomol. Chem*. **2005**, *3*, 2255.

[216] Bonger, K. M.; van den Berg, R. J. B. H. N.; Heitman, L. H.; Ijzerman, A. P.; Oosterom, J.; Timmers, C. M.; Overkleeft, H. S.; van der Marel, G. A. *Bioorg. Med. Chem.* **2007**, *15*, 4841.

[217] Moreno-Corral, R.; Höpfl, H.; Machi-Lara, L.; Lara, K. O. *Eur. J. Org. Chem*., **2011**, 2148.

[218] Lieb, D.; Friedel, F. C.; Yawer, M.; Zahl, A.; Khusniyarov, M. M.; Heinemann, F. W.; Ivanović-Burmazović, I. *Inorg. Chem*. **2012**, *52*, 222.

[219] Venneri, S., Masters Thesis: New Building Blocks for Dual-Property. Molecule-Based Magnets; Brock University: 2012.

[220] Pryor, K. E.; Shipps Jr, G. W.; Skyler, D. A.; Rebek Jr, J. *Tetrahedron* **1998**, *54*, 4107.

[221] Wang, J.; Slater, B.; Alberola, A.; Stoeckli-Evans, H.; Razavi, F. S.; Pilkington, M. *Inorg. Chem*. **2007**, *46*, 4763.

[222] Citterio, A.; Arnoldi, A.; Macri, C. *Chim. Indrustr*. **1978**, *60*, 14.

[223] Lawrence, J.; Lamm, S.; Pino, S.; Richman, K.; Braverman, L. *Thyroid* **2000**, *10*, 659.

[224] Lundberg, J. O.; Gladwin, M. T.; Ahluwalia, A.; Benjamin, N.; Bryan, N. S.; Butler, A.; Cabrales, P.; Fago, A.; Feelisch, M.; Ford, P. C. *Nat. Chem. Biol*. **2009**, *5*, 865.

[225] Bashall, A.; McPartlin, M.; Murphy, B. P.; Fenton, D. E.; Kitchen, S. J.; Tasker, P. A. *J. Chem. Soc., Dalton Trans*. **1990**, 505.

[226] Fenton, D.; Spey, S. *J. Chem. Soc., Dalton Trans*. **1999**, 4131.

[227] Floyd III, W. C.; Klemm, P. J.; Smiles, D. E.; Kohlgruber, A. C.; Pierre, V. C.; Mynar, J. L.; Fréchet, J. M.; Raymond, K. N. *J. Am. Chem. Soc*. **2011**, *133*, 2390.

[228] Radecka-Paryzek, W.; Patroniak, V.; Kubicki, M. *Polyhedron* **2003**, *22*, 2773.

[229] Radecka-Paryzek, W.; Patroniak, V.; Kubicki, M. *Inorg. Chem. Commun*. **2004**, *7*, 455.

[230] Patroniak, V.; Kubicki, M.; Mondry, A.; Lisowski, J.; Radecka-Paryzek, W. *Dalton Trans*. **2004**, 3295.

[231] Keypour, H.; Khanmohammadi, H.; Wainwright, K.; Taylor, M. *J. Iran. Chem. Soc*. **2004**, *1*, 53.

[232] Núñez, C.; Mato-Iglesias, M.; Bastida, R.; Macías, A.; Pérez-Lourido, P.; Platas-Iglesias, C.; Valencia, L. Eur. J. *Inorg. Chem*. **2009**, 1086.

[233] Arif, A. M.; Gray, C. J.; Hart, F. A.; Hursthouse, M. B. *Inorg. Chim. Acta* **1985**, *109*, 179.

[234] Arif, A. M.; Backer-Dirks, J. D. J.; Gray, C. J.; Hart, F. A.; Hursthouse, M. B. *J. Chem. Soc., Dalton Trans*. **1987**, 1665.

[235] Cook, D. H.; Fenton, D. E. *J. Chem. Soc., Dalton Trans*. **1979**, 810.

[236] Geary, W. J. *Coord. Chem. Rev*. **1971**, *7*, 81.

[237] Nelson, S. *Pure Appl. Chem*. **1980**, *52*, 2461.

[238] Cairns, C.; McFall, S. G.; Nelson, S. M.; Drew, M. G. *J. Chem. Soc., Dalton Trans*. **1979**, 446.

[239] Brücher, E. In Contrast Agents I; Springer: 2002, p 103.

[240] Bousquet, J. C.; Saini, S.; Stark, D. D.; Hahn, P. F.; Nigam, M.; Wittenberg, J.; J T Ferrucci, *J. Radiology* **1988**, *166*, 693.

[241] Mirfazaelian, A.; Fisher, J. W. *J. Toxicol. Environ. Health, Part A* **2007**, *70*, 1052.

[242] Caravan, P.; Das, B.; Dumas, S.; Epstein, F. H.; Helm, P. A.; Jacques, V.; Koerner, S.; Kolodziej, A.; Shen, L.; Sun, W.-C.; Zhang, Z. *Angew. Chem. Int. Ed*. **2007**, *119*, 8319.

[243] Lauffer, R. B.; Parmelee, D. J.; Dunham, S. U.; Ouellet, H. S.; Dolan, R. P.; Witte, S.; McMurry, T. J.; Walovitch, R. C. *Radiology* **1998**, *207*, 529.

[244] Wang, C.; Ravi, S.; Garapati, U. S.; Das, M.; Howell, M.; Mallela, J.; Alwarappan, S.; Mohapatra, S. S.; Mohapatra, S. *J. Mater. Chem*. B **2013**, *1*, 4396.

[245] Petoral Jr, R. M.; Söderlind, F.; Klasson, A.; Suska, A.; Fortin, M. A.; Abrikossova, N.; Selegård, L.; Käll, P.-O.; Engström, M.; Uvdal, K. *J. Phys. Chem. C* **2009**, *113*, 6913.

[246] Lee, H.-Y.; Li, Z.; Chen, K.; Hsu, A. R.; Xu, C.; Xie, J.; Sun, S.; Chen, X. *J. Nucl. Med.* **2008**, *49*, 1371.

[247] Hein, J. E.; Fokin, V. V. *Chem. Soc. Rev*. **2010**, *39*, 1302.

[248] Kolb, H. C.; Finn, M. G.; Sharpless, K. B. *Angew. Chem. Int. Ed*. **2001**, *40*, 2004.

[249] Takalo, H.; Kankare, J. *Acta Chem. Scand. B* **1987**, *42*, 373.

[250] Sidibe, A.; Hamon, F.; Largy, E.; Gomez, D.; Teulade-Fichou, M.-P.; Trentesaux, C.; Riou, J.-F. *Biochimie* **2012**, *94*, 2559.

[251] Fallahpour, R.-A.; Constable, E. C. *J. Chem. Soc., Perkin Transactions 1* **1997**, 2263.

[252] Oikawa, Y.; Sugano, K.; Yonemitsu, O. *J. Org. Chem.* **1978**, 43, 2087.

[253] Bonnet, C. S.; Buron, F.; Caillé, F.; Shade, C. M.; Drahoš, B.; Pellegatti, L.; Zhang, J.; Villette, S.; Helm, L.; Pichon, C. *Chem. Eur. J.* **2012**, *18*, 1419.

[254] Bolshakov, O. I.; Lebedyeva, I. O.; Katritzky, A. R. *Synthesis* **2012**, *44*, 2926.

[255] Kim, H.-Y.; Sohn, J.; Wijewickrama, G. T.; Edirisinghe, P.; Gherezghiher, T.; Hemachandra, M.; Lu, P.-Y.; Chandrasena, R. E.; Molloy, M. E.; Tonetti, D. A.; Thatcher, G. R. *Bioorg. Med. Chem*. **2010**, 18, 809.

[256] Madeira, K. P.; Daltoé, R. D.; Sirtoli, G. M.; Carvalho, A. A.; Rangel, L. B. A.; Silva, I. V. *Mol. Biol. Rep*. **2014**, 41, 5459.

[257] McMurry, T. J.; Parmelee, D. J.; Sajiki, H.; Scott, D. M.; Ouellet, H. S.; Walovitch, R. C.; Tyeklár, Z.; Dumas, S.; Bernard, P.; Nadler, S.; Midelfort, K.; Greenfield, M.; Troughton, J.; Lauffer, R. B. *J. Med. Chem*. **2002**, *45*, 3465.

[258] Caravan, P. *Acc. Chem. Res*. **2009**, *42*, 851.

[259] Kolodziej, A. F.; Nair, S. A.; Graham, P.; McMurry, T. J.; Ladner, R. C.; Wescott, C.; Sexton, D. J.; Caravan, P. *Bioconjugate Chem*. **2012**, *23*, 548.

[260] Bernhard, C.; Goze, C.; Rousselin, Y.; Denat, F. *Chem. Commun.* **2010**, *46*, 8267.

[261] Gatteschi, D.; Sessoli, R. *Angew. Chem. Int. Ed*. **2003**, *42*, 268.

[262] Guo, Y.-N.; Xu, G.-F.; Wernsdorfer, W.; Ungur, L.; Guo, Y.; Tang, J.; Zhang, H.-J.; Chibotaru, L. F.; Powell, A. K. *J. Am. Chem. Soc*. **2011**, *133*, 11948.

[263] Liu, J.-L.; Chen, Y.-C.; Zheng, Y.-Z.; Lin, W.-Q.; Ungur, L.; Wernsdorfer, W.; Chibotaru, L. F.; Tong, M.-L. *Chem. Sci.* **2013**, *4*, 3310.

[264] Ren, M.; Bao, S.-S.; Ferreira, R. A. S.; Zheng, L.-M.; Carlos, L. D. *Chem. Commun*. **2014**, *50*, 7621.

[265] Patroniak-Krzyminiewska, V.; Litkowska, H.; Radecka-Paryzek, W. *Montsh. Chem.* **1999**, *130*, 243.

[266] Radecka-Paryzek, W.; Litkowska, H. *J. Alloys Compd*. **2000**, *300–301*, 435.

[267] Shannon, R. D.; Prewitt, C. T. *Acta Cryst. Sect. B* **1969**, *25*, 925.

[268] Drago, R. S. Physical Methods in Inorganic Chemistry; Reinhold Publishing Corporation: New York, NY, 1965; Vol. 8.

[269] Oczko, G.; Macalik, L. *Polyhedron* **2010**, *29*, 1231.

[270] Zafiropoulos, T. F.; Perlepes, S. P.; Tsangaris, J. M. *J. Coord. Chem*. **1985**, *14*, 87.

[271] Bullock, J. I.; Tajmir-Riahi, H.-A. *J. Chem. Soc., Dalton Trans*. **1978**, 36.

[272] Jeletic, M.; Lin, P.-H.; Le Roy, J. J.; Korobkov, I.; Gorelsky, S. I.; Murugesu, M. *J. Am. Chem. Soc*. **2011**, *133*, 19286.

[273] Guo, Y.-N.; Xu, G.-F.; Guo, Y.; Tang, J. *Dalton Trans*. **2011**, *40*, 9953.

[274] Wu, S.-Q.; Xie, Q.-W.; An, G.-Y.; Chen, X.; Liu, C.-M.; Cui, A.-L.; Kou, H.-Z. *Dalton Trans*. **2013**, *42*, 4369.

[275] AlDamen, M. A.; Cardona-Serra, S.; Clemente-Juan, J. M.; Coronado, E.; Gaita-Ariño, A.; Martí-Gastaldo, C.; Luis, F.; Montero, O. *Inorg. Chem*. **2009**, *48*, 3467.

[276] Jiang, S.-D.; Wang, B.-W.; Sun, H.-L.; Wang, Z.-M.; Gao, S. *J. Am. Chem. Soc*. **2011**, *133*, 4730.

[277] Li, D.-P.; Wang, T.-W.; Li, C.-H.; Liu, D.-S.; Li, Y.-Z.; You, X.-Z. *Chem. Commun*. **2010**, *46*, 2929.

[278] Ruiz, J.; Mota, A. J.; Rodriguez-Dieguez, A.; Titos, S.; Herrera, J. M.; Ruiz, E.; Cremades, E.; Costes, J. P.; Colacio, E. *Chem. Commun.* **2012**, *48*, 7916.

[279] Ritchie, C.; Speldrich, M.; Gable, R. W.; Sorace, L.; Kögerler, P.; Boskovic, C. *Inorg. Chem*. **2011**, *50*, 7004.

[280] Lin, P.-H.; Sun, W.-B.; Yu, M.-F.; Li, G.-M.; Yan, P.-F.; Murugesu, M. *Chem. Commun.* **2011**, *47*, 10993.

[281] Tamburini, S.; Casellato, U.; Bertolo, L.; Alessandro Vigato, P. Eur. J. *Inorg. Chem*. **2005**, 2409.

[282] Zabrodsky, H.; Peleg, S.; Avnir, D. *J. Am. Chem. Soc*. **1992**, *114*, 7843.

[283] Rinehart, J. D.; Meihaus, K. R.; Long, J. R. *J. Am. Chem. Soc*. **2010**, *132*, 7572.

[284] Guo, Y.-N.; Xu, G.-F.; Guo, Y.; Tang, J. *Dalton Trans*. **2011**, *40*, 9953.

[285] Ruiz, J.; Mota, A. J.; Rodríguez-Diéguez, A.; Titos, S.; Herrera, J. M.; Ruiz, E.; Cremades, E.; Costes, J. P.; Colacio, E. *Chem. Commun*. **2012**, *48*, 7916.

[286] Boča, R.; Miklovič, J.; Titiš, J. *Inorg. Chem*. **2014**, *53(5)*, 2367

[287] AlDamen, M. A.; Clemente-Juan, J. M.; Coronado, E.; Martí-Gastaldo, C.; Gaita-Ariño, A. *J. Am. Chem. Soc*. **2008**, *130*, 8874.

[288] Luis, F.; Martínez-Pérez, M. J.; Montero, O.; Coronado, E.; Cardona-Serra, S.; Martí-Gastaldo, C.; Clemente-Juan, J. M.; Sesé, J.; Drung, D.; Schurig, T. *Phys. Rev. B* **2010**, *82*, 060403.

[289] Konig, S. N.; Chilton, N. F.; Maichle-Mossmer, C.; Pineda, E. M.; Pugh, T.; Anwander, R.; Layfield, R. A. *Dalton Trans*. **2014**, *43*, 3035.

[290] Aquilante, F.; De Vico, L.; Ferré, N.; Ghigo, G.; Malmqvist, P.-å.; Neogrády, P.; Pedersen, T. B.; Pitoňák, M.; Reiher, M.; Roos, B. O.; Serrano-Andrés, L.; Urban, M.; Veryazov, V.; Lindh, R. *J. Comput. Chem*. **2010**, *31*, 224.

[291] Gatteschi, D.; Sessoli, R.; Cornia, A. *Chem. Commun*. **2000**, 725.

[292] Blagg, R. J.; Ungur, L.; Tuna, F.; Speak, J.; Comar, P.; Collison, D.; Wernsdorfer, W.; McInnes, E. J.; Chibotaru, L. F.; Winpenny, R. E. *Nat. Chem*. **2013**, *5*, 673.

[293] Cucinotta, G.; Perfetti, M.; Luzon, J.; Etienne, M.; Car, P.-E.; Caneschi, A.; Calvez, G.; Bernot, K.; Sessoli, R. *Angew. Chem. Int. Ed*. **2012**, *51*, 1606.

[294] Long, J.; Vallat, R.; Ferreira, R. A. S.; Carlos, L. D.; Almeida Paz, F. A.; Guari, Y.; Larionova, J. *Chem. Commun*. **2012**, *48*, 9974.

[295] Long, J.; Rouquette, J.; Thibaud, J.-M.; Ferreira, R. A. S.; Carlos, L. D.; Donnadieu, B.; Vieru, V.; Chibotaru, L. F.; Konczewicz, L.; Haines, J.; Guari, Y.; Larionova, J. *Angew. Chem. Int. Ed*. **2015**, *54*, 2236.

[296] Murugesu, M. *Nat. Chem*. **2012**, *4*, 347.

[297] Pedersen, K. S.; Ungur, L.; Sigrist, M.; Sundt, A.; Schau-Magnussen, M.; Vieru, V.; Mutka, H.; Rols, S.; Weihe, H.; Waldmann, O. *Chem. Sci*. **2014**.

[298] Bruker; Bruker AXS Inc.: Madison, Wisconsin, USA, 2007.

[299] Sheldrick, G. M. University of Göttingen, Germany, 1996.

[300] Sheldrick, G. M. *Acta Cryst. Sect. A* **2007**, *64*, 112.

[301] Dolomanov, O. V.; Bourhis, L. J.; Gildea, R. J.; Howard, J. A.; Puschmann, H. J. *Appl. Crystallogr*. **2009**, *42*, 339.

[302] Veryazov, V.; Widmark, P.-O.; Serrano-Andrés, L.; Lindh, R.; Roos, B. O. *Int. J. Quantum Chem*. **2004**, *100*, 626.

[303] Karlström, G.; Lindh, R.; Malmqvist, P.-Å.; Roos, B. O.; Ryde, U.; Veryazov, V.; Widmark, P.-O.; Cossi, M.; Schimmelpfennig, B.; Neogrady, P.; Seijo, L. *Comp. Mater. Sci.* **2003**, *28*, 222.

[304] Allen, C.; Glauser, *J. Anal. Chem*. **1972**, *44*, 1694.

[305] Narahari, S. R.; Reguri, B. R.; Mukkanti, K. *Tetrahedron Letters* **2011**, *52*, 4888.

[306] Emmert, B.; Varenkamp, O. *Berichte der Deutschen Chemischen Gesellschaft* **1923**, *56*, 491.

[307] Hünig, S.; Wehner, I. *Synthesis* **1989**, 552.

[308] Iglesias, C. P.; Elhabiri, M.; Hollenstein, M.; Bünzli, J.-C. G.; Piguet, C. *Dalton Trans*. **2000**, 2031.

[309] Hommes, P.; Fischer, C.; Lindner, C.; Zipse, H.; Reissig, H.-U. *Angew. Chem. Int. Ed*. **2014**, *53*, 7647.

[310] Pryor, K. E.; Shipps, G. W.; Skyler, D. A.; Rebek, J. *Tetrahedron* **1998**, *54*, 4107.

[311] Dumont, A.; Jacques, V.; Desreux, J. F. *Tetrahedron* **2000**, *56*, 2043.

[312] Fallahpour, R.-A.; Neuburger, M.; Zehnder, M. *Polyhedron* **1999**, *18*, 2445.

[313] Ivchenko, P. V.; Nifant'ev, I. E.; Buslov, I. V. *Tetrahedron Letters* **2013**, *54*, 217.

7 APPENDIX

7.1 Crystallographic data

	9.1	**9.2**
Empirical formula	$C_8H_{28}Cl_3DyO_{22}$	$C_8H_{28}Cl_3HoO_{22}$
Formula weight	745.15	747.59
Temperature/K	150(2)	150(2)
Crystal system	Monoclinic	Monoclinic
Space group	$P2_1/c$	$P2_1/c$
***a*/Å**	13.1195(7)	13.121(4)
***b*/Å**	10.2129(6)	10.229(3)
***c*/Å**	17.5681(10)	17.634(5)
α/°	90	**90**
β/°	93.941(2)	93.558(8)
γ/°	90	90
Volume/Å^3	2348.4(2)	2362.3(12)
Z	4	4
ρ_{calc}mg/mm^3	2.164	2.1018
μ/mm^{-1}	3.618	3.786
F(000)	1524.0	1482.8
Crystal size/mm^3	0.43 x 0.27 x 0.28	0.14 x 0.14 x 0.22
Independent reflections	4806	7160
Goodness-of-fit on F^2	1.334	1.161
Final R indexes [I>=2σ (I)]	R_1 = 0.0208 wR_2 = 0.0514	R_1 = 0.0281 wR_2 = 0.1273

Table 7.1 Crystal data and structure refinement for **9.1** (Dy^{III}-12C4) and **9.2** (Ho^{III}-12C4).

	10.1	**10.1b**	**10.2**
Empirical formula	$C_{20}H_{50}Cl_3DyO_{27}$	$C_8H_{28}Cl_3O_{22}Y$	$C_{10}H_{30}Cl_3ErO_{22}$
Formula weight	991.45	671.56	775.95
Temperature/K	150(2)	150(2)	173
Crystal system	Monoclinic	Monoclinic	Orthorhombic
Space group	$P2_1/n$	$P2_1/c$	Pnma
***a*/Å**	15.8533(14)	13.139(1)	17.6319(11)
***b*/Å**	14.6908(14)	10.2303(7)	14.7648(8)
***c*/Å**	16.4867(15)	17.5916(14)	9.5931(6)
α/°	90	90	90
β/°	99.409(4)	93.866(3)	90
γ/°	90	90	90
Volume/Å^3	3788.06	2359.2(3)	2497.4(3)
Z	1	4	4
ρ_{calc}mg/mm^3	1.735	1.8906	2.064
μ/mm^{-1}	2.278	2.936	3.777
F(000)	2004.0	1358.8	1540.0
Crystal size/mm^3	0.32 x 0.29 x 0.45	0.14 x 0.09 x 0.09	0.09 x 0.05 x 0.11
Independent reflections	7642	5913	3779
Goodness-of-fit on F^2	1.233	1.299	1.081
Final R indexes [I>=2σ (I)]	R_1 = 0.0460 wR_2 = 0.1394	R_1 = 0.0417 wR_2 = 0.1421	R_1 = 0.0250 wR_2 = 0.0616

Table 7.2 Crystal data and structure refinement for **10.1** (Dy^{III}-15C5), **10.1b** (Y^{III}-15C5), and **10.2** (Er^{III}-15C5)

	11.1	**11.2**
Empirical formula	$C_{18}H_{45}Cl_{4.5}O_{31.5}Tb_{1.5}$	$C_{16}H_{38.67}Cl_4Dy_{1.33}O_{28}$
Formula weight	1163.46	1037.60
Temperature/K	150(2)	150(2)
Crystal system	Hexagonal	Orthorhombic
Space group	$P6_1$	Pbcn
***a*/Å**	9.9031(5)	13.4884(9)
***b*/Å**	9.9031(5)	22.4361(16)
***c*/Å**	44.999(4)	16.9130(12)
α/°	90	90
β/°	90	90
γ/°	120	90
Volume/Å^3	3821.8(4)	5118.3(6)
Z	4	6
ρ_{calc}mg/mm^3	2.0219	2.020
μ/mm^{-1}	3.183	3.325
F(000)	2319.8	3088.0
Crystal size/mm^3	0.07 x 0.11 x 0.06	0.12 x 0.09 x 0.09
Independent reflections	4245	5268
Goodness-of-fit on F^2	0.932	1.019
Final R indexes [I>=2σ (I)]	R_1 = 0.0279 wR_2 = 0.0749	R_1 = 0.0440 wR_2 = 0.1193

Table 7.3 Crystal data and structure refinement for **11.1** (Tb^{III}-18C6) and **11.2** (Dy^{III}-18C6)**.**

	11.3	**11.4**
Empirical formula	$C_{20}H_{40}O_{20}Cl_3Ho$	$C_{30}H_{30}N_2O_{20}Cl_3Er$
Formula weight	776.61	783.97
Temperature/K	150(2)	150(2)
Crystal system	Monoclinic	Monoclinic
Space group	Pc	$P2_1/c$
***a*/Å**	9.7970(8)	9.8027(6)
***b*/Å**	17.8698(15)	17.8702(13)
***c*/Å**	14.8669(12)	14.8422(11)
α/°	90	90
β/°	100.228(3)	100.180(3)
γ/°	90	90
Volume/Å^3	2561.4(4)	2559.1(3)
Z	4	4
ρ_{calc}mg/mm^3	2.0137	2.0347
μ/mm^{-1}	3.493	3.685
F(000)	1534.8	1558.4
Crystal size/mm^3	0.62 x 0.09 x 0.12	0.03 x 0.09 x 0.55
Independent reflections	10186	5239
Goodness-of-fit on F^2	1.011	1.008
Final R indexes [I>=2σ (I)]	R_1 = 0.0467 wR_2 = 0.1122	R_1 = 0.0339 wR_2 = 0.0896

Table 7.4 Crystal data and structure refinement for **11.3** (Ho^{III}-18C6) and **11.4** (Er^{III}-18C6)**.**

7.2 Relaxivity plots

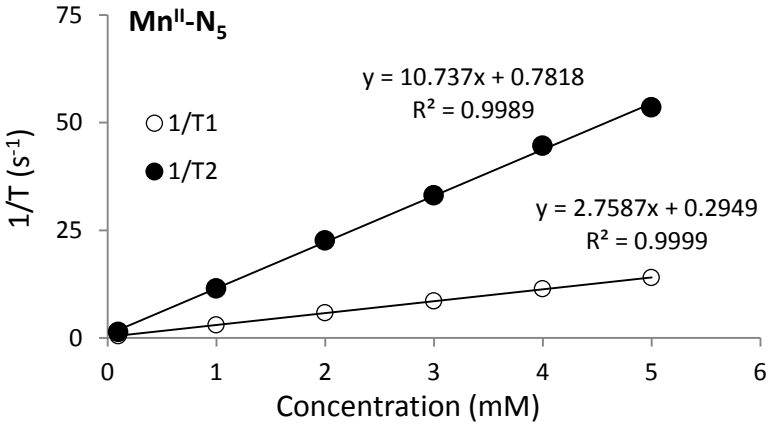

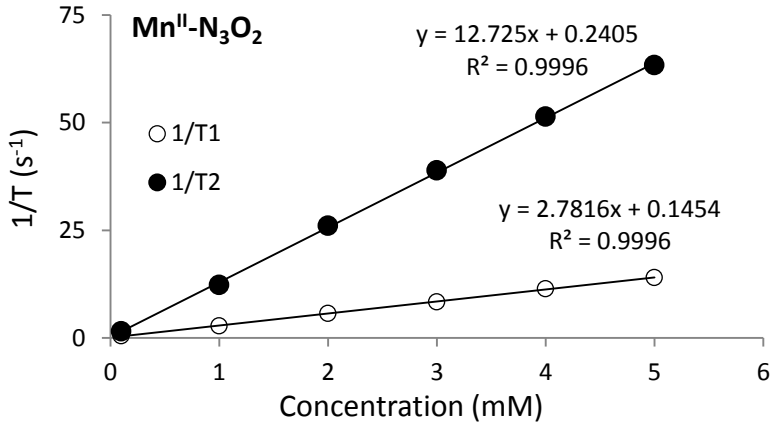

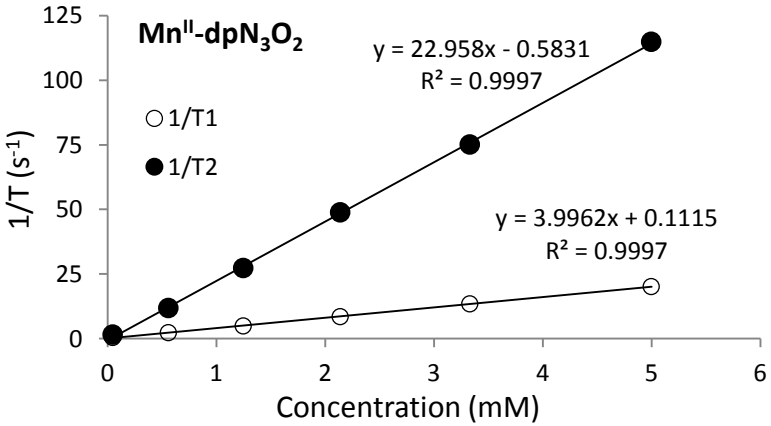

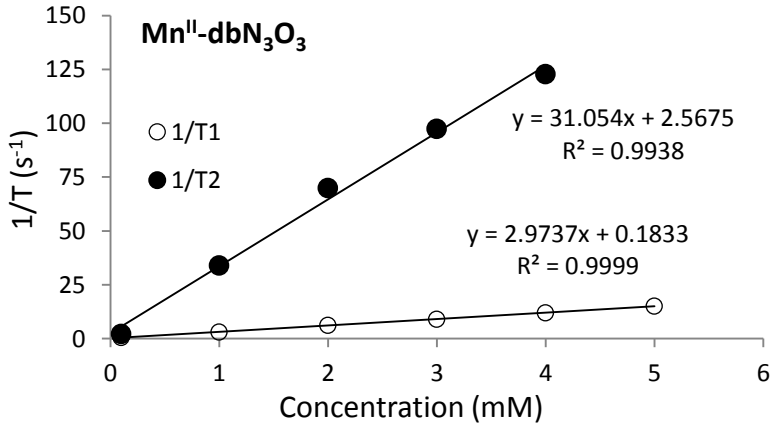

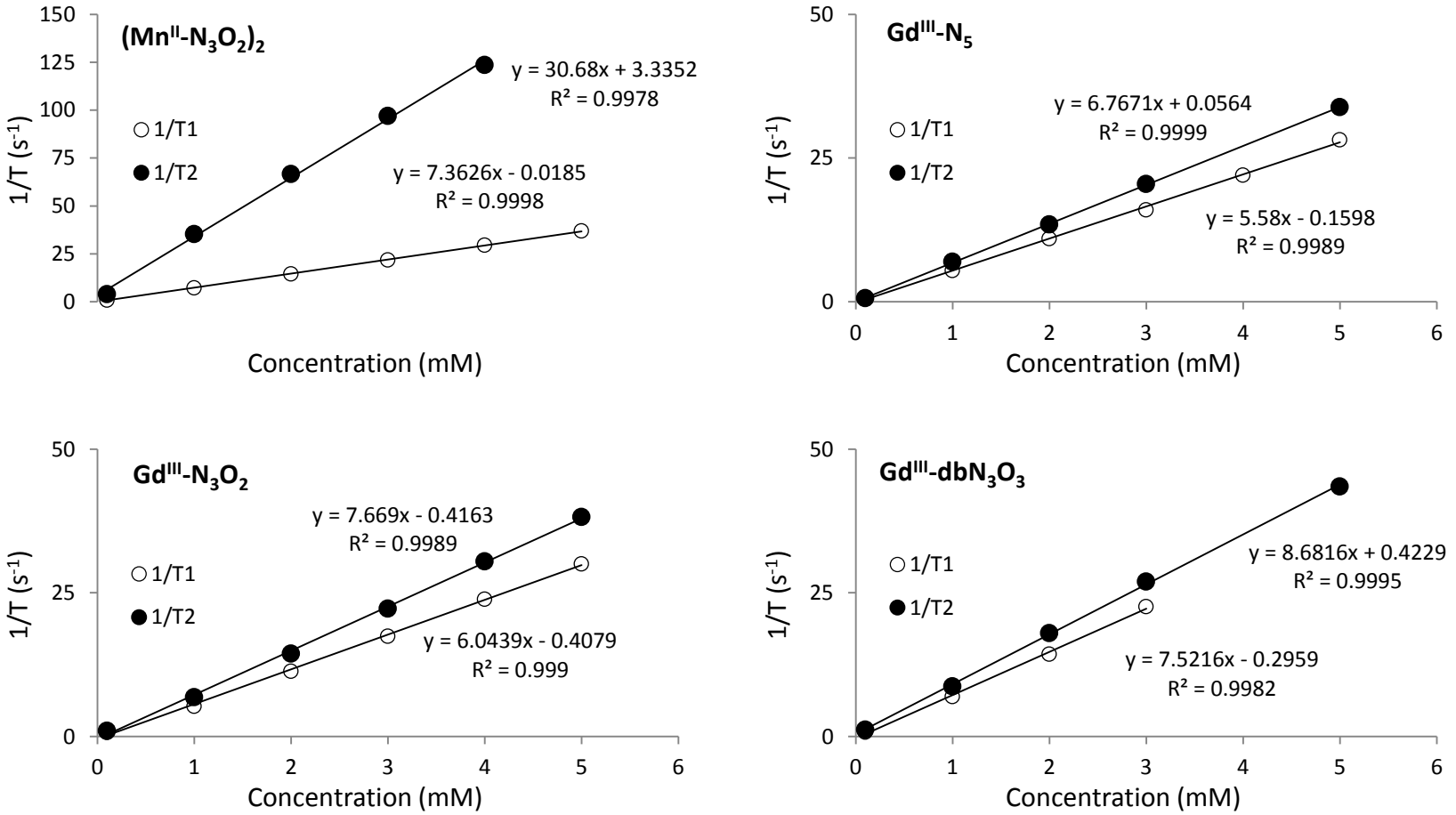

Figure 7.1 Relaxivity plots for the eight soluble, pure Mn^{II} and Gd^{III} complexes in aqueous solution (37°C, 60 MHz).